VNIVERSITAT DE VALÈNCIA

Interfaces and Connections in Vacuum Based Perovskite Solar Cells

Doctorado en Nanociencia y Nanotecnología

– PhD Thesis –

Arghanoon Moeini

Decembre 2024

Directors:

Prof. Dr. Hendrik Jan Bolink

Dr. Cristina Roldán Carmona

VNIVERSITAT DE VALÈNCIA

Dr. Hendrik J. Bolink y Dr. Cristina Roldán Carmona, Catedrático e investigadora de la Universitat de València en el Instituto de Ciencia Molecular (ICMol), certifican que la memoria presentada por la estudiante de doctorado Arghanoon Moeini, con el título "Interfaces and Connections in Vacuum Based Perovskite Solar Cells", corresponde a su tesis doctoral y ha sido realizada bajo su dirección y tutoría, autorizando mediante este escrito la presentación de la misma.

En Valencia, 2 de diciembre de 2024

Dr. Hendrik Jan Bolink	Dr. Cristina Roldán Carmona
(Director y tutor)	(Directora)

برای زنان و دختران سرزمینم

Index

Chapter 1: Introduction 11
1.1 The energy crisis 13
1.2 Photovoltaics market trend 14
1.3 The abundant energy source 15
1.4 The solar cell 16
1.4.1 The journey of the pair 17
1.5 Limitation 21
1.5.1 Intrinsic losses 21
1.5.2 Extrinsic losses 22
1.6 Perovskite 25
1.6.1 The framework 25
1.6.2 The geometry 25
1.6.3 The dance of ions 27
1.6.4 Chemistry behind the bandgaps 27
1.6.5 Perovskite for photovoltaics 30
1.7 Challenges for commercialization 30
1.7.1 Stability 32
1.7.2 Scalability 32
1.7.3 Environmental Impact 33
1.8 Fabrication 33
1.8.1 Solution based deposition methods 33
1.8.2 Thermal vacuum deposition 34
1.8.3 Fully sublimed devices 36
1.9 Hole transport materials 36
1.10 Self-assembled monolayers 36
1.11 The aim of the thesis 38
Chapter 2: Experimental Methodology and Characterization 39
2.1 Experimental methodology 41
2.2 Experimental section 41
2.2.1 Chemicals 41
2.2.2 Preparation 41
2.2.3 Active layer fabrication 43

2.2.4 solar cell of *p-i-n* stack 44
2.2.5 Module fabrication techniques 45
2.2.6 Atomic layer deposition (ALD) 48
2.3 Characterization 50
2.3.1 Thin film Characterization 50
X-ray Diffraction (XRD) 50
Nuclear Magnetic Resonance (NMR) 51
X-ray Photoelectron Spectroscopy (XPS) 51
Atomic force microscopy (AFM) 52
Scanning electron microscopy (SEM) 52
Contact angle 53
2.3.2 Optical Characterization 53
Ultraviolet-visible spectroscopy 53
Photoluminescence(PL) 54
2.4 Solar cell characterization 56
2.4.1 External Quantum Efficiency (EQE) 58
2.4.2 Hysteresis Index 59
2.4.3 Maximum power point tracking 60
2.4.4 Geometrical fill factor 60
2.4.5 Stability test 60
Chapter 3: Engineering Stable *p*-type Contacts Towards Efficient Fully Vacuum Deposited Perovskite Solar Cells 63
3.1 Introduction 67
3.2 Experimental methods 69
3.3 Results and discussion 69
3.4 Conclusion 82
Chapter 4: High-Performance Double A-Cation Perovskite Solar Cells via Co-Evaporation 83
4.1 Introduction 87
4.2 Results and discussion 88
4.3 Conclusion 97
4.4 Annex 98
Chapter 5: Co-Evaporation for Scalable Perovskite Mini-Modules: A Fully Sublimed Approach 99
5.1 Introduction 103

5.2 Results and discussion 104
5.3 Conclusion 116
5.4 Appendix Tables 117
Chapter 6: Conclusion 119
6.1 Conclusion 121
Chapter 7: Resumen en Castellano 125
7.1 Tecnología Fotovoltaica 127
7.1.1 La Celda Solar 127
7.2 Perovskita de Haluro Metálico 129
7.2.1 Fabricación 130
7.3 El objetivo de la tesis 131
7.4 Capítulo 3: 131
7.5 Capítulo 4 133
7.6 Capítulo 5 134
7.7 Conclusión 135
1 Resum en valencià 139
7.8 Tecnologia Fotovoltaica 141
7.9 La Cèl·lula Solar 141
7.10 Perovskita d'Halur Metàl·lic 143
7.11 Fabricació 144
7.12 Deposició Tèrmica en Buit 144
7.13 L'objectiu de la tesi 145
7.14 Capítol 3: 145
7.15 Capítol 4 147
7.16 Capítol 5 148
7.17 Conclusió 149
Appendix A: List of Abbreviations 153
Appendix B: List of Figures 157
Appendix C: List of Equations 165
Bibliography: 169
Acknowledgment: 187

Chapter 1: Introduction

1.1 The energy crisis

Global warming is one of the most pressing challenges faced by our current world, this is primarily caused by the uncontrolled use of fossil fuels to meet the high energy demand. The Earth´s average surface temperature has already increased by approximately 1.2°C above pre-industrial levels,[1] causing extreme weather events, air pollution and the greenhouse gas emissions are continuously increasing.[2] In order to address these concerns, the International Energy Agency (IEA) has emphasized on the need for a radical transformation of the global energy system, shifting the focus from fossil fuels towards renewable sources. Renewable energy sources are expected to east this transformation, to account for 80% of new power capacity additions by 2030.[3]

As of 2024, global energy consumption has reached approximately 620 exajoules, equivalent to around 172 terawatts of continuous power usage throughout the year. To put this into perspective, the sun's total power output is 3.9×10^{14} terawatts, emphasizing the immense potential of solar energy as a renewable resource.[4] Photovoltaic (PV), technologies that convert solar power into electricity, are expected to contribute significantly to the renewable energy market. Proof of this is that since 2020, investment in the clean energy sector has risen by 40%, a trend anticipated to continue.

Among renewable energy sources, solar power has been a leading option due to its abundant supply, widespread availability, and minimal environmental impact. The shift towards solar energy is viewed as a key strategy in mitigating global warming and reducing air pollution caused by the energy sector.[5] As depicted in **Figure 1-1**, solar energy sources are expected to contribute substantially to increasing global energy generation in the coming years, highlighting the expansive potential of this renewable alternative.

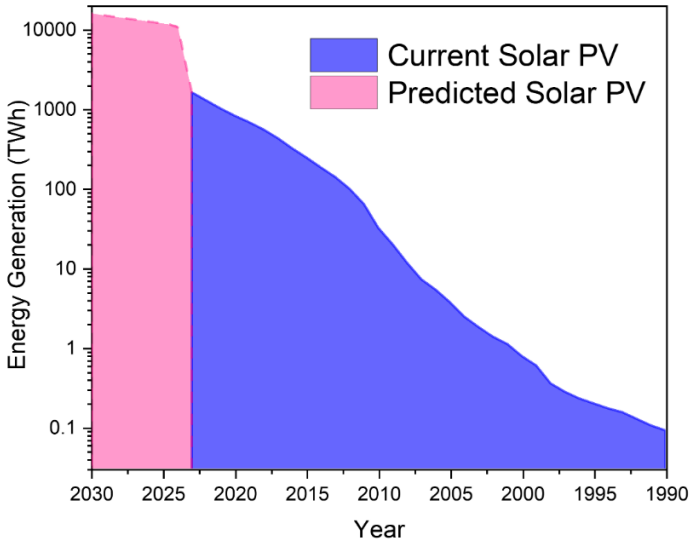

***Figure 1-1**: Historical and predicted generated energy from photovoltaic technologies from1999-2030.[4]*

1.2 Photovoltaics market trend

The PV market is currently dominated by crystalline silicon technology, which accounts for approximately 95 % of the market. While the highest efficiency attained with single junction silicon-based solar cells has reached more than 26-27% thus far, and continues to improve, the high complexity and associated costs of manufacturing highlights the need for concurrent research and development of alternative solar cell technologies.[6]

The second generation of PV technologies includes thin-film approaches such as cadmium telluride (CdTe), amorphous silicon (a-Si), and copper indium gallium selenide (CIGS). While these technologies exhibit lower efficiencies compared to first-generation silicon-based cells, they offer advantages in terms of flexibility and reduced fabrication costs. These thin-film technologies are well-suited for large-scale utility projects and building-integrated photovoltaic applications.[7]

The third generation of emerging photovoltaic technologies include novel materials and designs, including organic photovoltaics (OPVs), dye-sensitized solar cells (DSSCs), quantum dots, Gallium Arsenide (GaAs), multi-junction cells, and most significantly, perovskite solar cells (PSCs). The key advantages of this category are the potential for lower costs using cheaper materials and simpler manufacturing processes, as well as the possibility of combining different technologies to achieve efficiency levels exceeding 40% in laboratory settings.[8,9] As these generations of PV technologies enter the market, they change the distribution of shares within the PV market, as illustrated by **Figure 1-2** over the past 20 years.

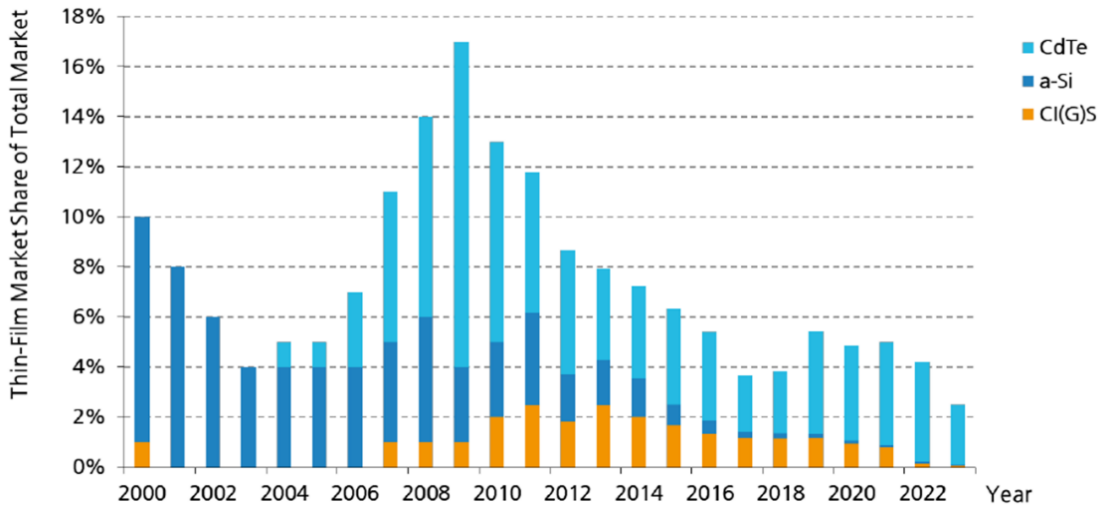

***Figure 1-2**: Market share distribution of thin-film PV in the commercial sector (2020-2023). Adapted from reference [5]*

1.3 The abundant energy source

The sun is considered a blackbody emitter, in other words, an ideal object that absorbs all incoming radiation without any reflection, and emits radiation only based on its temperature. The average solar irradiance reaching Earth is estimated to be 1,361 watts per square meter.[10] However, this value fluctuates based on various atmospheric factors. These include absorption and scattering effects, as well as local conditions such as water vapor, clouds, and pollution. Furthermore, the latitude, season, and time of day influence the distance traveled by solar radiation, leading to variations in the irradiance reaching the Earth's surface. Despite these factors, the energy received by the Earth's surface in one hour exceeds our current total annual energy consumption.[11]

The amount of energy received on Earth can be quantified by the concept of air mass (AM). AM is a measure of the path length that sunlight travels through Earth's atmosphere before reaching the surface, causing a reduction in light power. This relationship is expressed mathematically as

$$Air\ Mass = \frac{1}{cos\theta} \qquad \textbf{Equation 1—1}$$

where θ represents the zenith angle, which is the angle between the sun and the vertical. **Figure 1-3-a** shows a schematic representation of the AM0 (no atmospheric interface) and AM 1.5 (at zenith angle of 48.2°) which is approximately the sunlight conditions at mid-latitudes on a clear day). **Figure 1-3-b** illustrates the solar intensity spectrum as a function of wavelength.[12]

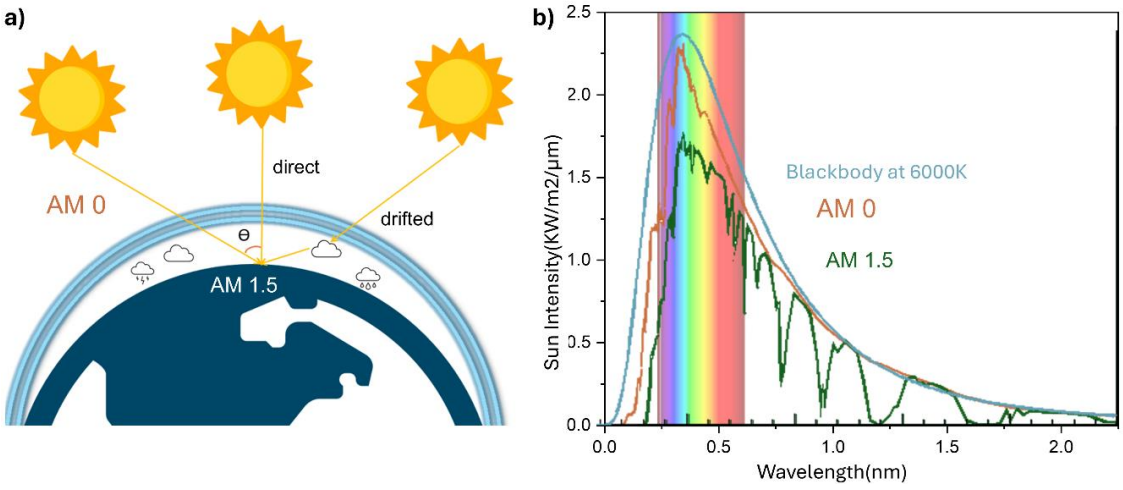

Figure 1-3: a) *Schematic of sun radiation towards the earth.* ***b)*** *The spectral irradiance from the sun as a black body, just outside the atmosphere (AM0) and (AM1.5G) terrestrial solar spectrum.*

The AM 1.5 solar spectrum represents a realistic average condition for many locations on Earth, where sunlight travels through 1.5 times the atmosphere's thickness compared to when the sun is directly overhead. This standard is widely used for testing and rating the performance of solar panels, as it results in an average irradiance of approximately

1,000 W/m^2 at the Earth's surface. The American Society of Testing and Materials (ASTM) organization responsible for developing standard procedures for material testing has defined the ASTM G197-14 standard, referred to as AM1.5G, as an internationally recognized reference spectrum for solar irradiation, encompassing both direct and diffuse components of solar radiation reaching the Earth.[13] This spectrum has been consistently utilized as the standard for solar irradiance analysis in the present thesis, representing typical conditions when the sun is at an angle of about 48° above the horizon.[14]

1.4 The solar cell

The sun's rays, upon reaching Earth, can be harnessed into generating electricity through the photovoltaic effect. The photovoltaic effect is the fundamental mechanism that enables the conversion of sunlight into electrical energy in solar cells. This phenomenon occurs when photons are absorbed by semiconductors, exciting electrons to higher energy states. These excited electrons later could lose this energy in the form of heat. If the energy of the incident photons exceeds the energy difference between the highest occupied molecular orbital (HOMO) and lowest unoccupied molecular orbital (LUMO) for organics, or the valence band (VB) and conduction band (CB) for inorganic semiconductors, electron-hole pairs will be generated. Electrons are thus elevated to the CB while leaving behind "holes" in the VB. This can only happen if the incident photon energy equals or exceeds the material's energy difference between the valence band maximum and the conduction band minimum, known as the band gap (E_g).

The band gap is an inherent material property that can be either direct or indirect in nature. Schematic diagrams in **Figure 1-4** illustrate the a) indirect and b) direct bandgap mechanisms. The excited electrons and remaining holes are the mobile charges that give the material its unique transport properties and enables the photovoltaic effect.[15]

The predominant technology in the current photovoltaic market relies on silicon that has an indirect bandgap which requires higher thickness and a higher energy input to produce a comparable power output when contrasted with direct bandgap semiconductor materials. Whereas direct bandgap materials can harvest the available sunlight using much less material in thin films with thicknesses in the range of a micrometer.[16]

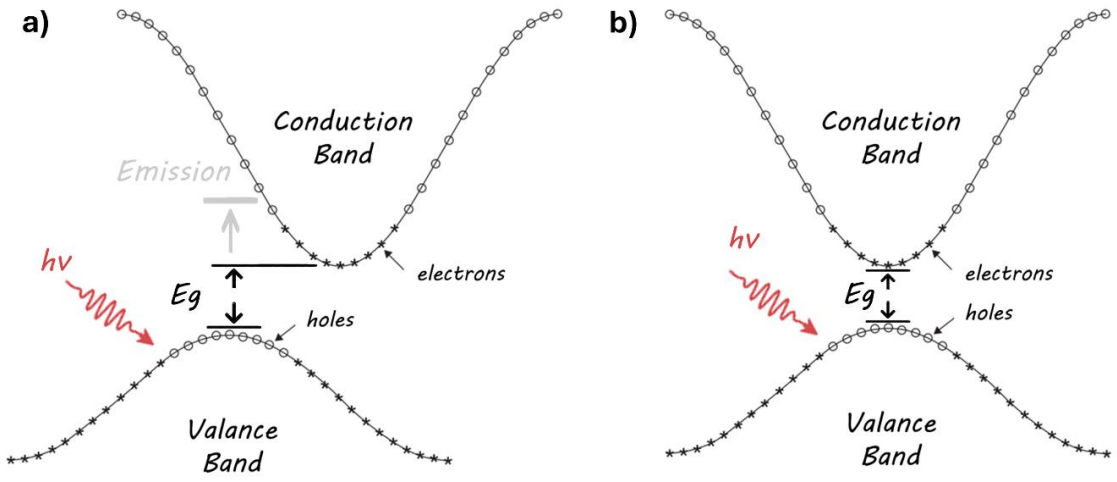

Figure 1-4: *The schematic of the* ***a)*** *indirect bandgap material and* ***b)*** *direct bandgap material.*

The proportion of incoming radiation that is absorbed per unit distance at each wavelength is called absorption coefficient. Materials with a high absorption coefficient can absorb a significant portion of incident light even when present in very thin layers, thereby enhancing the efficiency of photon-to-electron conversion and consequently minimizing the material costs. Thin film PVs such as CdTe and perovskite have a high absorption coefficient in contrast to the crystalline silicon.[17]

1.4.1 The journey of the pair

To optimally convert solar rays into electrical energy, the formation and dynamics of electron-hole pairs should be studied. These charge carriers, driven by an internal electric field, move toward respective electrodes, ultimately generating an electric current when connected to an external circuit. The efficiency of the conversion is heavily influenced by factors such as charge carrier dynamics, carrier lifetime, and the effectiveness of charge separation and extraction through the device's electrodes.

Photo-induced charge carriers dynamics

When photons with energy equal to or greater than the material´s bandgap is absorbed, it generates electron-hole pairs. In certain materials, especially those with lower dielectric constants, these pairs can form bound states known as excitons due to the Coulombic attraction between the electron and hole. The dielectric constant is a measure of the material's ability to reduce this attraction, influencing whether free carriers or excitons are formed. Excitons can decouple into free carriers in the absorber material, with the binding energy determining how easily this dissociation occurs at room temperature. Once these carriers are free, they have certain diffusion lengths and mobilities. The diffusion length represents the distance carriers can travel before interacting with the material again, while mobility describes their ease of movement under an electric field. Both properties are essential for efficient charge separation and extraction, which directly impact solar cell performance and energy conversion efficiency.

Carrier lifetime

The carrier lifetime, which is a material-dependent property, refers to the average time an electron or hole exists before annihilation. In more technical terms, the lifetime of the active material equals the amount of time that the minority carriers persist before being neutralized. The longer the carrier lifetime, the higher the probability that these charge carriers will be collected by the external circuit before they recombine. Speedy recombination results in lost energy that could have contributed to electricity generation, making carrier lifetime a crucial parameter in solar cell performance. Materials like crystalline silicon (1 µs to 1 ms)[18]and perovskites (100 ns to 20 µs)[19] have longer carrier lifetimes in comparison to other photovoltaics, making them appealing for commercial use.

Recombination is a process where electrons and holes reunite, releasing energy in the form of heat. This can occur through radiative recombination, which involves the direct interaction of an electron with a hole, leading to the emission of a photon. Alternatively, nonradiative recombination can take place where the energy is transferred to other particles and dissipated as heat (**Figure 1-5-a**). One form of nonradiative recombination is Auger recombination as shown in **Figure 1-5-c**, where the energy is transferred to another electron or hole, which then loses this energy as heat. Another common nonradiative mechanism is the Shockley-Read-Hall(SRH) recombination, where defects within the semiconductor create energy levels inside the bandgap. These energy levels serve as traps for electrons or holes. An electron may first be captured by a trap, then a hole is captured by the same trap, leading to recombination. The energy released during this process is typically transferred to the lattice as phonons, resulting in heat rather than light, leading to energy losses. Recombination losses can also be induced by the interfaces for charge collection. (**Figure 1-5-d**)

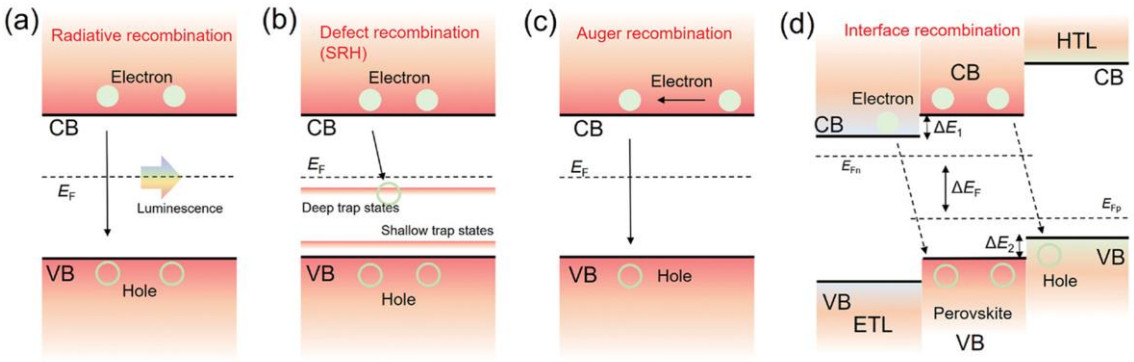

Figure 1-5: *Different types of recombination mechanism of electron-hole pair. adapted from reference* [20]

In practical solar cells, trap-assisted recombination (**Figure 1-5-b**) is often the dominant mechanism, leading to significant energy losses. Having a material with high defect tolerance is crucial for minimizing these recombination losses in the design and optimization of high-efficiency solar cells. While an ideal, defect-free material is almost

impossible to achieve, photovoltaic materials with high defect tolerance can maintain superior performance despite the presence of defects, such as vacancies, interstitials, and grain boundaries, which can act as recombination sites for charge carriers. Among all PV material technologies, perovskites[21] demonstrate this capability, attaining high efficiencies even with a relatively high density of defects. In contrast, materials like GaAs and c-Si require considerably greater purity and defect control to achieve their high efficiencies.[22]

Separation of the carriers

The mere presence of long-lived charged carriers without efficient separation is insufficient for effective solar energy conversion without their proper separation. Because they will eventually recombine, leading to energy losses rather than electricity generation. A key factor in free charge carrier separation is the material's permittivity (dielectric constant) which has an inverse relationship with exciton binding energy, where lower exciton binding energy promotes more effective charge separation. Materials like perovskite and GaAs exhibit the highest dielectric constants among common photovoltaic materials, further facilitating efficient charge separation.[23–25] The concept of Fermi level (E_f), which is the energy at which the probability of finding an electron is 50% at absolute zero, reflecting the equilibrium distribution of electrons becomes important at this stage. In intrinsic semiconductors, the E_f is typically located near the center of the bandgap. (**Figure 1-6-a**). By introducing impurities (doping), E_f can be shifted closer to the CB in *n*-type materials or the VB in *p*-type materials, effectively altering the electron or hole concentrations.

By sandwiching the absorber layer between p-type and n-type materials, a *p-i-n* junction can be established. In this structure, the intrinsic layer (*i*-layer) provides a region for photon absorption and carrier generation, with the built-in electric field facilitating carrier transport toward opposite sides (**Figure 1-6-b**). Having a *p-i-n* junction, a precise alignment of band diagrams positions(the CB and VB, or the HOMO and LUMO levels in organic materials) is needed for the transfer of the carriers. Though introducing additional interfaces may increase complexity and the potential for recombination, the *p-i-n* structure remains the main strategy for maximizing PV performance by improving charge separation and extraction.[26]

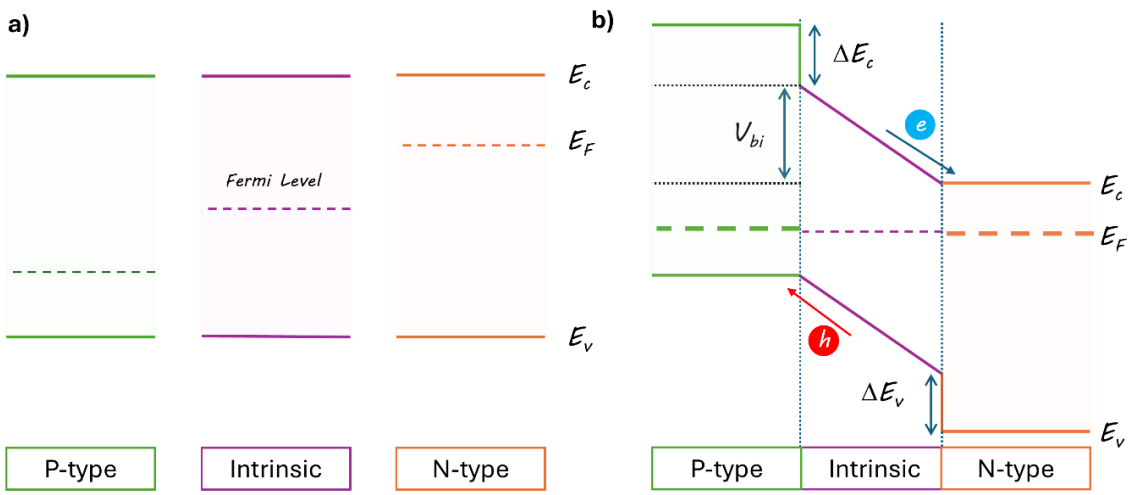

Figure 1-6: *The potential profile of a p-i-n junction,* ***a)*** *in equilibrium state and* ***b)*** *sandwiched with extrinsic doped semiconductors and the introduction of the built-in electric field.*

Charge extraction

After the generation of free charged carriers and keeping them from recombination by making an internal electric field, the final step in achieving effective solar cell is the extraction of these carriers. A key parameter influencing charge injection and extraction is the work function (ϕ), defined as the energy required to remove an electron from the E_f to the vacuum level. Material-specific properties, such as electron affinity and ionization potential, define the relative band alignment. The polarity of the incorporated material defined by the electric dipole moment (μz) is the assisting elements in this process.[27–29]

To facilitate charge separation and minimize recombination losses, devices commonly incorporate electron and hole transport layers (ETL and HTL). Typically, a transport layer consists of a material selectively permeable to one type of charge carrier to ensure selective passage of one charge carrier type while blocking the other. The selective materials chosen for these layers should exhibit high electron and hole mobilities to ensure efficient charge collection while minimizing losses. Additionally, these transport layers must exhibit smooth, defect-free surfaces for uniform charge transport and optimal contact with the absorber layer.

The electrodes are vital for charge extraction and must form ohmic contacts with minimal resistance. Typically, transparent conductive oxides(TCO), such as indium tin oxide (ITO) or fluorine-doped tin oxide (FTO), are used for the front electrode, allowing light to enter the device while maintaining conductivity. A reflective metal electrode serves as the counter electrode. The device structure can vary between *p-i-n* and *n-i-p* configurations, with the order of layers determining the charge extraction direction. **Figure 1-7** shows both device structures with their corresponding layers.

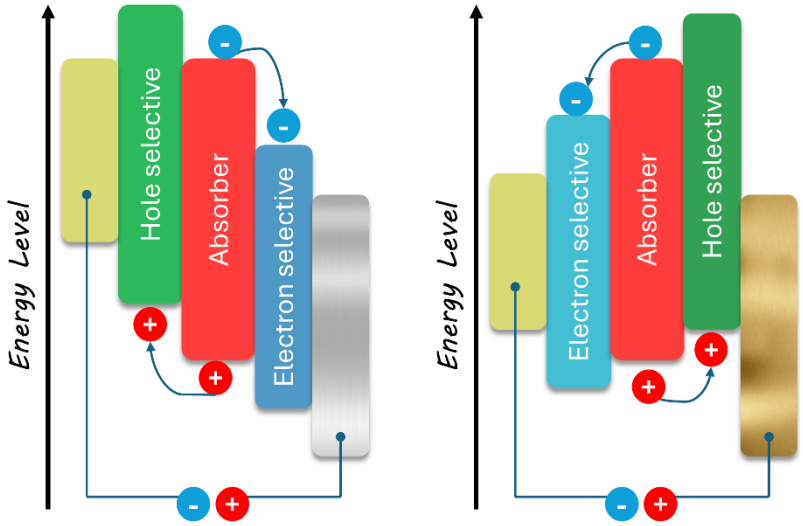

Figure 1-7: *The extraction and injection mechanism in p-i-n (**left** panel) and n-i-p (**right** panel) single junction solar cell.*

1.5 Limitation

There are several commonly occurring imperfections in photovoltaic devices, leading to limitations. In general, the losses are categorized into intrinsic losses and extrinsic losses, the intrinsic limitations are normally associated with the property of the materials, and they are more complicated to overcome however the extrinsic losses can be avoided.

1.5.1 Intrinsic losses

Solar cells face inherent limitations that prevent the complete conversion of sunlight into electrical energy. These include losses from insufficient photon energies, thermalization, radiative recombination, Carnot and angle mismatch. While unavoidable in single-junction devices, innovative designs can mitigate some of these fundamental efficiency constraints.[27]

Radiative limit

The Shockley-Queisser limit, often referred to as the radiative efficiency limit, defines the theoretical maximum efficiency of a single-junction solar cell depending on the material bandgap. **Figure 1-8-a** shows the maximum achievable efficiency for each band gap.[28] Assuming that radiative recombination is the only unavoidable form of recombination, the lifetime of the minority carriers can be considered at its maximum potential. This allows for the calculation of a 33.16% (under AM 1.5G illumination) maximum efficiency at a cell temperature of 300 K, corresponding to a semiconductor bandgap of 1.34 eV. The analysis of Shockley and Queisser assumed that photons with energy below the bandgap do not interact with the solar cell, while all photons with higher energy are absorbed, generating electron-hole pairs. Their model also included several simplifying assumptions, such as one electron-hole pair per photon and excess photon

energy being lost as heat, as well as non-concentrated sunlight illumination. While these assumptions facilitated the efficiency limit calculation, they do not fully capture the complexities of real-world solar cells. **Figure 1-8-b** shows different types of photovoltaics and their potential for high efficiency, with GaAs having the theoretically highest efficiency for a bandgap of about 1.42 eV, which is very close to the optimal bandgap for single-junction solar cells.[29]

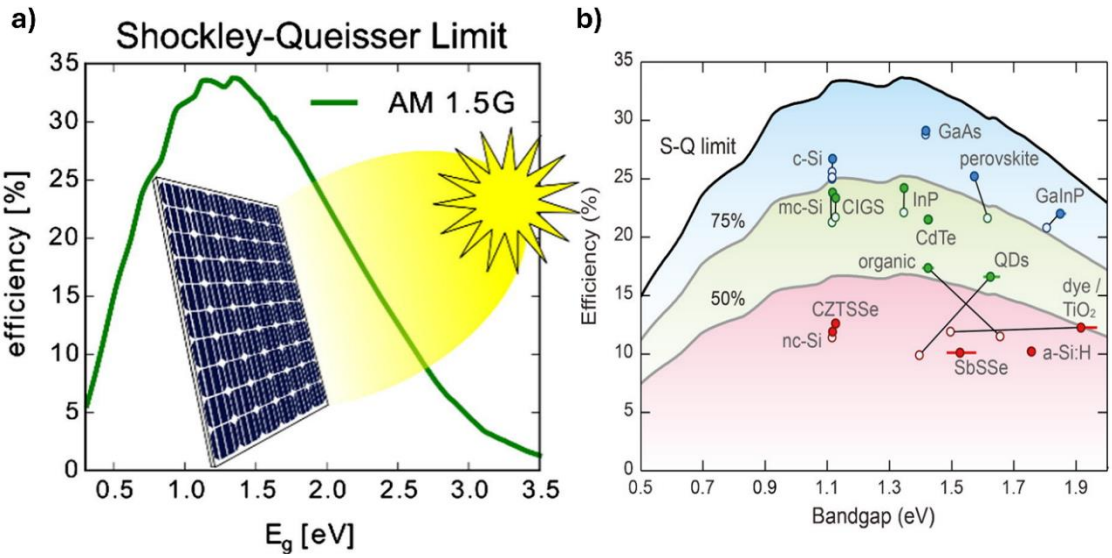

Figure 1-8: a) *The maximum theoretical conversion efficiency of the solar cell base on the radiative limit as a function of its bandgap adapted from reference [28]. **b)** Different single junction photovoltaic materials efficiency based on the radiative limit adapted from reference [30]*

To surpass this radiative limit several strategies have been explored including multi-junction solar cell architectures, which employ materials with different bandgaps to capture a broader range of the solar spectrum, light management techniques and reducing the recombination by bulk or surface passivation techniques. Additionally, integrating various PV technologies or utilizing concentrator systems to increase the illumination intensity on the solar cell have been applied.[30]

1.5.2 Extrinsic losses

Additionally, there are extrinsic limitations that are caused by factors such as design choices, fabrication defects, and external environmental conditions. These extrinsic limitations can be categorized as non-radiative recombination losses, series resistance losses, shunt resistance losses, parasitic absorption losses, and shadowing losses. Unlike the intrinsic limitations, these extrinsic factors can be minimized or avoided through careful device design and optimization.[31–33] Minimizing these loss mechanisms is one of the main steps for improving solar cell efficiency. There are various loss mechanisms in a PV cell, some illustrated in **Figure 1-9**, most of which are outside the scope of this work and the complexity of the topic encourages targeting each area indiviually.[34,35]

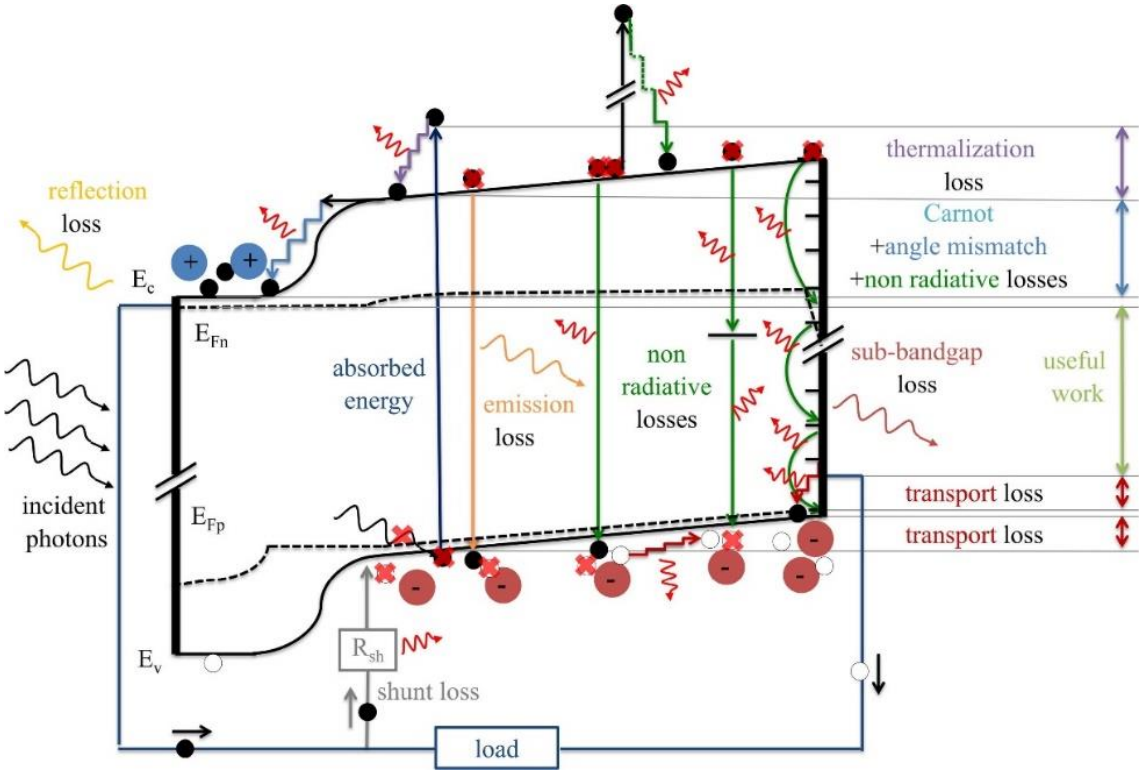

Figure 1-9: *The conversion loss mechanisms of a PV cell illustrated on a p–n junction diagram adapted from reference* [36]

Interface losses

Non-radiative recombination generally is one of the major factors limiting the efficiency of solar cells, and significant research has focused on minimizing it. However, non-radiative recombination at the interfaces is considered a more dominant issue and it needs to be studied on its own. Additionally, mismatch losses caused by the interface's misalignment contribute to interface limitations and has been a major focus of chapter 3 of this thesis.

Bulk non radiative recombination losses

Trap-assisted recombination, also known as Shockley-Read-Hall recombination, is a form of non-radiative recombination that can be attributed to defects within the absorber layer. The fabrication of a defect-free absorber layer, or one that is more resistant to defects, can reduce these losses in solar cells. This has been extensively investigated in chapter 4 of this thesis.

Shadowing losses

The total area of the solar cell determines its efficiency; a reduction in the active area for facilitating interconnection of cells in series would lower the generated voltage. As solar cells are scaled up from the laboratory to the industrial module scale, optimizing the utilization of the available area becomes increasingly crucial. **Chapter 5:** of this thesis,

among other aims, has investigated approaches to address contact shading limitations and minimize losses in active areas.

To overcome extrinsic limitations, the development of novel materials has become a focal point in enhancing solar cell efficiency. Among these, perovskite materials have attracted significant attention due to their unique properties, including tunable bandgaps, high absorption coefficients, and relatively low-cost processing. The versatility and high potential efficiency of perovskite solar cells position them as a strong contender to rival traditional photovoltaic technologies.

1.6 Perovskite

In 1839, the German mineralogist Gustav Rose discovered a remarkable mineral comprising calcium, titanium, and oxygen, ($CaTiO_3$) and he chose to honor Perovski, a Russian mineralogist, by designating this newly found mineral as "perovskite." Rose could not have anticipated that this discovery would pave the way for a groundbreaking new domain in the field of materials science either. [37]

Fast forward to 1926, when Victor Goldschmidt, a pioneering crystallographer, explored the structural complexities of crystals. During his research, Goldschmidt adopted the term "perovskite" to describe a specific group of crystals that shared this distinct structure. His work popularized the use of "perovskite", forever linking Perovski' s name to one of the most significant and versatile crystal structures known today.

1.6.1 The framework

Perovskite refers to a wide variety of synthetic and natural materials that share a common crystalline structure with formula ABX_3, where A is typically a monovalent cation, B is a metal cation (often divalent), and X is an anion, usually a halide. The three-dimensional (3D) perovskite structure is primarily held together by ionic bonds and consists of corner-sharing $[BX6]^{4-}$ octahedra, with the A cations occupying the interstitial sites or cavities formed by the octahedral framework.

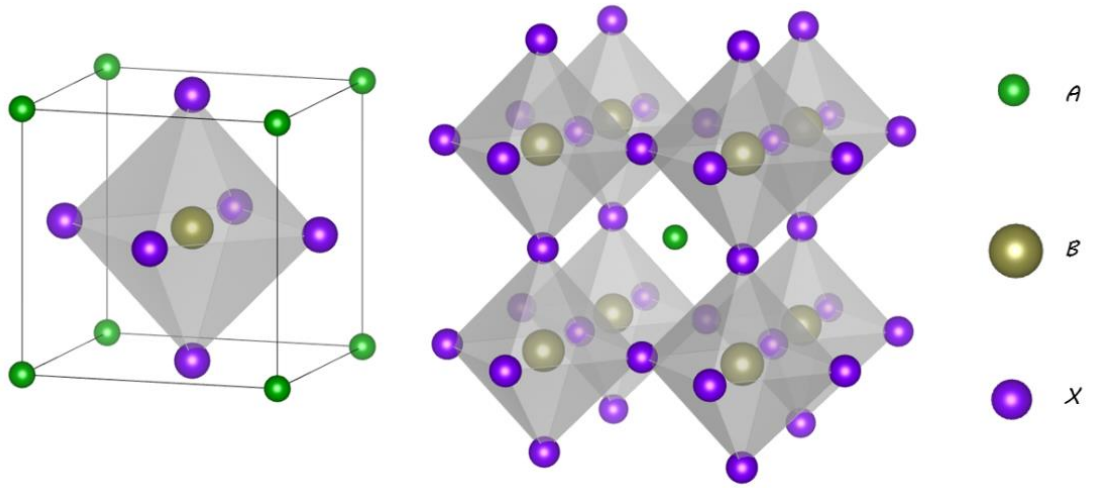

Figure 1-10: *Perovskite unit cell for 3D structure illustration.*

1.6.2 The geometry

A critical concept in determining whether this 3D perovskite structure can form is the atomic radius of its components. This concept, known as the Goldschmidt tolerance factor, predicts the stability of the perovskite crystal structure based on the ionic packing within the material. When the ratio of the ionic radii falls within the range of 0.7 to 1.1, the perovskite structure is likely to form in a stable manner, making it a versatile and widely applicable material in various fields, including solar cells, superconductors, and more.

$$t = \frac{r_A + r_x}{\sqrt{2}(r_B + r_x)}$$ **Equation 1—2**

Where r_A, r_B, and r_X are the ionic radii of A, B, and X, respectively. With *t* values between 0.8 and 1.0, the formation of a cubic perovskite structure is favorable. For the smaller values from the range the A-site cation is too small and bigger on the contrary.[38,39]

To further understand the details of the octahedral arrangement formed, the octahedral factor (μ), which is the ratio of the atomic radii of the center component to the adjacent anions, is often considered in selecting a suitable B-site cation and achieving a stable cage environment of 6 anions for the perovskite structure. This factor is typically expected to fall within the range of 0.4 to 0.7.

$$\mu = \frac{r_B}{r_x}$$ **Equation 1—3**

In photovoltaics, A site cations are normally small organic molecules such as methylammonium (MA= CH_3NH_3), formamidinium (FA= $CH(NH_2)_2$, CH_3NH_3), or small ions such as Cs^+. Additionally, by incorporating a mixture of different A-site cations, the crystal structure can be fine-tuned in view of the tolerance factor. B site is typically a metal cation like Pb^{2+} or Sn^{2+} and X is a halide or a mixture of them.[40,41]

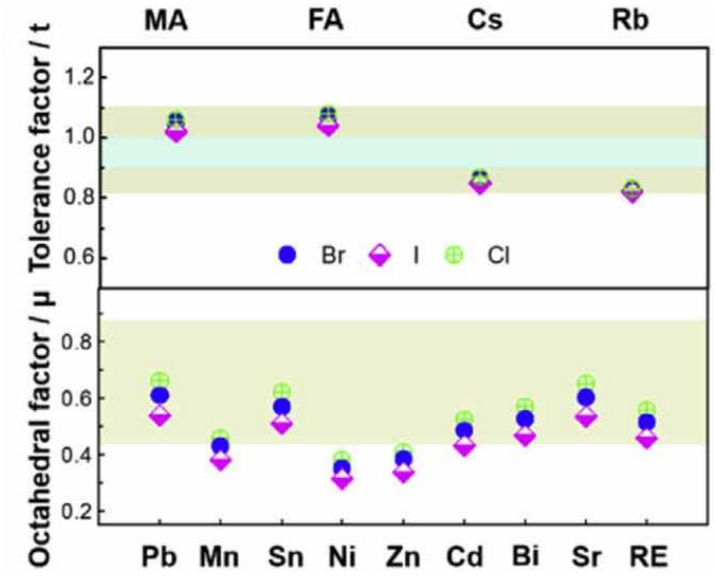

Figure 1-11: *The possible A and B site cations for the perovskite based on tolerance and octahedral factor. Adapted from reference [40]*

1.6.3 The dance of ions

Distortions from the ideal cubic perovskite structure can arise due to size change between the components, leading to the formation of non-perovskite structures. When the $t \sim 1$, the perovskite tends to have symmetric stable cubic structure. If we consider the unit cell a cube the length of the edges a, b and c are considered equal (a=b=c) However, as the tolerance factor decreases, the perovskite structure may shift first to tetragonal where one of the edges is elongated (a=b≠c) and with lower amount to the orthorhombic phase where another edge change size and hence none of the edges are equal (a≠b≠c) configurations, reflecting reduced symmetry. In all the above mentioned cases the angle between the edges is perpendicular. Under unconventional conditions, such as high pressure, other phases like hexagonal or low-dimensional structures (e.g., 2D perovskites) may form, though these are outside the scope of this discussion.

Temperature affects the crystal structure; as it increases, phase transitions can occur, altering the symmetry. These structural changes induced by the components and temperature can significantly influence the optoelectronic properties of the material, such as bandgap, carrier mobility, and stability, affecting the performance of devices. The perovskite crystal structure and its phases are sensitive to the specific chemical composition. For instance, cesium lead bromide perovskite ($CsPbBr_3$) typically exhibits a cubic phase at higher temperatures (**Figure 1-12-a**) but transitions to a tetragonal phase as the temperature decreases (**Figure 1-12-b**), and further to an orthorhombic phase at even lower temperatures (**Figure 1-12-c**).[42,43]

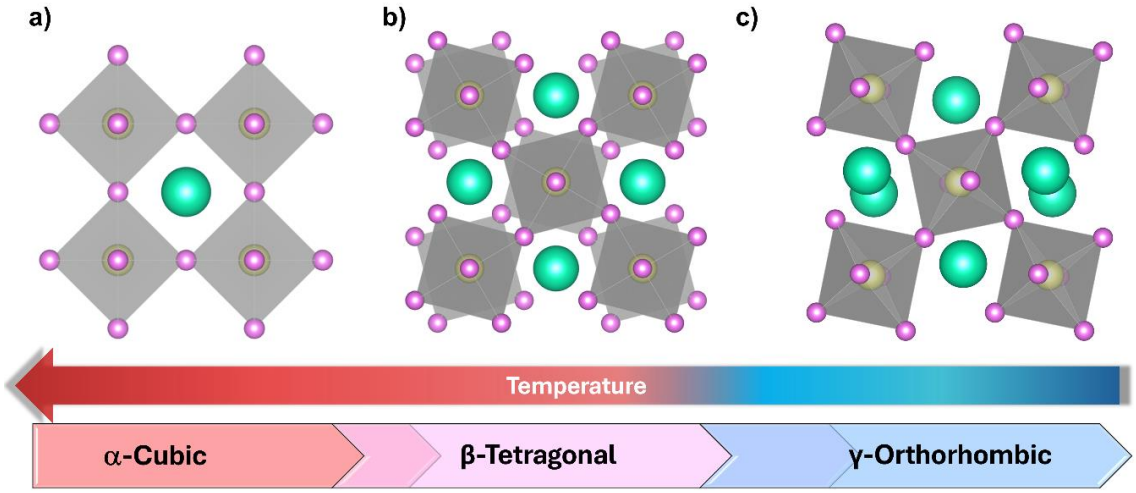

Figure 1-12: a)*Cubic phase of $CsPbBr_3$ achieved in high temperature.* ***b)****Tetragonal phase in middle temperature.* ***c)*** *Orthorhombic phase of the inorganic perovskite in room temperature.*

1.6.4 Chemistry behind the bandgaps

The bandgap of perovskite materials can be tuned by adjusting their chemical composition. Substituting the halide anions with less electronegative species leads to redshift in the bandgap, affecting both the conduction and valence band positions.

Additionally, replacing the lead with tin reduces the bandgap, while incorporating larger cations at the A-site causes distortion in the structure, influences the VB and can increase the overall bandgap. However, its effect on the bandgap is not as significant as halide change.[44]

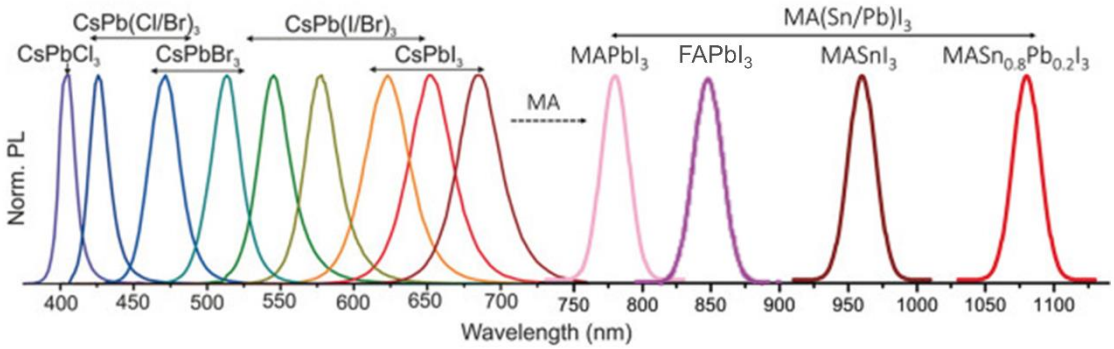

Figure 1-13: *Illustration of bandgap change in form of is the photoluminescence for different perovskite compositions adapted from reference [45]*

Based on the Shockley-Queisser limit, the highest achievable solar cell efficiency occurs at a bandgap of approximately 1.48 eV.[28] To reach this optimal bandgap, the composition of the perovskite material must be altered. For instance, the widely studied and easily fabricated $MAPbI_3$ perovskite has a bandgap of around 1.58 eV.

In perovskite photovoltaics, commonly utilized small cations include Cs, MA, and FA, as they enable the tolerance factor to fall within an optimal range for perovskite formation. Larger alternative cations, such as methylene diammonium, acetamidinium, and guanidinium, are also capable of forming halide perovskites; however, these can induce crystal structure distortions that may lead to phase instability.[46] Among conventional cations, FA is relatively large (**Figure 1-14-a**), contributing to a favorable optical bandgap and enhanced thermal stability (**Figure 1-14-b**). Nonetheless, $FAPbI_3$ is not stable at room temperature. To address this, halide alloying has been explored to improve stability, yet halide migration upon illumination can shrink crystal dimensions, diminishing the active material's stability. Additionally, substituting Pb with Sn has been investigated, but Sn's susceptibility to oxidation can adversely affect device stability.[47] A promising approach is to mix A-site cations in precise ratios to achieve higher efficiencies. As shown in **Figure 1-14-c**, various compositional adjustments can be made to retain a cubic and stable perovskite structure.

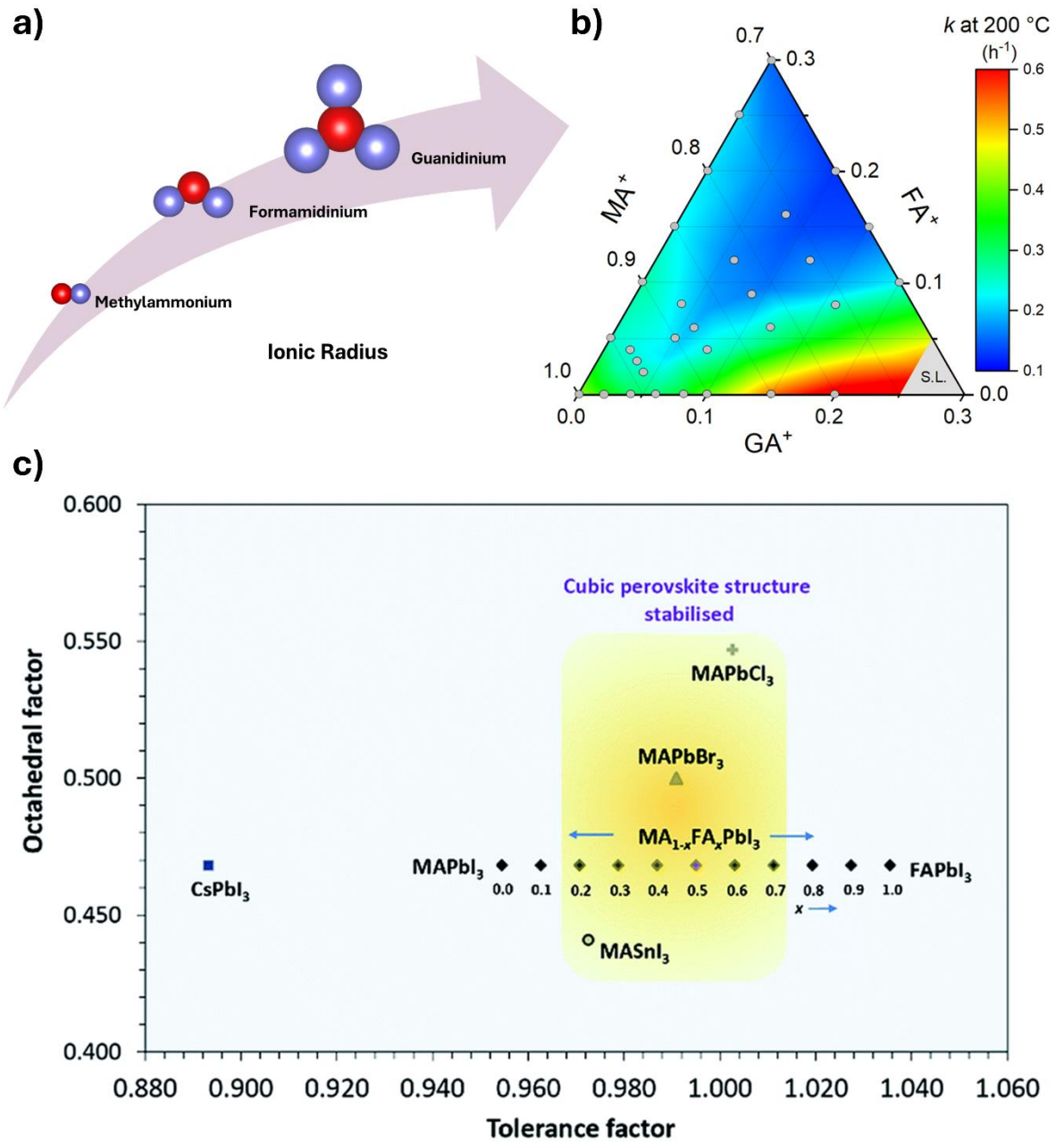

Figure 1-14: a) *Schematic of size increment in MA, FA and Guanidinium cation.* ***b)*** *Compositional mapping of cation degradation gained with thermogravimetry analysis (TGA) for the cations at 200C based on their thermal degradation rate adapted from reference [48]* ***c)*** *Perovskite crystal stability factor for hybrid lead halide composition of $MA_{1-x}FA_xPbI_3$, considering $0.3 < x < 0.8$ shows the greatest structural stability in cubic phase adapted from reference [49]*

1.6.5 Perovskite for photovoltaics

Perovskite absorbers have been used extensively in the last 15 years to prepare photovoltaic devices. They are promising materials for PV and other optoelectronic applications considering the following reasons**:**

- **Tunable Bandgap**: Perovskite materials offer a tunable bandgap ranging from approximately 1.2 eV to 2.3 eV, achieved through modifications in chemical composition. This tunability makes perovskites adaptable to various photovoltaic applications.[50]
- **Low Exciton Binding Energy**: Exhibiting low exciton binding energies, typically between 2–25 meV, perovskites enable efficient exciton separation, critical for optimizing solar cell performance.[51,52]
- **High Absorption Coefficient**: With optical absorption coefficients often exceeding 10^5 cm^2, perovskites can efficiently absorb light even in thin layers allowing for thin film photovoltaic technologies. [50]
- **Long Diffusion Length**: Perovskites demonstrate long carrier diffusion lengths, generally between 1–10 micrometers, which aids in reducing recombination losses and enhances overall solar cell efficiency.[53,54]
- **High Defect Tolerance**: Known for their high defect tolerance, perovskites maintain robust performance despite the presence of defects, which would typically compromise device efficiency in other materials.[55]

1.7 Challenges for commercialization

The perovskite solar cell efficiency has been steadily increasing since 2009,[56] reaching a record of 26.7%. [57] **Figure 1-15** shows the evolution of different PV cells' efficiencies over the years. However, for PSCs to transition from laboratory-scale success to widespread commercial adoption, significant challenges must be addressed, particularly in the areas of stability and upscaling.

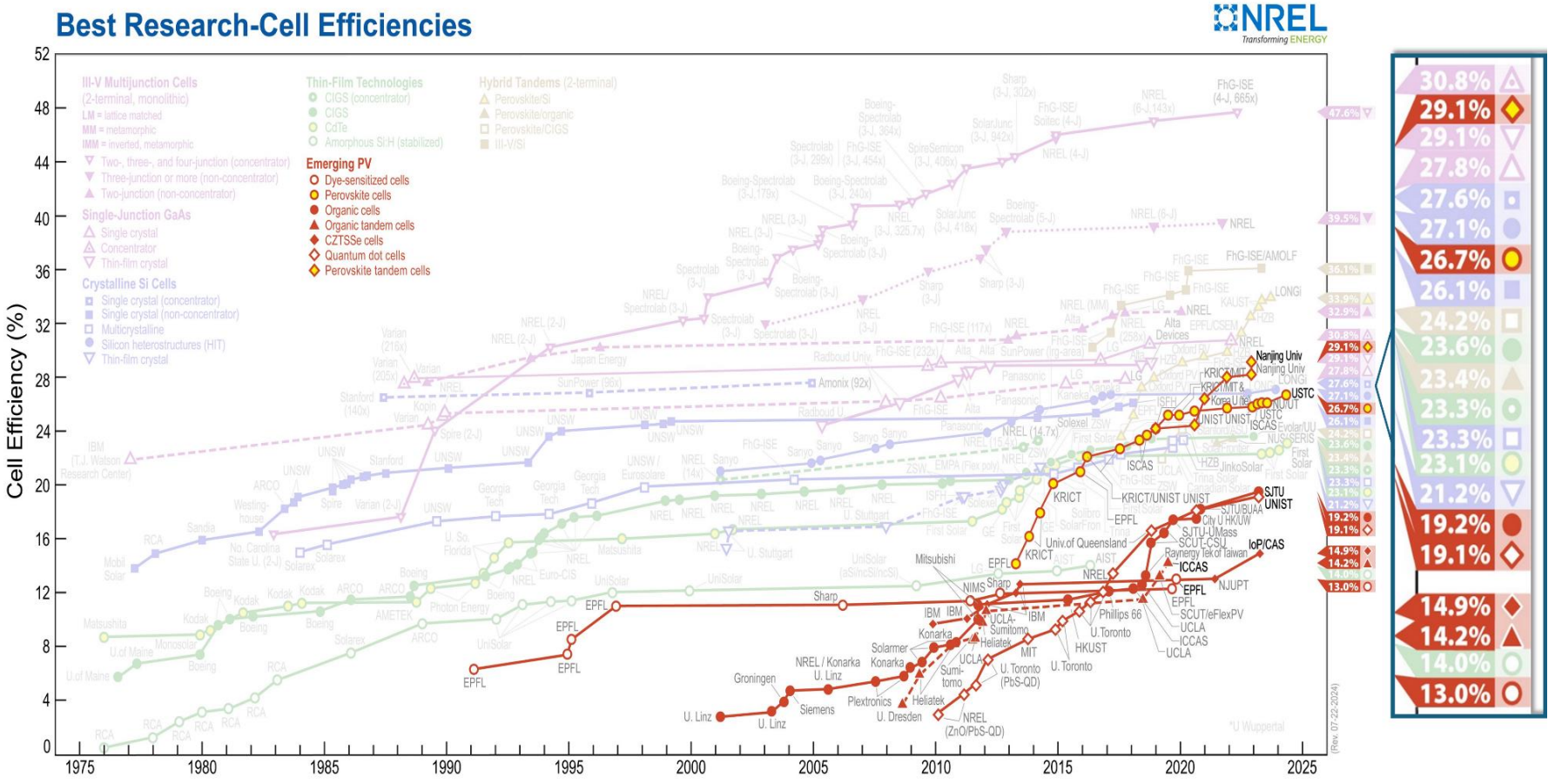

Figure 1-16: *Best solar cell efficiencies chart throughout years of research with focus on emerging photovoltaics adapted from NREL website.*

1.7.1 Stability

The golden triangle for commercialization of perovskite is an equilibrium between cost, efficiency and durability. Stability remains one of the most critical barriers to commercialization. Unlike traditional silicon-based PV technologies, which can sustain over 80% of their initial performance for more than 25 years, PSCs are prone to degradation under environmental stresses such as light, heat, and moisture. Considering their lower fabrication cost even if they would have a shorter lifetime, they might still be justified however the current stability reports are not enough for commercialization and research is being focused on it. The adoption of the ISOS protocols in testing and evaluating stability has become crucial, providing standardized procedures to ensure that these improvements are accurately measured and comparable across different studies. **Figure 1-17** shows a comparison of the different influential parameters for market entry.[58–61]

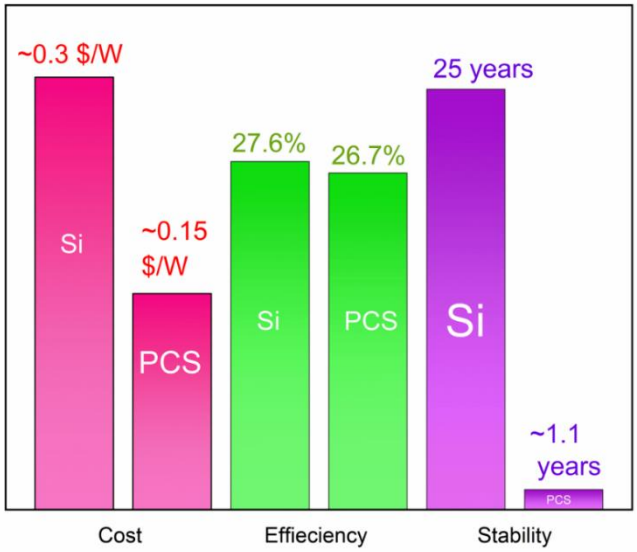

Figure 1-17:*The comparison of perovskite and silicon solar cells golden triangle of solar cells, cost, efficiency, and stability. The cost has been considered for the silicon wafer, cell processing, and module assembly however the perovskite is an estimation because it still has not entered the market.*

Improving the stability of perovskite materials is being studied through various methods such as adjusting the chemical composition, developing better encapsulation techniques and charge transport layers, and designing innovative device structures. While substantial progress has been made, achieving long-term stability comparable to established solar technologies remains an ongoing challenge.

1.7.2 Scalability

Upscaling presents a significant challenge in the path to commercialization. Although small-area perovskite devices have achieved high efficiency, replicating these results in larger modules is difficult due to challenges like ensuring uniform film deposition, managing defects, optimizing interfaces, and addressing the issue of sheet resistance in the transparent electrode. High sheet resistance in larger modules can lead to significant

power losses. Current research is focusing on scalable fabrication methods, with particular emphasis on vapor deposition techniques.

1.7.3 Environmental Impact

The toxicity of lead in perovskites has prompted extensive research into lead-free alternatives and effective containment strategies. Unfortunately, the lead-free perovskites have not yet achieved the performance of their lead-based counterparts.[62] Encapsulation methods have the potential to enhance stability and prevent lead from leaching into the environment. The fabrication of perovskite solar cells often involves toxic solvents, which pose significant health and environmental risks. Minimizing the use of such solvents or finding safer alternatives is an important aspect of developing environmentally friendly devices.

These considerations highlight the need for a holistic approach to the development and commercialization of perovskite solar cells, balancing performance improvements with environmental and safety concerns.

1.8 Fabrication

The development of perovskite solar cells can be achieved through either solution processing or dry vacuum deposition methods.

1.8.1 Solution based deposition methods

Solution-processing techniques, such as spin coating, allow for flexible fine-tuning of the perovskite layer properties, making them well-suited for small-scale research. However, these solution-based approaches encounter significant challenges when scaling up for large-scale manufacturing, including the need for solvent management, material waste, and difficulties in achieving uniform film deposition over large surface areas. Using solvents for fabrication of the active layer also poses limitations for the underlying layer due to chemical orthogonality. While techniques like doctor blading and slot-die coating have demonstrated potential for large-area deposition, they still face reproducibility challenges. Factors such as temperature, humidity, and solvent evaporation have a substantial impact on the crystallization kinetics and film morphology, leading to inconsistencies that hinder commercial viability due to quality control issues and reduced production yields. Additionally, microscale fluid dynamics can cause defects that degrade photovoltaic performance and stability.[63–65]

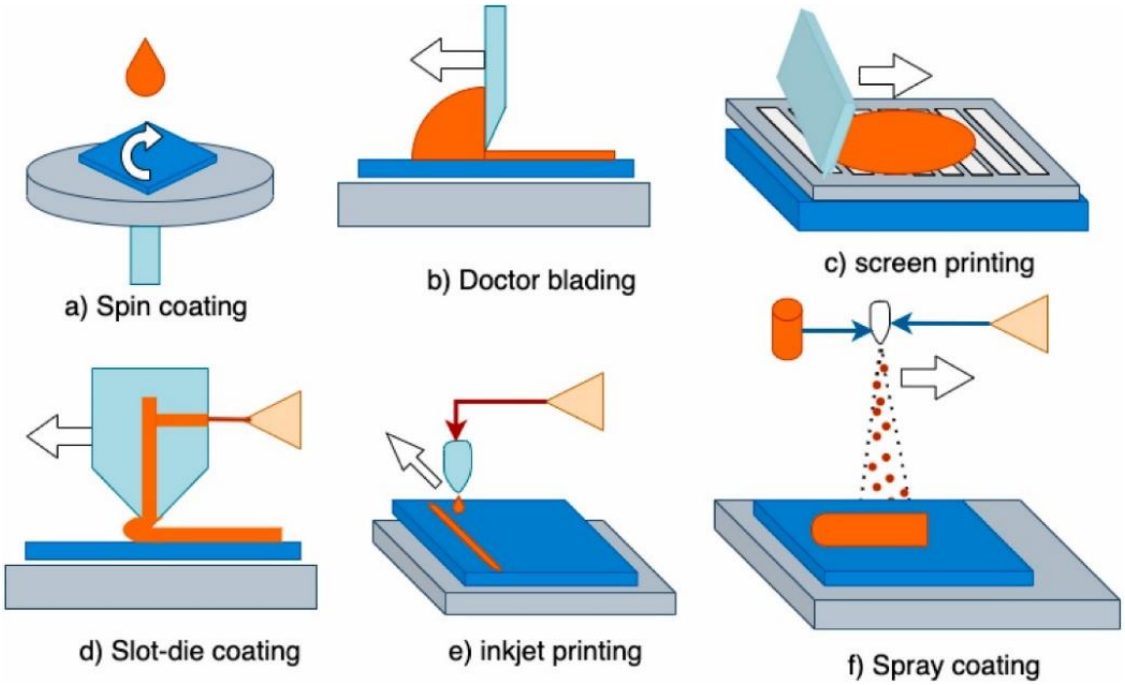

Figure 1-18: *Various solution-based fabrication methods of the perovskite solar cell adapted from reference*[65]

1.8.2 Thermal vacuum deposition

Thermal vacuum deposition is a form of physical vapor deposition that involves the sublimation of the precursors from a temperature-controlled target under high vacuum conditions (approximately 1×10^{-6} Pa). The use of high vacuum significantly reduces the sublimation temperature, thereby reducing decomposition reactions of these precursors. Over the past two decades, a variety of well-established vacuum deposition techniques have been extensively developed and applied. These include single-source evaporation (**Figure 1-19-a**)[66] and multiple-source evaporation, also known as co-evaporation (**Figure 1-19-b**).[67] Additionally, a subsequent approach, sequential evaporation, has emerged, which may involve either two consecutive single-source evaporation steps (**Figure 1-19-c**) [68] or a combination of single-source evaporation and the use of a solvent or further conversion of the active material.[69,70]

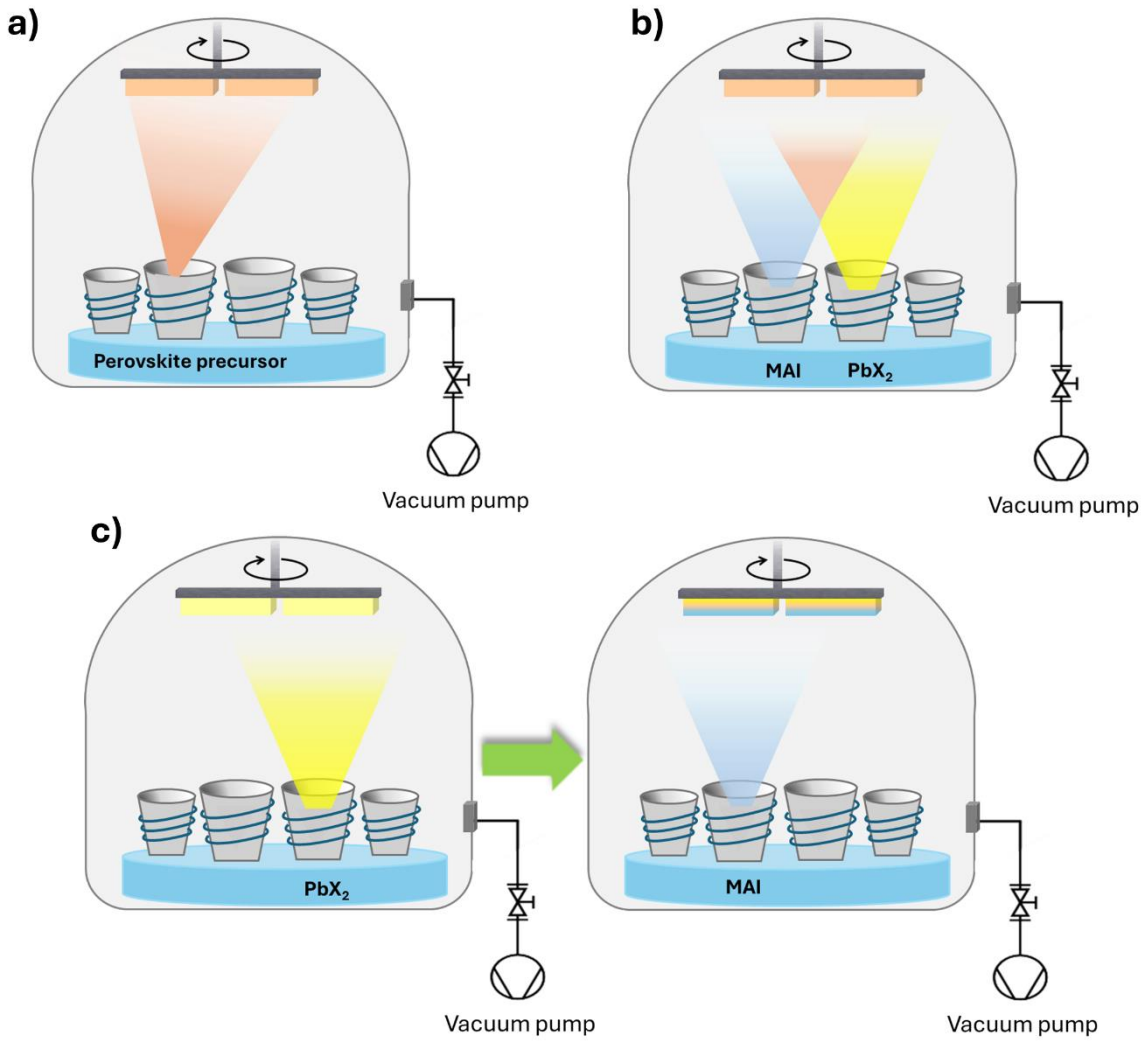

Figure 1-19: a) *Flash evaporation or single source thermal vacuum deposition.* ***b)*** *Co-evaporation of a double source perovskite.* ***c)*** *Sequential vacuum deposition of the perovskite.*

Advantages of vacuum sublimation

If the geometrical factors inside the evaporation chamber do not change, the variables that need to be controlled even in the case of multiple source evaporation are lower in comparison to solution process methods, ensuring the **r**eproducibility of the results. This method also has the potential of producing thick films simply by increasing the evaporation duration, from 800 nm (the solution process limitation with a few reported exceptions)[71] to microns. The produced films are uniform and compact and have the potential to be deposited on top of textured silicon, and multiple layers can be deposited on top of each other. **Figure 1-20** shows the conformal coating of a co-evaporated perovskite film on top of textured silicon made in our lab. The inherent possibility of adapting to industrial-scale fabrication is undoubtedly the boldest advantage of the method.

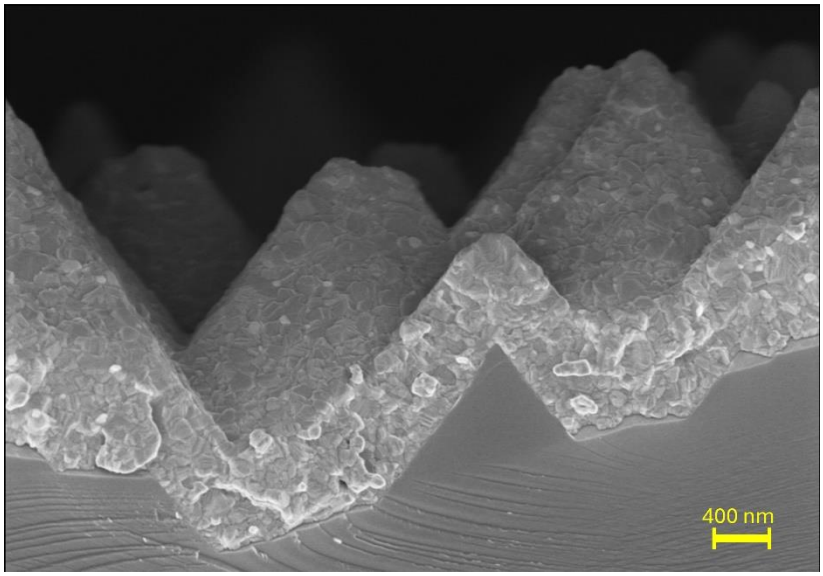

Figure 1-20: *Evaporated perovskite active layer deposited on the textured silicon as an indication of conformal coating of co-evaporation.*

1.8.3 Fully sublimed devices

While vacuum deposition offers advantages for perovskite deposition, to convert this layer into a solar cell, hole and electron transport layers as well as electrodes need to be placed on either side of the perovskite layer. Hence, it is important that all these layers can be deposited using vacuum based techniques such as maintaining a fully dry deposition process. Most of the currently developed fully evaporated stacks use small molecule organic materials or metal oxides for charge transport layer.[72–74] Recently the use of self-assembled monolayers (SAMs) has emerged as a quite popular choice among solution process perovskite community demonstrating higher thermal stability.[75]

1.9 Hole transport materials

Traditional HTMs have mobile dopants leading to ion immigration and chemical reaction at the HTL-perovskite interface making it one of the most probable points of degradation initiation. The choice of vacuum processed HTM is limited.[76–78] In the widely adopted *p-i-n* device architecture, the hole transport layer is deposited prior to the perovskite layer. The choice of hole transport material and its surface roughness can influence the formation of the thermally evaporated active layer, demonstrating once more the importance of the hole transport layer selection. [79]

1.10 Self-assembled monolayers

Self-assembled monolayers are highly organized molecular assemblies that form through the spontaneous adsorption of chemically functionalized organic molecules onto a solid surface, either from a vapor or liquid phase.

The molecules that form SAMs typically consist of three key components: an anchoring(head) group, a spacer (tail) group, and a terminal or functional group. The anchoring group is the reactive part that binds to the substrate, and its chemical nature

determines the strength and type of interaction at the interface. Common anchoring groups include thiols, carboxylic acids, phosphoric acids, and silanes, each providing a distinct binding energy and interaction based on the substrate's surface. Phosphonic acids provide a more robust assembly through mono, bi and trident connections. The orientation and packing density of the molecules are determined by the spacer group. This molecular organization directly impacts the SAM's physical and chemical properties, such as electronic conductivity, optical characteristics, and the ability to facilitate or inhibit charge transport. The terminal group incorporated into the SAM defines the properties of the new surface(**Figure 1-21**). The ability to tailor each of these groups is the key advantage of SAMs, making them valuable in various fields, especially surface modification.

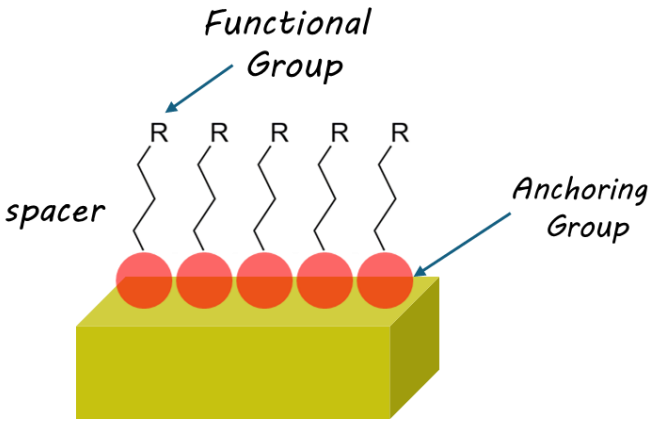

Figure 1-21: *The schematic of self-assembled monolayers different parts.*

In photovoltaics, SAMs have found significant applications due to their ability to tune surface properties and enhance charge transfer. They are employed to improve energy level alignment at interfaces, enabling efficient charge transfer and minimizing recombination losses. SAMs have shown promise as hole transport materials, with carbazole-based SAMs demonstrating reduced interfacial recombination and enhanced device stability. SAM-based HTMs are attractive because they offer minimal recombination losses, improved stability, and the potential for scalable, dopant-free interfaces.

1.11 The aim of the thesis

This thesis aims to bring vacuum-deposited perovskite solar cell technology one step closer to commercialization by improving three critical aspects: efficiency, stability and scalability. The main objective of the thesis includes optimizing the interfaces and forming effective connections that enhance the yield without compromising the efficiency. This is pursued by focusing on the interfaces between the perovskite and the charge extraction layer and on methods to increase the active area. Throughout this work special emphasis has been given to the hole transport layer interface since it is identified as one of the weakest links in terms of stability.

Stability:

To improve the stability of the device, the strongly oxidizing interlayer consisting of dopants like F6-TCNNQ (or similar molecules) needs to be removed. The aim is therefore to find alternatives for these strongly oxidizing molecules as interlayers.

Efficiency:

To improve power conversion efficiency, the gap between the obtained performance and the radiative limit needs to be overcome. The aim is to do this by adjusting the methylammonium to formamidium ratio in $FAMAPbI_3$ low bandgap perovskites.

Scalability:

The aim is to improve the area of the solar cell while using low conductive transparent conductive oxides as front electrode. This implies that the cells must be placed in series, and it is important to see how this can be achieved

While each chapter addresses a different challenge within the realm of perovskite solar cells, collectively they contribute to improving interfaces and forming reliable connections with the ultimate goal of moving this perovskite technology closer to commercialization. By addressing issues such as stability, efficiency, and scalability, this thesis aims to make a contribution to the field of solar energy generation.

Chapter 2: Experimental Methodology and Characterization

2.1 Experimental methodology

This chapter provides an overview of the critical materials and preparation techniques used in this thesis. This chapter also presents the diverse characterization techniques employed to evaluate the thin films' composition, crystallinity, optical properties, and the complete solar cell and minimodule(MM) performance.

2.2 Experimental section

2.2.1 Chemicals

Phenylphosphonic acid (SAM 1), 4-flurobenzylphosphonic acid(SAM 2), (3-Trifluoromethyl)phenyl)methyl-phosphonic acid(SAM 3), decylphosphonic acid(SAM 4), 1H,1H,2H,2H-Perfluorooctanephosphonic(PFOPA for short or SAM 5) were purchased from Sigma Aldrich. CH_3NH_3I (MAI), MoO_3, bathocuproine (BCP), and 1,3,4,5,7,8-hexafluorotetracyanonaphthoquinodimethane (F6-TCNNQ) was purchased from Luminescence Technology Corp(LumTec). Formamidinium iodide (FAI) was supplied by Greatcell. ((N4,N4,N4,N4-tetra([1,1-biphenyl]-4-yl)-[1,1:4,1-terphenyl]-4,4-diamine) called TaTm and (2-(3,6-Dimethoxy-9H-carbazol-9-yl)ethyl)phosphonic acid called MeO-2PACz were purchased from Tokyo Chemical Industry (TCI). Fullerene (C60) (purity >99.95%) was purchased from Creaphys GmbH, PbI_2 in the form of beads (99.999% metal basis) was purchased from Alfa Aesar.

2.2.2 Preparation

Fabrication processes were designed and conducted in a class 10,000 cleanroom environment(**Figure 2-1**) to ensure high-quality fabrication and minimize contamination from dust particles. Additionally, critical fabrication steps were carried out in an inert nitrogen-filled glovebox unless mentioned to protect sensitive materials from degradation due to oxygen and moisture exposure.

Throughout this work, the solar cells have been fabricated in a bottom-up architecture from a 3 x 3 cm^2 glass substrate with an integrated ITO. For the cell structure the substrates have been supplied by Naranjo Substrates. For Mini modules(MMs) fabricated the same size substrate with full ITO coverage from Colorado Concept Coatings LLC. have been used.

Prior to deposition, the glass substrates underwent thorough cleaning. The standard cleaning protocol involved sequential sonication in water with soap, Mili-Q water, and isopropanol baths. Subsequently, the substrates were dried using nitrogen flow and then placed in a UV ozone cleaner for 20 minutes to ensure removal of organic contamination. This cleaning procedure was consistently applied. After cleaning, the substrates were transferred to a nitrogen-filled glovebox. For fully evaporated stacks, the clean substrates were not removed from the inert atmosphere during fabrication. For wet deposition of the

SAMs, the substrates were dip-coated overnight in a 0.1 mM ethanol solution in a different glovebox .

Figure 2-1: *A picture of the cleanroom environment, the gloveboxes and different thermal vacuum chambers.*

In this thesis, multiple specialized evaporation chambers were utilized to deposit various layers. However, all these chambers are integrated within the same glovebox, which minimizes the substrate's exposure to degrading agents and facilitates a continuous, manufacturing process.

Figure 2-2: *Inside one of the vacuum chambers used for vacuum sublimation in the current thesis.*

For charge transport layers, dual source thermal evaporation has been sequentially employed in a chamber with a pressure lower than 3×10^{-5} mbar. Efforts have been made to separate the sources for hole-selective and electron-selective materials. Compounds such as *F6-TCNNQ* (a *p*-type dopant with high electron affinity), TaTm, BCP, C_{60}, (PFOPA

or SAM5), and MeO-2PACz were all deposited in this chamber. Metal electrodes, LiF and MoO_3 were thermally sublimed in a separate chamber dedicated to metal evaporation.

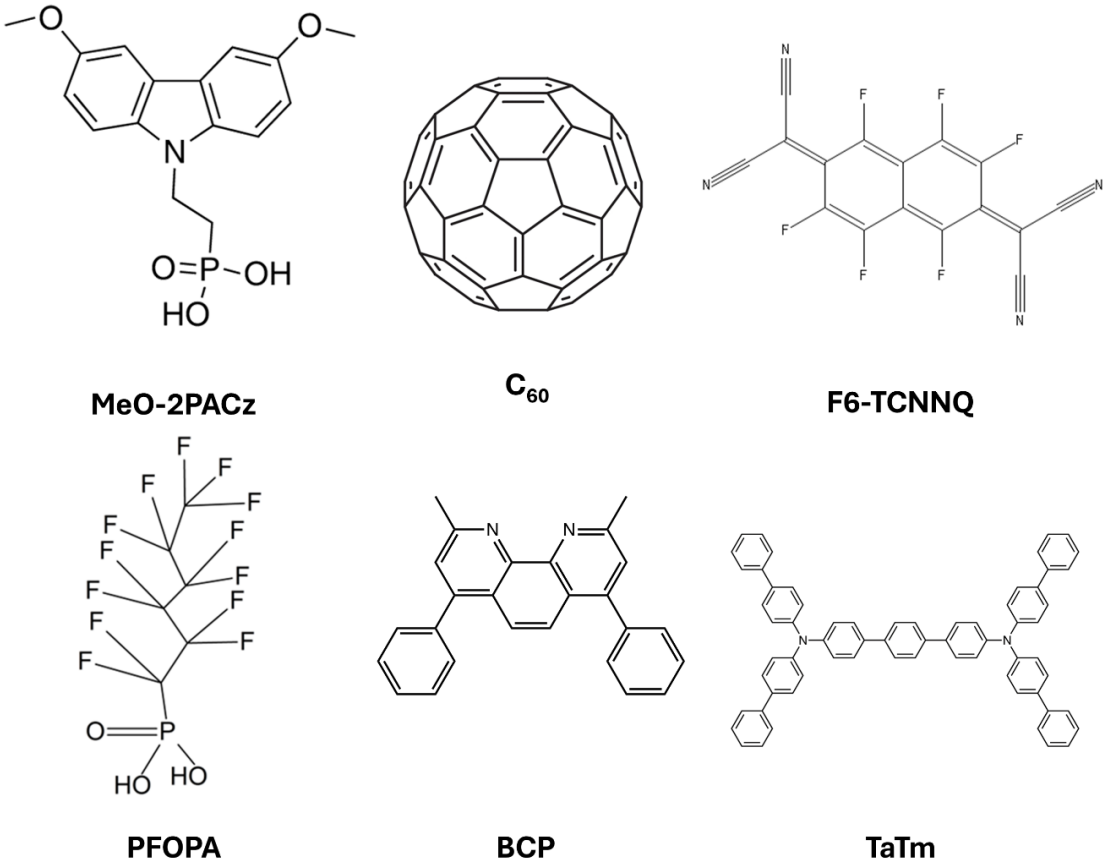

Figure 2-3: *The molecular structure of self-assembled monolayers and common charge transport layers used in this thesis.*

2.2.3 Active layer fabrication

In this thesis the perovskite absorber layer is prepared using a multisource co-evaporation method. The co-evaporation setup consists of a vacuum chamber integrated into a nitrogen-filled glovebox. The chamber is first pumped down with a roughing pump and later with a turbo pump to lower the pressure to approximately 10^{-6} mbar. The chamber has four temperature-controlled evaporation sources with ceramic crucibles, each dedicated to a different material protecting the precursor. Most of the co-evaporation of the perovskite is done with dual source or triple source precursors. Quartz crystal microbalances (QCM) are used to precisely monitor the sublimation rate of the perovskite precursor. Protective walls are used to prevent cross-reading. The sources are oriented at a 90-degree angle to the chamber base, with an approximate distance of 20 cm to the substrate holder as can be seen in **Figure 2-4** left panel.

Additionally , to obtain a more accurate measurement of the deposition rate at any given moment, an initial calibration of each precursor material is performed. For this, the material density (ρ), acoustic impedance (Z ratio), and tooling factors are required to accurately determine the thickness and evaporation rate of the sublimated material. The

tooling factor accounts for the difference in material deposited on the substrate versus the quartz crystal microbalance due to the varying distances between the source, substrate, and QCM sensor. This tooling factor can be further verified by comparing the actual obtained thickness with the desired one using techniques such as surface profilometry, atomic force microscopy (AFM), or cross-sectional scanning electron microscopy (SEM).

The substrates are positioned above the thermal sources, maintained at an appropriate distance to avoid interference from the source heat, and rotated to achieve a uniform coating through the evaporation process. This distance allows the use of different substrate types. Prior to reaching the desired deposition rate, the substrates are shielded with a shutter to prevent uneven coating. Normally a corresponding QCM to each source is positioned next to the source for reading the produced rate at the position of the source. **Figure 2-4** right panel shows a schematic for better visual demonstration of sensors and their sensors. A unique QCM is assigned to the substrate to have more accurate reading on the converted ultimate composition of the vapors reaching the substrates.

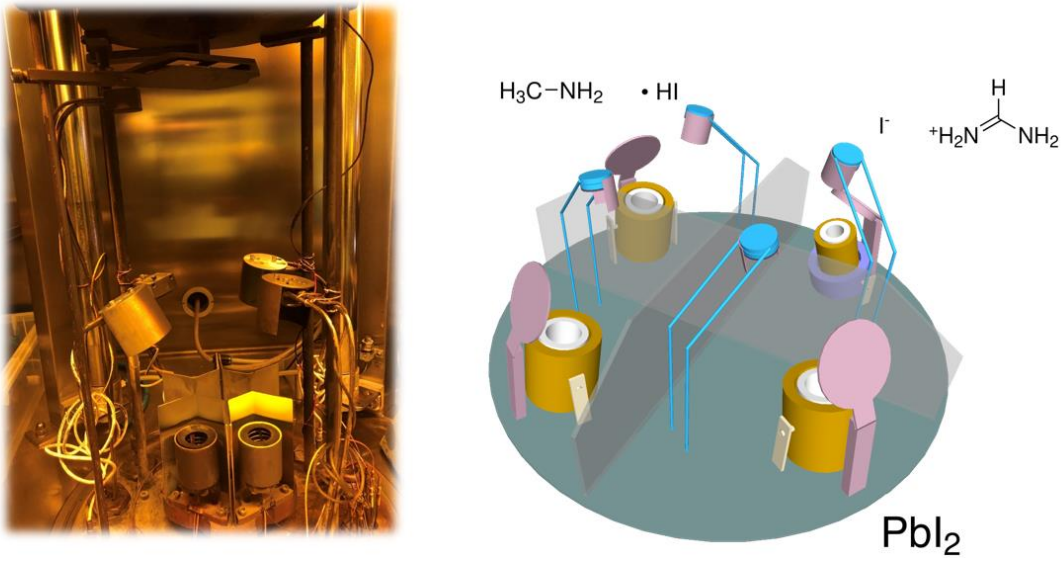

Figure 2-4: Left panel) *Picture of the vacuum chamber.* ***Right panel)*** *The schematic of the evaporator sources used for the fabrication of double A-cation perovskite and their position.*

2.2.4 solar cell of *p-i-n* stack

The bottom-up structure of a *p-i-n* device archetype consist of the following layers: Glass substrate/TCO/ HTL/ Perovskite/ETL/metal electrode. In this work a prepatterned ITO with the active area of 0.05 cm^2 was used. As a baseline structure for the HTL, either 2.5 nm of F6-TCNNQ as a p-dopant or 6 nm of MoO_3 was deposited, followed by a 10 nm TaTm deposition to facilitate hole extraction by promoting an ohmic contact to the electrode by increasing conductivity or lowering the CB. Following the perovskite layer, a 12 nm layer of fullerene C60 is employed as the ETL to enable electron extraction and

hole blocking. The C60 thickness has been reduced from the previously reported >20 nm to lower the absorption of this thick layer. Consequently, 7 nm of BCP is deposited before the deposition of the 100 nm metal electrode(**Figure 2-5**). Additional to the charge-selective properties of the materials in contact with the perovskite, the optimization of carrier injection and extraction at the transparent conductive oxide and metal contacts is also needed. This is achieved by forming ohmic contacts in this baseline and minimizing the losses, and this has been tried to be maintained for all other alternatives. One of the main goals of this thesis is to find alternative replacements for dopant or MoO_3 due to their chemical instability. Moreover, the substitution of BCP with ALD-deposited metal oxide has formed a benign barrier for charge extraction, while also serving as a useful barrier for ion diffusion and degradation of the metal electrode.

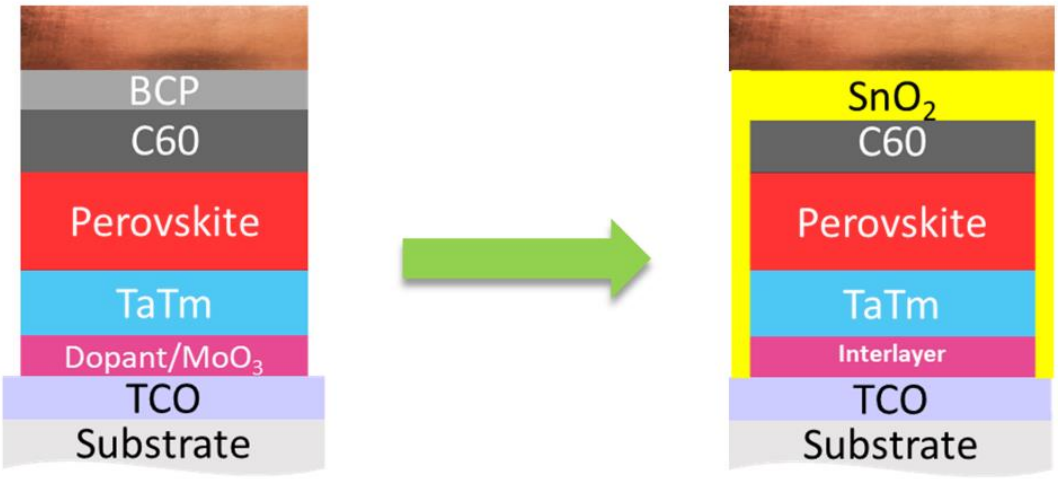

Figure 2-5: Left) *A p-i-n baseline device stack.* ***Right)*** *The improved structure used in this thesis.*

2.2.5 Module fabrication techniques

Scaling up laboratory-sized perovskite solar cells requires an increase in the TCO area, but this increase contributes to elevated sheet resistance, significant heating and consequently leading to a drop in overall efficiency. For the transition to larger areas while maintaining good performance, researchers have developed a continuous series of interconnected cells, known as modules. Unlike single cells, modules consist of multiple smaller cells connected in series within a single substrate.[80,81] This series connection allows the voltages of individual cells to be additive, while the current generation is limited by the narrowest cell stripe. In this transition a certain parameter called cell to module (CTM) factor also called upscaling loss ($F_{upscaling}$) is introduced to evaluate the amount of loss contributed to the area (A) increase.

$$f_{\text{upscaling}} = \frac{\left(1 - \frac{PCE_{\text{module}}}{PCE_{\text{cell}}}\right) \cdot 100\%}{\log \frac{A_{\text{module}}}{A_{\text{cell}}}} \qquad \textbf{Equation 2—1}$$

The key factor in this approach is the optimization of the layout and interconnection. Structures up to 100 cm^2 are referred to as MMs, while larger structures are called modules.[82] Various production methods for MMs have been explored, including the use of shadow masks for cell separation. The most efficient method reported so far has been laser scribing[83] ;however, their long-term thermal stability and the effect of laser scribing has not been studied.

Template based patterning

One alternative method for fabricating MMs is the use of shadow masks for cell separation. This approach is particularly suited for fully evaporated structures, where different shadow masks are designed for each layer of the solar cell. During the deposition process, these masks create defined regions on the substrate, effectively separating the cells without the need for physical scribing. The advantage of the shadow mask technique is that it avoids the potential degradation associated with laser scribing, as there is no direct interaction with the perovskite material that could cause damage. This method results in MMs that are generally more resistant to degradation, contributing to longer-term stability. However, the shadow mask method does come with a trade-off: it typically results in a higher CTM factor, reducing the overall efficiency of the MM compared to those fabricated using laser scribing. Despite this, the shadow mask technique remains a valuable option in scenarios where durability is prioritized over maximum efficiency. **Figure 2-6** shows a MM of three subcells of 1cm^2 fabricated on a 3 x 3 cm^2 substrate glass fabricated in our lab with shadow masks.

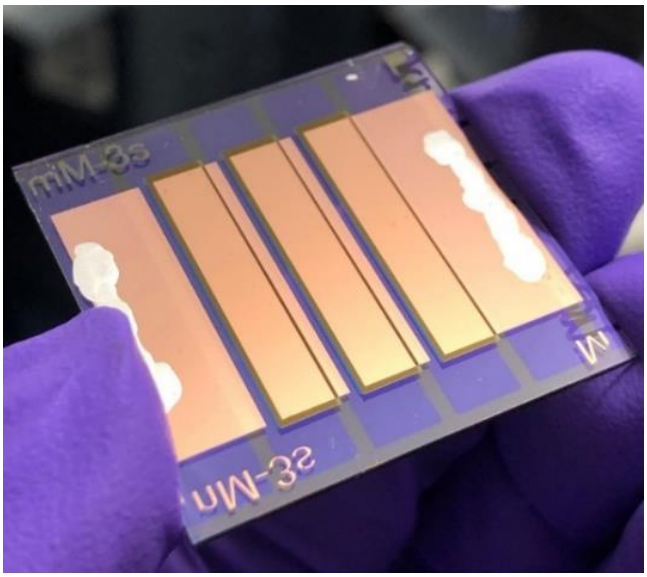

Figure 2-6: *Fully evaporated MM fabricated by the template patterning.*

Laser scribing

Laser scribing offers a method for separating individual cells and creating interconnected cells in series to form a module. This process involves ablation of a precise amount and depth of material from the surface. The precision and control provided by laser scribing are vital for producing high-efficiency modules with minimal

inactive areas. The scribing procedure was carried out in Imec Imomec thin film PV group in Energy Ville in Genk Belgium. The samples fabricated in Valencia have been shipped to the facility taking advantage of a modified M-Solv MSV500 system, integrated into an M-Braun inert-gas glovebox to protect the moisture-sensitive perovskite layers. The glovebox maintained an atmosphere with less than 1 ppm of oxygen and water, ensuring the integrity of the perovskite during processing. The laser system employed a 3-wavelength 10 picosecond pulsed laser, with each wavelength optimized for specific scribing tasks. Software-adjustable optics allow the spot sizes at the workpiece to be set in the range 10 – 50 um and the pulse energy to be adjusted. The laser wavelengths are 1064 nm (infrared), 532 nm (green) and 355 nm (ultraviolet) each being used for different ablation purposes. This method is also called P1, P2, P3 as shown in **Figure 2-7** which each section is described in the following:

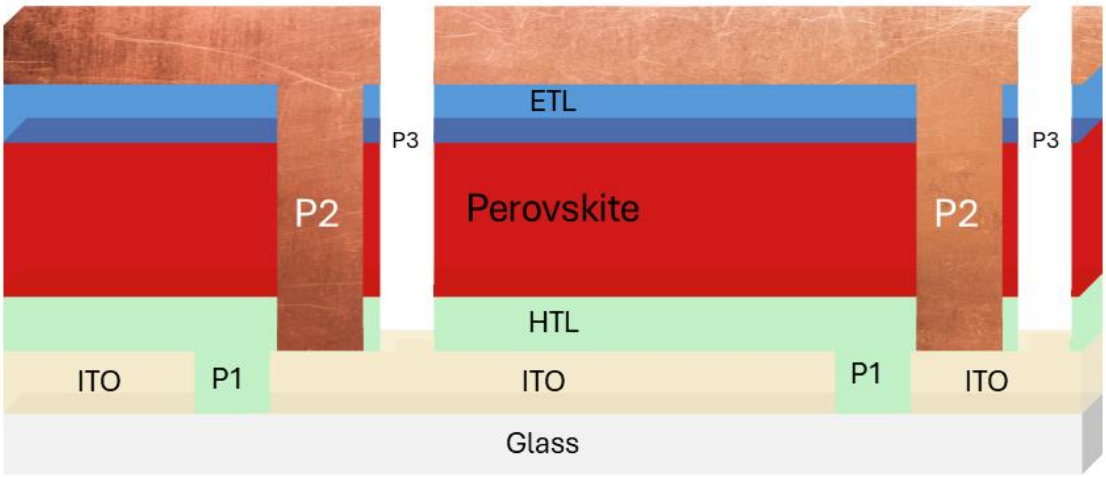

Figure 2-7: *Schematic illustration of a P1,P2,P3 laser ablation pattern.*

P1 Scribe: isolation of bottom electrode

The fabrication of perovskite MMs begins with the P1 scribe, which isolates the conductive bottom transparent electrode layer, typically ITO, without damaging the underlying substrate. This creates separation lines between individual cells, ensuring their independent operation within the module. The precision of the P1 scribe is vital, as it lays the foundation for the entire module and prevents electrical shorts between adjacent cells.

P2 Scribe: interconnection of cells

After separating the TCO and depositing the device stack up to the metal electrode , a subsequent P2 scribe is performed to establish the electrical connections between the previously isolated cells. This step selectively removes the perovskite absorber layer and any adjacent transport layers, exposing the underlying bottom electrode without

damaging it. This scribe is a very critical step because any deviation might cause the perovskite exposure to other layers, lowering the lifetime of the module. A green laser is specifically chosen for the P2 scribe, as its wavelength can effectively absorb and remove these layers without causing damage to the bottom electrode. The careful optimization of the laser power for this step depending on the types of the layer is an important factor that affects the yield.[84] This crucial step enables the formation of series connections between the individual cells, allowing the voltages accumulation while maintaining a consistent current flow throughout the module. Ensuring accurate alignment with the previous P1 scribe, while minimizing the amount of inactive area, guarantees a continuous electrical path and optimal use of active materials resulting in optimization of the overall module performance. Many labs use mechanical scribing as an alternative method, primarily due to the lack of laser systems integrated into inert atmospheres in perovskite research facilities. Although mechanical scribing is less efficient and precise than laser scribing, high efficiencies have still been reported with this method.[85] This is likely because mechanical scribing is more accessible despite its drawbacks, such as increased debris and larger dead areas. While fewer studies have directly compared the two techniques, laser scribing is generally favored for its cleaner and more accurate results.

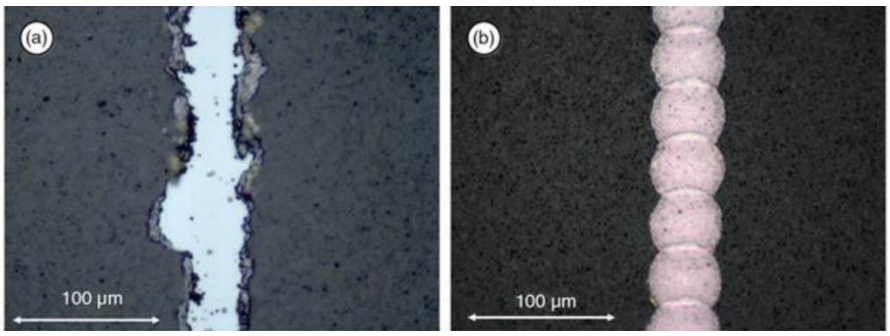

Figure 2-8: ***a)*** *a mechanical P2 scribe, and* ***b)*** *a laser-scribed line adapted from reference.*[86]

P3 Scribe: isolation of the top electrode

After the deposition of the metal back electrode , the concluding scribing step, P3, separates the top metal electrode of each individual cell to prevent electrical short circuits between adjacent cells. The P3 scribe utilizes a UV laser, selected for its precision and capacity to generate fine, clean separation lines. This step ensures the complete isolation of each cell within the MM, enabling the module to function as intended with minimized power losses. The P3 scribe finalizes the series connection process, guaranteeing the module's readiness for subsequent encapsulation and testing.

2.2.6 Atomic layer deposition (ALD)

In this thesis, ALD was utilized to enhance the stability and longevity of perovskite solar cells through the deposition of protective layers. A SnO_2 layer was applied as a barrier to replace the commonly used BCP layer, offering superior electron transport properties and

environmental protection. Additionally, a 20 nm thick layer of Al_2O_3 was deposited as an encapsulant. The ALD process was chosen for its ability to produce highly conformal, pinhole-free films that not only shield the outer surfaces but also fill interstitial spaces within the device layers, creating a compressed stack that enhances mechanical stability and restricts layer expansion. Both SnO_2 and Al_2O_3 layers were deposited at a low temperature of 40°C to ensure compatibility with the underlying perovskite layers, preventing damage and preserving the integrity of the devices.[87]

2.3 Characterization

2.3.1 Thin film Characterization

After deposition of the active layer, the thin film properties have been confirmed through various techniques .

X-ray Diffraction (XRD)

X-ray diffraction analysis was used to study the crystallographic properties of the bulk perovskite thin films. This technique provided critical insights into the structural quality of the thin film. It is a widely used technique to obtain detailed information on crystal structure, crystallite size, orientation and phase purity. The technique operates based on Bragg's law

$$2d \cdot sin\theta = n\lambda \qquad \textbf{Equation 2—2}$$

where *d* stands for the distance between planes of atoms, θ is the angle of the incident X-ray beam with respect to the atomic plane, *n* is an integer number and λ is the wavelength of the X-ray. This relates the distance between atomic planes in a crystal to the positions of the peaks in the diffractogram. In crystalline materials, where atoms are arranged in a regular three-dimensional lattice, an incident X-ray beam is diffracted by the atomic planes. For a given crystalline material with an ordered three-dimensional atomic arrangement, an incident X-ray beam interacts with the atoms and is scattered or diffracted.[88]

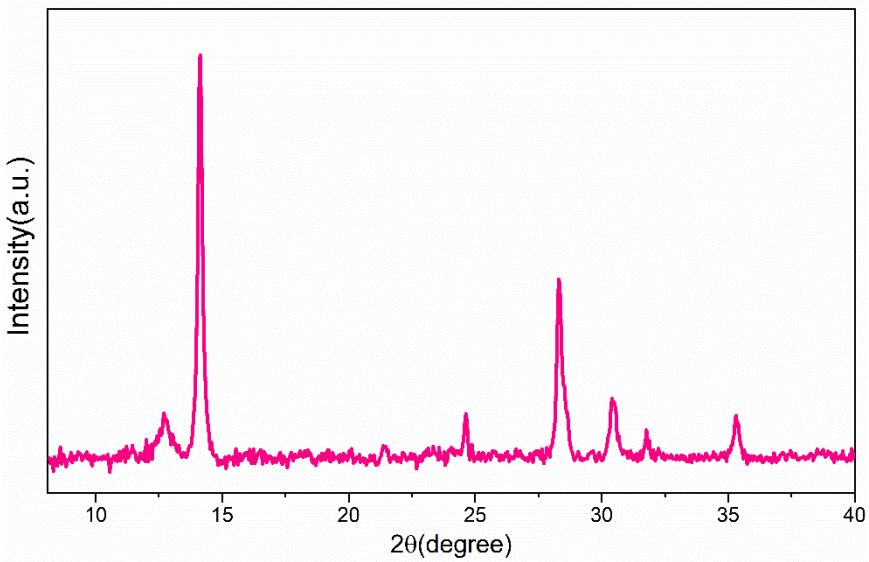

Figure 2-9: *An example of an XRD spectra of MAPbI perovskite with excessive PbI_2 peak.*

The XRD measurements were performed using an Empyrean diffractometer from Malvern Panalytical, equipped with a Cu Kα anode operated at 45 kV and 40 mA. Scans were conducted in the 2θ range of 8° to 40°. The analysis of the XRD patterns provided

crucial information on the phase composition, crystallinity, and potential presence of secondary phases or defects within the perovskite films. The results revealed well-defined peaks indicative of high crystallinity and uniform grain growth, which are essential for optimal charge transport and overall device efficiency. The reference peaks have been adapted from ICSD IZ Karlsruhe – Leibniz Institute for Information Infrastructure.

Nuclear Magnetic Resonance (NMR)

Nuclear magnetic resonance spectroscopy is an analytical tool that provides insights into the local chemical environment of nuclei. In the context of perovskite structures, the A-site is typically occupied by organic cations such as MA and FA. Determining the ratio of these cations incorporated in the final perovskite film is crucial for tuning the material's optoelectronic properties. Proton (1H) liquid NMR is particularly useful for this purpose, as it is a fast experiment and offers detailed information about the molecular environment of hydrogen atoms within these organic cations. By analyzing the chemical shifts and integration of the proton signals, this technique allows for the precise quantification of the relative amounts of the organic cations. To acquire enough sample material to be detectable by ^{1H}NMR, five substrates of 3 by 3 are coated with a 600 nm-thick perovskite film in a single sublimation run. The perovskite layers of these plates are then dissolved in 1 mL of deuterated DMSO solvent. A typical ^{1H}NMR spectrum is obtained using a 400 MHz Bruker AV400 NMR spectrometer.

X-ray Photoelectron Spectroscopy (XPS)

X-ray Photoelectron Spectroscopy is a powerful surface analysis technique widely utilized to investigate the elemental composition, chemical states, and electronic environment of materials. The technique works by exposing a sample to X-rays, which induce the emission of photoelectrons from the surface. By measuring the kinetic energy of these emitted photoelectrons, XPS provides detailed information about the elements present on the surface, their chemical states, and the relative abundance of different species within the top few nanometers of the sample. The binding energy of an electron is determined using the energy of the X-ray source, the known value of the spectrometer work function and the kinetic energy measured in the XPS experiment, following the equation

$$\mathrm{h}\nu = \mathrm{BE} + \mathrm{KE} + \varphi_{spec} \qquad \textbf{Equation 2—3}$$

where $h\nu$ stands for the energy of the X-ray, *BE* for the binding energy of the emitted electron, *KE* for the kinetic energy of the electron and $\phi spec$ for the work function of the spectrometer. The binding energy depends on the element and the orbital from which the electron is ejected, making it independent of the X-ray energy source and valuable for determining the sample's composition.[89,90]

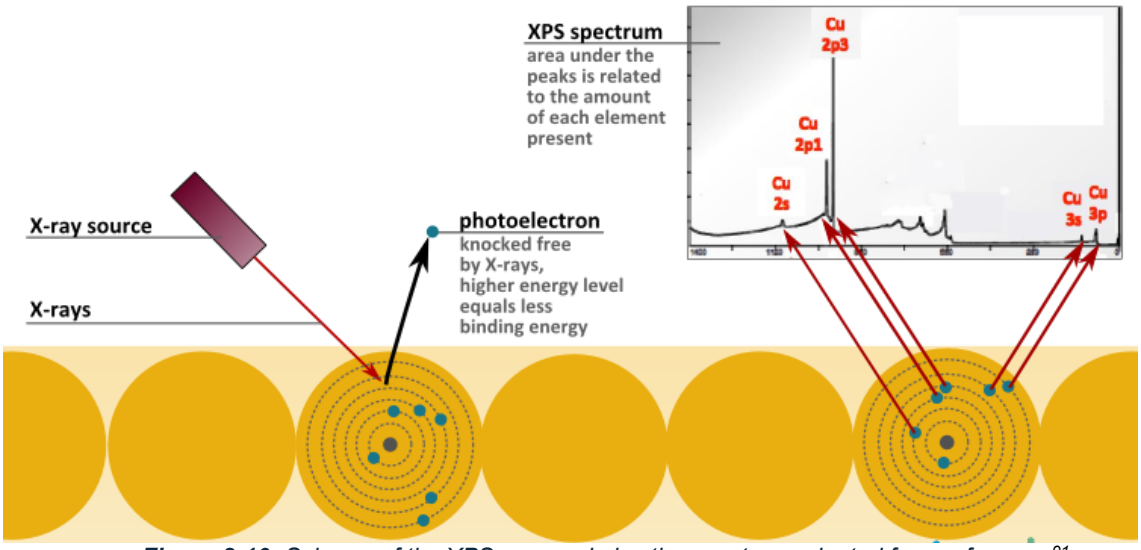

Figure 2-10: *Scheme of the XPS rays and also the spectrum adapted from reference* [91]

XPS is particularly valuable for studying thin films, surface coatings, and interfaces, where surface composition plays a critical role in material performance. It is especially useful for characterizing modifications on conductive surfaces, such as ITO, where SAMs are employed to tailor surface properties. XPS allows for the confirmation of successful SAM formation and the identification of specific chemical bonds, providing insights into changes in surface chemistry. In this thesis, XPS experiments were conducted using a Thermo Scientific K-Alpha X-ray photoelectron spectrometer, with Al K-α X-ray radiation as the source. The XPS data were analyzed using Avantage V5.9925 software.

Atomic force microscopy (AFM)

AFM is a high-resolution imaging technique utilized to characterize the surface topography and roughness of thin films on the nanometer scale. This technique operates by scanning a sharp probe across the surface, generating a detailed three-dimensional map of the surface morphology. In the present study, AFM was employed to evaluate the uniformity and smoothness of the self-assembled monolayer deposited film, confirming the absence of island-like structures or aggregate formation. Furthermore, the surface roughness measurements obtained from AFM analysis revealed altered roughness values, suggesting the presence of the deposited monolayers on the surface. The measurements were performed with a Bruker Multimode AFM equipped with a Nano Scope V. This was done in tapping mode using silicon tips with a natural resonance frequency of 300 kHz and an equivalent constant force of 40 N/m. The resulting data was then processed using Gwyddion scanning probe microscopy.

Scanning electron microscopy (SEM)

SEM is a technique used to characterize the surface morphology of thin films. By scanning the sample surface with a focused beam of electrons, SEM can provide high-resolution images that reveal information about the topography, crystalline structure, and

chemical composition of the material. The incident electrons, typically with energies ranging from 2 to 40 keV, interact with the sample to produce secondary, backscattered, and X-ray signals, each providing different types of information. Secondary electrons, originating from the top few nanometers of the sample surface, offer the highest spatial resolution, below 1 nm, and provide topographic details. Backscattered electrons, emitted from the bulk of the sample, have higher energies and can provide compositional information, though with slightly lower resolution than secondary electrons. Additionally, the removal of inner shell electrons by the incident beam can lead to the generation of characteristic X-rays, which are detected by an energy dispersive spectrometer for rapid, qualitative elemental analysis. The SEM images were collected using a field emission scanning electron microscope (HR-FESEM), ZEISS Gemini SEM 500 model, with a secondary electron in lens detector using an accelerating voltage of 0.7-1.0 kV.

Contact angle

Contact angle measurement is a technique that evaluates the wettability of a surface by a liquid, providing insights into the surface energy, cleanliness, and chemical composition. In this method, a droplet, typically water, is deposited on the surface, and the angle formed between the droplet's edge and the surface is measured. This angle, known as the contact angle, indicates the hydrophilic or hydrophobic nature of the surface. In this work the measurements were carried out with a Ramé-hart model 200 U4 series instrument together with drop image pro Software.

2.3.2 Optical Characterization

Ultraviolet-visible spectroscopy

Ultraviolet-visible spectroscopy(UV-Vis) is a technique used to measure the absorption of light in the UV and visible spectral regions (100-700 nm) by a material. When the incident light with a specific wavelength and intensity goes through a sample, a portion of the light is absorbed by the material, resulting in a reduced intensity of the transmitted light. The degree of absorption, known as absorbance, can be quantitatively described by the Lambert-Beer law. Where A is absorbance, I_0 is the intensity of light at the source or the intensity of the light transmitted by a transparent surface like glass, and I is the intensity of the transmitted light.[92]

$$A = \log(\frac{I}{I_0}) \qquad \textbf{Equation 2—4}$$

For perovskite films deposited on transparent substrates, the optical characterization is typically conducted using a transmission configuration. In this setup, the substrate is placed on a flat holder with a small aperture to ensure the incident light can be fully transmitted. This arrangement simplifies the measurement process and is well-suited for

smooth, thin films as is also shown in **Figure 2-11**. In this thesis, absorbance spectra were acquired using a fiber optics-based Avantes Avaspec 2048 spectrometer.

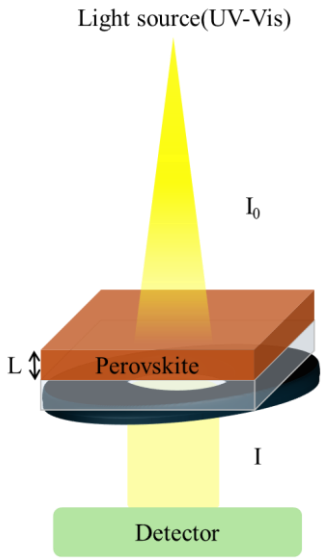

Figure 2-11: *Schematic of the UV-Vis absorption measurement setup for perovskite film.*

Calculating the absorbance (*A*) from Equation 2—4 and knowing the distance that the light travels which is equal to the thickness of the absorber layer (*L*), it is possible to obtain the absorption coefficient (α) :

$$\alpha = 2.303\frac{A}{L} \qquad \textbf{Equation 2—5}$$

A method proposed by Tauc[93] and later developed by Davis and Mott[94] assumes that the absorption coefficient which depends on the absorbed light is a function of the optical bandgap of material in the following mathematical order:

$$(\alpha h\nu)^n = B(h\nu - E_g) \qquad \textbf{Equation 2—6}$$

where *B* is a constant, *n* is 2 or ½ if the material´s bandgap is direct or indirect respectively, and E_g is the optical band gap of the film. For determining the optical bandgap, the intercept of the graph of $(\alpha h\nu)^n$ versus energy is calculated.[95] A sample graph for this calculation is shown in **Figure 2-12-a** left side and the calculation results are shown in **Figure 2-12-b**.

Photoluminescence(PL)

When a material is excited by light, typically in the ultraviolet or visible range, it can re-emit light at a different wavelength through the process of photoluminescence. The emitted light is then collected and analyzed to obtain the PL spectrum, which provides

valuable information about the bandgap, the defect states, and the efficiency of radiative recombination within the film.

In this thesis, PL spectra is obtained with the same spectrometer coupled with an in house built structure for filtering the laser energy with a 650 nm red light filter and fiber optics. The films were excited with a diode laser from Integrated Optics, emitting at a wavelength of 522 nm. The emitted PL spectra was recorded with auto integration time, ensuring sufficient signal collection for accurate analysis. **Figure 2-12-a** right side shows a sample irradiance spectrum of a perovskite deposited on glass. Measurement points were circular, with a diameter of 3 mm, providing a representative sampling of the film's photoluminescent properties.

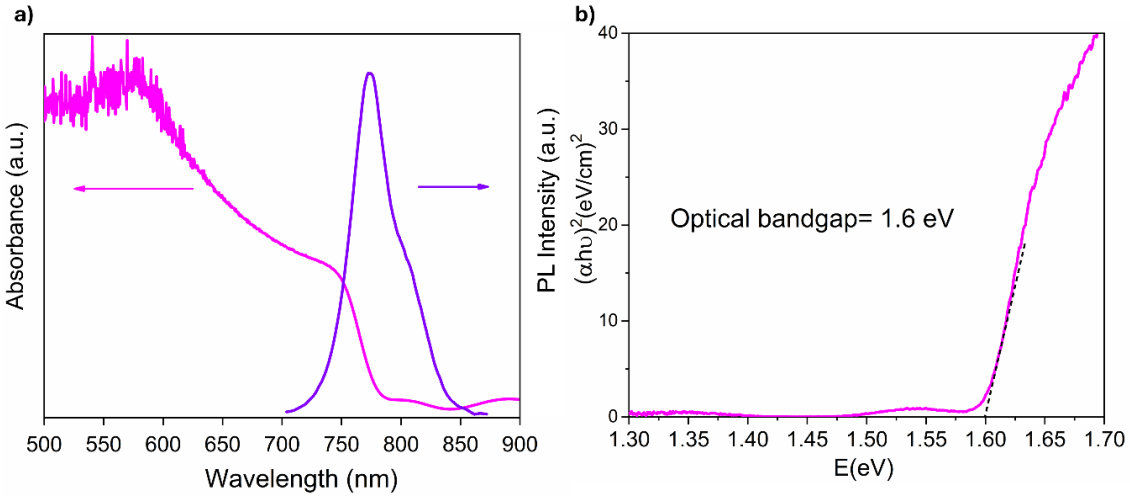

Figure 2-12: a) *The photoluminescent spectra(purple) and the absorbance spectra(magenta) of MAPI film on glass.* ***b)*** *The optical bandgap of a MAPI film calculated by Equation 2—6 using the absorbance spectra on the panel a.*

2.4 Solar cell characterization

The electrical behavior of solar cells is characterized by a diode model, as depicted in the circuit diagram in **Figure 2-13**. An ideal diode (same as a solar cell in dark condition) allows the current flow only in forward bias and blocks all current flowing in reverse voltage.

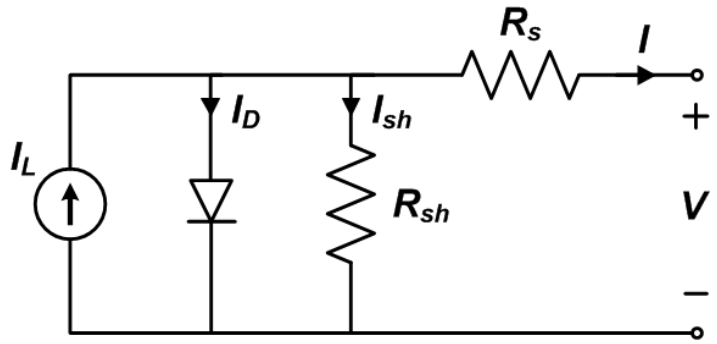

Figure 2-13: *A Simplified equivalent circuit of a solar cell under illumination conditions.*

With certain illumination intensities, carrier generation creates a photocurrent that shifts the forward biased current. The current in a solar cell is described by the classic Shockley diode equation:

$$I = I_{ph} - I_0 \left\{ e^{\frac{qV}{nkT} - 1} \right\} \qquad \textbf{Equation 2—7}$$

where I_0 is the saturated reverse current, I_{ph} is the generated photocurrent, q is the electron charge (1.6×10^{-19} C), V is the applied voltage, K is the Boltzmann's constant (1.3807×10^{-23} J/K), and T is the absolute temperature in Kelvin.[96,97] The short-circuit current, I_{sc}, is the current flowing through the device when the voltage across it is zero. Conversely, the open-circuit voltage, V_{oc}, is the maximum voltage that can be generated by the solar cell when no current is flowing. By setting the current to zero in the Shockley diode equation, an expression for the open-circuit voltage can be derived, representing the maximum achievable voltage when the current is zero under illumination. If we consider the zero current in **Equation 2—7**, the open circuit voltage would be as follows:

$$V_{oc} = \frac{nkT}{q} \ln \left(\frac{I_{ph}}{I_0} + 1 \right) \qquad \textbf{Equation 2—8}$$

In this thesis all the measurements were done under 1-sun illumination with a Wavelabs solar simulator at 100 mW/cm^2 intensity. **Figure 2-14** shows the current voltage behavior of a solar cell solar cell both in the dark and under illumination.

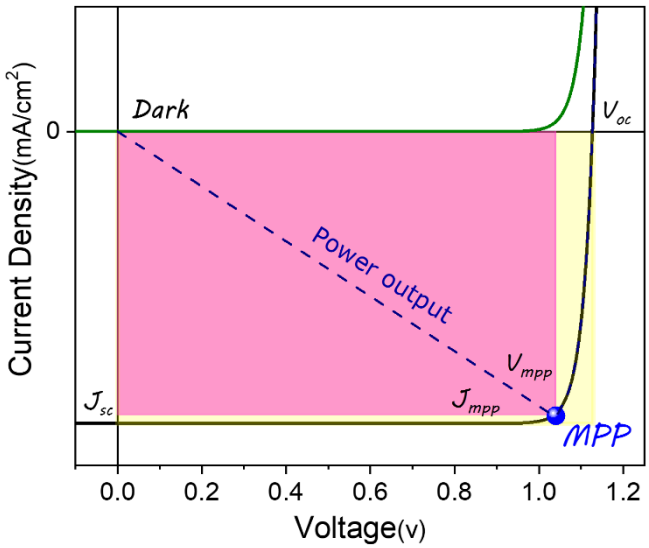

Figure 2-14:: *The current-voltage behavior of a solar cell under dark and illumination conditions.*

The point at which the device has the maximum power output under illumination is known as the maximum power point(MPP) and its voltage and current density respectively are called V_{mpp} and J_{mpp}. Maximum power output of the device is calculated based on:

$$Maximum\ power\ output = J_{mpp} \times V_{mpp} \qquad \textbf{Equation 2—9}$$

The ratio of the maximum power output to the open-circuit voltage and short-circuit current density would suggest a value called fill factor(FF). In another word, this is a ratio of real values to ideal values.

$$Fill\ Factor = \frac{Maximum\ power\ output}{V_{oc} \times J_{SC}} \qquad \textbf{Equation 2—10}$$

The fill factor essentially measures the squareness of the IV curve. A higher fill factor indicates a more rectangular shape, meaning the solar cell is more efficient in converting sunlight into electrical energy. It is influenced by factors such as the quality of the semiconductor material, the resistance within the cell, and the presence of recombination losses.

The power conversion efficiency (PCE) of any photovoltaic device is the ratio of the electrical energy output to the solar input energy (typically 100 mW/cm^2).

$$Power\ Conversion\ Efficiency = \frac{V_{oc} \times J_{SC} \times FF}{solar\ power} \qquad \textbf{Equation 2—11}$$

The current density-voltage characterization of this thesis for small area cells was obtained using a Keithley 2612A Source-measure unit under Wavelabs Sinus 70 LED solar simulator. Before the measurements the lamp was calibrated using a silicon reference cell equipped with an infrared cut-off filter (KG-3, Schott). The J-V curves were

recorded between -0.2 and 1.2 V with 0.01 V steps, integrating the signal for 20 ms after a 10 ms delay. This corresponds to a speed of about 0.3 V/s. The layouts used to test the solar cells have areas of 0.0825 cm^2 and were measured through a shadow mask with 0.05 cm^2 aperture area.

The performance mechanism is not just defined by these parameters, and they are influenced by several other critical parameters such as:

- Leakage current: This residual current typically arises from undesirable defects and imperfections within the diode structure.
- Shunt resistance(R_{SH}): The magnitude of the leakage current is determined by the shunt resistance. A low shunt resistance can lead to power losses in solar cells by providing an alternative current pathway for the light-generated current. This can reduce both the photocurrent flowing through the solar cell and the photovoltage.[98]
- Series resistance(R_s): The series resistance is another loss mechanism that limits the performance of solar cells. It originates from the resistance inherent to the device components, including the absorber, transport materials, metal contacts, and interconnections.[99] The primary impact of series resistance is a reduction in the fill factor, although excessively high values may also diminish the short-circuit current.[100]

2.4.1 External Quantum Efficiency (EQE)

The external quantum efficiency EQE(λ) also called incident photon to current efficiency(IPCE) is the ratio of the incident photons and electron hole pairs on the solar cell that lead to current generation. It is wavelength dependent and is usually measured by illuminating the solar cell with monochromatic light of wavelength λ and measuring the photocurrent through the solar cell.

In this thesis most of the EQEs were measured using Enli Tech QE-R setup, which consist of a chopped probe beam of monochromatic light that generates a short circuit current on the test sample. The system is calibrated using a silicon reference cell. The current measured per wavelength is then converted to voltage by a current/voltage amplifier which allows the signal processing by a lock in amplifier for improve signal to noise ratio. The setup allows white light biasing as well, however in this thesis the measurements were performed in the dark and short circuit conditions.

EQE is normally expressed as a percentage, in an ideal solar cell in short circuit condition, all the photons are converted into free carriers (EQE=100%), this is an indication of the efficiency of photon to electron conversion. By analyzing the EQE spectrum, it is possible to identify wavelength-dependent inefficiencies, such as optical and electrical losses, including parasitic absorption and front and rear surface recombination, that affect the overall performance. In lower wavelength normally the front side of the absorber is targeted, and it would transfer to the back part in higher wavelengths. These insights can guide material or structural optimizations to enhance cell efficiency. Additionally, EQE measurements can be used to calculate the integrated

current density, and the bandgap of the absorber can be determined from the EQE spectrum, providing a valuable comparison to the bandgap obtained from optical measurements. There are a few reports on the current mismatch calculated from different measurements that have been reported[101] and is a common phenomenon and this work is also no exception. A small deviation in the mismatch is considered acceptable throughout this thesis. [102]

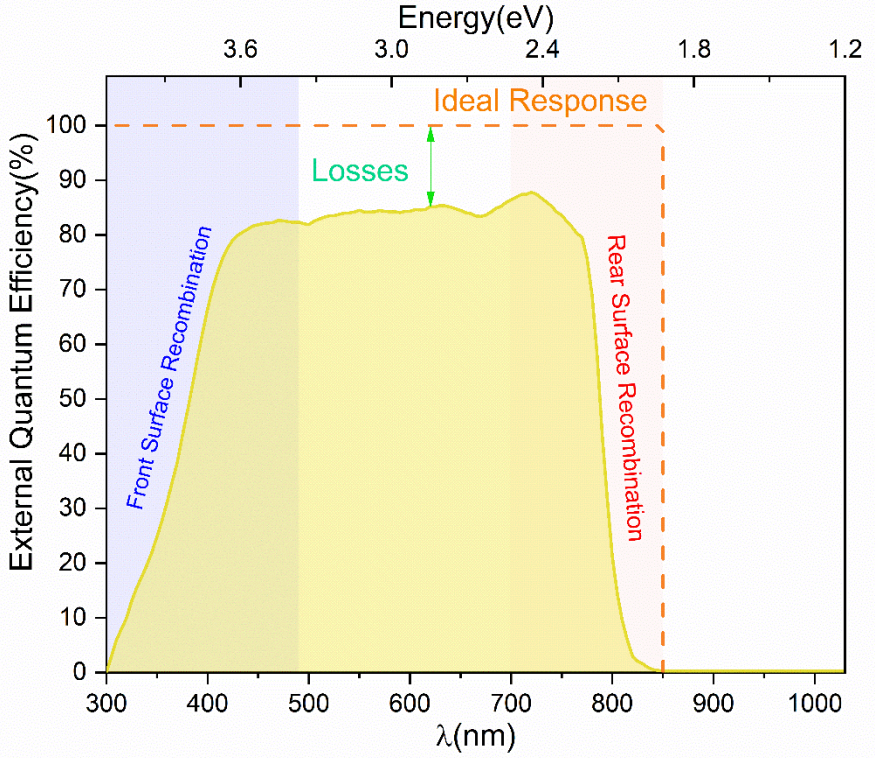

Figure 2-15: *The external quantum efficiency as the function of the wavelength and bandgap energy.*

2.4.2 Hysteresis Index

Photocurrent voltage hysteresis is known to be the difference of behavior under forward and reverse bias which depends on the scan rate and the direction of the scanning. The source of this in perovskite solar cells is associated with different phenomenon like ion migration, trap assisted charge recombination, etc.[103,104] The hysteresis index can give us a realistic view on the severity of this hysteresis and is shown as:

$$HI = \frac{PCE_{RS} - PCE_{FS}}{PCE_{RS}} \qquad \textbf{Equation 2—12}$$

Lowering this index could be considered as an indication of higher quality absorber with lower bulk defects and better charge transport/extraction interfaces.

2.4.3 Maximum power point tracking

The Maximum Power Point (MPP) on the JV curve corresponds to the point where the product of voltage and current is at its highest **(Equation *2—10*)**, indicating the optimal operating condition of the solar cell under illumination. Maximum Power Point Tracking (MPPT) measures this condition over time, allowing for continuous adjustment to maintain maximum power output. This technique is particularly valuable for detecting issues like instant photodegradation, as any deviation from the MPP can indicate a drop in performance.

2.4.4 Geometrical fill factor

Scaling up to larger area modules would introduce some inactive regions within the device that do not contribute to the overall performance. To optimize efficiency and space utilization, a parameter known as the geometrical fill factor(GFF) is defined as follows:

$$GFF = \frac{Active\ area\ of\ the\ module}{Aperture\ area\ of\ the\ module} \qquad \textbf{Equation 2—13}$$

2.4.5 Stability test

To achieve the goal of commercialization of the perovskite solar cells they need to prove a promising lifetime resilient to extrinsic degradation. The first standard to be used in the community was adapted from International Electrotechnical Commission (IEC), however this is not specific to the field.[105] To achieve this goal in the perovskite community, some scientists came together in International Summit on Organic Photovoltaic (ISOS) to establish a protocol for unanimous testing specially as a reference guideline for the possibility of comparable results in 2020.[106] This is also not wholesome for all perovskite solar cell, but it can be considered the most reliable for now. These protocols include shelf-life, outdoor, light soaking, thermal cycling and light–humidity–thermal cycling testing. Performing all of these requires extensive work, however we have tried to do a few of these tests for the experiments in upcoming chapters.

Shelf life

This is a dark storage test called (ISOS-D) which provides information on the tolerance of the solar cells to the ambient conditions without exposure to light. Ambient exposure can favor the appearance of traps or charge carrier barriers through moisture, oxygen or temperature.

Thermal stability

As a second step, the introduction of thermal stressing (constant 65 or 85 °C with relative humidity < 20%) on a cell in the dark has been chosen. At elevated temperatures thermal degradation could be favored due to instabilities in the interfaces or the bulk of the absorber or unfavorable phase transition. Some bulk elements, such as MA, have low

thermal stability[48,107] also iodide is prone to reacting with silver electrode.[108] Additionally organic charge transport layers, which are very common in fully sublimed structures, are susceptible to degradation in high temperatures which is a simulation of operational condition. Therefore, thermal stressing provides insights for future improvement pathways.

More severe conditions like light soaking stress, which measures the cell under constant operational conditions (harsher than reality), and a mixture of different testing conditions like damp heat test, which is a combination of elevated humidity and temperature, and eventually an actual outdoor testing are the future steps for gaining insight. However, these comprehensive assessments are outside of the scope of this work.

Chapter 3: Engineering Stable *p*-type Contacts Towards Efficient Fully Vacuum Deposited Perovskite Solar Cells

Perovskite photovoltaics have recently achieved significant breakthroughs in cell efficiency, while offering simple and low-cost processability. Vacuum-based techniques are gaining increased attention due to their scalability and material versatility. However, fully vacuum-deposited devices remain rare, partly due to the limited availability of charge transport materials compatible with vacuum-deposition. Additionally, sublimed organic contact materials often require high work function interlayers, like MoO_3, or molecular oxidants, which complicate device stability. In this study we explore the use of simpler non-extended conjugation self-assemble monolayers (SAMs) as alternatives to these interlayers, demonstrating improved hole extraction, higher fill factors, and enhanced long-term stability compared to state-of-the art vacuum-deposited architectures. As proof of concept, devices incorporating methylammonium lead iodide perovskite ($MAPbI_3$) and SAM interlayers achieve power conversion efficiencies exceeding 19.5 %, approaching the highest reported values for fully evaporated stacks, along with remarkable thermal stability at 85 ºC.

3.1 Introduction

Metal-halide perovskites have rapidly emerged as a leading material class for photovoltaic and optoelectronic applications due to their excellent optoelectronic properties, structural flexibility, and low-cost manufacturing,[109–113] enabling high PCE with strong integrability. To date, the record efficiency of PSCs has exceeded 25%[114] but the device's long-term stability and the development of scalable and reliable fabrication methods are the pending challenges for their commercialization. Most of the investigations reported in the literature have focused on solution-based fabrication methods, prepared either using small- or large-scale techniques like spin-coating, slot-die coating or inkjet printing.[115–121] However, many of these methods may be less pertinent for their transfer to market as they employ toxic solvents that are detrimental to the environment.[122] Physical vacuum deposition is a mature solvent-free technology already established in the semiconductor industry,[123] which has recently gained increasing attention in the perovskite field. Among different advantages, vacuum deposition provides superior control over the layer thickness, intrinsic purity of the sublimed materials, and it allows preparation of multilayer stacks with conformal coating over different types of substrates. This is of special interest to broaden the market towards alternative applications like building integrated PVs, Internet of things (IoT) or multi-junction tandem solar cells.[70,124,125] Since 2016, efficient devices (> 20% PCE) using vacuum-deposited perovskites have been successfully demonstrated in both *p*-type/intrinsic/*n*-type (*p-i-n)* and *n*-type/intrinsic/ *p*-type (*n-i-p*) configurations, combining either organic polymers, small-molecular-weight semiconductors,[126] or inorganic metal oxides (i.e. SnO_2, TiO_2 or NiO_x) as charge selective layers.[127–129] Nevertheless, despite the promise of vacuum deposition, finding stable charge-selective layers to realize fully evaporated devices, particularly for HTL, remains a challenge.[72,130,131]

In search for the ideal HTL, one should ensure high hole mobility, high thermal and chemical stability, and adequate electronic level alignment to provide ohmic charge transfer to the electrode. In addition, the substrate plays a crucial role in the growth of VD perovskites and may promote detrimental chemical reactions taking place at the interface. This happens when inorganic metal oxides like CuO_x[132], NiOx[133], or MoO_x[134], are used. In these metal oxides the acid–base reactions result in local degradation of the perovskite and the formation of an electrical barrier for hole harvesting.[130,135–137]

As an alternative, sublimable "small molecule" semiconductors like arylamine or polythiophene derivatives are good candidates,[127,128,138,139] however their intrinsic nature provides a non-ohmic interface with the ITO, hindering charge injection/collection. These small, conjugated materials can only obtain good device performances if they are used as very thin layers (< 3 nm). However, this is highly prone to coating defects. Alternatively, the co-deposition or adding an interlayer of a oxidizing material can also improve the formation of ohmic contacts.[140–142] The later, usually consists of strong electron-acceptor

dopants,[32] like cyano-quinodimethane derivatives (F4-TCNQ and F6-TCNNQ) or metal oxides such as MoO_3[74,143] or W_2O_3,[144] which induce a density of free positive charges at the interface with the organic semiconductor, enabling in ohmic charge transport.[39,40] A typical example is the hole selective interface MoO_3/ TaTm, being an intrinsic semiconductor successfully utilized in multiple high-efficiency devices. Unfortunately, these interlayers are unstable towards elevated temperatures,[145] thus compromising device stability. Indeed, little information can be obtained regarding the lifetime of efficient (>18%) fully vacuum deposited PSCs using these interlayers, except for few reports, which in majority show very short stability tests with timescales ranging from seconds to ~200h. [123,146–150]

In the scope of future high-throughput commercialization, it is crucial to ensure stable interfaces with minimal parasitic absorption, ideally based in low-cost materials suitable for a variety of substrates and areas. A recent trend in perovskite PV is the use of phosphonic acids containing carbazole molecules that can self-assemble on metal oxide surfaces (SAMs) HTMs. These materials have demonstrated minimal recombination losses and improved device stability, in part due to the critical chemical design that leads to reduced interfacial recombination.[150–153] However, simpler SAMs which lack the extended π- conjugation and electron delocalization also present an opportunity for creating stable, dopant-free interlayers that can be paired with sublimable intrinsic semiconductors, expanding the potential of fully evaporated devices. Despite few works using simpler SAMs as electrode modifiers,[154,155] or surface passivates for metal oxides, the use of SAM interlayers in perovskite PVs remain largely unexplored.

Here, we investigate simple, non-extended conjugated phosphonic acid SAMs referred to as simple SAMs to evaluate their hole extraction properties as interlayers at the widely used ITO/TaTm interface, comparing them with benchmark interlayers such as MoO_3 or F6-TCNNQ. We explored a series of phosphonate systems featuring increasing amounts of fluorine-terminated groups, in both alkyl and simple aromatic structures, designed to introduce a permanent dipole moment at the interface and modulate the work function (ϕ) of ITO. These modified interfaces are then integrated into *p-i-n* fully vapor-deposited perovskite solar cells, and their performance and stability are compared to state-of-the-art devices. Remarkably, devices using the archetypal methylammonium lead iodide perovskite (MAPbI) and simple-structure SAM interlayers achieve an impressive average power conversion efficiency PCE~19.5%, closely matching record efficiencies reported for fully evaporated stacks. Our results reveal a strong correlation between device efficiency and the induced high ϕ, leading to improved hole extraction, higher *FF*, and overall enhanced performance. Furthermore, there is a significant stability advantage, the absence of unstable oxides or dopants results in superior thermal stability under prolonged stress at 85ºC, bringing the performance closer to the durability observed in solution-processed analogues. This approach holds great potential for broader applications, offering the flexibility to adapt to various device architectures and perovskite

formulations, with promising potential for compatibility with conformal coverage on large-area and textured substrates—an important factor for scaling up to industrial production.

3.2 Experimental methods

Cell fabrication**:** The patterned ITO glass substrates were cleaned as explained in chapter 2. Following UV-ozone cleaning, the next step of substrate preparation involved immersing the ITO substrates overnight in 1 mmol/l phosphonic acid solution in ethanol, annealing at 100°C for 10 minutes and subsequently rinsed with pure ethanol before transferring to the sublimation vacuum chambers. The SAMs investigated include phenylphosphonic acid (SAM 1), 4-flurobenzylphosphonic acid (SAM 2), (3-Trifluoromethyl)phenyl)methyl-phosphonic acid (SAM 3), decylphosphonic acid (SAM 4), and 1H,1H,2H,2H-Perfluorooctanephosphonic (SAM 5).

3.3 Results and discussion

Figure 3-1-a shows the chemical structures of the SAM molecules and TaTm, along with the device architecture used in this study. We selected commercially available SAMs with phosphonic acid as the anchoring group to ensure a strong, reproducible interaction with the ITO surface, as this group can form multiple stable bonds.[156] The investigated SAM molecules feature increasing levels of fluorine-terminated groups, contributing to variations in dipole moment, film coverage and packing. After modifying the ITO electrodes with SAMs deposition, they were transferred directly to the vacuum deposition system without any additional processing for the fabrication of fully evaporated stack as explained in chapter 2 in detail.

Figure 3-2 illustrates the changes in wettability of the ITO surface, measured by water contact angle. The contact angle (θ) of bare-ITO (UV-ozone treated) increases significantly after surface treatment, from ~ 0º to 43º for SAM 1, due to the presence of the hydrocarbon tail group. The introduction of fluorine enhances this effect, with θ reaching 50.7º for SAM 2 (1 fluorine) and 71.2º for SAM 3 (3 fluorine moieties). The most dramatic increase occurs for the aliphatic SAMs – 90º for SAM 4 and 97º for SAM 5 – indicating strong hydrophobicity at these new interfaces. This increased hydrophobicity is noteworthy because polar hydrophilic oxides like ITO are often chemically incompatible with non-polar organic thin films.[157] Therefore the enhanced surface hydrophobicity improves direct electrical contact with TaTm, reducing the risk of delamination of the upper organic. Additionally **Figure 3-2** presents the 3D scan images and root mean square (RMS) roughness data for the same contacts, measured by AFM. The RMS roughness of the bare-ITO surface remains relatively unchanged after different monolayers deposition (3.6 nm to 4.7 nm), indicating a uniform and flat surface without significant island formation. However, there is a complete transformation in the energy landscape of the interfaces.

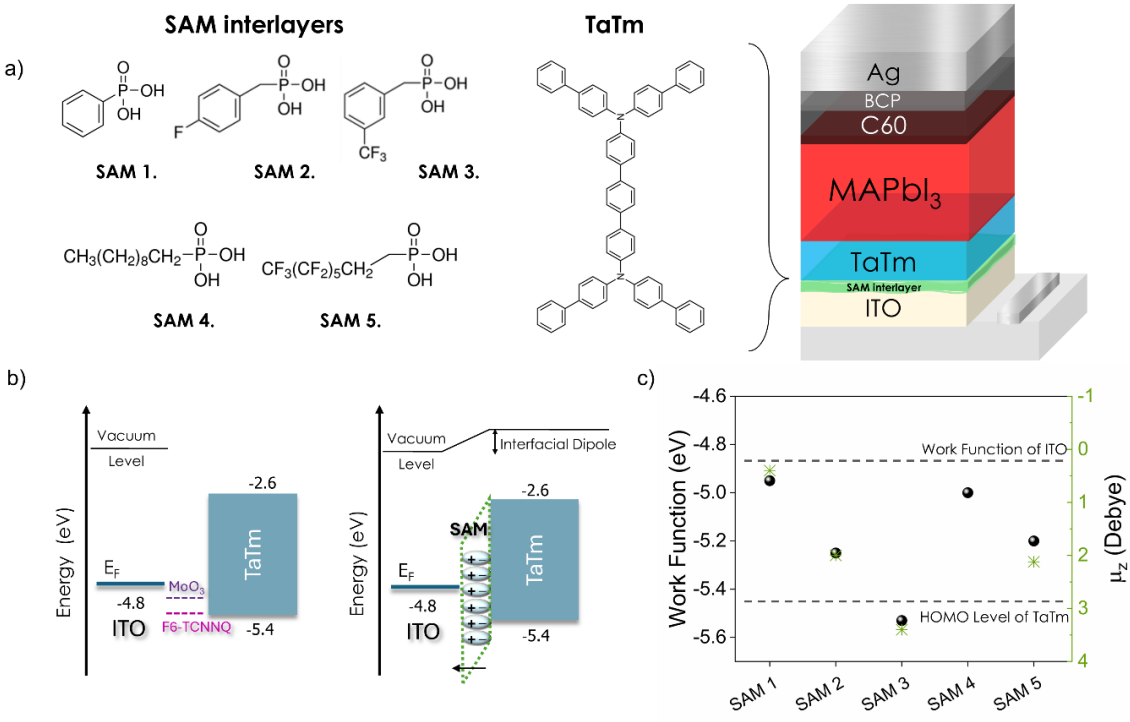

Figure 3- 1: a) *Chemical structures of SAMs, TaTm and device architecture of p-i-in VD-PSCs.* ***b)*** *Schematic showing the energy level diagram of the p-type ITO/TaTm contact containing typical MoO_3 or F6 _TCNNQ high ϕ materials (left) and SAM interlayer (right).* ***c)*** *ϕ of the SAM-modified ITO interfaces measured by KP technique. The values for the bare ITO and HOMO of TaTm are indicated with inset lines as reference. The values of μ_z, taken from literature [57–60], are also included except for SAM 4.*

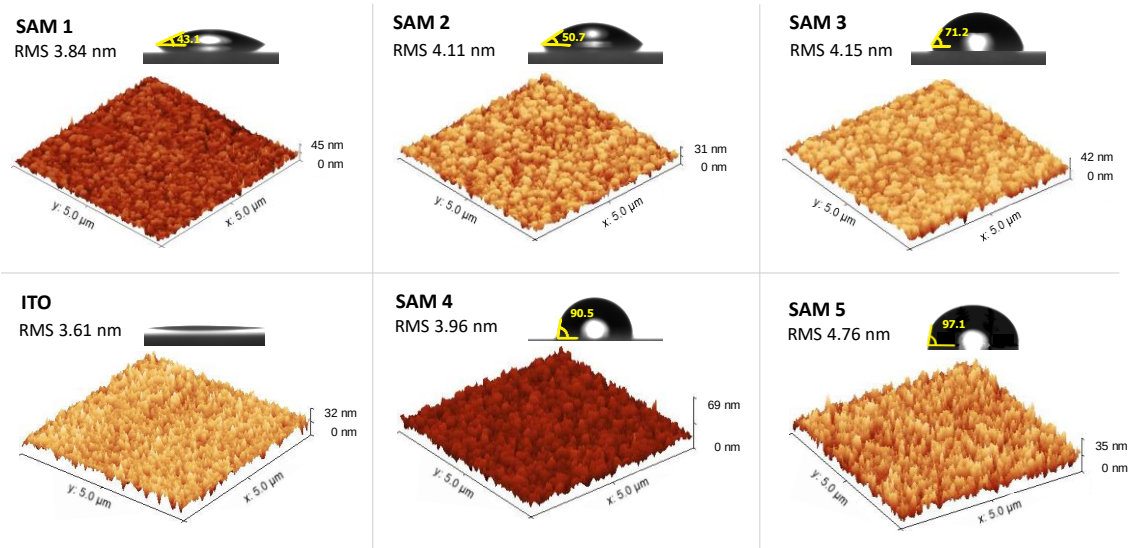

Figure 3- 2: *AFM 3D images (5x5 μm) and the corresponding RMS roughness of the ITO-SAM interlayers studied in this work. The bare ITO is also included for reference. The inset shows the contact angle measured for each interlayer.*

Figure *3-1*-b shows a schematic of the energy level alignment diagrams of ITO/TaTm contacts. The bare ITO surface has a large energy gap (~ 0.6 eV) between its Fermi level (E_F~4.8 eV),[53,54] and the highest occupied molecular orbital (HOMO) of TaTm (~ 5.4 eV).[158] Typically, this gap is bridged using thin interlayers included as references in the left panel

of **Figure *3-1*-b** such as MoO_3 or dopants like F6-TCNNQ.[159,160] Instead, here we use SAM 1 - 5 to modulate the interface properties via surface dipoles, aiming to closely match these energy levels (right panel, **Figure *3-1*-b**). Because the modulation of the interface depends strongly on the SAM dipole orientation, as well as molecular packing and density, we measured the shift in ϕ for each sample using Kelvin probe technique (KP) (**Figure *3-1*-c**). The dashed lines represent the ϕ value for the bare-ITO, and the HOMO level of TaTm, shown here as references. For comparison, the molecular dipole projection onto the surface normal axis (μ_z) for those SAMs that are available in literature is also included.[161,162] Consistent with previous studies, we observe an increase in the ϕ that aligns with the trend of μ_z, for the new interfaces. In the case of aryl-derivatives, a gradual increase in ϕ is observed when adding fluorine units, from 0.14 eV (SAM 1) to a maximum change in ϕ of 0.73 eV (SAM 3). For the aliphatic derivatives, the increase is more moderate, from 0.19 eV (SAM 4) to 0.4 eV (SAM 5). Such increase in ϕ indicates the formation of a surface dipole pointing outward (i.e. with its positive pole facing the ITO), which hence can provide better control of the energy band alignment with the HTM and promote the formation of ohmic contact.

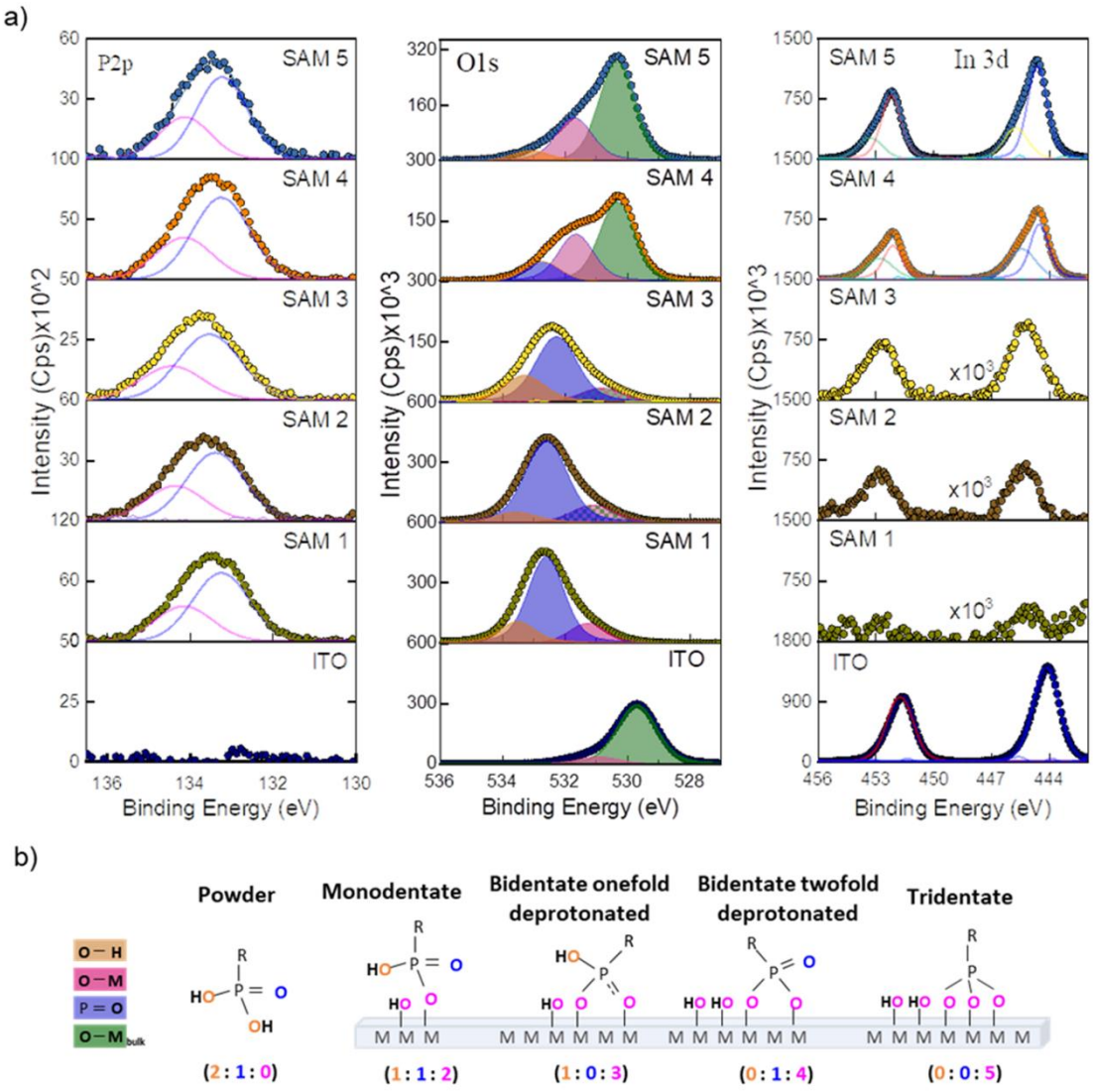

Figure 3-3: a) *High resolution P 2p, O 1 s, and In 3d XPS spectra of SAMs 1- 5 deposited on ITO (1×1)cm². The intensity of the In 3d signals for SAMs 1-3 have been multiplied by a factor of 10³.* ***b)*** *Schematic sketch of the binding configurations of phosphonic acids to oxide surfaces. The label shows each type of oxygen chemical environment in a different color, with the theoretical intensity ratio of the O 1s components in brackets.*

To gain insights into the chemical bonding and structural modifications at the ITO-SAM surface, XPS analysis was conducted. The spectra were measured using a monochromatized Al K-alpha with a photon energy of 1486.6 eV, allowing for highly surface sensitive measurements. **Figure 3-3** presents the relevant XPS core level regions, showing the *P 2p*, *O 1s*, and *In 3d* signals from the ITO-SAM interfaces. In the *P 2p* region, the primary component of the P–O bond (~ 132.8 eV) appears as a doublet, corresponding to the spin–orbit splitting of the *P 2p* level, with the expected separation of 0.9 eV.[163] Compared to the powder samples (**Figure 3-4**), we observe a general change in the peak intensities and shift to lower binding energy. These shifts suggest modifications in the chemical environment of the phosphorus atoms, consistent with the formation of metal-phosphonate bonds with the ITO.

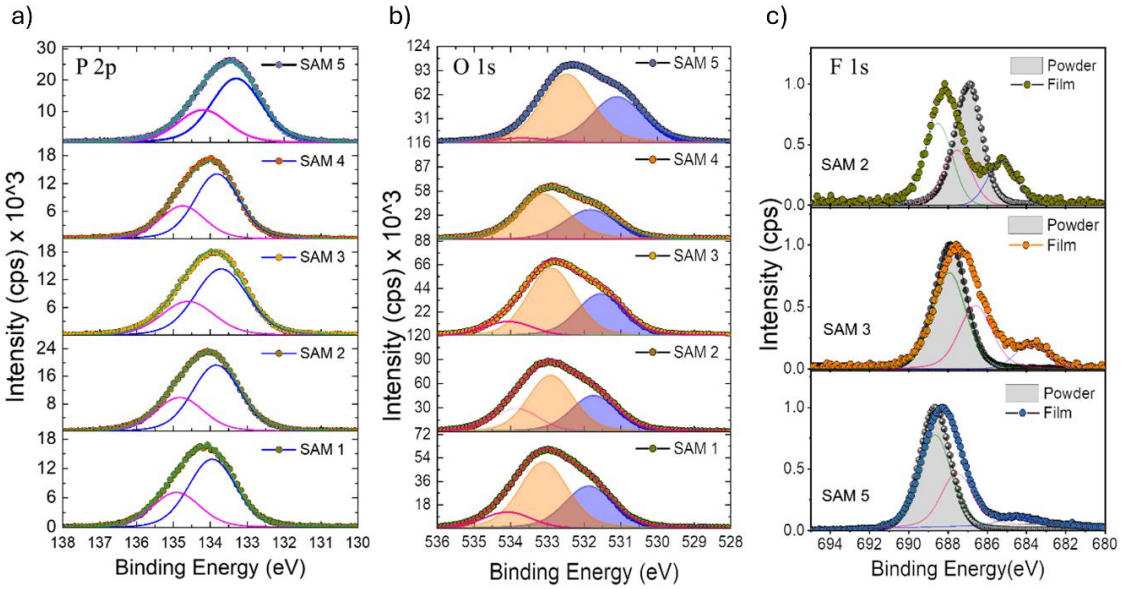

Figure 3-4: *XPS spectra of* ***a)****P 2p,****b)*** *O 1s and obtained for SAMs 1-5 in powder state.* ***c)****The F 1s spectra for the powder and thin films for F containing SAMs.*

Similarly, the *O 1s* signal (530-532 eV) shows changes in both peak position and relative peak intensities, due to variations in P=O and P–OH bonds after surface functionalization. **Figure 3-3-b** presents a schematic of possible bonding configurations for phosphonic acids to ITO. Each oxygen atom's chemical environment corresponds to a distinct binding energy, meaning that various bonding configurations will display multiple *O 1s* components with different intensity ratios (see in brackets the theoretical ratios of the *O 1s* components, arranged from high- to low- binding energy). According to the schematic, when the molecule is in powder state (left side of **Figure 3-3-b**), the *O 1s* spectrum mainly consists of two peaks corresponding to P–OH (~ 533.5 eV, orange) and P=O (~ 532.5 eV, blue) groups, with a 2:1 intensity ratio.(see **Figure 3-4-b** for powder XPS *O1s* spectra) Occasionally, a minor peak (~ 534 eV) is observed, generally associated to adsorbed species like water or oxygen. However, after SAM deposition, two new peaks emerge corresponding to the substrate oxygen atoms (~ 530.5 eV, green) and the covalent P–O–M bonds (~ 531.5 eV, pink), providing different intensity profiles for each monodentate, bidentate, or tridentate configurations. The *O 1s* peaks in **Figure 3-3-a** are color-coded for clarity. For the aryl-based SAMs (SAM 1, SAM 2 and SAM 3), the signal deconvolutes into three components, with the main peak at ~ 532.5 eV (P=O), and minor peaks at ~ 533.5 eV (P–OH) and ~ 531.5 eV (P–O–M). The prevalence of P=O alongside P–OH and P–O–M could indicate the formation of weakly bounded monodentate configurations.[62–64] However, the absence of substrate oxygen signal (~530 eV) and the intensity profile of O 1s for SAMs 1–3 suggests the accumulation of non-binding molecules possibly forming multilayer structures. This is further supported by the minimal *In 3d* signal (444 – 445 eV), which is characteristic of the ITO substrate. Such significant reduction indicates that the surface atoms of *In* are either chemically altered or no longer exposed to the XPS probing depth, consistent with thick molecular layer

coverage. In contrast, the *O 1s* signals of aliphatic SAMs (SAM 4 and SAM 5) are dominated by the substrate oxide peak (~ 530 eV), and the P–O–M bond (~ 531.6 eV), with a small shoulder at ~ 532.5–533.07 eV. As depicted in **Figure 3-3-b**, the dominance of the P–O–M signal (pink) suggests strong bonding configurations, like tridentate or bidentate deprotonated bindings. In this case, the *O 1s* intensity ratios for SAM 4 and 5 (0:1:3 and 1:0:5 respectively) align with the formation of a monolayer featuring mixed tridentate and bidentate deprotonated configurations. This is corroborated by the much higher *In 3d* signal, comparable to that of the bare ITO substrate.

Finally, the *F 1s* signal changes notably after surface functionalization (**Figure 3-4**), shifting from a single peak (~ 688 eV) to multiple deconvoluted peaks. In the 688–686.5 eV range, these peaks suggest distinct chemical environments, likely due to van der Waals interactions within the fluorinated structure, which indicates less homogeneous molecular packing compared to the powder. However, the peak at ~ 684.5 eV likely corresponds to the formation of metal-fluorine bonds with the ITO.[164] We note that this is particularly significant for SAM 2 and SAM 3, where multilayers are observed. **Table 3-1** summarizes the peak positions and their relative contributions to the *O 1s* signal for each SAM interlayer.

Table 3-1: *Binding energy photoemission of O1s signal for ITO and SAM interlayers. The relative contribution of each peak to the total signal is indicated in brackets.*

	P–OH	P = O	M–OH / P–O–M	Metal Oxide (bulk)
SAM 1	533.5 (17%)	532.6 (68%)	531.3 (15%)	_
SAM 2	533.6 (10%)	532.6 (75%)	531.1 (15%)	_
SAM 3	533.3 (26%)	532.3 (62%)	_	530.7 (12%)
SAM 4	_	532.7 (13%)	531.6 (35%)	530.3 (52%)
SAM 5	533.1 (6%)	_	531.6 (29%)	530.3 (65%)
ITO			531.0 (9%)	529.8 (91%)

We additionally evaluated the ITO-SAM/TaTm hole extraction interfaces by fabricating fully vacuum deposited PSC. The device architecture includes modified ITO-SAM, followed by a previously reported architecture containing TaTm (7 nm) / $MAPbI_3$ (800 nm)/ C60 (25 nm)/ BCP(8 nm)/ Ag (100nm) in which C60 is fullerene and BCP is bathocuproine, as also shown in **Figure 3-1-a**. To ensure reliable statistics, we fabricated at least 30 cells for each device configuration, and for the top performing devices at least 40 cells were characterized.

Figure 3-5-a shows the XRD pattern of the as-deposited $MAPbI_3$ film, along with top and cross-sectional SEM images. The films consist of a polycrystalline material with small grains (< 200 nm in diameter), typical of vacuum co-deposited PSCs, and a minor presence of residual PbI_2 phase at 12.5°.[165] The UV-vis absorption and PL spectra, shown in **Figure 3-5-b**, confirm the high absorption coefficient and a bandgap of about 1.6 eV, typical for $MAPbI_3$. Initially, we analyzed devices containing the intrinsic semiconductor,

TaTm, alongside those incorporating baseline interlayers like MoO_3 and F6-TCNNQ. The representative *J–V* curves, and EQE of reference devices are summarized in **Figure 3-5-c** and **d**, with the specific PV values listed in **Table 3-2**.

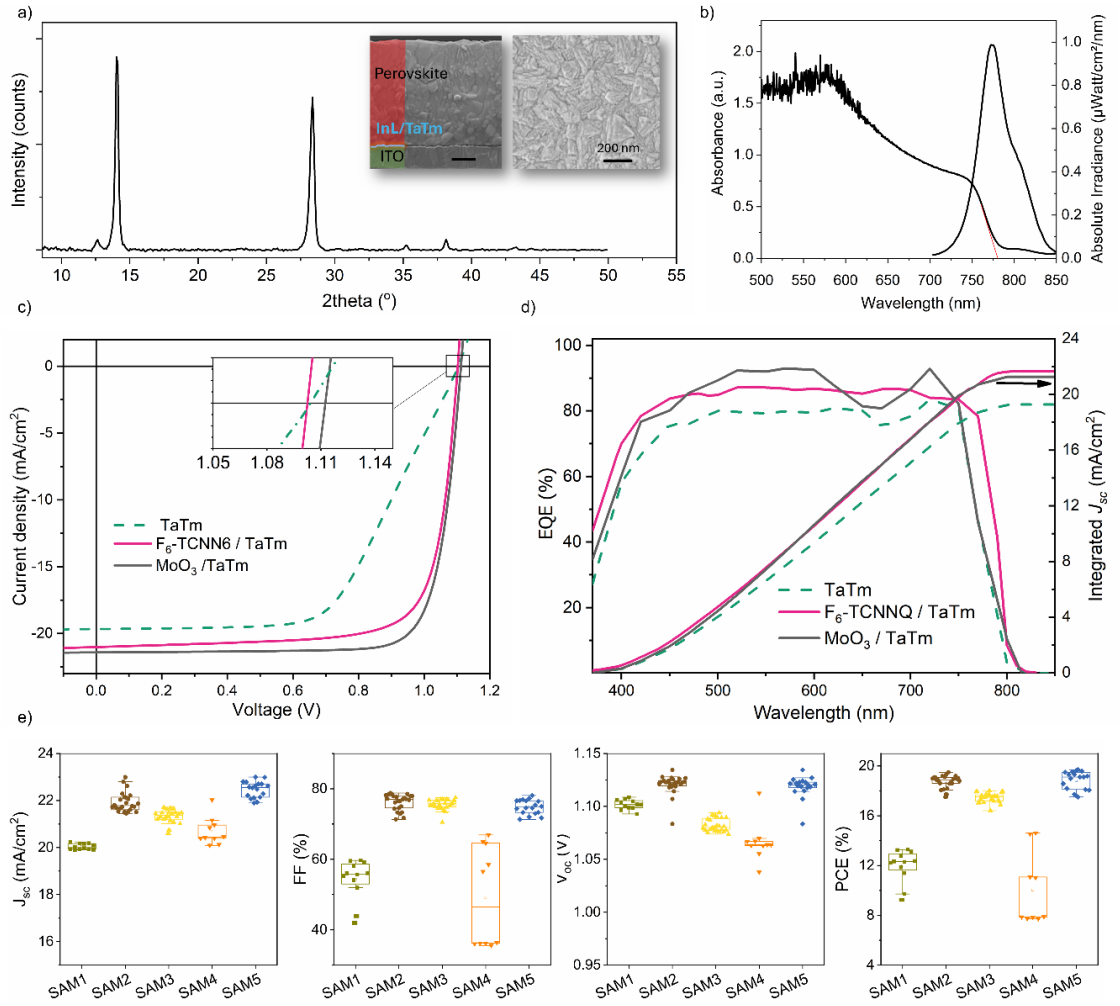

Figure 3-5: ***a)*** *XRD patterns,* ***b)*** *UV-Vis optical absorption and PL spectra, of co-sublimed perovskite films.* ***c)*** *J–V and* ***d)*** *EQE curves obtained for the reference vacuum deposited p-i-n PSCs, under 100 mW/cm² illumination.* ***e)*** *Statistical analysis of photovoltaic parameters obtained for cells containing SAM-modified ITO interfaces.*

Table 3-2: *Photovoltaic parameters obtained for J-V curves shown in Figure 3-5-c.*

		PCE	Voc	Jsc	FF
TaTm (7nm)	**Forward**	12.16	1.09	20.06	55.69
	Reverse	12.53	1.09	20.12	57.04
F_6-TCNNQ/TaTm	**Forward**	17.64	1.10	21.01	76.13
	Reverse	17.74	1.10	21.07	76.33
MoO_3/TaTm	**Forward**	18.73	1.11	20.55	81.86
	Reverse	18.64	1.11	20.6	81.38

A statistical comparison of the photovoltaic parameters is shown in **Figure 3-6**. Despite the cell configuration, similar average J_{sc} (~ 20.6 mA/cm^2), and V_{oc} (~ 1.1 V) are observed, but notable differences appear in the average FF. Devices with only a 7 nm TaTm layer exhibit low FF values (~ 55.5%), and a reduced slope near the V_{oc} (**Figure 3-5-c**), indicating significant series resistance. This behavior is expected due to the low conductivity of TaTm and the large energy mismatch with the ITO, resulting in an average power conversion efficiency (PCE) of ~ 12%. While reducing the TaTm thickness to 3 nm improves the FF (~ 70%) (**Figure 3-6**),[140] such thin layers are prone to inhomogeneities, leading to inconsistent device performance. On the other hand, the introduction of MoO_3 and F6-TCNNQ interlayers significantly enhances device efficiency. While V_{oc} (~ 1.1 V) and J_{sc} (> 20 mA/cm^2) show little change except for a small gradual increase, the FF improves markedly to ~ 80%, resulting in PCE values exceeding 19%.The increased improvement in *Jsc* is also consistent with the increased current integrated from EQE (**Figure 3-5-d**). Such behavior, well documented in literature, has been attributed to the generation of interfacial positive charges induced by these high ϕ interlayers, which promotes ohmic behavior and a boost in device performance. However, these interfaces suffer from instability issues, making this strategy less appealing for vacuum technology. Interestingly, we achieve comparable efficiency by introducing ITO-SAM (1 to 5)/TaTm interfaces. The photovoltaic performance, shown in **Figure 3-5-e**, depends strongly on the SAM chemical structure. For the non-fluorinated interlayers, SAM 1 and SAM 4, the J_{sc} is slightly below 21 mA/cm^2, but the FF remains low, barely surpassing 60%. These values are well below those of the MoO_3 or F6-TCNNQ interlayers and are similar to pristine TaTm devices. For the aryl derivative SAM 1, the V_{oc} remains at ~ 1.1 V, while in the case of the aliphatic SAM 4, it slightly drops to 1.05 V, resulting in PCE of ~ 12% for both.

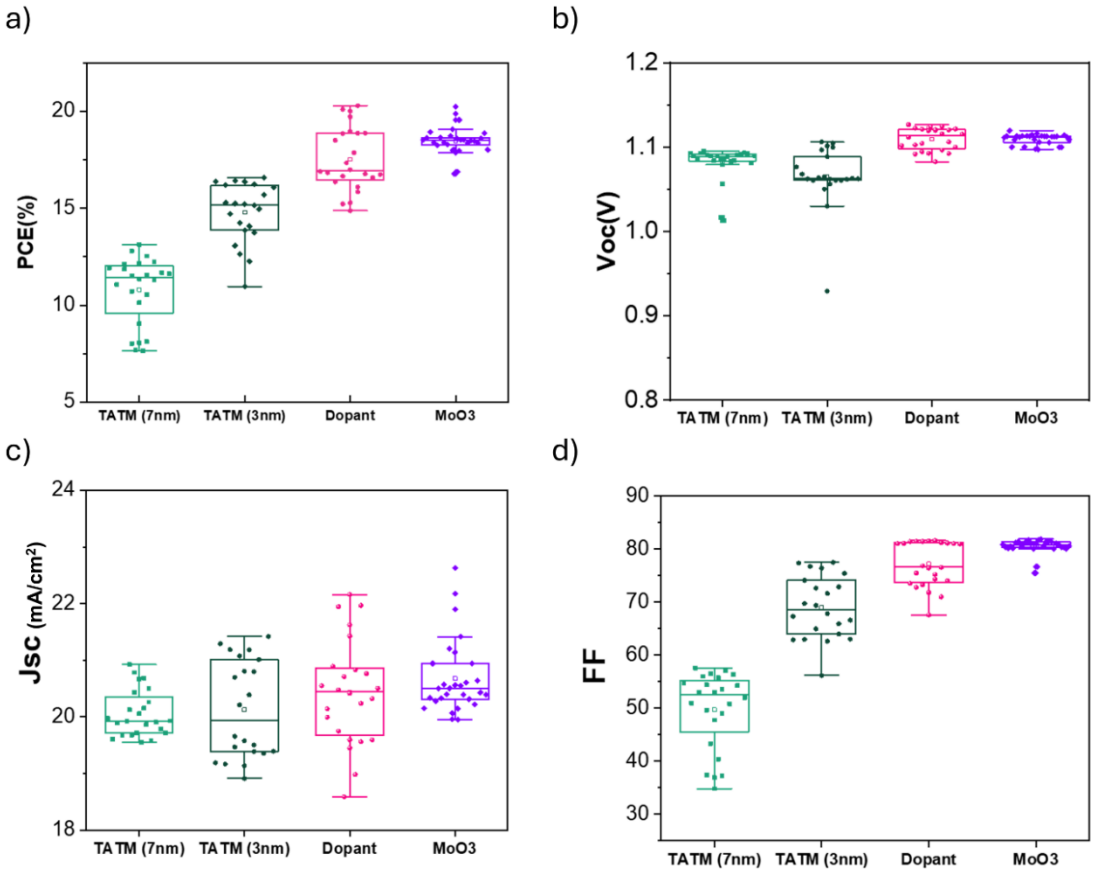

Figure 3-6: *Statistical data for PCE, Voc, Jsc and FF obtained from more than 100 cells (at least 23 cells per condition) prepared with the different interlayers investigated in this study. The top bar shows the maximum value, the bottom bar shows the minimum value, and the rectangle shows the region containing 25–75% of the data, obtained for each condition.*

This aligns with the lower ϕ values observed for SAM 1 and SAM 4 (**Figure 3-1-c**), reflecting hindered charge extraction at the interface. In contrast, using fluorinated derivatives, SAM 2, SAM 4 and SAM 5, significantly improves the FF to around 80%, with PV parameters closely matching those of the reference devices. Notably, SAM 2 and SAM 5 deliver high V_{oc} (~ 1.13 V) and J_{sc} (~ 22 mA/cm^2), surpassing the reference cells. This results in an average efficiency of ~ 19%, with negligible J–V hysteresis. Even in the case of SAM 3, where alignment with the TaTm HOMO level may not be optimal, the device still exhibits improved J_{sc} and FF compared to the 7 – 3 nm TaTm-only devices, reaching an average PCE of ~18%.

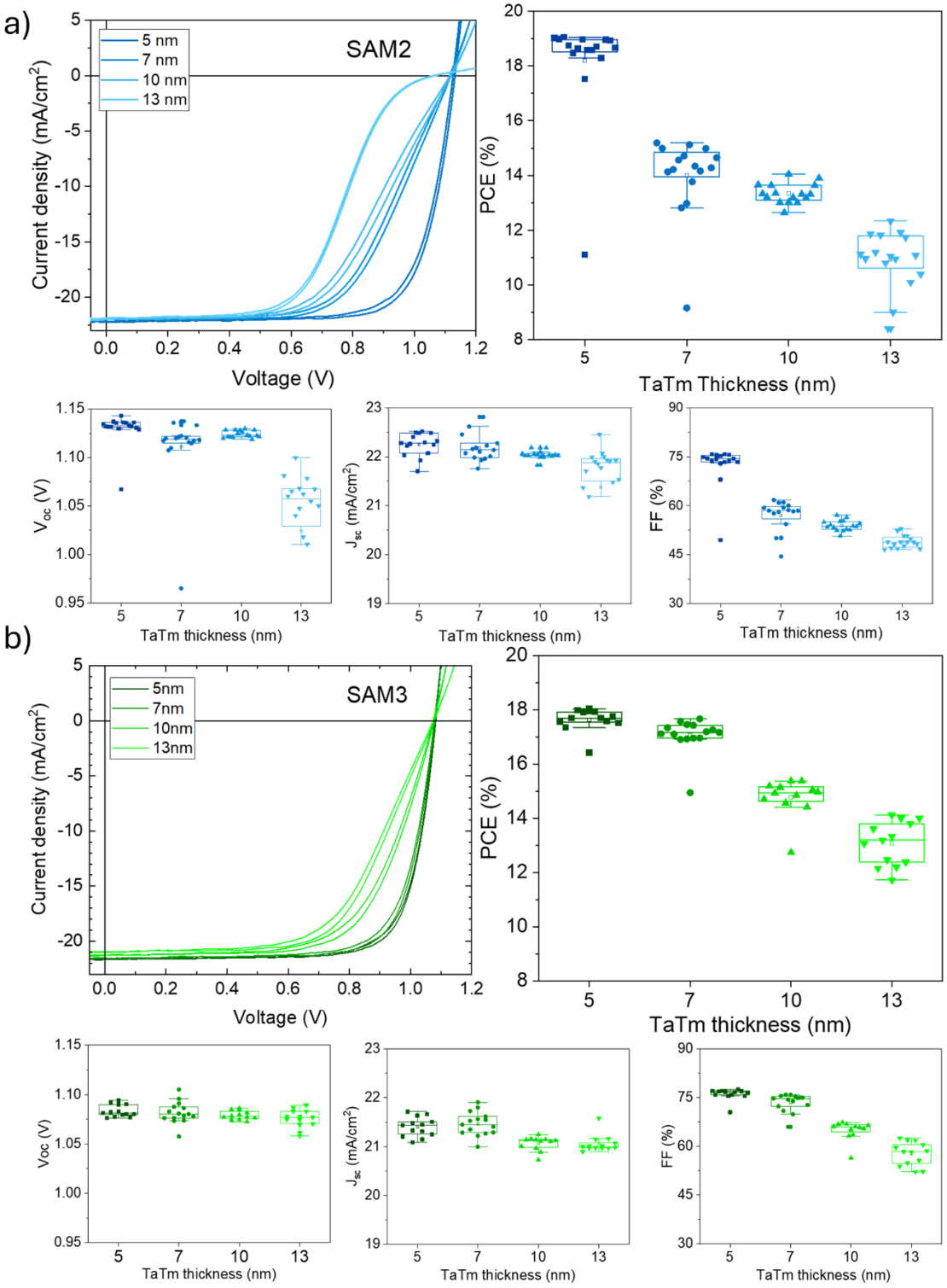

Figure 3-7: *Thickness optimization for TaTm using* ***a.*** *SAM 2 and* ***b.*** *SAM 3 as interlayer. The data include typical J–V curves obtained for each condition, including the forward and reverse scans. It also contains statistical data for PCE, V_{oc}, J_{sc} and FF obtained from a minimum of 50 cells (at least 16 cells per condition). The top bar shows the maximum value, the bottom bar shows the minimum value, and the rectangle shows the region containing 25–75% of the data, obtained for each condition.*

A summary of the device optimization for SAM 2, SAM 3, with varying TaTm thickness from 5 to 13 nm, can be found in **Figure 3-7-a** and **b** respectively. In both cases, the device's performance is significantly impacted by TaTm thickness. Notably, a substantial performance drop is observed for thicker layers (10 - 13 nm) due to the strong resistance

introduced by the intrinsic semiconductor. In contrast, when the TaTm thickness is reduced, the behavior differs depending on the SAM interlayer. For the aryl-derivatives, SAMs 2 and 3, the photovoltaic parameters J_{sc}, V_{oc} and FF consistently improve, with the best performance achieved at a Tatm thickness of 5 nm.

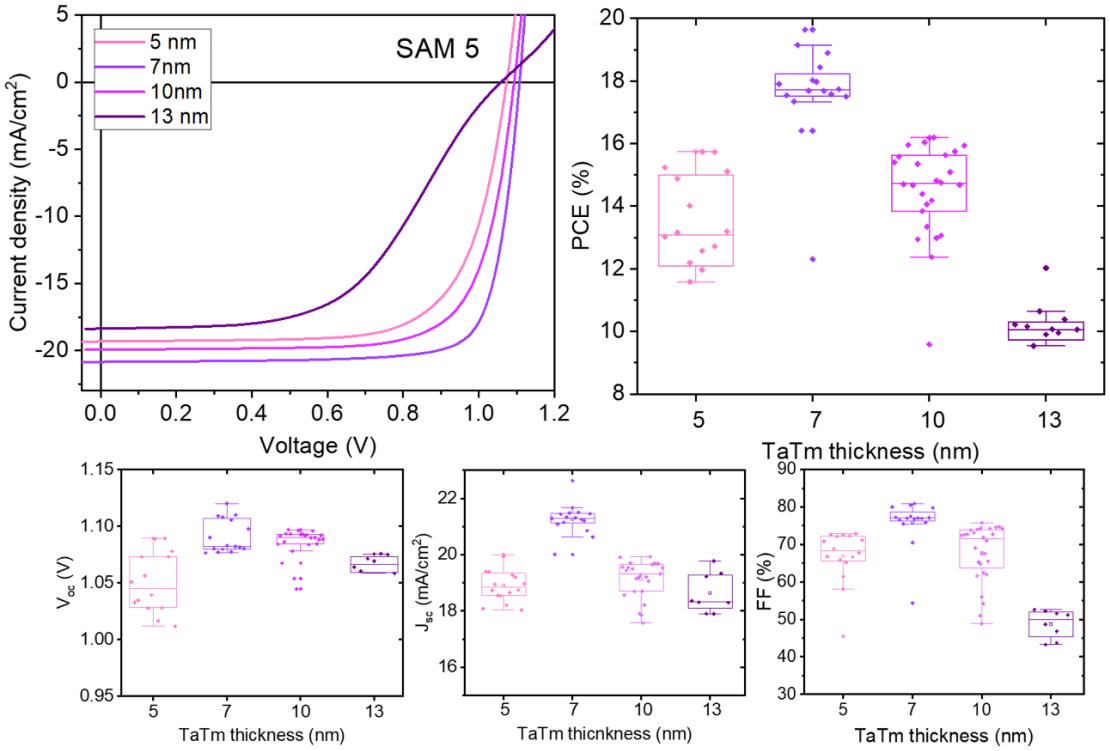

Figure 3-8: *Thickness optimization for TaTm using SAM 5 as interlayer. The data include typical J–V curves obtained for each condition, including the forward and reverse scans. It also contains statistical data for PCE, V_{oc}, J_{sc} and FF obtained from more than 70 cells (at least 13 cells per condition). The top bar shows the maximum value, the bottom bar shows the minimum value, and the rectangle shows the region containing 25–75% of the data, obtained for each condition.*

However, the aliphatic SAM 5 shows a different trend as shown in **Figure 3-8**. While its performance also improves as the thickness decreases, it experiences a sharp decline in efficiency when the TaTm thickness falls below 7nm, due to a drop in all key photovoltaic parameters. We attribute this behavior to the thinner nature of SAM 5, as suggested by the XPS analysis, making it more susceptible to coverage defects and enhanced charge recombination as the TaTm layer becomes thinner. As a result, the optimal TaTm thickness varies from 5 nm to 7 nm, in the case of SAM 5. The champion cells for each configuration, including the *J–V* curves and EQE, are summarized in **Figure 3-9**, and listed in **Table 3-3**.

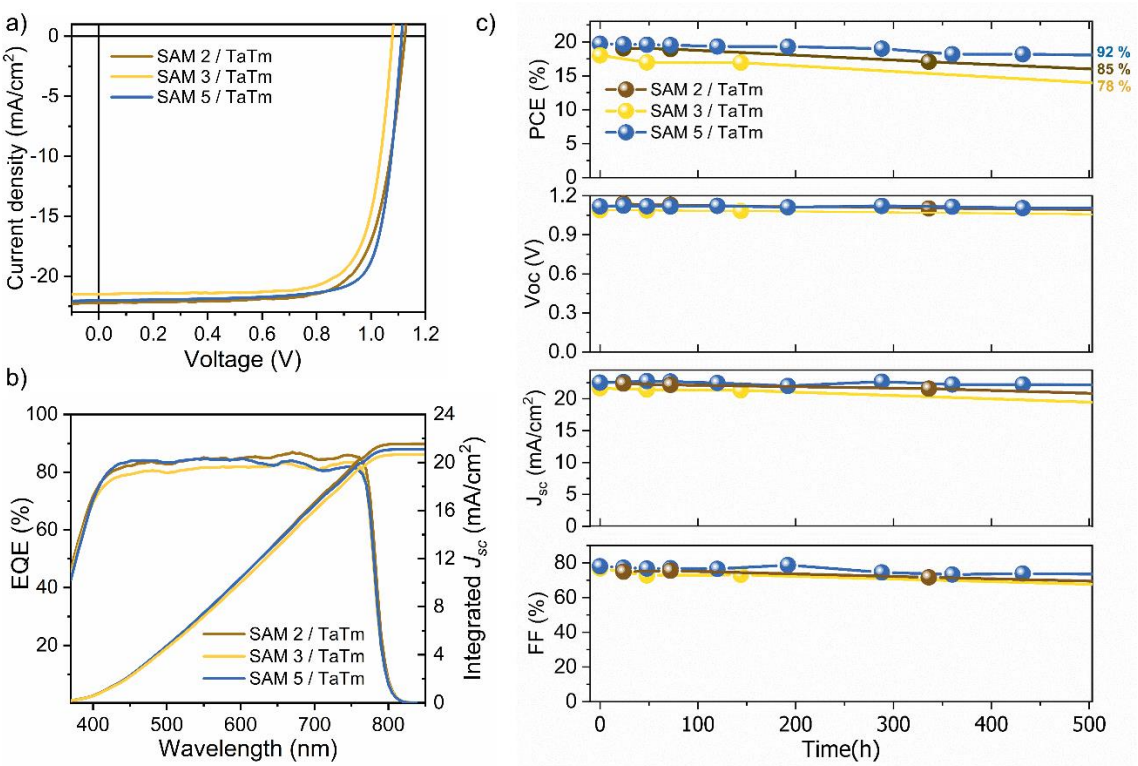

Figure 3-9: a) *J-V and* ***b)*** *EQE curves of the champion cells using SAM 2, 3, and 5.* ***c)*** *Device stability under continuous thermal stress at 85 °C, measured in N_2 atmosphere.*

High photon-to-current conversion efficiencies of over 80% are observed across most of the ultraviolet-visible spectrum, resulting in integrated current densities of 20.7, 21.13 and 21.6 mA/cm^2 for SAM 3, SAM 2 and SAM 5 respectively, in line with the *J–V* curves.

Table 3-3: *PV parameters of the J–V scans under forward and reverse bias obtained for the champion cells shown in Figure 3-9.*

		PCE	Voc	Jsc	FF
SAM2	**Forward**	19.19	1.11	22.62	76.63
	Reverse	19.50	1.12	22.80	76.46
SAM3	**Forward**	17.63	1.08	21.66	75.30
	Reverse	18.02	1.08	21.66	76.83
SAM5	**Forward**	19.65	1.12	22.63	77.24
	Reverse	19.71	1.12	22.54	78.13

Notably, the monolayer SAM 5 outperforms among the others, with J_{sc}, V_{oc} and FF values of 22.6 mA/cm^2; 1.12 V; 77.3 % respectively, leading to an overall efficiency of 19.65 % (see *J–V* hysteresis measurements in **Figure 3-10**).

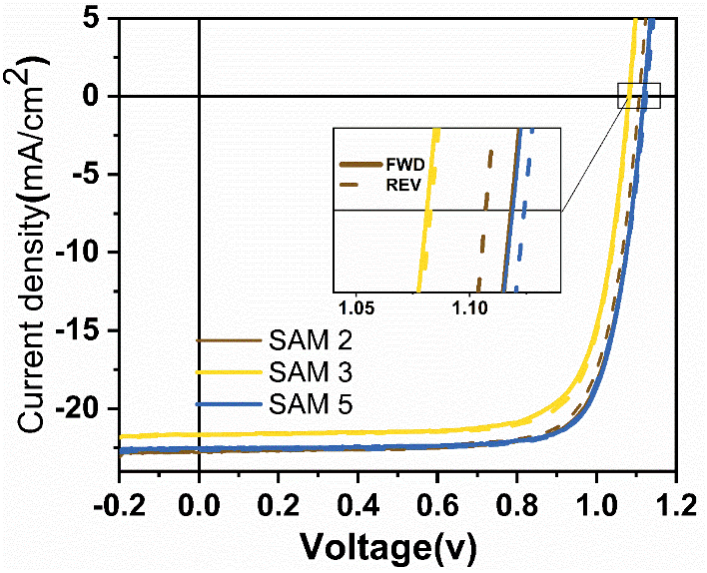

Figure 3-10: *J-V scans obtained under forward and reverse bias of (-0.2 to 1.2V), for the champion cells containing SAM 2, SAM 3 and SAM 5 as interlayers.*

The results suggest that device performances comparable to state-of-the art fully vacuum deposited PSCs can be achieved by combining an intrinsic semiconductor with simple, stable SAM interlayers, provided the interface induces a sufficient change in ϕ.

The stability of the devices was also evaluated under high temperature conditions. The stability curves for unsealed solar cells using SAM 2, 3 and 5, measured under continuous thermal stress (500 h) at 85 ºC in nitrogen atmosphere are shown in **Figure 3-9-c**. For comparison, the stability of devices with MoO_3 or F6-TCNNQ under the same conditions is provided in the left panel of **Figure 3-11**. A significant improvement in device stability is observed when substituting MoO_3 or F6-TCNNQ with SAM 2, SAM 3 or SAM 5. As shown in **Figure 3-11**, the MoO_3 or F6-TCNNQ interlayers degrade rapidly, losing over 20 % or their initial efficiency within just 100 h. After this point, their performance sharply declines, with efficiency dropping below 50 % once the test reaches 500 h. A closer examination of the device parameters reveals that while *Voc* (and to a lesser extent *Jsc*) is relatively well preserved, particularly for MoO_3 interlayer, the main factor contributing to poor performance is the drop in *FF,* which decreases to 75% of its initial value after just 100 hours of testing. In contrast, the SAM interlayers exhibit no significant signs of *FF* degradation, and both *Voc*, and *Jsc* show only a gradual but minor decrease. As a result, cells with SAM interlayers retain over 78 % of their initial efficiency after 500 h, with SAM 2 and 5 maintaining 85% and 92% efficiency respectively. Therefore, not only the charges are more efficiently extracted to external contacts, but also, they result in enhanced thermal stability for the devices. Importantly, SAM 5 demonstrates exceptional long-term stability, retaining 90 % of its initial efficiency after 1000 hours of testing as shown in the right panel of **Figure 3-11**. These findings suggest that the degradation dynamics of the interface might be influenced by the type of molecule and its molecular packing. Controlling these interactions could broaden the scope of SAMs, opening new possibilities for novel p-type contacts in fully evaporated devices.

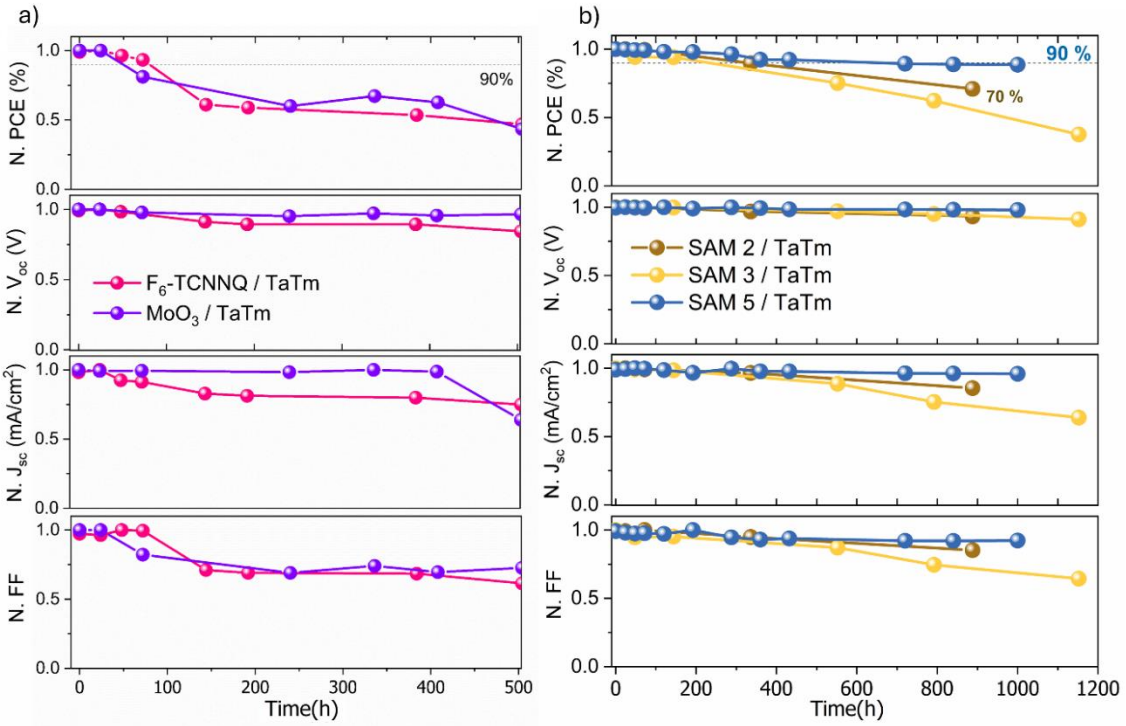

Figure 3-11: a) *Thermal stability test of $MAPbI_3$ PSCs at 85 °C containing reference interlayers, MoO_3 and F6-TCNNQ. The dashed line indicates the value for 90 % drop of initial efficiency.* ***b)*** *Photovoltaic parameters of the champion cells for 1000h under heating temperature of 85°C in N_2 atmosphere.*

3.4 Conclusion

In conclusion, we evaluated several simple structure SAMs as novel high ϕ interlayers to use as *p*-type contacts in combination with intrinsic sublimable semiconductors. By incorporating modified ITO-SAM electrodes to overcome the energy barrier at the TaTm interface, we observed improvements in both efficiency and stability of fully vacuum deposited PSCs, primary due to the preservation of FF stability over time. Our findings indicate that aryl-derivatives SAMs tend to form multilayers unlike their aliphatic analogues, leading to small differences in the optimal TaTm thickness. Exploiting this simple concept allows the fabrication of fully evaporated $MAPbI_3$ solar cells with PCE exceeding 19 %, while also enhancing thermal stability. These results highlight the versatility of SAMs as stable, efficient interlayers for fully vacuum deposited PSCs, and open the door to further exploration of *p*-/*n*-type contacts in the quest for even higher efficiencies and greater stabilities.

Chapter 4: High-Performance Double A-Cation Perovskite Solar Cells via Co-Evaporation

This chapter focuses on the fabrication, characterization, and performance analysis of fully vacuum-deposited PSCs with varying MA and FA content. Two compositions, FAMAPI and MAFAPI, were prepared using a co-evaporation process, with deposition rates monitored by substrate-mounted QCMs. The targeted compositions were confirmed via ^{1}H-NMR and EDX analyses, showing a 2:1 MA-to-FA ratio for MAFAPI and 0.16:1 for FAMAPI, with an intentional 20% excess of PbI_2 for defect passivation.

Performance evaluations revealed a significant efficiency advantage for MAFAPI-based devices, achieving a PCE of 21.8%, compared to 19.45% for FAMAPI. This is among the highest PCE reported for a fully evaporated perovskite based solar cell to date. The superior efficiency of MAFAPI devices was attributed to higher current densities and reduced recombination losses. Drift-diffusion simulations using SIMsalabim quantified the performance differences, with the bulk trap density identified as a key factor. MAFAPI films exhibited fewer bulk traps than FAMAPI, consistent with predictions that MA-rich perovskites mitigate intragrain planar defects, such as stacking faults, twins, and dislocations. These defects in FAMAPI facilitated higher Shockley-Read-Hall recombination, limiting current generation and increasing losses relative to the radiative limit. Stability tests confirmed the robustness of MAFAPI devices, with only a 10% PCE decline over 1000 hours in dark storage.

4.1 Introduction

The two most used vacuum deposition methods for PSCs are co-sublimation and sequential sublimation of the precursors.[166–169] In co-sublimation, the perovskite semiconductor is grown in a single step by simultaneously subliming all the precursors required for the final perovskite composition. Whereas in sequential deposition, the inorganic precursors are typically deposited first, and at a second step the organic precursors are deposited followed by an annealing step completing the conversion to a fully formed perovskite film. Recently, PSCs in *n-i-p* configuration achieved PCE values exceeding 24 % using this method. These cells employed a solution processed HTL and are thus not fully vacuum processed, however they demonstrate that high quality perovskite layers can be achieved using vacuum deposition methods.[129]

Co-sublimation of the perovskite layer has resulted in solar cells with PCE's as high as 20.83%, in fully evaporated *n-i-p* devices which typically outperforms their *p-i-n* counterpart[73] (all other layers of the device stack are also prepared by vacuum deposition methods). However, the highest reported efficiency for a *p-i-n* structure is 20.4%, using $MA_{0.47}FA_{0.53}PbI_3$ perovskite composition. This was accomplished by incorporating evaporated MeO-2PACz anchoring groups to stabilize the formamidinium lead iodide (FAPI) phase, and by introducing different ratios of MAI to stabilize the pure FAPI fabrication process. The device stack consisting of Glass/ITO/MeO-2PACz/FAMAPI/C60/BCP/Cu, was entirely fabricated using thermal vacuum evaporation.[170]

Previously, our group reported the preparation of co-sublimed formamidium, methylammonium lead iodide (FAMAPI) and their integration into thin film solar cells. The first report used superstrate configuration, in which the solar cells are deposited on ITO coated glass substrates and finished with a metallic top electrode. In the superstrate configuration the sunlight enters through the bottom substrate into the cell.[171] In that report the ratio of FA and MA was varied over a limited range and the effect of these compositional changes on the solar cell performance was rather limited. In a more recent report, a similar FAMAPI perovskite was integrated into a substrate architecture, consisting of a metal coated substrate and a top (semi-) transparent electrode. In the substrate configuration, the sunlight enters the cells through the top contact. When comparing superstrate with substrate configuration, the PCE was similar in both cases, yet the FF and J_{sc} were different. Due to better light-incoupling the J_{sc} is higher in the substrate configuration cell, yet the FF was slightly lower than in the superstrate configuration.[172]

Additionally in a publication by Li et al. an argument was made that a higher concentration of MA relative to FA in the perovskite film can mitigate the formation of intragrain planar defects, including stacking faults, twins, and dislocations. These structural imperfections can facilitate charge recombination processes, thereby limiting

the solar cell's PCE. Consequently, devices fabricated with this MA-enriched perovskite composition are expected to demonstrate enhanced carrier lifetimes, reduced V_{oc} deficit and hysteresis, as well as improved PCE.[173] We therefore decided to extend the range of MA versus FA in co-sublimed FAMAPI perovskite films and integrate them into superstrate configuration devices as defined as a *p-i-n* baseline in chapter 1 of the current thesis. Interestingly, when the FA to MA ratio is reduced the crystallization of the FAMAPI films changes, leading to a different preferential orientation with a lower excess of PbI_2 present. With these reduced FA films, the PCE of the fully evaporated devices reaches values as high as 21.8 %, one of the best values reported for fully vacuum deposited devices.

4.2 Results and discussion

Perovskite thin films were prepared in a vacuum chamber equipped with several thermal sources, quartz crystal microbalance (QCM), and integrated into a nitrogen-filled glove box. In this way, exposure of the precursors and the deposited material to the ambient atmosphere is prevented. The active layer was deposited via co-evaporation of the three precursor materials: lead iodide (PbI_2), MAI, and FAI. These precursors were individually weighted and heated in separate thermally controlled crucibles, which were isolated by thermal shields to prevent cross-contamination. The evaporation rates of the FAI and PbI_2 were carefully monitored and controlled by QCMs at two critical stages: during the initial vaporization process and again when the materials reached the substrate surface. This was necessary due to the varied behaviors of evaporation. The deposition rates of organic ammonium cations are not easily monitored by microbalance crystal sensors, as their sticking coefficient on gold surfaces is very low. Only in the presence of PbI_2 a reliable reading of the QCM can be obtained as demonstrated in a detailed study.[174] Even with the inclusion of PbI_2, minor deviations may occur between the optimized readings from the QCM sensors near the sources and the one situated close to the substrate, so the substrate sensor which is calibrated for PbI_2 has been the reference for the reading meaning that the ratio for the organics given in this work are defined as the difference with PbI_2 and do not correspond to the exact deposition rates. This emphasizes the importance of the substrate-mounted sensor for precise monitoring of the deposition rates.

Two different perovskite active layer compositions, denominated as FAMAPI and MAFAPI, were fabricated via co-evaporation. Substrate-mounted QCM sensors measured the deposition rates, which were 0.50 Å/s for PbI_2, 0.04 Å/s for FAI, and 0.17 Å/s for MAI in the case of MAFAPI, and 0.50 Å/s for PbI_2, 0.16 Å/s for FAI, and 0.05 Å/s for MAI in the case of FAMAPI. The evaporation course followed the same order for both compositions. It should be noted that these rates are not absolute as all readings are taken from the substrate QCM. The final perovskite compositions were confirmed by performing EDX measurements to determine the inorganic ratios for both compositions.

The I/Pb ratio in both cases shows approximately 2.8:1 stochiometric ratio as presented in (**Table 4-1**). The deviation from the 3:1 stochiometric ratio was intentional, with an excess of PbI_2 (approximately 20%)added due to reports on its passivation effect.[175–177]

Table 4-1: *The atomic concentration ratio obtained from EDX analysis of FAMAPI and MAFAPI for I and Pb.*

	Element	Atomic concentration	Weight concentration
MAFAPI	I	30.43	55.90
	Pb	10.83	32.50
	I/Pb	2.88	1.76
FAMAPI	I	33.38	56.80
	Pb	11.55	32.10
	I/Pb	2.81	1.72

Additionally, it is important to also confirm the relative amounts of the organic cations in the final perovskite film and verify the accuracy of the deposition method. ^{1}H-NMR was used to determine the relative ratios of the organics in the perovskite film taking advantage of the relative chemical shift in the ppm of the protons on FA and MA.[178] To ensure sufficient material above the detection limit of ^{1}H-NMR, five substrates of at least 600 nm with a dimension of 3x3 cm^2 were each deposited in a single sublimation run, and the perovskite layers were dissolved in 1mL deuterated dimethyl sulfoxide (d-DMSO).

A typical ^{1}H-NMR spectrum obtained for liquid samples of the MAFAPI is shown in **Figure 4-1-a** and FAMAPI in **Figure 4-1-b** , we have identified the different protons of MA and FA with Greek letters. Both the α proton of FA and the δ and χ proton of MA can be clearly identified in both cases.[179,180] The γ and β protons of FA have a lower signal due to proton exchange between these two amine groups.[181] This observation is consistent with the ^{1}H-NMR spectrum of powdered FAI that was used in this evaporation. (**Figure 4-2**)

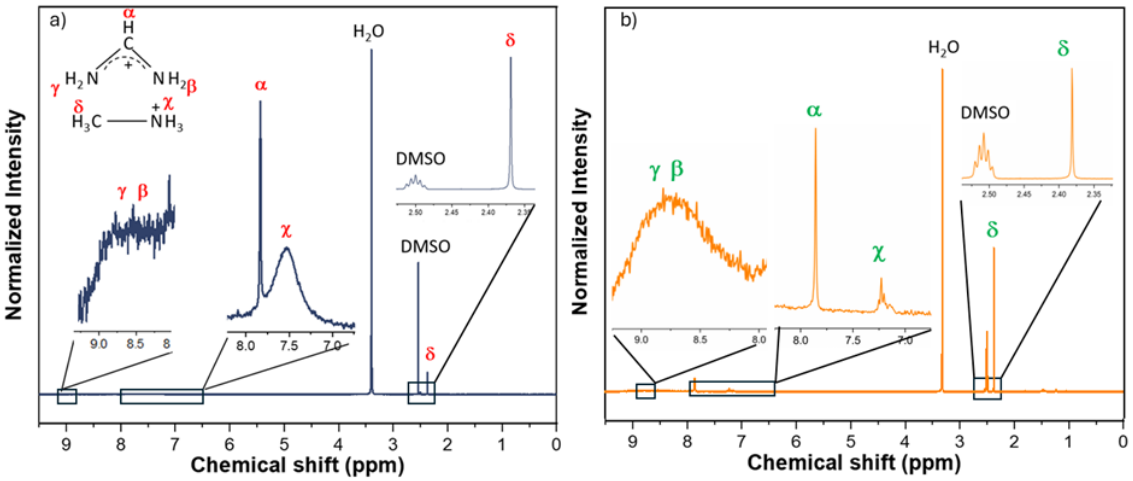

Figure 4-1: *The ^{1}H-NMR spectra of **a)** MAFAPI and **b)**FAMAPI perovskite film dissolved in d-DMSO with the attribution of each proton.*

By integrating the peaks of the different signals, a ratio of the protons in MA and FA is obtained. See **Figure 4-1** and **Table 4-2**. The 3 protons of (χ) of MAI (7.5 ppm) have been compared to the single α proton in FAI (7.85 ppm) and β and γ 4 protons together at (8.7 ppm). Although the peak resolutions were relatively low and there are some overlapping of the signals in case of α proton in FAI (7.85 ppm), they were adequate to reveal a 2:1 ratio between MA and FA in case of MAFAPI and 0.16:1 in case of FAMAPI.

Table 4-2: *The organic cations deposition rates, the corresponding protons in accordance with ^{1}H-NMR specra showed in Figure 1, chemical shift, integration, expected theoretical formula and the final formula.*

Organic cation	Δrate (A°/s)*	Type of Proton	Chemical shift (ppm)	Integral of the NMR peak	Integral divided by each proton	Theoretical formula**	Measured formula***
MAFAPI							
MA^+	0.17	—NH3 (χ)	7.5	2.1	0.7		
		—CH3 (δ)	2.38	2.1	0.7		
FA+	0.04	—CH (α)	7.85	0.30	0.30	$MA_{0.77}FA_{0.22}PbI_3$	$MA_{0.70}FA_{0.30}PbI_3$
		—NH2 (β)	8.6	0.60	0.30		
		—NH2 (γ)	8.9	0.60	0.30		
FAMAPI							
MA^+	0.05	—NH3 (χ)	7.5	0.45	0.15		
		—CH3 (δ)	2.38	0.45	0.15		
FA^+	0.16	—CH (α)	7.85	0.85	0.85	$MA_{0.25}FA_{0.75}PbI_3$	$MA_{0.15}FA_{0.85}PbI_3$
		—NH2 (β)	8.6	1.70	0.85		
		—NH2 (γ)	8.9	1.70	0.85		

**Δrate on the substrate QCM = the increase in the rate read on the substrate sensor upon cation coevaporation*
*** based on the ratio between the Δrates*
**** based on the ratio between the integrals of the NMR*

The integration results for a better ratio visualization have been also provided in the annex of this chapter (**Figure 4-8** and **Figure 4-9**). By also comparing the δ and χ proton of MA, we have an internal reference to verify the reliability of this method.

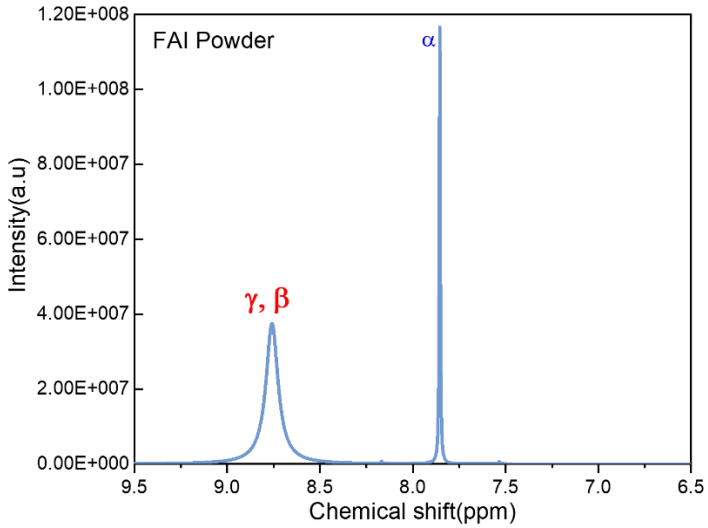

Figure 4-2: *the ^{1}H-NMR spectra of the commercial FAI powder indicating the protons in accordance with Figure 4-1 symbolization.*

From this analysis, it is observed that the targeted composition (via the sublimation rates) is close to the obtained composition, albeit with a slightly lower amount of MA^+. This slight deviation is in line with previous reports.[182]

The XRD of both FAMAPI and MAFAPI shown in **Figure 4-3-a** were compared. The peak at 2 theta of 12.5° is ascribed to PbI_2 which indicates that in both films there is some unreacted PbI_2 remaining which is in line with the EDX results. The preferential orientation of the MAFAPI is in [111] direction, evident from the intense peak at 2theta of 24.5°. In contrast, no preferential orientation is observed in FAMAPI film. The cross sectional SEM image of the MAFAPI perovskite, which was obtained by cutting a full solar cell device stack as illustrated in **Figure 4-3-b**, shows rather large grains that appear to span the full distance between bottom and top electrode **Figure 4-3-c**. This is somewhat unexpected as usually vacuum deposited perovskites have rather small grain sizes.

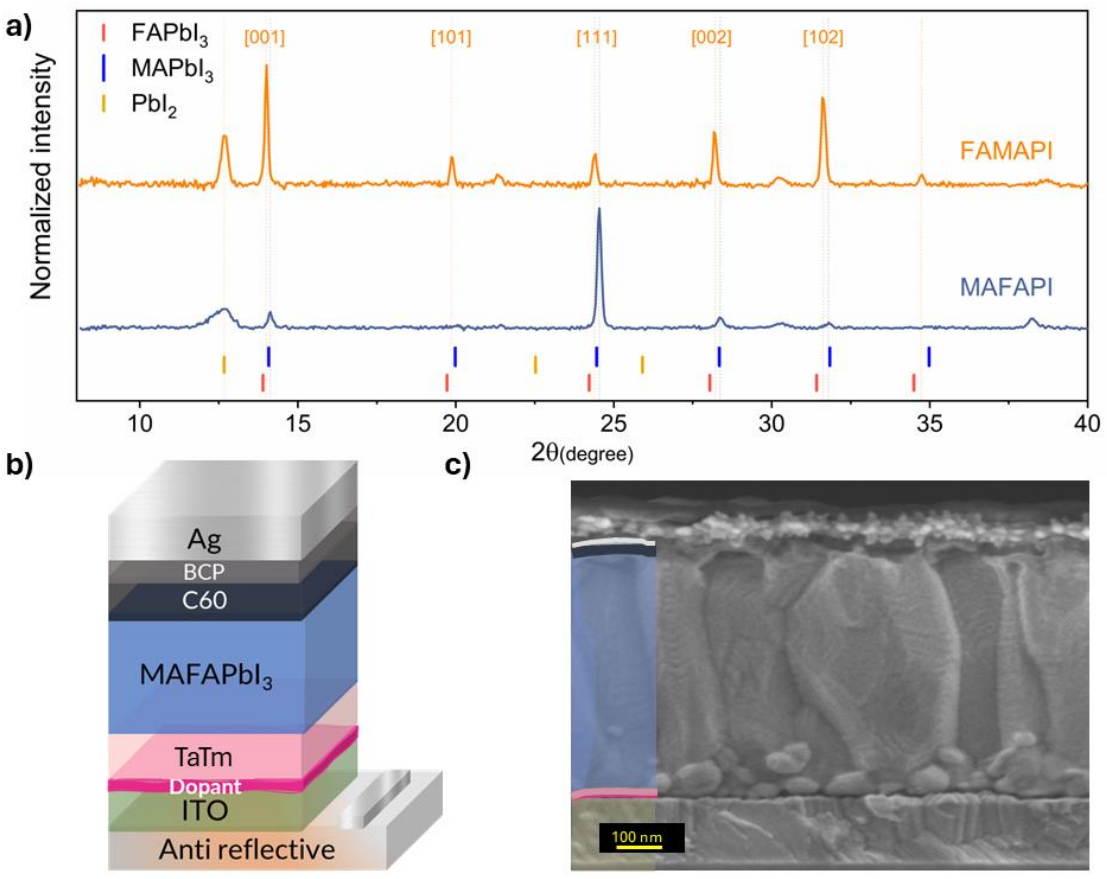

Figure 4-3: ***a)*** *XRD pattern of the FAMAPI and MAFAPI perovskite films and the reference of single A-cation counterparts.* ***b)*** *Schematic of the device structure.* ***c)*** *SEM image of the cross section of a fully evaporated solar cell using MAFAPI as the absorber layer. The different layers in the cross section are identified with colors and are correlated to the device layout scheme depicted in panel b.*

To check the change in the optical bandgap we have calculated the bandgap by Tauc plot calculations (**Equation 2—6**)of both perovskite films with direct bandgaps indicating the bandgap of 1.52 eV and 1.55 eV for FA rich and MA rich perovskite and shown in **Figure 4-4**

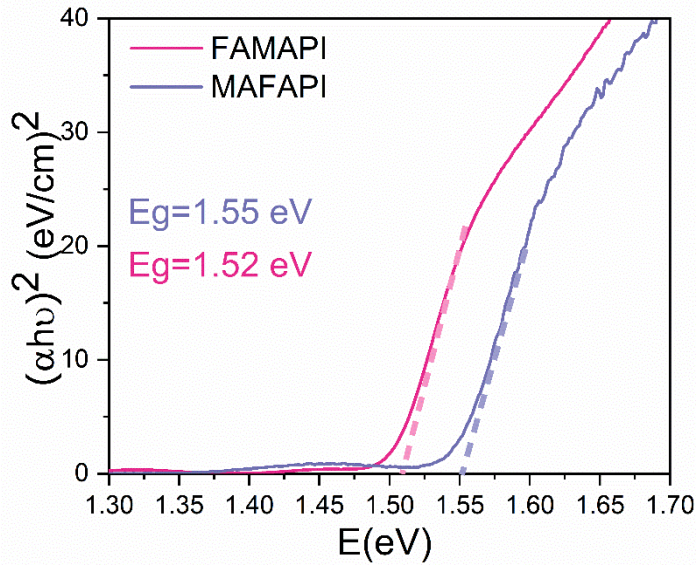

Figure 4-4: *The band gap of FAMAPI and MAFAPI perovskite measured by direct bandgap Tauc plot.*

To evaluate if indeed the MAFAPI perovskite can lead to improved performances in a photovoltaic cell fully evaporated solar cells were prepared with the following architecture LiF (85nm) as an antireflective coating, glass (0.7 mm), ITO (140 nm), F6-TCNNQ (2.5nm), TaTm (10nm), perovskite active layer ($MA_{0.7}FA_{0.3}PbI_3$) of about 700 nm, C_{60} (10nm), BCP(7nm) and Ag(100nm) (**Figure 4-3:-b**). This structure has been previously reported for the FAMAPI absorber.[183] The performance of a typical solar cell composed of MAFAPI containing the *J-V* characteristics obtained while illuminating the champion cell is depicted in **Figure 4-5-a**. The champion device achieves the V_{oc} of 1.1 V, J_{sc} of 24.24 mA/cm^2 and FF of 81.86, leading to a power conversion efficiency (PCE) of 21.8. Both forward and reverse scan are displayed and virtually no difference can be seen between the two curves, which is in accordance with measured negligible hysteresis index **Equation 2—*12*** of only 0.005. The key performance parameters of the champion and average values are depicted in **Table 4-3**.

Table 4-3: *The PV parameters of the champion and the average value MAFAPI and FAMAPI solar cell with a structure shown in Figure 4-3-b.*

		PCE(%)	V_{oc}(V)	J_{sc}(mA/cm^2)	FF
MAFAPI					
	Champion	21.83	1.10	24.24	81.86
	Average	21.26 ± 0.49*	1.10 ± 0.004	23.81 ± 0.5	81.07 ± 0.99
FAMAPI					
	Champion	19.50	1.06	23.01	79.84
	Average	19.24±0.25*	1.07 ± 0.006	22.87 ± 0.08	78.45 ± 1.02

**Minimum of at least 20 devices*

The PCE of 21.8 % of the champion cell is significantly higher than what we previously obtained using FAMAPI as the absorber (19.45%). This is among the highest PCE reported for a fully evaporated perovskite based solar cell to date. In **Figure 4-5-b**, the EQE as a function of wavelength is depicted. The EQE resembles the absorption spectrum of the MAFAPI absorber and has a maximum of 92.84 % at 720 nm. By integrating the EQE with the solar spectrum we obtain the current density the cell can generate, which is 22.93 mA/cm^2. This is slightly lower than the J_{sc} obtained from the J-V scans however, measuring lower J_{sc} (an average of about 4-5%) from EQE in comparison to the J-V scan under simulated 1-Sun illumination has been reported to occur often in perovskite based solar cells.[101,102] Even though the current density of the MAFAPI devices is around 89 % of the radiative limit, there is still some room for improvements. Recently, we showed that this is due to inefficient charge extraction and sub-optimal light-incoupling. The latter is caused by the very flat surface of the vacuum deposited perovskite films which leads to light reflection losses and interference effects.[184] The MAFAPI based cells were operated under mpp tracking using an algorithm described in chapter 2. In **Figure 4-5-c**, the MPP versus time is depicted for a short duration. Despite some small fluctuations the cell continuously generates more than 21 mW/cm^2 which is in line with the PCE that is derived from the J-V scans. This is expected as our cells show negligible hysteresis between forward and reverse scans. The voltage applied during the mpp tracking was 0.96 V, which is very close to the Vmpp obtained from the J-V analysis and in line with the high FF observed.

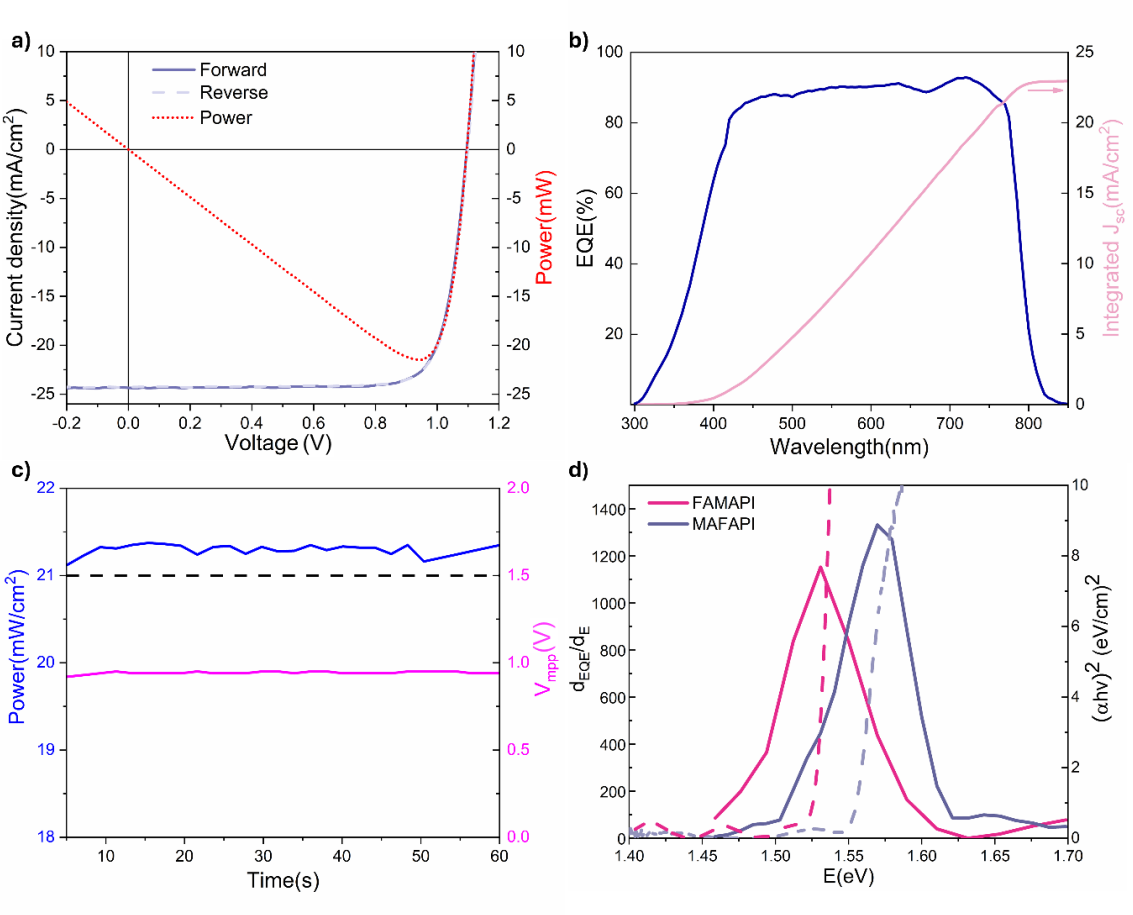

Figure 4-5: *Characterization of the MAFAPI solar cell while illuminated at 1 sun intensity.* ***a)*** *The J-V curve under illumination on forward (solid line) reverse (dotted line) and power output of the device (right axis).* ***b)*** *The external quantum efficiency (left axis) and integrated short circuit current density (right axis).* ***c)*** *The mpp tracking of the cell and applied voltage at Vmpp obtained from a panel.* ***d)*** *The band gap of FAMAPI, Eg= 1.513 calculated by EQE derivative (solid line) and Eg= 1.520 Tauc-plot (dotted line) calculations compared to the band gap of the MAFAPI Eg=1.555 calculated by EQE derivative and Eg= 1.550 by Tauc-plot calculations.*

In **Figure 4-5-d**, the d_{EQE}/d_E are displayed for both types of devices, from this, it is apparent that there is a small difference in the bandgap of the semiconductor. With MAFAPI having a slightly higher bandgap (1.55 eV) than FAMAPI (1.51 eV). This is expected as the increase size of FA^+ leads to a larger tilting and thus a decrease in the bandgap. As a result, it is expected that the FAMAPI based device has a slightly higher J_{sc} and a slightly lower V_{oc} than that using MAFAPI. The bandgaps obtained from the Tauc-plots and the d_{EQE}/d_E agree well with each other.

To assess the shelf life stability the devices were kept in the glovebox in the dark and were only exposed to the ambient atmosphere for a short period of time for the purpose of efficiency measurements. The device efficiency dropped by 10 % after 1000 hours (**Figure 4-6**), which was primarily due to a drop in FF and V_{oc}. The J_{sc} after a small initial decline remained stable. This is similar in the case of the previously reported thermal stability of FAMAPI in superstrate structure.[183]

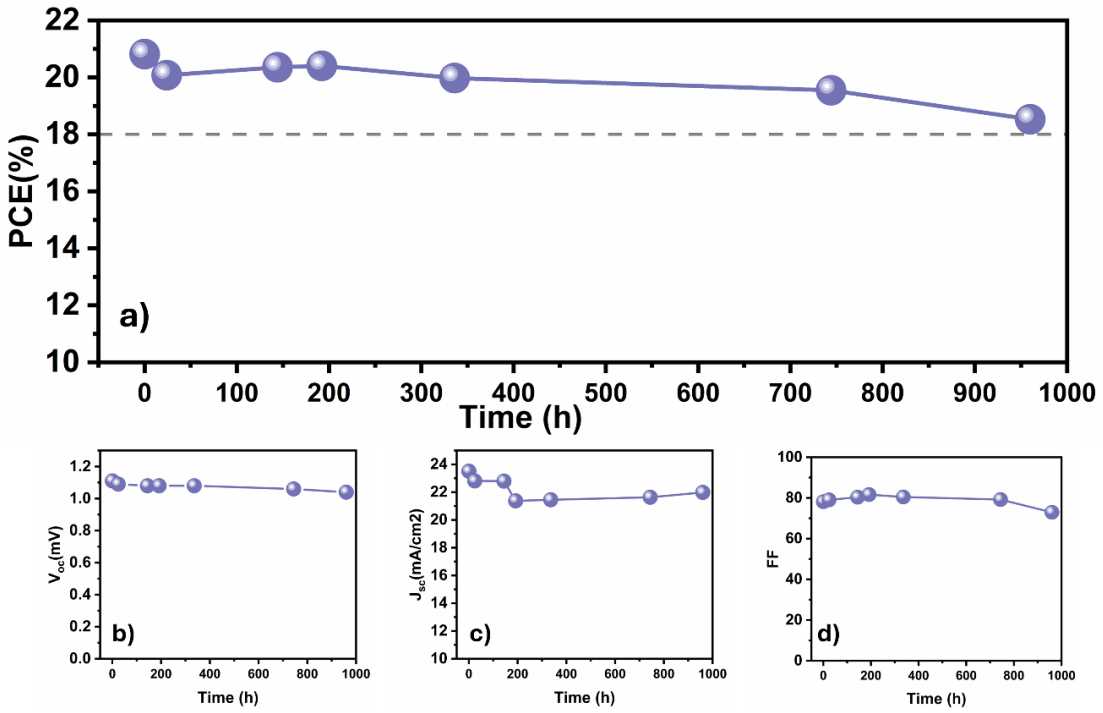

***Figure 4-6**: shelf-life of the fully evaporated MAFAPI PSC **a)**The PCE **b)** The V_{oc} **c)** The J_{sc}. **d)** The FF evolution over 1000 hours storage in the glovebox in the dark.*

The radiative limit for the J_{sc} and V_{oc} for solar cells with a bandgap of 1.51 and 1.55 eV as also shown in **Table 4-4** are 28.64 and 27.26 mA/cm^2 and 1.24 and 1.28 V, respectively. The relative V_{oc} loss with respect to the radiative limit is similar for both types of devices. There is, however, a significant difference in the relative loss of the J_{sc} values between them, for the MAFAPI based device this is only 11% whereas in the case of FAMAPI based devices this is nearly 20%.

***Table 4-4:** The photovoltaic parameters values for different perovskites based on radiative limit from the reference.[28]*

Perovskite	Bandgap (eV)		PCE (%)	V_{oc} (V)	J_{sc} (mA/cm^2)	FF
MAFAPI						
	1.55	Radiative limit	31.5	1.28	27.26	90.3
		Experimental values	21.83	1.1	24.24	81.86
		Loss percentage	30.7	14.06	11.08	9.347
FAMAPI						
	1.51	Radiative limit	32.04	1.24	28.64	90.1
		Experimental values	19.50	1.06	23.01	79.84
		Loss percentage	39.14	14.65	19.66	11.39

To understand where this difference between the solar cells employing MAFAPI and FAMAPI comes from, we analyzed the experimental data and fitted the *J-V* curves using drift-diffusion freeware "Simsalabim".[185] As a starting point for the fitting, a parameter-set that was previously employed for a MAPbI solar cell was used, which had identical charge transport layers as in the current work. The parameters such as the bandgap and the layer thickness have been adjusted to each sample. To quantify the deviation between simulated *J-V* and measured curves, normalized root mean square (RMS) values have been used. These RMS values are calculated by means of **Equation 4—1**

$$r = \frac{\sqrt{\sum_i (J_i^{(sim.)} - J_i^{(meas.)})^2}}{[\max\ (J^{(sim.)}, J^{(meas.)}) - \min\ (J^{(sim.)}, J^{(meas.)})]^2} \qquad \textbf{Equation 4—1}$$

Where J_i is the current density based on the simulations(sim.) and measured(meas.) values, and r the normalized RMS. [186,187]

In view of the paper by Li et al.[173],one possible source of this difference in current generation is imperfections and accompanying traps states in the perovskite layer. Therefore, the autofit-function of SIMsalabim was employed allowing only the following parameters to be altered; bulk traps (n_t), interface traps ($i_{st\text{-}L}$ and $i_{st\text{-}R}$) and the generated electron-hole pairs (G_{ehp}). The autofit function results in fits with RMS values below 2 % for 5 samples of the FAMAPI and MAFAPI device data each.

***Table 4-5** : Table of fitted device parameters used during drift-diffusion simulations for a MAPbI reference device taken from reference[186,187], and the MAFAPI and FAMAPI based devices.*

Parameter	Symbol	MAPI	MAFAPI	FAMAPI
Valence band	*VB*	5.44	5.30	5.25
Bulk trap density	n_{tr}	2.15×10^{21}	2.53×10^{21}	5.67×10^{21}
Interface trap density at ETL	i_{stL}	1.02×10^{16}	3.69×10^{14}	3.42×10^{14}
Interface trap density at HTL	i_{stR}	6.02×10^{14}	1.68×10^{14}	1.67×10^{14}
Generate electron hole pairs	*Gehp*	2.96×10^{27}	2.56×10^{27}	2.54×10^{27}

Two representative fits used in the simulation are displayed in **Figure 4-7-a** together with the experimental J-V curves. The fitting parameters that lead to these good matching fits are displayed in **Table 4-5** for both MAFAPI and FAMAPI based cells. For clarity, the interface and bulk trap densities for both the MAFAPI and FAMAPI based devices are displayed in **Figure *4-7*-b**. Due to the larger number of bulk traps required for the accurate auto-fit, the current lost to SRH recombination J_{SRH} is significantly larger for the FAMAPI cells. This is in clear agreement with the hypothesis that the FA induces a higher bulk trap density, which leads to a Jsc that is further away from the radiative limit.[29]

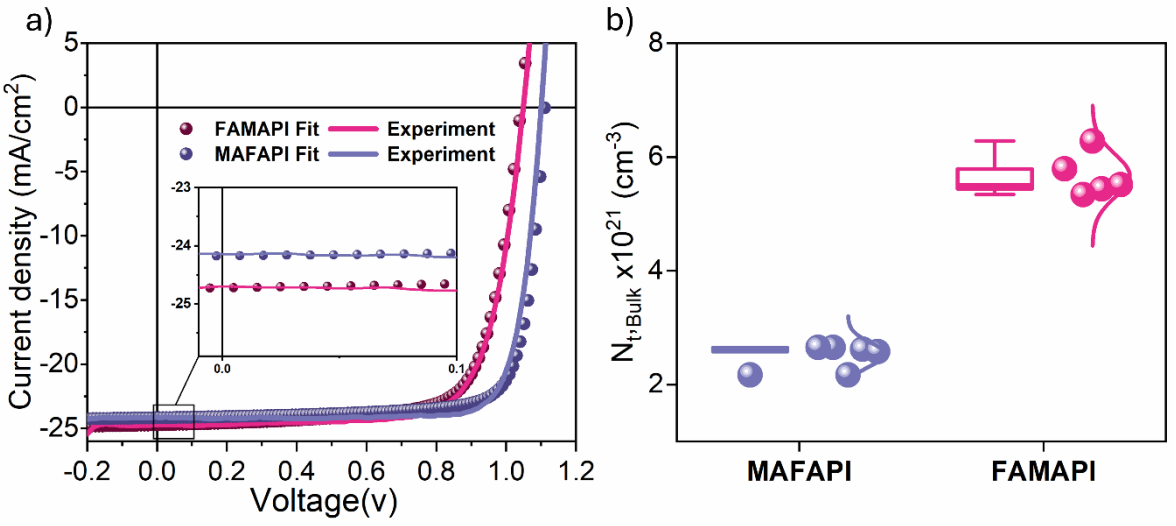

Figure 4-7: a) *Experimental and fitted JV curves for MAFAPI and FAMAPI devices.* ***b)*** *The bulk trap density required to enable a fit with an RMS below 2 %.*

4.3 Conclusion

In conclusion, we have prepared fully vacuum processed perovskite solar cells based on a MA and FA containing lead iodide perovskite. Using sublimation rates the relative amounts of MA and FA can be controlled as we confirmed via ^{1}H-NMR analysis on the deposited perovskite films. The solar cells employing perovskites with a higher MA content compared to FA exhibited higher PCE than those using a perovskite with larger FA content. This difference in efficiency is mainly due to a higher current density. Using a freeware simulation software SIMsalabim we were able to obtain good fits of the experimental curves by varying only a few parameters. From this analysis, the bulk trap density appears to be the main difference between the MAFAPI and the FAMAPI perovskites. This is in line with a recent publication that predicts a lower amount of intragrain planar defects, including stacking faults, twins, and dislocations when the MA to FA ratio is increased. With these high MA containing MAFAPbI$_3$ co-evaporated perovskite in a fully evaporated stack we obtained PCE as high as 21.8 % that only decreases by 10 % after 1000 hours of dark storage.

4.4 Annex

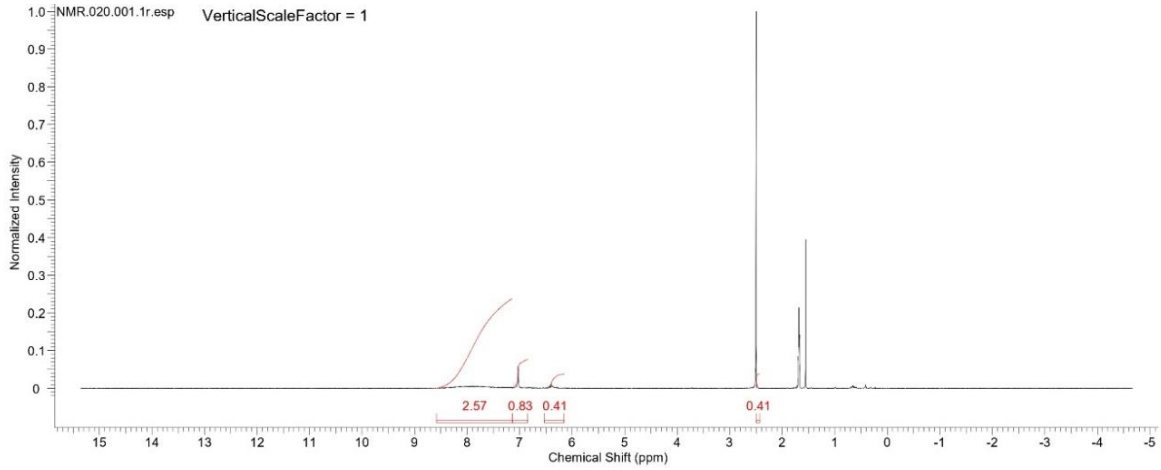

Figure 4-8: *The ^{1}H-NMR Spectra of the FAMAPI with the estimated ratios of the cations.*

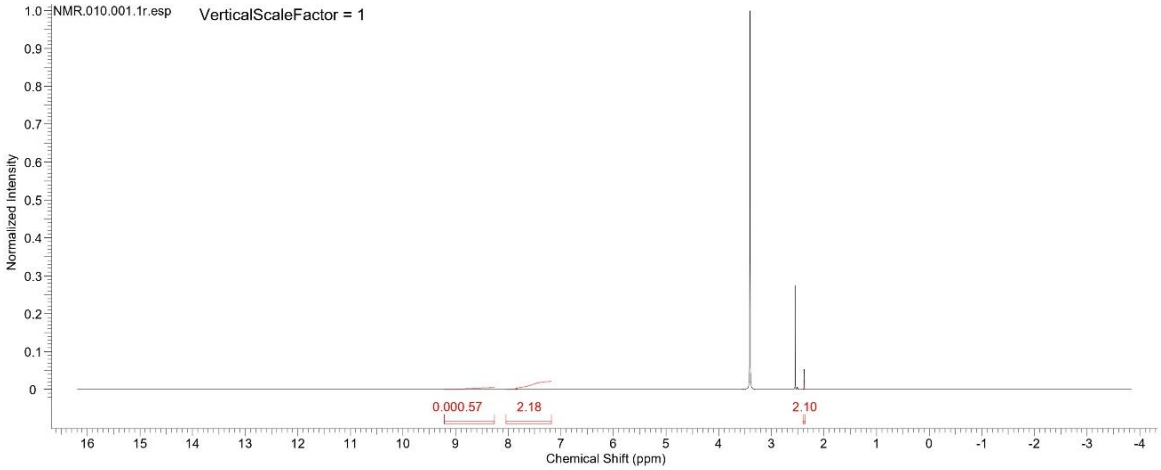

Figure 4-9: *The ^{1}H-NMR Spectra of the MAFAPI with the estimated ratios of the cations.*

Chapter 5: Co-Evaporation for Scalable Perovskite Mini-Modules: A Fully Sublimed Approach

This chapter investigates the scalability and performance of fully vacuum-deposited PSCs and mini-modules (MMs) through experimental approaches focusing on material choices, fabrication processes, and characterization techniques. Three device layouts with increasing active areas were fabricated using laser scribing (P1, P2, P3), enabling precise sub-cell interconnections and achieving a high GFF of up to 99%. Small-area devices (0.05 cm^2) fabricated entirely via in situ vacuum deposition demonstrated a champion PCE of 20.29%. However, ex situ processing introduced degradation, with efficiency losses of ~12% due to environmental exposure during transport.

To mitigate these losses, alternative HTLs were explored, including vacuum-deposited SAMs and ALD SnO_2. SAMs demonstrated superior uniformity and stability compared to solution-processed counterparts, with SEM analysis showing enhanced grain growth and improved film quality. Devices incorporating SAM-based HTLs exhibited minimal ex situ losses (~10%) and maintained thermal stability under 85°C stress tests. Integration of SnO_2 as an ETL and an encapsulant reduced ex situ degradation and enhanced device durability, enabling an ex situ cell efficiency of 18.37% and an MM aperture efficiency of 17.45%. For semi-transparent MMs, replacing the opaque electrode with soft-sputtered ITO resulted in efficiencies of 15.69% and a GFF of 99%. These devices demonstrated minimal upscaling losses (~1.6%) and retained 98% of their initial efficiency after 500 hours of dark storage.

This study highlights the potential of vacuum-deposited SAMs and optimized device architectures to achieve scalable, stable PSCs, providing valuable insights for improving large-area fabrication techniques.

5.1 Introduction

To date, most of the highest-performing PSCs have been fabricated via solution-based methods, which face significant scalability challenges, including film uniformity across large areas, solvent usage, and reproducibility.[188,189] As discussed in previous chapters, vacuum-based deposition methods offer key advantages for scalability, ensuring consistent optoelectronic properties across larger areas. Additionally, the controlled environment of vacuum deposition minimizes external variables that can impact film quality, maintaining high-quality interfaces between the perovskite absorber and charge transport layers. As these interfaces critically influence charge extraction and device efficiency, they are essential for the performance of large-area devices. Moreover, the existing infrastructure for thin-film technologies, like CdTe and CIGS, can be adapted for large-scale perovskite fabrication. [190] However, scaling up introduces challenges in maintaining uniform, defect-free interfaces, along with additional complexities such as increase in sheet resistance of the TCO due to longer current paths, which can lower the PCEs.[191] Optimizing the cell design by connecting subcells in series can enhance the output voltage while maintaining the same output current.[192] Laser scribing enables monolithic connections on the device architecture, minimizing series resistance. The process, as already explained in chapter 2, involves dividing the TCO into smaller electrode subcells (P1 step), selectively removing the subsequent layers down to the ITO layer without damaging it (P2 step), and carefully applying a P3 scribe to isolate the metal electrode. In this case, the area between the P1 and P3 scribed lines does not contribute to charge generation and is considered inactive, reducing the overall module efficiency. This is why the GFF (**Equation 2-12**), becomes critical in mini-module(MM) devices as losing just 0.68% of the active area in a large-area module can reduce efficiency by approximately 3%.[193] With GFFs typically ranging from 90 to 95% in commercial modules (5% to 10% power output loss), vacuum deposition aids in minimizing inactive regions, providing enough precision to carefully structure the active areas, and improving overall performance.

On the other hand, considering the high purity and density of vacuum deposited perovskite absorber, they are expected to exhibit greater resistance to environmental degradation from factors like moisture, oxygen, and UV exposure, potentially enhancing their stability. However, based on available information, no direct comparative studies using identical device stacks have confirmed this hypothesis. Indeed, stability challenges persist, particularly at interfaces where metal oxides or other interlayers degrade the perovskite over time. This implies that as device areas increase, optimizing the interfacial layers become more complex, emphasizing the need for further research to ensure long-term operational stability.

Despite the efficiency of PSCs fabricated via vacuum deposition still lagging behind their solution-processed counterparts[124], advancements in perovskite MMs show promise, with efficiencies exceeding 18%[85,129,169,194,195] and reaching 20% in some

cases.[196,197] Techniques like co-sublimation or sequential deposition have enabled MM with active areas over 10 cm^2 to achieve GFFs above 95 %, demonstrating scalability without major efficiencies losses.[196,197] Nevertheless, achieving the practical GFF limit of 99%, requires further optimizations of laser scribing parameters for sublimed structures,[198–202] along with improved interfacial layers and better understanding of sublimed perovskite films. Once this is achieved, alternative configurations, like semi-transparent near infrared MM, could further enable integration into buildings, offering space-saving solutions for domestic and commercial applications.

In this study, we present a comprehensive comparison between small-area perovskite solar cells and MMs, both fabricated entirely via thermal vacuum deposition. We investigate the influence of different HTLs, such as evaporated SAMs, and various perovskite compositions. Additionally, we successfully fabricate high-efficiency semi-transparent MMs with a high GFF and minimal efficiency losses during upscaling. Our findings emphasize the scalability of vacuum-deposited perovskite devices, providing valuable insights for designing advanced MMs with enhanced performance and stability.

5.2 Results and discussion

Throughout this chapter, the scalability of fully sublimed photovoltaics was assessed using three layouts with increasing active area, as shown in **Figure 5-1-a**. Fabrication was conducted across two institutes: the University of Valencia (UVEG) in Spain and the Interuniversity Microelectronics Centre (IMEC) in Belgium. Following the baseline configuration described in the thesis introduction for *p-i-n* small area high efficiency cells (also **Figure 5-1-b**), devices included a *p*-doped TaTm HTL, a $MAPbI_3$ active layer, fullerene, BCP as electron transport components and copper opaque electrode. In each deposition batch, the three layouts were included. First, a control cell with 0.05 cm^2 active area was entirely fabricated at UVEG, in a process referred to as *in situ*. This allowed us to verify the initial efficiency, which yielded a champion cell with PCE of 20.29%. Second, utilizing the same design, a four-cell MM was fabricated with laser scribing (P1, P2, P3) for interconnection. Here, stacks were deposited at UVEG on TCO substrates pre-scribed with P1 by IMEC. The modules were partially completed up to the BCP layer, and later sent to IMEC for P2 laser scribing, electrode deposition, and P3 scribing, finalizing the device fabrication there. Third, to evaluate interface degradation during transport, 0.125 cm^2 reference cells completed up to BCP (the same as the modules) were sent to IMEC for finalization, termed here as *ex situ*. The inset of **Figure 5-1-b** shows a SEM image of the inactive region in the fabricated MM, which measures 100 µm. This corresponds to a high GFF of 99%. We note that the same scribing has been applied to all modules fabricated in this chapter with a small deviation.

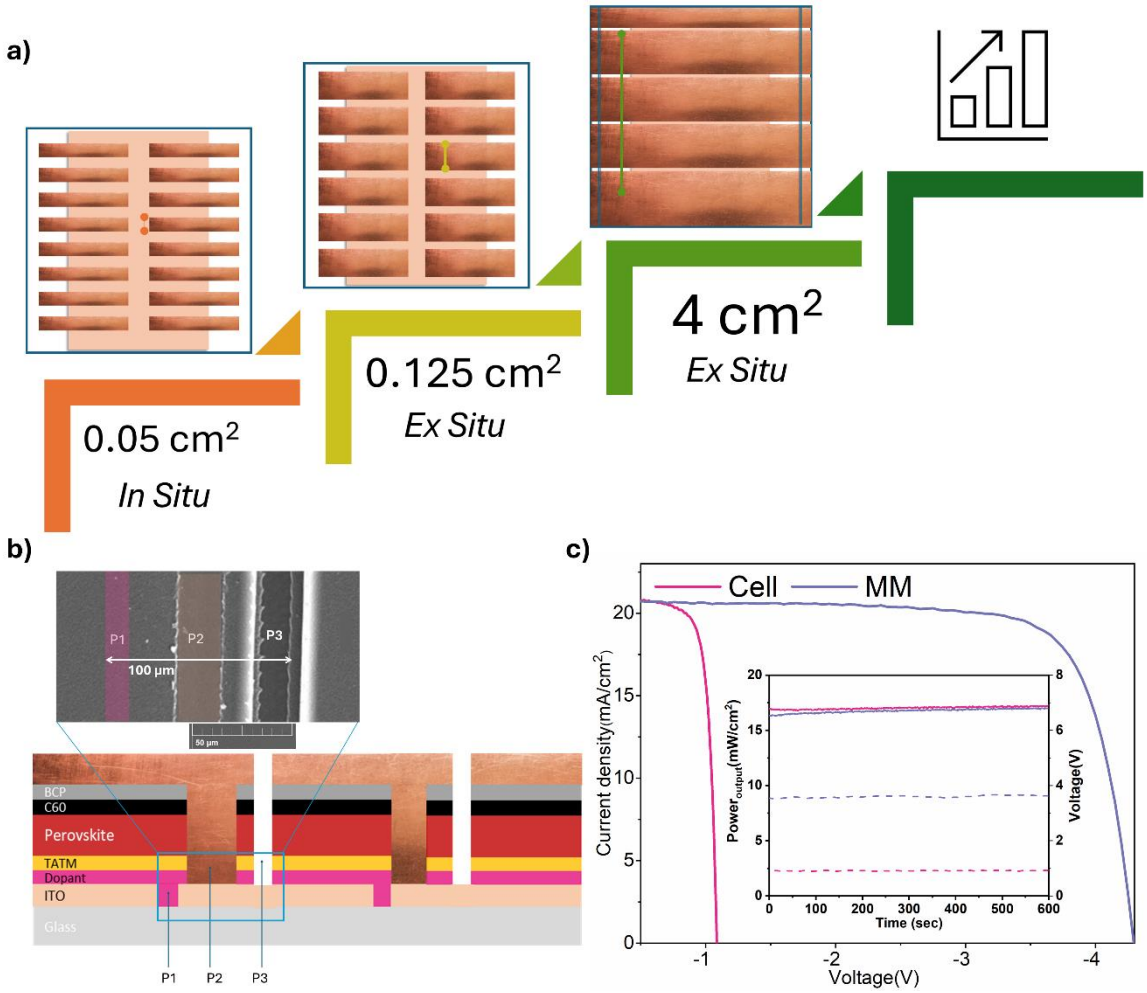

Figure 5-1: a) *Different solar cell device layouts used in this chapter with their respective active areas of each cell.* ***b)*** *The schematic of a MM device stack fabricated by laser scribing with a zoomed-in SEM image of the area distance between P1 to P3.* ***c)*** *J-V sweep and photovoltaic parameters of cell of ex situ of 0.125 cm² and MM with an inset of mpp tracking of the cell and module.*

Because the *ex situ* samples were exposed to the same potential degradation conditions experienced by the larger MM samples when shipped from Spain to Belgium, they allowed for a consistent evaluation of environmental impact before assessing the upscaling losses. Notably, the champion *ex situ* device exhibited a degradation loss of approximately 12% after just 48 hours of transport from UVEG to IMEC, which is significant compared to the stability of the *in situ* cells that were fully completed and encapsulated at UVEG. The *J-V* curves of the *ex situ* cell, as well as the corresponding 4-subcell (1 cm²) MMs using F6-TCNNQ (p-dopant) and TaTm as hole-selective layers, are presented in **Figure 5-1-C**. The inset graph shows mpp tracking for both the cell and MM under 1 sun illumination. The *ex situ* fabricated cell demonstrated an efficiency of 17.69%, while the corresponding MM achieved an aperture efficiency of 17.06%, reflecting only a ~ 1% decrease in performance. Remarkably, this efficiency drop is among the lowest reported for fully evaporated MMs.[85,196]

While these results are promising, especially given the challenges associated with ex-situ processing, the observed efficiency drop during sample shipping was concerning. As

highlighted in Chapter 3, the dopant in the HTL accentuates interface degradation, contributing to device instability. Therefore, improving stability in the HTL became a priority to achieve reliable device performance before advancing MM efficiency. The focus thus shifted to developing more stable HTLs compatible with large area fully evaporated stacks. One of the viable alternatives for a more stable HTL is the use of SAMs based on phosphonic acid, which has gained vast popularity in small-area perovskite solar cells. This approach can improve the interface and enhance charge extraction, ultimately enhancing the stability of the device structure. However, their reliance on solution-based processing methods poses limitations for large-area applications due to potential issues with surface coverage uniformity. Utilizing vacuum-based deposition could address these challenges, improving the overall uniformity and scalability of the device fabrication process.

As mentioned in Chapter 3: , *1H,1H,2H,2H-Perfluorooctanephosphonic or SAM5*, is an example of a non-conjugated fluorinated SAM that can be combined with TaTm as HTL to form a stable *p*-type interface.

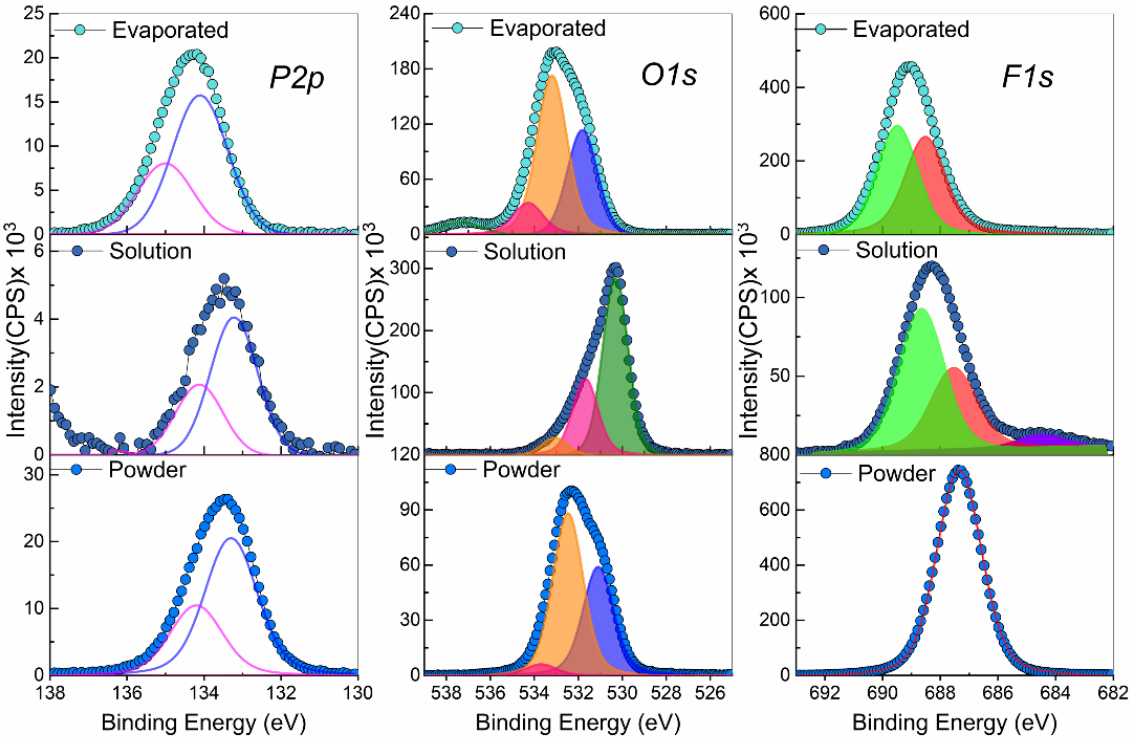

Figure 5-2: *The XPS spectra of SAM 5 from top to bottom from vacuum deposited, solution deposited or powder from left to right of F 1s, O 1s, P 2p, and In 3d.*

Figure 5-2 illustrates the XPS spectra (*P*, *O* and *F* signals) of SAM5 films deposited on ITO via solution-process and thermal evaporation, using the spectrum of the powder form as a reference. No new peaks indicating molecular degradation are observed after

vacuum deposition, but the evaporated SAM exhibited higher peak intensities for all elements, consistent with the transformation from a monolayer to a thin film.

On the other hand, carbazole-containing SAMs have been reported to improve device lifetime as a standalone hole transport monolayer.[203] The deposition of these SAMs via thermal vacuum sublimation has been previously demonstrated,[151] which results in the formation of a layer rather than a perfect monolayer. However, it still provides enhanced surface coverage without significant increase of the series resistance.[204,205] For this work, we have selected (2-(3,6-Dimethoxy-9H-carbazol-9-yl)ethyl)phosphonic acid (*MeO-2PACz*), hereafter referred to as C-SAM, due to its optimal sublimation temperature and reported stability enhancements.[203] Moreover, we reduced the thickness of the sublimed C-SAM layer compared to the original reported work, which then eliminated the need for an additional cleaning step that involved solvent application after SAM evaporation.

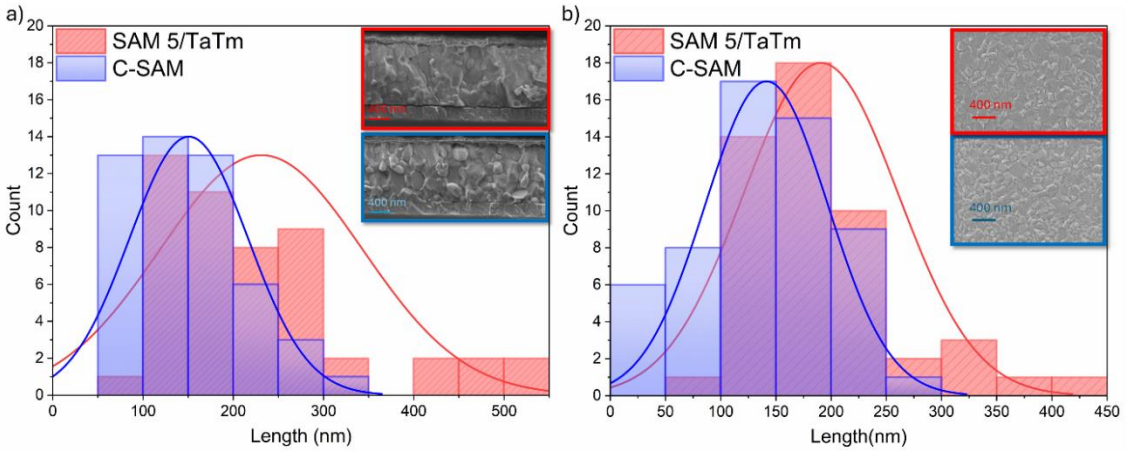

Figure 5-3: *The distribution of grain sizes for* ***a)*** *cross section and* ***b)*** *top view SEM of co-evaporated perovskite on evaporated SAM 5/ TaTm and C-SAM.*

To better understand the nature of the co-evaporated perovskite layer on different SAM interlayer materials, a comparative SEM analysis of the grain sizes in the top-view and cross-sectional morphologies was conducted (**Figure 5-3**). The analysis revealed that the co-evaporated MAPI forms larger grains on evaporated SAM 5/TaTm surface compared to the standalone C-SAM. This observation aligns with previous reports in the literature, highlighting the influence of the interlayer material on grain growth during deposition.[136]

Figure 5-4-a and **b** illustrate the device configurations for SAM 5/TaTm and C-SAM, respectively. Panels **c - f** compare the photovoltaic characteristics of 16 pixels (0.05 cm^2 active area each) on a 3 × 3 cm^2 substrate, contrasting solution-processed versus vacuum-deposited layers. We observe a broader variability for the solution-processed SAMs, suggesting non-uniform layer coverage, whereas the more consistent and homogeneous data distribution for evaporated SAMs highlights their superior uniformity in layer deposition.

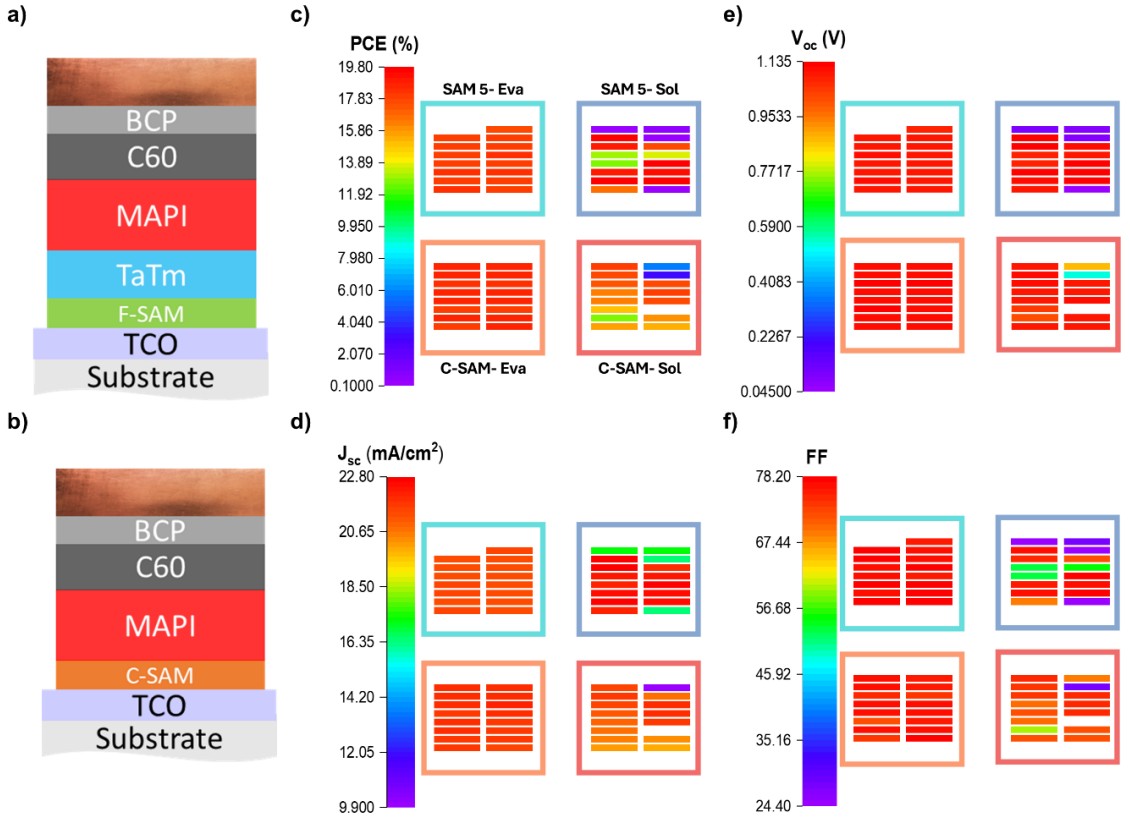

Figure 5-4: a) *The device configuration for SAM 5/TaTm.* ***b)*** *The device configuration for C-SAM.* ***c*** *to* ***f)*** *The distribution of PV parameters for evaporated and solution-processed SAMs in 3x3 cm² with 16-pixel devices, each with an active area of 0.05 cm².*

The EQE and J-V characteristics of representative small-area cells are presented in **Figure 5-5**. The champion and average PV parameters for the previously discussed deposition techniques have been summarized in **Table 5-1**. While the evaporated SAMs may not form a monolayer, potentially increasing series resistance and slightly reducing the FF, this trade-off is justified by their scalability advantages. The minimal difference in V_{oc} is likely due to variations in HTL materials and the thinner perovskite layer C-SAM, which might affect the built-in potential and charge recombination dynamics. Optimizing SAM 5 and similar derivatives as ITO surface modifiers could enable more efficient and stable fully evaporated devices, surpassing their solution-processed counterpart on larger surfaces.

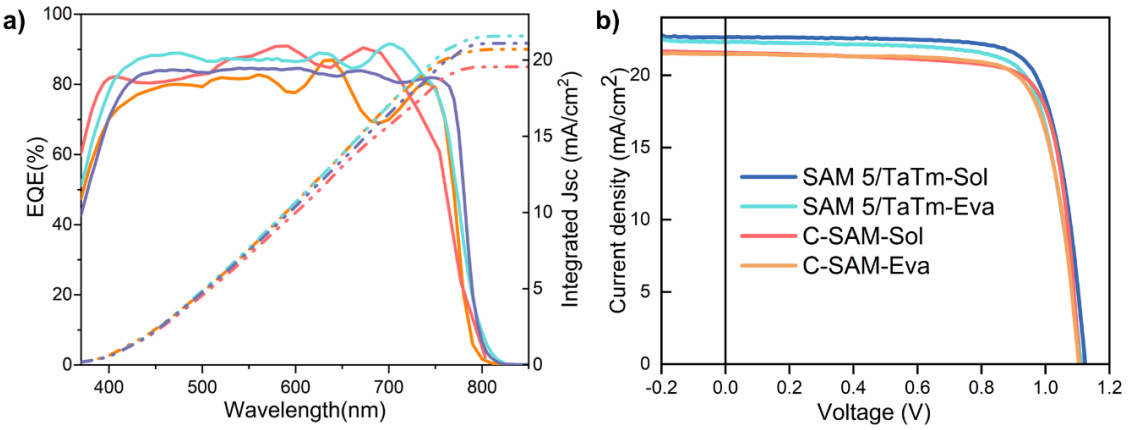

Figure 5-5: a) *EQE and integrated current density.* ***b)*** *The current-voltage graph of the champion solution processed and evaporated SAM 5/TaTm and C-SAM.*

Table 5-1: *The champion and average PV parameters of at least 15 devices for different HTLs depending on the deposition technique.*
**The perovskite thickness is 800 nm, ** The perovskite thickness is 500 nm.*

		PCE(%)	V_{oc}(V)	J_{sc}(mA/cm^2)	FF
Dopant/TaTm **Evaporated**	Champion	20.29	1.12	22.15	81.44
	Average	18.95 ± 0.67	1.12 ± 0.002	21.89 ± 0.66	81.17 ± 0.21
SAM 5/TaTm **Solution***	Champion	19.64	1.12	22.63	77.24
	Average	17.46 ± 2.77	1.11 ± 0.015	22.44 ± 0.27	69.89 ± 3.15
SAM 5/TaTm **Evaporated***	Champion	18.76	1.11	22.27	75.77
	Average	18.46 ± 0.27	1.11 ± 0.007	22.02 ± 0.12	75.81 ± 1.47
C-SAM **Solution****	Champion	18.61	1.10	21.56	78.07
	Average	15.40 ± 5.52	0.99 ± 0.25	20.83 ± 0.85	69.53 ± 11.79
C-SAM **Evaporated****	Champion	18.22	1.10	21.34	77.54
	Average	18.11 ± 0.11	1.09 ± 0.004	21.40 ± 0.07	77.15 ± 0.58

To better understand the stability of large-area surfaces, and its relation to SAM coverage, the average shelf stability of PV parameters was analyzed for at least 15(*in situ*) devices each with an active area of 0.05 cm^2. The devices were stored in an N_2 atmosphere at room temperature, in the dark and exposed to O_2 atmosphere during measurements (**Figure 5-6**). Results indicate that evaporated SAMs not only yield higher averages but also exhibit superior stability, while the solution-processed approach may produce higher PV performance in only a few small-area cells. This variability is likely due to the inherent inconsistencies of solution-based processes, which can contribute to long-term performance deterioration in large-area devices. This emphasizes the significance of vacuum deposition techniques for large-area applications, as they provide more consistent and uniform coverage, resulting in improved stability and performance across expanded areas.

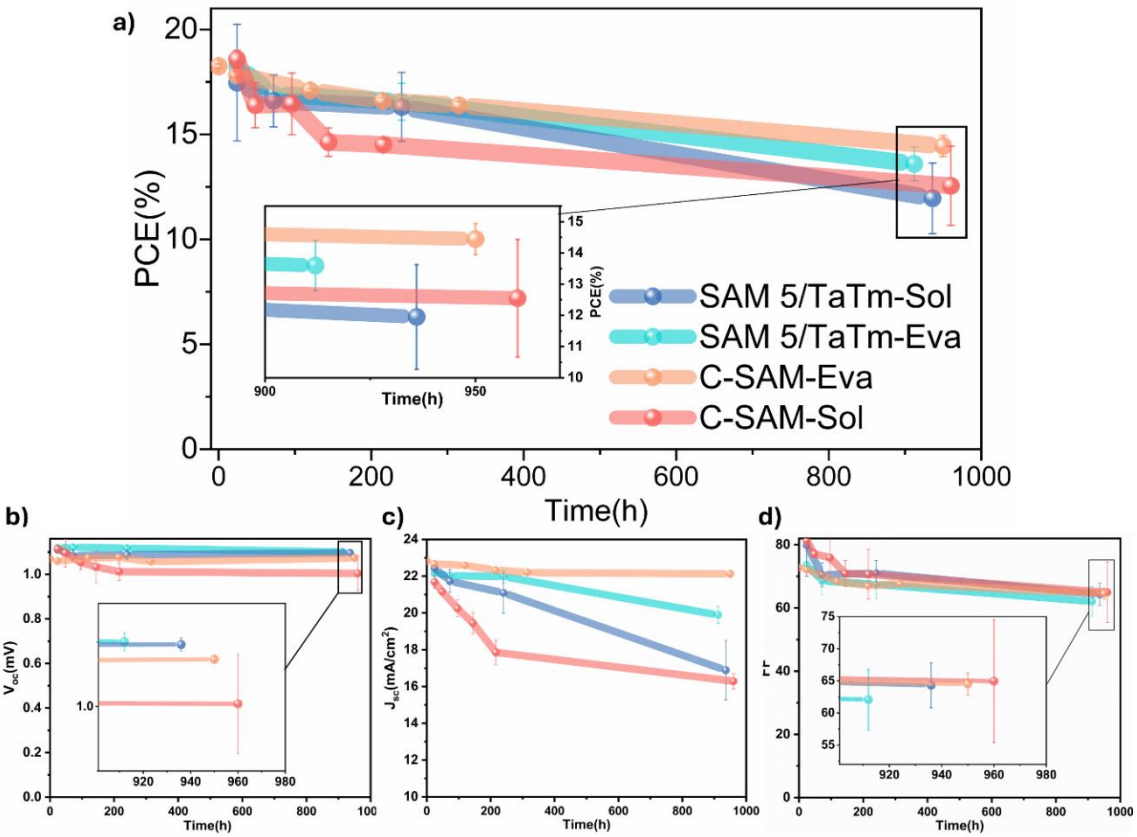

Figure 5-6: *Comparison of the shelf life stability of PV parameters of solution processed (-Sol) and vacuum deposited(-Eva) SAM 5/TaTm and C-SAM interlayers.* ***a)*** *PCE with a zoomed in inset at 1000h.* ***b)*** *The Voc with a zoomed in inset.* ***c)*** *The Jsc.* ***d)*** *the FF with a zoomed in inset at 1000h.*

Next, we compare the thermal stability of devices using *p*-dopant/TaTm, SAM 5/TaTm, and C-SAM as contact interfaces. The devices were thermally stressed at 85°C in N_2 atmosphere, kept in the dark, and periodically taken out to O_2 atmosphere for measurement. **Figure 5-7** contains the average thermal stability for 16 fully evaporated cells for each type of configuration. As observed in **Figure 5-7,** devices with *p*-dopants as interlayers show initial higher efficiencies, but they experience a rapid decline over time, making them less suitable for long-term applications. In contrast, those containing evaporated SAMs as interlayers show improved thermal stability, with SAM5/TaTm slightly outperforming C-SAM. Both SAM-based configurations are therefore promising candidates for large-scale fabrication due to their superior homogeneity and enhanced durability under thermal stress.

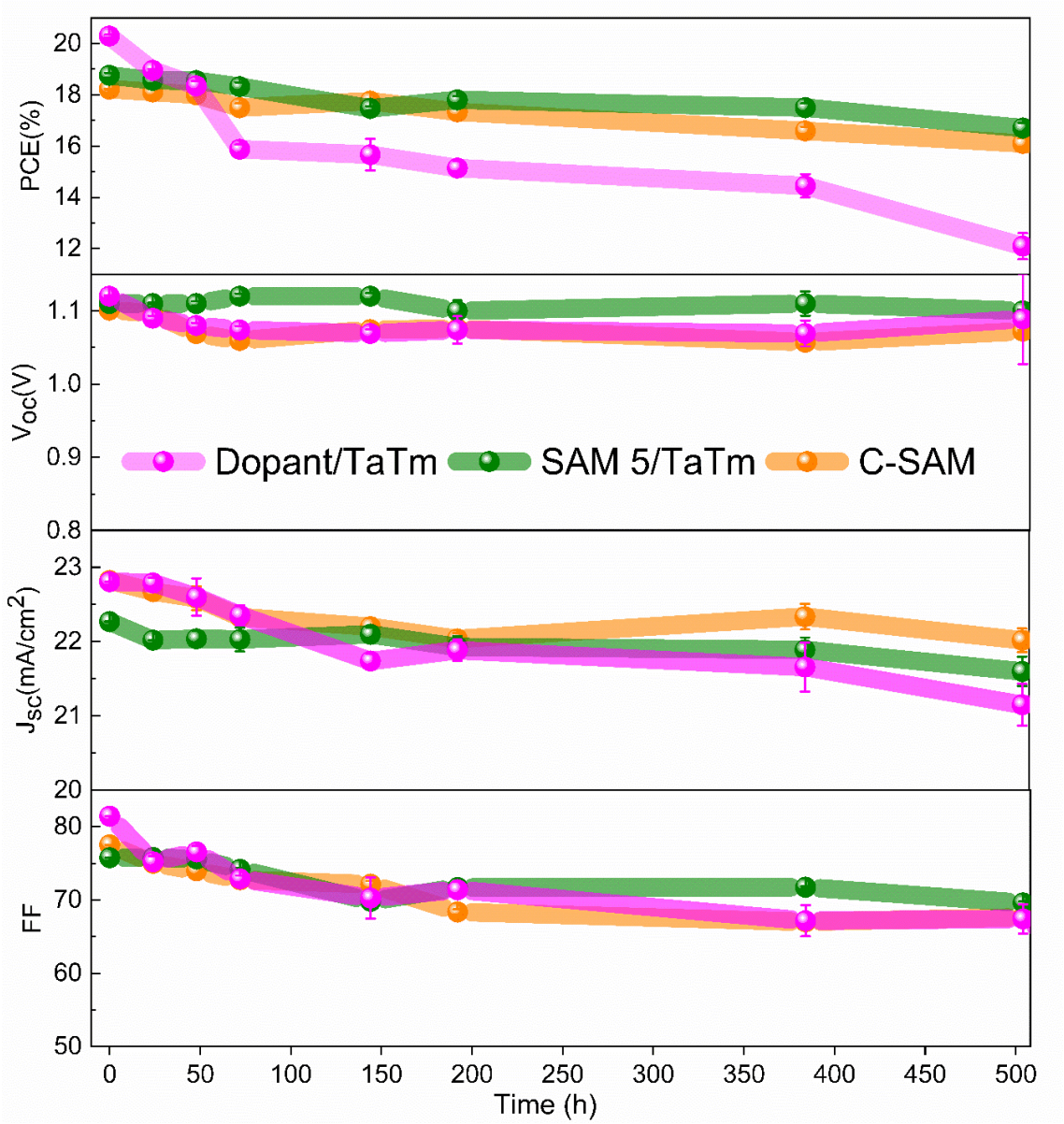

Figure 5-7: *The thermal stability of fully evaporated stacks with alternative HTLs for 500h at 85°C.*

Once the improved stability of the SAM containing devices was confirmed, we have fabricated MMs following the same procedure involving laser scribing method in the two laboratories in Spain and Belgium, as explained in chapter 2 of the thesis. **Figure 5-8-a** shows the behavior of the *ex situ* small- area cells under 1sun illumination and the **Figure 5-8-b** shows the behavior of the corresponding MM and the inset how they operate under maximum power situation.

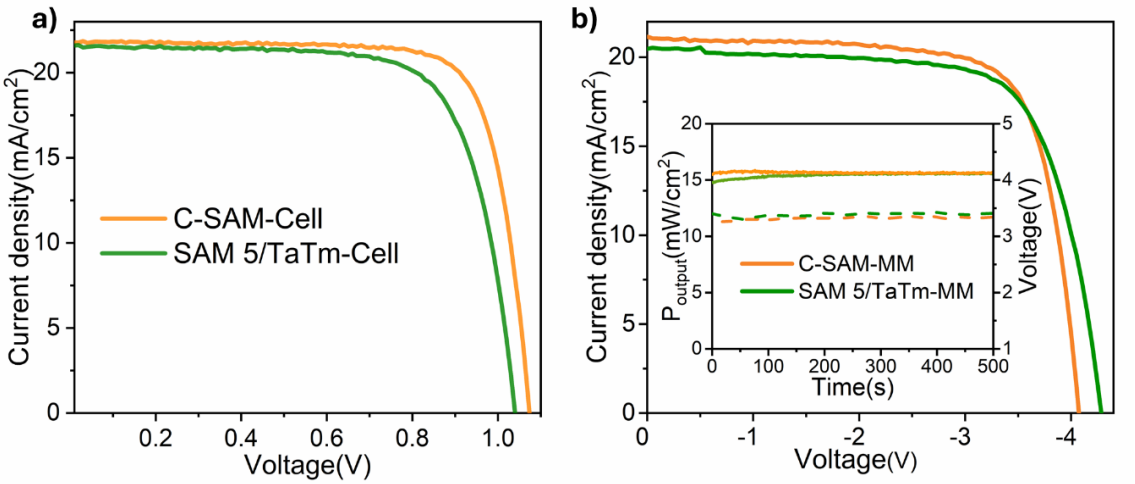

Figure 5-8: a) *The J-V curve for the ex situ cells with different evaporated HTL employed.* ***b)*** *The J-V graph of the ex situ MMs fabricated with different evaporated HTLs. The inset shows the MPP tracking of the MMs with their corresponding* V_{mpp}.

To have a reference for the amount of loss of each cell we have defined the loss factor, $f_{ex-situ}$ as indicated in the following equation:

$$f_{ex\ situ} = \frac{PCE_{ex\ situ}}{PCE_{in\ situ}} \qquad \textbf{Equation 5—1}$$

The *in situ* and *ex situ* PV parameters for all the structures mentioned in this work, as well as their $f_{ex-situ}$, are summarized in **Table 5-2** in the Appendix of this chapter. When comparing the PV stability between *in situ* and *ex situ* cells, we observe that the *ex situ* degradation for the different cell configurations is in line with the stability results reported in **Figure 5-6** and **Figure 5-7**. Specifically, the *ex situ* losses are 12.8% for *p*-dopant/TaTm, 10.9% for SAM5/TaTm, and 10% for C-SAM. ***Table 5-3*** in the appendix of this chapter, includes a comparison of the PV parameters for the *ex situ* cell and MMs, and their corresponding upscaling losses. The upscaling losses associated with increasing the device area were calculated by **Equation 2—1**. In summary, SAM 5 leads to an upscaling loss of approximately 3%, while C-SAM only loses around 1.6% of efficiency. For a better visual illustration, the average results were also summarized in **Figure 5-9**. All in all, the data confirms that C-SAM exhibits lower *ex situ* and upscaling losses. Additionally, from a fabrication standpoint, it eliminates one of the layers and reduces materials usage, making it a promising candidate for further optimization. Consequently, for the upcoming test, we have decided to continue our investigation using the evaporated C-SAM as the HTL.

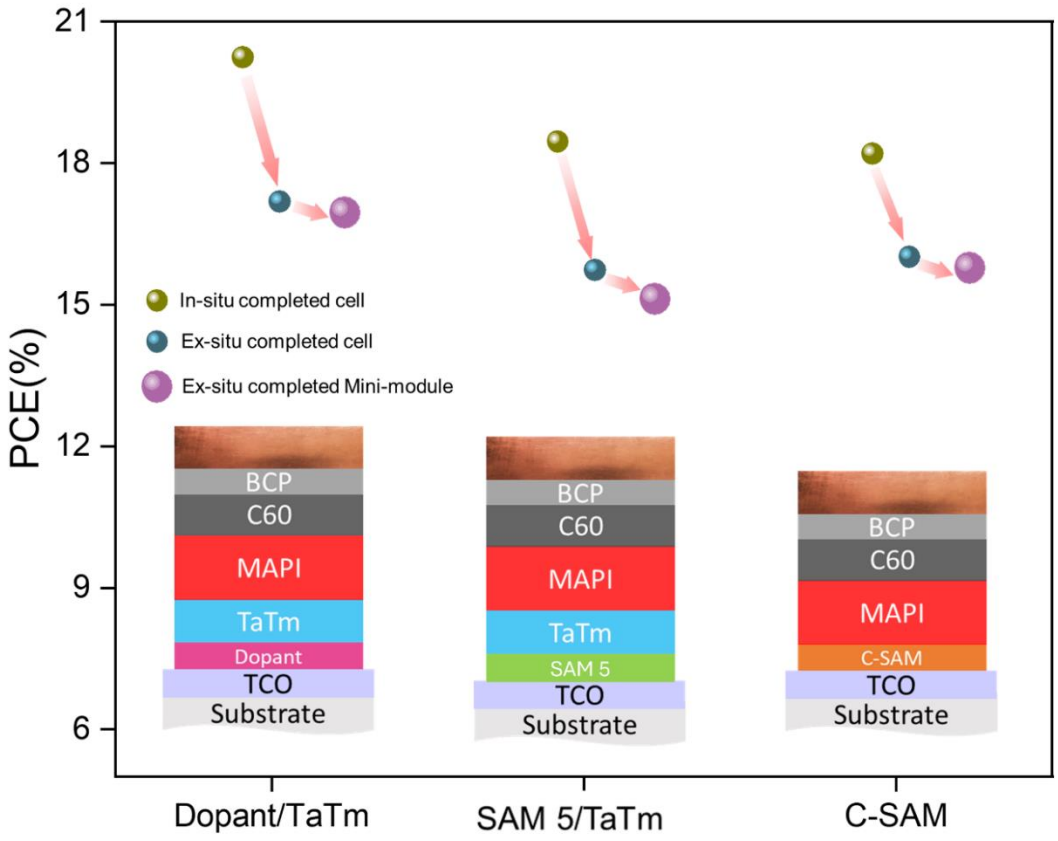

Figure 5-9: *The efficiency and its decline in different stacks due to in-situ and ex-situ fabrication and the upscaling loss contributed to cell to module fabrication.*

To further mitigate *ex situ* fabrication losses, the BCP layer was replaced with a thin SnO_2 film deposited via ALD. This substitution enhances the overall device stability,[206] serving not only as an ETL, but also as an encapsulant, thereby reducing *ex situ* degradation during transportation to Belgium. Similarly, the MA cation is more prone to thermal degradation compared to FA cation.[207–210] While a single-cation $FAPbI_3$ active layer offers a potential alternative, it is inherently unstable at room temperature, transitioning to a less effective yellow non-perovskite phase. To address this, incorporating a small amount of MA leading to $FAMAPbI_3$ perovskite (also named as FAMAPI), improves the stability of the co-evaporated film.[172,182] This adjustment slightly reduces the bandgap compared to $MAPbI_3$, as illustrated in **Figure 5-10-a**, providing a bandgap reduction from 1.58 to 1.51 eV. This perovskite composition has already been reported by our group[172] and also mentioned in the previous chapter of this thesis. For ensuring the incorporation of FA within a MAPI perovskite we have performed XRD analysis as shown in **Figure 5-10-b**. The shifting of the 2theta angle toward lower angles is an indication of incorporation of FA into the lattice structure, which is in line with the bandgap change. For visual purposes the inset shows the [111] peak at 24.5° for MAPI which has shifted to 24.32° for FAMAPI. The shift exists in all the peaks and the difference increases by going to higher scanning angels.

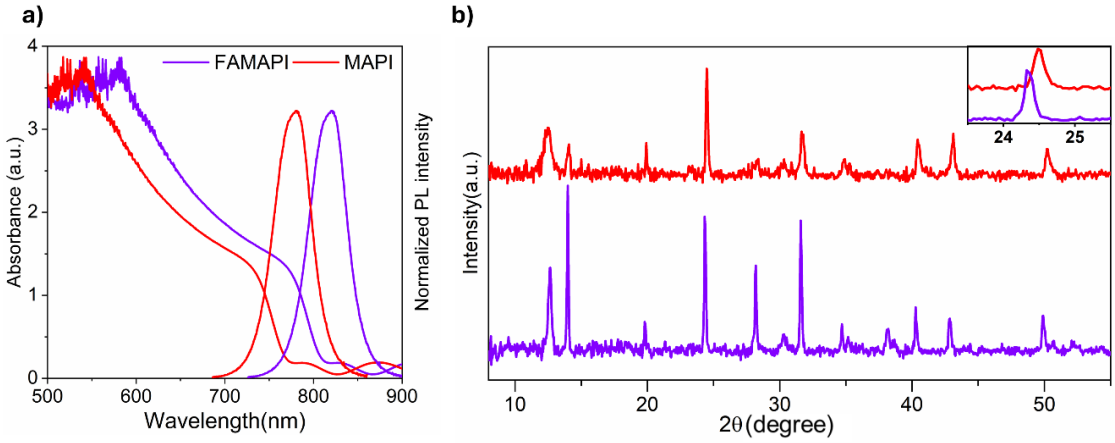

Figure 5-10: a) *The UV-Vis and PL of MAPI and FAMAPI perovskite.* ***b)*** *The XRD pattern of MAPI and FAMAPI showing the shift in peaks that confirms the incorporation of FA in the structure.*

To quantify the ratio of FA to MA in the final film, ^{1}H-NMR analysis the same as explained in the previous chapter was conducted, providing a composition of $FA_{0.85}MA_{0.15}PbI_3$ which is in agreement with the optical measurements (see results in **Figure 4-1** and **Table 4-2**). Based on the improved results, the device architecture selected for the rest of the study is the one shown in **Figure 5-11-a**.

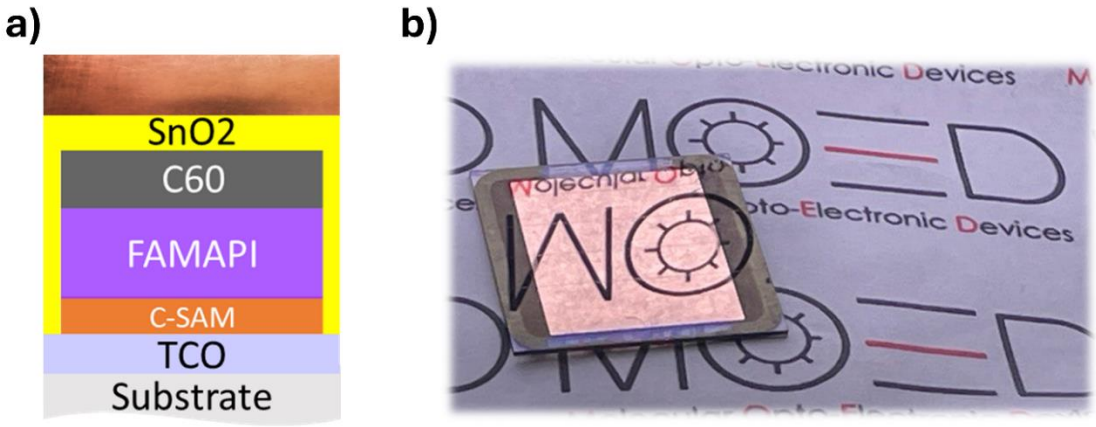

Figure 5-11: a) *The optimized device structure incorporating ALD SnO_2.* ***b)*** *An actual picture of opaque MM.*

The *J-V* characteristics of the best-performing *ex situ* cell and MM are presented in **Figure 5-12-a**. As summarized in **Table 5-2**, the *in situ* cell achieves 19.5% efficiency, while the *ex situ* cell reached 18.37%, reflecting a minimal performance loss of only 3.5% due to the combination of SnO_2 ETL, and the improved stability of the FAMAPI perovskite layer. Additionally, the MM based on this architecture reached an aperture efficiency of 17.45%, with an upscaling loss of approximately 3.3%. This higher loss, compared to that of the previous sections, is primary attributed to the lower GFF (see values in **Table 5-3**). However, the MM maintained 98% of its initial efficiency after 500 hours of dark storage, demonstrating negligible degradation, thus stronger stability for the optimized architecture.

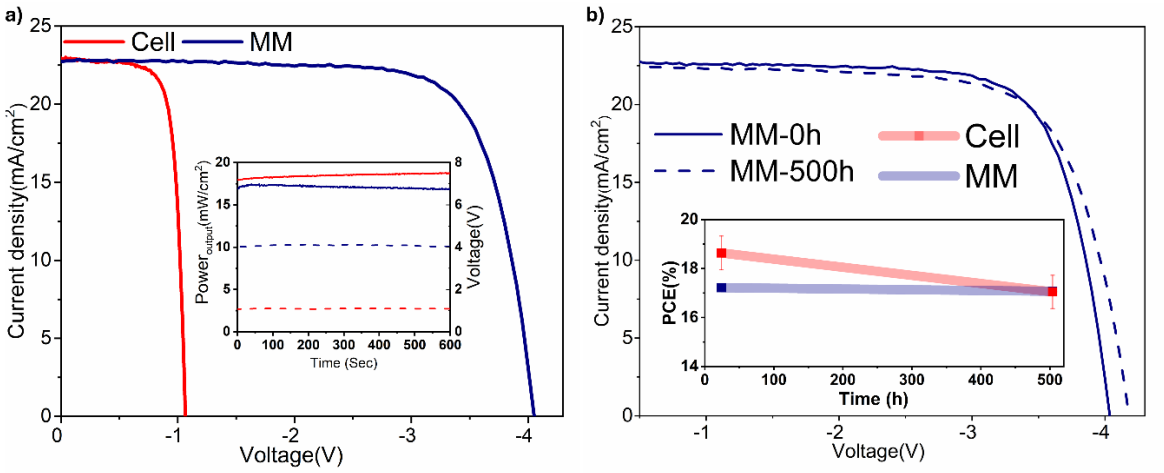

Figure 5-12: a) *The ex situ cell and module J-V graph and the mpp tracking of cell and MM.* ***b)*** *The comparison of call and its corresponding module in zero hour and after 500h of storage in the dark.*

The improved structure is also applicable for semitransparent solar cells (STSC), replacing the opaque copper electrode with soft-sputtered ITO. Due to ITO's higher sheet resistance the sub-cell area was reduced, resulting in 7 sub-cells within the same 3x3 cm^2 substrate, rather than 4, shortening current paths but complicating GFF control. As shown in **Figure 5-13**.

The *ex situ* semitransparent cells achieve 15.88% efficiency, with a 3.7% *ex situ* loss. The semitransparent minimodule(STMM) attains 15.69% aperture efficiency, with PV values of 7.7 V, 19.4 mA/cm^2, and 72% of FF, with a GFF of 99% (upscaling loss of 0.79%). This efficiency was obtained by increasing the perovskite thickness to 850 nm.

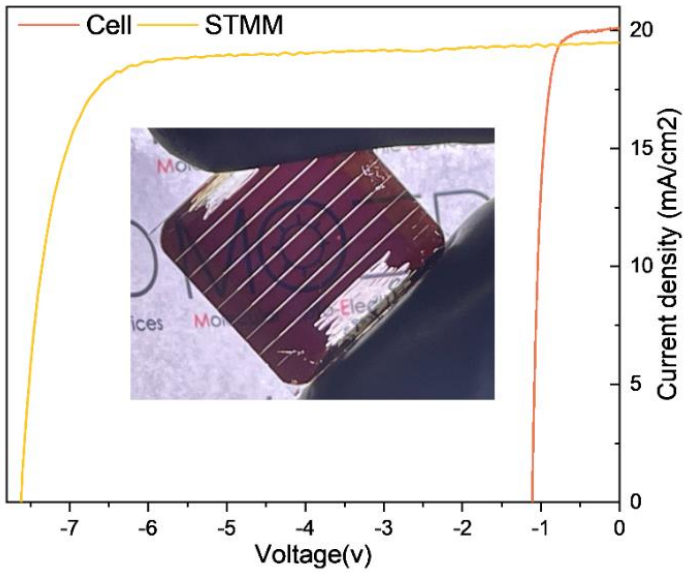

Figure 5-13: *The current voltage behavior of cell and STMM of 7 series cells in a semitransparent structure with the picture of an actual cell.*

5.3 Conclusion

In summary, this work focuses on exploring material choices and fabrication processes to improve fully vacuum deposited PSCs, acknowledging that these findings are steps toward solving ongoing challenges rather than offering a complete solution. The study highlights the ongoing challenges for achieving scalable and stable PSCs and modules with the aim of contributing to the improvement of this technology.

We investigate fully evaporated device architectures, addressing issues related to stability, scalability, and performance consistency. Achieving reliable, high-efficiency solar modules require careful consideration of the materials and processes used at both small and large scales. The academic community has produced numerous small-scale studies, but the lack of access to inert laser integration for module manufacturing hinders further research progress. Given that upscaling and long-term stability are the ultimate objectives, this limitation is crucial in terms of reducing *ex situ* performance losses and facilitating collaborative efforts. Our work employed laser scribing to precisely isolate and interconnect sub-cells within the MM, without damaging critical layers. Although the scribing process created inactive regions, a high GFF of 99% was achieved, ensuring efficient utilization of the surface area and maintaining high PCE.

The employment of vacuum-deposited SAMs, either as a standalone HTL or as an interface modifier, demonstrates potential for enhancing device uniformity and long-term stability. Our approach, combined with the use of compact ALD-deposited SnO_2, has significantly mitigated the *ex situ* performance losses observed, enabling MMs with increased stability during 500 hours of test. Exploring alternative sublimable HTLs with increased resistance to degradation will be crucial in addressing the stability challenges encountered in fully evaporated PSCs.

This study also highlights the need for consistent reports of solar cell and module performance under the same conditions by emphasizing the role of *ex situ* loss in the final efficiency of larger area devices. This could provide better insights into upscaling losses and the factors that affect performance. Although the upscaling loss observed here was around 3%, the results underscore the complexity of maintaining performance across different device sizes, particularly for *ex situ* processed devices, which are more vulnerable to degradation. Consistent and detailed reporting of performance across both small-scale cells and larger modules is crucial for gaining a clearer understanding of upscaling challenges, which is essential for further advancing the development of perovskite PV.

5.4 Appendix Tables

Table 5-2: *The PV values of the champion cells fabricated in situ and ex situ and their corresponding loss.*

Structure	In-Situ Cell				Ex-Situ Cell				$F_{Ex\text{-}situ}$ (%)
	PCE (%)	V_{oc}(v)	J_{sc} (mA/cm²)	FF	PCE (%)	V_{oc}(v)	J_{sc} (mA/cm²)	FF	
ITO/Dopant/TaTm/MAPI/C60/BCP/Cu	20.29	1.12	22.15	81.55	17.69	1.09	21	77.12	12.8
ITO/SAM 5/TaTm/MAPI/C60/BCP/Cu	18.76	1.11	22.27	75.77	16.33	1.04	21.5	72.9	10.9
ITO/C-SAM/MAPI/C60/BCP/Cu	18.22	1.10	21.34	77.54	16.39	1.06	22	70.39	10
ITO/C-SAM/FAMAPI/C60/SnO_2/Cu	19.05	1.10	22.95	75.032	18.37	1.06	23	75.48	3.59
ITO/C-SAM/FAMAPI/C60/SnO_2/ITO	16.5	1.11	20.65	72.01	15.88	1.11	20.2	70.74	3.7

Table 5-3: *The PV value of the cells fabricated ex situ, the corresponding minimodule, geometrical fill factor and the corresponding upscaling loss.*

Structure	Cell				Module Aperture Area Values				GFF	$F_{upscaling}$ (%)
	PCE (%)	V_{oc}(v)	J_{sc} (mA/cm²)	FF	PCE (%)	V_{oc}(v)	J_{sc} (mA/cm²)	FF		
ITO/Dopant/TaTm/MAPI/C60/BCP/Cu	17.69	1.09	21	77.12	17.06	4.3	20.76	76.4	99	0.49
ITO/SAM 5/TaTm/MAPI/C60/BCP/Cu	16.33	1.04	21.5	72.9	15.51	4.3	20.48	70.5	98.7	3.35
ITO/C-SAM/MAPI/C60/BCP/Cu	16.39	1.06	22	70.39	15.99	4.1	21	74.17	98.9	1.06
ITO/C-SAM/FAMAPI/C60/SnO_2/Cu	18.37	1.06	23	75.48	17.45	4.2	22.56	73.77	97.8	3.32
ITO/C-SAM/FAMAPI/C60/SnO_2/ITO	15.88	1.11	20.2	70.74	15.69	7.7	19.4	72.09	99	0.79

Chapter 6: Conclusion

6.1 Conclusion

In summary, this thesis, titled *"Interfaces and Connections in Vacuum-Based Perovskite Solar Cells,"* focused on addressing critical challenges in vacuum-deposited PSCs, namely stability, efficiency, and scalability.

Particular attention was given to the HTL interface, identified as a critical bottleneck for achieving stability in *p-i-n* devices. By employing alternative materials for the HTL interface, significant improvements in overall device stability were realized. Additionally, modifications to the perovskite composition successfully reduced defect densities within the perovskite absorber, thereby enhancing device efficiency. Through the strategic incorporation of stable HTLs in fully sublimed devices, this work demonstrated minimal upscaling losses. These results show the potential of fully vacuum-deposited structures for scalable, high-performance perovskite solar cells.

In Chapter 3: **Engineering Stable *p-type* Contacts Towards Efficient Fully Vacuum Deposited Perovskite Solar Cells** we introduced several simple-structure non-conjugated fluorinated SAMs as high work function interlayers to use as p-type contacts in combination with intrinsic sublimable semiconductors(TaTm). This is mainly done to search for an alternative to the chemical dopants that are a limiting factor in the stability of fully evaporated solar cells. By modifying the ITO electrodes with SAMs, the energy barrier at the TaTm interface was minimized , resulting in efficiency and stability improvements. Notably, the integration of these SAM-modified ITO electrodes preserved the FF stability over time. Leveraging this straightforward yet effective interface modification enables the fabrication of fully evaporated MAPbI solar cells with PCE exceeding 19 %, maintaining 90% of the initial efficiency after more than 1000 hours of thermal stressing.

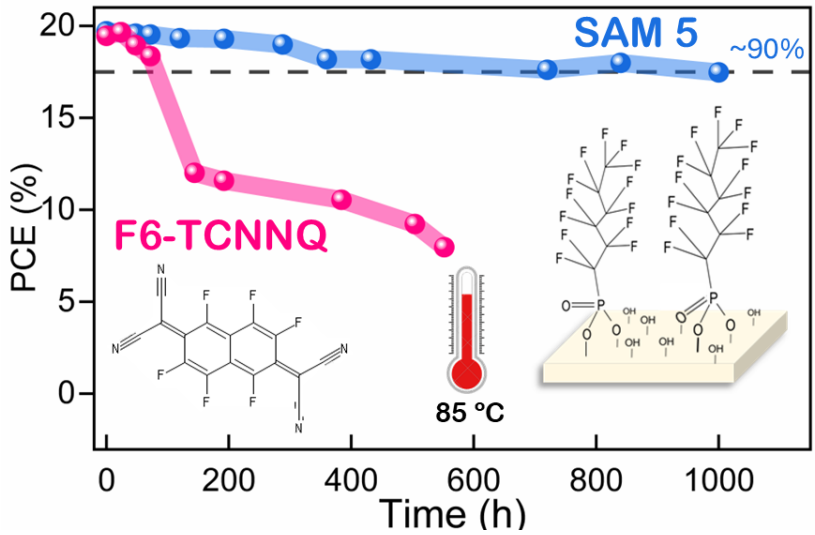

***Figure 6-1**:The thermal efficiency improvement employing SAM5 in comparison to F6-TCNNQ dopant.*

Chapter 4: **High-Performance Double A-Cation Perovskite Solar Cells via Co-Evaporation,** by using characterization techniques like EDX, NMR and SEM we gained insights into the role of the A-site cation on the properties of the perovskite absorber film. The PV results demonstrate that a MA-rich composition leads to improved performance. This improved performance was analyzed using SIMsalabim software which revealed that a reduction of bulk trap densities is at the origin of it. This reduction in trap density leads to improved J_{sc} and thus efficiency of MAFAPI devices. The optimization effort led to achieving a remarkable efficiency of 21.83% which is among the highest reported value for a fully evaporated perovskite solar cell fabricated using co-evaporation technique to date.

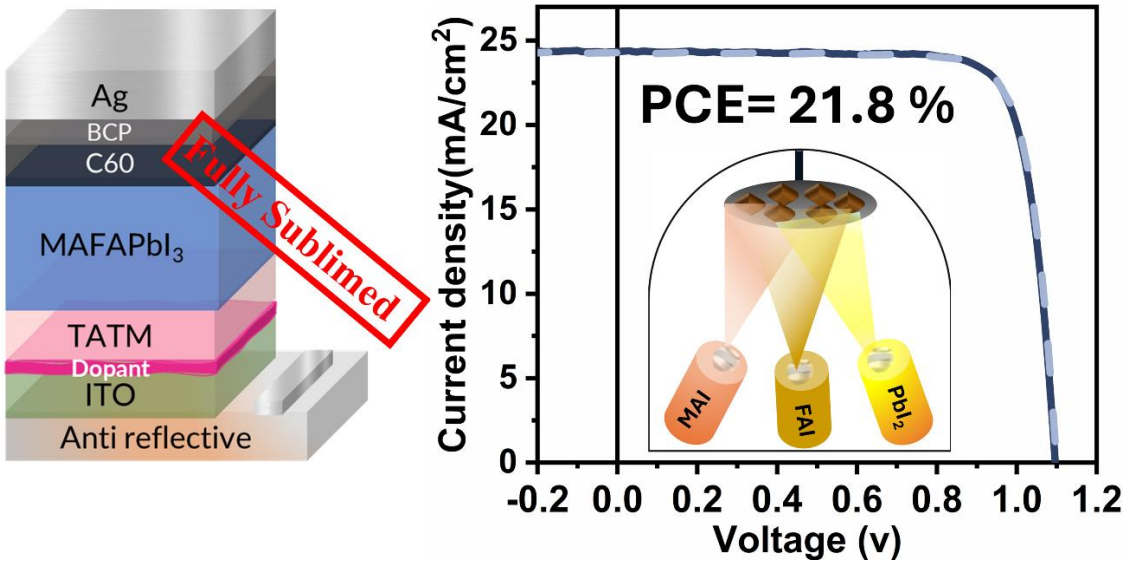

Figure 6-2: *The fully sublimed stack and the champion J-V curve of MAFAPI solar cell achieved with it.*

Chapter 5: **Co-Evaporation for Scalable Perovskite Mini-Modules: A Fully Sublimed Approach,** we have studied the upscaling potential of fully evaporated stacks while mitigating the efficiency losses. This has been developed through optimization of laser scribed fully vacuum processed solar cells and minimodules. We improved the stability of the unfinished stack, which in turn enhanced the stability of the corresponding larger-area monolithically connected cells. A minimodule with an aperture area of 4 cm^2, geometrical fill factor of 99 and power conversion efficiency of 17.45% was fabricated. This was achieved primarily through improving the stability of the fully sublimed stack, starting from the hole transport layer, by thermal evaporation of SAMs suitable for large area application. Secondly, by incorporating FA into the absorber layer by changing the perovskite from MAPI to FAMAPI and finally incorporating a compact moisture-repellent electron selective layer that also works as an encapsulant. Additionally, we improved the stability of the unfinished stack, which in turn enhanced the stability of the corresponding larger-area monolithically connected cells. The minimodule preserved 98% of its initial power conversion efficiency after more than 500 hours of dark storage.

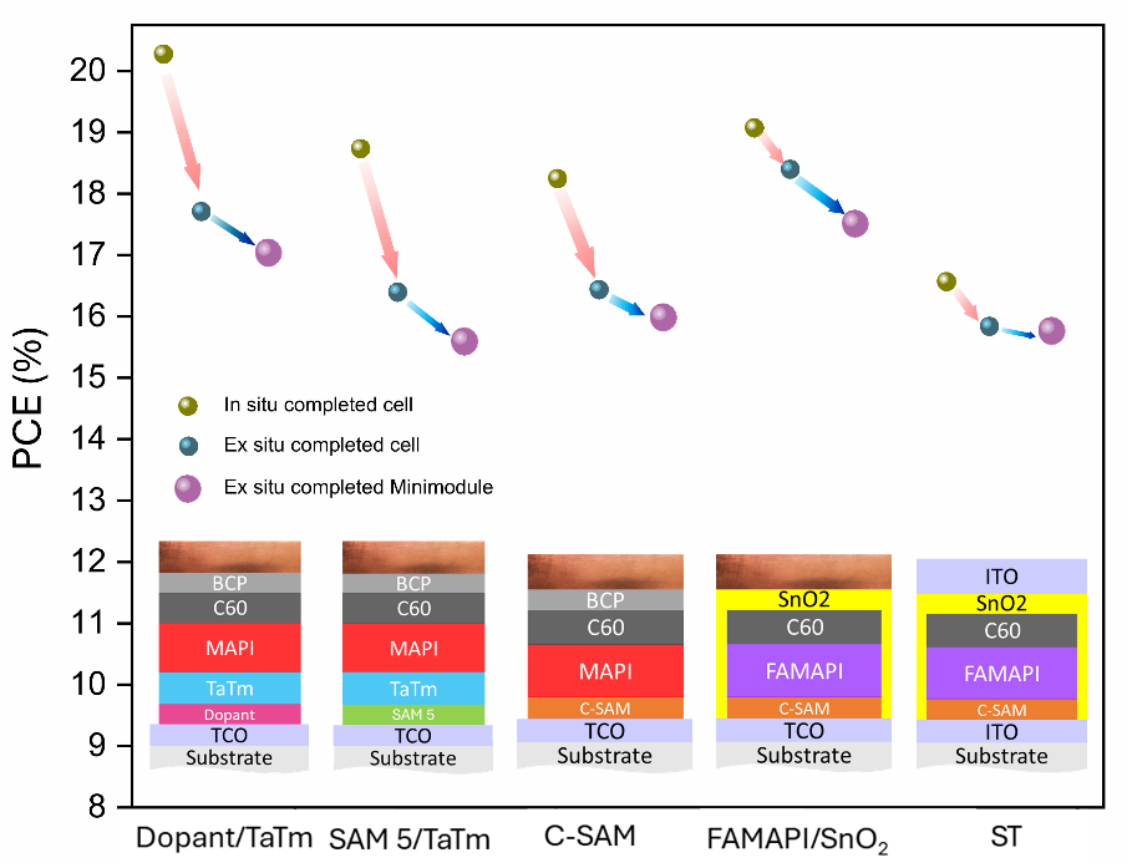

Figure 6-3: *The efficiency of fabricated in situ cells, ex situ cells and ex situ MMs aperture area PCE for different device stack. The first three have been employed to lower the ex situ loss (red arrow) and the last 2 for upscaling loss blue arrow.*

In conclusion, this thesis has advanced the field of vacuum-deposited perovskite solar cells by addressing critical challenges in stability by improving the ITO-HTL interface, the efficiency by fine tuning perovskite composition and scalability, by successful development of high-performance minimodules. Ultimately, realizing the potential of perovskite technology at an industrial level will require not only material and process innovations but also advances in module encapsulation, device integration, and lifecycle assessment to ensure environmental sustainability. The groundwork laid in this thesis provides a foundation for these future explorations.

Chapter 7: Resumen en Castellano

7.1 Tecnología Fotovoltaica

El calentamiento global es uno de los desafíos más urgentes que enfrenta el mundo actual, provocado principalmente por el uso descontrolado de combustibles fósiles para satisfacer la alta demanda energética. La temperatura promedio de la superficie terrestre ya ha aumentado aproximadamente 1.2 °C por encima de los niveles preindustriales, causando eventos climáticos extremos, contaminación del aire y un aumento continuo de las emisiones de gases de efecto invernadero. Entre las fuentes de energía renovable, la energía solar ha destacado como una opción líder debido a su abundante suministro, amplia disponibilidad y bajo impacto ambiental. La transición hacia la energía solar es vista como una estrategia clave para mitigar el calentamiento global y reducir la contaminación ambiental causada por el sector energético.

El mercado fotovoltaico está actualmente dominado por la tecnología de silicio cristalino, que representa aproximadamente el 95% del mercado. Aunque las eficiencias más altas logradas con celdas solares de silicio de unión simple han superado el 26-27% y continúan mejorando, la alta complejidad y los costes asociados con su fabricación subrayan la necesidad de investigar y desarrollar tecnologías alternativas de celdas solares.

7.1.1 La Celda Solar

La cantidad de energía recibida en la Tierra puede cuantificarse mediante el concepto de masa de aire (AM). El espectro solar AM 1.5 representa una condición promedio realista para muchas ubicaciones en la Tierra. Este estándar es ampliamente utilizado para probar y calificar el rendimiento de los paneles solares, ya que resulta en una irradiancia promedio de aproximadamente 1,000 W/m^2 en la superficie terrestre.

Los rayos del sol, al alcanzar la Tierra, pueden ser aprovechados para generar electricidad a través del efecto fotovoltaico, que es el mecanismo fundamental que permite la conversión de la luz solar en energía eléctrica en las celdas solares. Este fenómeno ocurre cuando los fotones son absorbidos por semiconductores, excitando electrones a estados de mayor energía. Si la energía de los fotones incidentes supera la diferencia energética entre la banda de valencia, BV, y la banda de conducción, BC, se generarán pares electrón-hueco. Los electrones son elevados a la banda de conducción, dejando "huecos" en la banda de valencia. Este proceso solo puede ocurrir si la energía del fotón iguala o supera la diferencia de energía, conocida como la banda prohibida (bandgap), que puede ser de naturaleza directa o indirecta.

El coeficiente de absorción determina qué proporción de luz un material puede absorber a una longitud de onda específica, siendo crucial para materiales fotovoltaicos. Un coeficiente alto permite absorber más luz en capas delgadas, optimizando la generación de pares electrón-hueco y reduciendo costes. Cuando un fotón con energía igual o superior al bandgap del material es absorbido, un electrón de la BV se excita a la

BC, generando un par electrón-hueco, que puede disociarse y producir corriente eléctrica. Sin embargo, los electrones y huecos generados también pueden recombinarse entre sí, limitando así la producción de corriente eléctrica. Esta recombinación puede ser radiativa (emisión de fotones) o no radiativa, también conocida como Shockley-Read-Hall (SRH). Ésta última se debe a defectos energéticos en el bandgap, como impurezas o dislocaciones cristalinas, que actúan como trampas para los electrones y huecos. Las pérdidas por recombinación también pueden ocurrir en las interfases, inducidas por defectos o mala alineación energética. Para evitar esto, las capas de absorción (intrínsecas, *i*) se colocan entre materiales de tipo *p* y *n*, formando una unión *p*-*i*-*n*. En esta estructura, la capa intrínseca proporciona un área para la absorción de fotones y generación de portadores, mientras que el campo eléctrico incorporado facilita el transporte de portadores hacia lados opuestos.

Para facilitar la separación de carga y minimizar las pérdidas por recombinación, los dispositivos comúnmente incorporan capas de transporte de electrones (ETL) y de huecos (HTL). Típicamente, una capa de transporte consiste en un material selectivamente permeable a un tipo de portador de carga, mientras bloquea al otro. Los materiales selectivos elegidos para estas capas deben exhibir altas movilidades de electrones y huecos, que garanticen una recolección de carga eficiente, y minimizar las pérdidas. Además, estas capas de transporte deben tener superficies lisas y libres de defectos para un transporte de carga uniforme y un contacto óptimo con la capa absorbente. En el paso final, los electrodos forman contactos óhmicos con resistencia mínima para extraer la carga de la celda solar. Típicamente, se utilizan electrodos basados en óxidos conductores transparentes (TCO), como el óxido de indio y estaño (ITO), para el electrodo frontal, permitiendo que la luz entre al dispositivo mientras se mantiene la conductividad. Un electrodo metálico reflectante actúa como el electrodo contrario. La estructura del dispositivo puede variar entre las configuraciones *p*-*i*-*n* y *n*-*i*-*p*, dependiendo del orden de las capas y la dirección de extracción de carga.

Las celdas solares enfrentan limitaciones inherentes que impiden la conversión completa de la luz solar en energía eléctrica. Estas limitaciones incluyen pérdidas debido a energías insuficientes de los fotones y procesos de recombinación. El límite de Shockley-Queisser, a menudo referido como el límite de eficiencia radiativa, define la eficiencia máxima teórica de una celda solar de unión simple según el bandgap del material. Adicionalmente, existen limitaciones extrínsecas causadas por factores como decisiones de diseño, defectos de fabricación y condiciones ambientales externas. Estas limitaciones extrínsecas pueden categorizarse como pérdidas por recombinación no radiativa, pérdidas por resistencia en serie, pérdidas por resistencia lateral (sheet resistance en inglés), pérdidas por absorción parasitaria y pérdidas por sombreado. A diferencia de las limitaciones intrínsecas, estos factores extrínsecos pueden minimizarse o evitarse mediante un diseño y una optimización cuidadosa del dispositivo. Minimizar estos mecanismos de pérdida es uno de los pasos clave para mejorar la eficiencia de las celdas solares.

7.2 Perovskita de Haluro Metálico

El término "perovskita" se refiere a una amplia variedad de materiales sintéticos y naturales que comparten una estructura cristalina común con la fórmula ABX_3, donde A es típicamente un catión monovalente, B es un catión metálico (a menudo divalente) y X es un anión, usualmente un haluro. La estructura tridimensional (3D) de la perovskita está principalmente unida por enlaces iónicos y consiste en octaedros $[BX_6]^{4-}$ que comparten vértices, con los cationes A ocupando los sitios intersticiales o cavidades formadas por la red octaédrica. En aplicaciones fotovoltaicas, los cationes en el sitio A suelen ser pequeñas moléculas orgánicas como metilamonio (MA = CH_3NH_3), formamidinio (FA = $CH(NH_2)_2$) o iones pequeños como Cs^+. El sitio B típicamente está ocupado por un catión metálico como Pb^{2+} o Sn^{2+}, mientras que X es un haluro o una mezcla de ellos.

Los absorbedores de perovskita son materiales prometedores para aplicaciones fotovoltaicas y otros dispositivos optoelectrónicos debido a las siguientes razones

Bandgap Ajustable: Los materiales de perovskita ofrecen un bandgap ajustable que varía entre aproximadamente 1.2 eV y 2.3 eV, logrado mediante modificaciones en la composición química, lo que los hace adaptables a diversas aplicaciones fotovoltaicas. Esto es particularmente importante, ya que de acuerdo con el límite de Shockley-Queisser, la mayor eficiencia alcanzable en una celda solar ocurre con un bandgap de aproximadamente 1.48 eV.

Baja energía de enlace de excitones: Con energías de enlace de excitones bajas, típicamente entre 2–25 meV, las perovskitas permiten una separación eficiente de excitones (par electrón-hueco), crucial para optimizar el rendimiento de las celdas solares.

Alto coeficiente de absorción: Con coeficientes de absorción ópticos que a menudo superan los 10^5 cm^2, las perovskitas pueden absorber luz de manera eficiente incluso en capas delgadas, permitiendo tecnologías fotovoltaicas de película delgada.

Alta longitud de difusión: Las perovskitas demuestran longitudes de difusión de portadores largas, generalmente entre 1–10 micrómetros, lo que ayuda a reducir las pérdidas por recombinación y mejora la eficiencia global de las celdas solares.

Alta tolerancia a defectos: Conocidas por su alta tolerancia a defectos, las perovskitas mantienen un rendimiento robusto a pesar de la presencia de defectos que normalmente comprometerían la eficiencia del dispositivo en otros materiales.

La estabilidad de las perovskitas sigue siendo una de las barreras más críticas para su comercialización. Actualmente se está abordando desde diversas perspectivas, como ajustar la composición química, desarrollar mejores técnicas de encapsulación y capas de transporte de carga, y diseñar estructuras innovadoras de dispositivos. Por otro lado, aunque los dispositivos de área pequeña han alcanzado eficiencias altas, replicar estos

resultados en módulos más grandes es difícil, existiendo desafíos como garantizar una deposición uniforme de películas, manejar defectos cristalinos, optimizar interfaces y abordar el problema de la resistencia eléctrica lateral en el electrodo transparente. Las investigaciones actuales, entre ellas esta Tesis, se centran en métodos de fabricación escalables, con énfasis particular en técnicas de deposición en fase de vapor.

7.2.1 Fabricación

El desarrollo de las celdas solares de perovskita (PSCs) puede lograrse mediante métodos de procesamiento en disolución, o por deposición térmica en vacío, entre otras. Las técnicas de procesamiento en disolución permiten un ajuste flexible de las propiedades de la capa de perovskita, lo que las hace adecuadas para investigaciones a pequeña escala. Sin embargo, estos métodos enfrentan desafíos significativos al trasladarse la fabricación a gran escala, incluyendo la necesidad de gestionar disolventes, residuos de materiales, y dificultades para lograr una deposición uniforme en grandes áreas superficiales.

Deposición Térmica en Vacío

La deposición térmica en vacío es una forma de deposición física de vapor que implica la sublimación de los precursores por temperatura controlada bajo condiciones de alto vacío (aproximadamente 1×10^{-6} Pa). El uso de alto vacío reduce significativamente la temperatura de sublimación, minimizando reacciones de descomposición de estos precursores. Aunque la deposición en vacío ofrece ventajas para la deposición de perovskita, la mayoría de los dispositivos fabricados enteramente por evaporación térmica utilizan como capas de transporte de carga materiales orgánicos de moléculas pequeñas, u óxidos metálicos en combinación con otros materiales. Estos materiales contienen dopantes orgánicos que conducen a la migración iónica y a reacciones químicas en la interfaz, lo que la convierte en uno de los puntos más probables de inicio de la degradación.

En la arquitectura de dispositivo *p-i-n*, ampliamente adoptada, la capa de transporte de huecos (HTL) se deposita antes que la capa de perovskita. Sin embargo, la disponibilidad de semiconductores HTL, y compatibles con deposición térmica al vacío es limitada, y su rugosidad superficial puede influir en la formación de la capa activa evaporada térmicamente, destacando una vez más la importancia de la selección del HTL. Entre las diversas opciones disponibles en literatura, las monocapas autoensambladas (SAMs) de materiales transportadores de carga han destacado recientemente como una alternativa viable y económica, que proporciona mayor estabilidad térmica al dispositivo, especialmente SAMs derivados de carbazol. Las SAMs son ensamblajes moleculares altamente organizados que se forman mediante adsorción espontánea de moléculas orgánicas funcionalizadas sobre una superficie sólida, habitualmente desde una fase líquida. Las moléculas que forman las SAMs constan típicamente de tres componentes clave: un grupo de anclaje (cabeza), un espaciador (cola) y un grupo terminal o funcional, el cual le aporta las propiedades deseadas. El grupo ancla es la parte reactiva que se une al sustrato, y su naturaleza química determina la

fuerza y el tipo de interacción en la interfaz. Entre las opciones existentes, los ácidos fosfónicos destacan por proporcionar un ensamblaje más robusto a través de conexiones mono, bi y tridentadas. A esto se añade el efecto del grupo espaciador, que determina la orientación y la densidad de empaquetamiento molecular. Esta organización impacta directamente en las propiedades físicas y químicas de las SAMs, como la conductividad electrónica, las características ópticas y la capacidad para facilitar o inhibir el transporte de carga. Finalmente, el grupo terminal define las propiedades añadidas específicas de la nueva superficie.

7.3 El objetivo de la tesis

Esta tesis tiene como objetivo acercar la tecnología de celdas solares de perovskita depositadas al vacío un paso más hacia la comercialización, mejorando tres aspectos críticos: eficiencia, estabilidad y escalabilidad. El objetivo principal de la tesis incluye la optimización de interfaces clave, en especial la interfaz de la capa HTL, uno de los puntos más débiles en términos de estabilidad, así como la formación de conexiones efectivas que incrementen el rendimiento sin comprometer la eficiencia. Esto se ha llevado a cabo mediante mejoras en las interfaces entre el TCO, la capa de extracción de carga y la perovskita, añadiendo metodologías que permitan aumentar el área activa:

Estabilidad: Para mejorar la estabilidad del dispositivo, es necesario eliminar la capa intermedia fuertemente oxidante compuesta por F6-TCNNQ (o dopantes moleculares similares).

Eficiencia: Para mejorar la eficiencia de conversión, es necesario superar la brecha entre el rendimiento obtenido experimentalmente, y el límite teórico radiativo. El objetivo es lograrlo ajustando la composición de la perovskita y minimizando pérdidas por recombinación, modificando la proporción de MA a FA para estabilizar la perovskita de bajo bandgap $FAMAPbI_3$.

Escalabilidad: El objetivo es aumentar el área de la celda solar utilizando óxidos conductores transparentes de baja conductividad como electrodo frontal. Esto implica que las celdas deben colocarse en serie, y es importante explorar cómo se puede lograr esto de manera eficiente.

Si bien cada capítulo aborda un desafío diferente dentro del ámbito de las PSC, en conjunto contribuyen a mejorar las interfaces y formar conexiones confiables, con el objetivo final de acercar esta tecnología de perovskita a la comercialización. Al abordar los problemas de estabilidad, eficiencia y escalabilidad, esta tesis busca realizar una contribución significativa al campo de la generación de energía solar.

7.4 Capítulo 3:

Este capítulo investiga la aplicación de SAMs no conjugadas como nuevas capas intermedias para celdas solares de perovskita fabricadas mediante técnicas de deposición al vacío, con un enfoque en mejorar la eficiencia y la estabilidad térmica. Es estudio se centra en la interfaz ITO/ HTM, en particular TaTm (N4,N4,N4,N4-tetra([1,1-bifenil]-4-il)-[1,1:4,1-terfenil]-4,4-diamina), y aborda desafíos relacionados con la

necesidad de incluir capas de activación intermedias de alta función de trabajo, tales como MoO_3 o 1,3,4,5,7,8-hexafluorotetracianonaftoquinodimetano (F6-TCNNQ), necesarias para proporcionar un buen contacto óhmico, pero altamente inestables bajo estrés térmico.

Se han investigado cinco SAMs comercialmente disponibles, cada una con diferentes estructuras moleculares, que permiten modular el momento dipolar superficial en la interfaz del ITO, facilitando así una mejor extracción de carga y alineación de energía. Se han utilizado técnicas analíticas como AFM y XPS para estudiar la morfología, la química superficial y las configuraciones de enlace en las interfaces modificadas con SAM.

Las mediciones de AFM muestran superficies uniformes y lisas, con valores de rugosidad RMS consistentemente inferiores a 5 nm, confirmando la ausencia de formación de islas significativas. A su vez, los análisis vía XPS han revelado que las SAMs derivadas de arilos (por ejemplo, SAM 2 y SAM 3) tienden a formar multicapas, lo que afecta el grosor óptimo de la capa de TaTm. En cambio, las SAMs alifáticas (por ejemplo, SAM 5) forman monocapas con enlaces químicos fuertes a la superficie del ITO. Estas características de enlace suelen correlacionarse con una mejor extracción de carga y menores pérdidas por recombinación.

Las superficies de ITO modificadas con SAMs se han analizado en términos de cambios en la hidrofobicidad de la superficie y propiedades electrónicas, revelando un aumento gradual en el ángulo de contacto, y la función de trabajo (ϕ), proporcional al contenido de flúor de en su estructura molecular.

Para comprender el impacto de las SAMs en el rendimiento del dispositivo, se han fabricado PSCs con la arquitectura ITO-SAM/TaTm/$MAPbI_3$/C_{60}/BCP/Ag. El grosor de la capa de TaTm se optimizó para cada molécula SAM, confirmando una dependencia de éste con su estructura molecular. Por ejemplo, las SAMs derivadas de arilos (SAM 2 y SAM 3) requieren capas más delgadas de TaTm (~ 5 nm) para un rendimiento óptimo, mientras que la SAM alifática 5, que forma monocapas robustas, proporciona mejores resultados con capas de TaTm ligeramente más gruesas (~ 7 nm). Estas variaciones destacan la importancia de diseñar interfaces adaptadas a las propiedades específicas de cada SAM.

Estas diferencias también se reflejan en el rendimiento fotovoltaico, ya que SAM 5 muestra mayor eficiencia y estabilidad, atribuida a su enlace robusto y empaquetamiento molecular uniforme, alcanzando una eficiencia de conversión de potencia (PCE) del 19.65%, comparable con las PSCs totalmente depositadas al vacío de última generación. Este rendimiento se atribuye a su enlace robusto con la superficie de ITO, y su capacidad para inducir un dipolo superficial favorable.

Además de lograr una alta eficiencia, los dispositivos basados en SAM muestran una notable durabilidad térmica. Bajo pruebas continuas a 85°C durante 1,000 horas en atmósfera controlada de nitrógeno, SAM 5 retiene más del 90% de su eficiencia inicial, en contraste con los dispositivos con capas intermedias tradicionales como MoO_3 y F6-TCNNQ, que se degradan tras 500 horas de prueba. Además, las pruebas de estabilidad

también indican descensos mínimos en FF y V_{oc}, lo que demuestra una estabilidad robusta de la interfaz durante períodos prolongados.

7.5 Capítulo 4

Este capítulo presenta una investigación sobre la deposición al vacío de películas delgadas de perovskita, enfocándose en métodos de co-sublimación para la fabricación de perovskitas de yoduro de plomo basadas en FA y MA. El trabajo detalla los procedimientos experimentales, técnicas de caracterización y resultados de rendimiento de dispositivos para dos composiciones de perovskita, FAMAPI y MAFAPI, destacando la influencia de la proporción MA/FA en el rendimiento fotovoltaico y la estabilidad.

Las capas activas se han fabricado mediante co-evaporación de tres precursores: PbI_2, MAI y FAI. El estudio requiere especial cuidado en el monitoreo de las velocidades de evaporación para los componentes orgánicos, ya que solo pueden medirse de manera confiable en presencia de PbI_2. Las velocidades de deposición usadas para MAFAPI han sido 0.50 Å/s para PbI_2, 0.04 Å/s para FAI y 0.17 Å/s para MAI, mientras que para las películas FAMAPI han sido 0.50 Å/s, 0.16 Å/s y 0.05 Å/s, respectivamente. Estas composiciones se han confirmado mediante análisis EDX y ^{1}H-NMR.

La caracterización estructural ha revelado diferencias entre ambas composiciones. Los difractogramas de XRD indican que las películas MAFAPI presentan una orientación preferencial [111], mientras que las películas FAMAPI carecen de una orientación clara. A su vez, las imágenes de SEM muestran que las películas MAFAPI exhiben tamaños de grano más grandes, una característica atípica en perovskitas depositadas al vacío. El bandgap de las películas, calculado mediante gráficos de Tauc, también es ligeramente mayor para MAFAPI (1.55 eV) que para FAMAPI (1.52 eV), lo que puede correlacionarse con el menor tamaño iónico del MA en comparación con el FA.

Para evaluar el rendimiento de estas películas, se han fabricado celdas solares completamente evaporadas con la estructura vidrio/ITO/F6-TCNNQ/TaTm/perovskita (FAMAPI o MAFAPI)/C60/BCP/(plata)Ag. Los dispositivos MAFAPI han demostrado una eficiencia PCE máxima de 21.8%, significativamente superior al 19.45% registrado para los dispositivos FAMAPI. Esta mejora se atribuye principalmente a un mayor J_{sc}, lo cual se ha respaldado por mediciones de EQE, alcanzando un valor máximo del 92.84 % a 720 nm para dispositivos basados en MAFAPI. Es de destacar que estas celdas muestran una histéresis insignificante y un rendimiento estable bajo seguimiento de MPP.

Las pruebas de estabilidad durante almacenamiento en oscuridad también han proporcionado resultados muy positivos, donde los dispositivos MAFAPI mantienen el 90% de su eficiencia inicial después de 1,000 horas de test en atmósfera controlada de nitrógeno. La degradación existente se debe principalmente a una reducción en FF y V_{oc}, mientras que el J_{sc} se mantiene estable. Ello sugiere que la mayor estabilidad de las películas MAFAPI podría estar vinculada a la mayor concentración de MA, ya que reduce la prevalencia de defectos planares intergranulares, como fallos de apilamiento y dislocaciones. Para comprender mejor las diferencias de rendimiento entre los dispositivos FAMAPI y MAFAPI, se han analizado las curvas J-V utilizando simulaciones

de drift-diffusion con ayuda del software SIMsalabim. Los resultados indican que las películas MAFAPI exhiben menores densidades de trampas por defectos en comparación con las películas FAMAPI. Esto es consistente con la hipótesis de que un mayor contenido de MA reduce los defectos estructurales, factor clave para obtener superior J_{sc} y mayor eficiencia.

Este estudio demuestra el potencial de los métodos de co-sublimación para controlar la composición de MA y FA en películas de perovskita depositadas al vacío. La composición optimizada de MAFAPI conduce a mayores eficiencias y mejor estabilidad, alcanzando un 21.8%. Este hallazgo subraya la importancia de un ajuste preciso en la composición, destacando la viabilidad de lograr celdas de perovskita eficientes y depositadas enteramente al vacío.

7.6 Capítulo 5

Este capítulo presenta un estudio sobre el desarrollo y escalabilidad hacia minimódulos (MMs) de perovskita enteramente depositados al vacío, con un enfoque en la optimización de materiales, técnicas de fabricación y evaluación del rendimiento. Los MMs se han diseñado utilizando un método rentable para conectar celdas en serie mediante ablación láser. El estudio experimental se ha llevado a cabo en tres configuraciones de dispositivo con áreas activas crecientes.

El proceso ha constado de tres etapas diferenciadas: en primer lugar se han fabricado celdas de área pequeña (0.05 cm^2) en la Universidad de Valencia (UVEG), utilizadas como control para evaluar el rendimiento base (denominadas *in situ*). Estas celdas han alcanzado una eficiencia PCE máxima de 20.29%. En segundo lugar, se han fabricado MMs de cuatro celdas conectadas en serie (1 cm^2), combinando pasos de procesamiento entre dos centros de investigación, UVEG y el Centro Interuniversitario de Microelectrónica situado en Bélgica (IMEC). En tercer lugar, se han procesado celdas de referencia (0.125 cm^2) fabricadas parcialmente entre UVEG e IMEC (de manera idéntica a los MMs), lo que permitió estudiar la degradación del rendimiento durante el transporte (llamadas *ex situ*). Tras este análisis, las celdas *ex situ* han mostrado una pérdida significativa de eficiencia (~12%) debido a la degradación de las interfaces durante el transporte.

Para abordar este problema, se han investigado alternativas más robustas para usar como transportadores de carga, tales como el uso de SAMs depositadas al vacío, y SnO_2 depositado por ALD. Basándonos en la optimización del capítulo 3, se investigó la viabilidad de tres tipos de HTLs: SAM 5, TaTm y un SAM derivado del carbazol muy utilizado en literatura (MeO-2PACz). Estos materiales han sido seleccionados por su alto potencial para mejorar la estabilidad interfacial, la uniformidad y la durabilidad general del dispositivo. Los resultados han corroborado que las SAMs depositadas al vacío proporcionan una cobertura uniforme, y mejoran la reproducibilidad en comparación con las capas procesadas en disolución. Como dato, las celdas de área pequeña *in situ*

fabricadas con HTLs basadas en SAM muestran una mejor estabilidad térmica, manteniendo su eficiencia bajo pruebas de estrés a 85°C.

Los análisis estructurales y morfológicos también han revelado que las SAMs depositadas al vacío mejoran la calidad de las películas de perovskita, promoviendo un mayor crecimiento de grano y reduciendo la densidad de defectos. Además, los dispositivos basados en SAM muestran pérdidas *ex situ* mínimas (~10%) y mantienen alta eficiencia después de 500 horas de almacenamiento en la oscuridad. Una vez comprobada la estabilidad, la optimización de los parámetros de ablación láser ha sido crítica para lograr altos valores de FF geométrico (GFF) y minimizar el área inactiva existente en los MMs. De hecho, mediante ablación precisa se consiguen interconexiones eficientes sin dañar las capas críticas del dispositivo, preservando su integridad durante el proceso de escalabilidad. De este modo se ha conseguido un GFF del 99%, con pérdidas mínimas de rendimiento.

Para mejorar aún más la estabilidad del dispositivo, se han fabricado MMs basados en FAMAPI. Mediante análisis ^{1}H-NMR se ha verificado el control preciso de las proporciones de MA y FA en las composiciones de perovskita, asegurando la reproducibilidad y la formación de películas de alta calidad, en concordancia con las mediciones ópticas del bandgap. También se ha optado por incorporar SnO_2 depositado por ALD como ETL y encapsulante, lo que ha mejorado aún más la estabilidad del dispositivo, reduciendo la degradación *ex situ* durante el transporte. En concreto, se ha demostrado una transición desde celdas de área pequeña a MMs con pérdidas mínimas de eficiencia: la celda *ex situ* alcanzó un PCE de 18.37%, mientras que el MM correspondiente logró una eficiencia de apertura del 17.45%, reflejando solo una pérdida de tan solo ~3.3% durante la escalabilidad. Además, los MMs han mostrado un rendimiento estable con una degradación insignificante, reteniendo el 98% de su eficiencia inicial tras 500 horas de almacenamiento en atmósfera inerte de nitrógeno. A su vez, se han fabricado mini módulos semitransparentes (STMMs) reemplazando el electrodo opaco de cobre con ITO depositado por pulverización catódica, logrando una eficiencia del 15.69% con un GFF del 99%. A pesar de la mayor resistencia lateral del ITO, la minimización de las regiones inactivas mediante grabado láser óptimo ha permitido pérdidas de escalabilidad mínimas, cercanas al ~1.6%.

7.7 Conclusión

En resumen, esta tesis, titulada **“Interfaces y Conexiones en Celdas Solares de Perovskita Basadas en Vacío,”** se ha centrado en abordar los desafíos críticos en las PSCs depositadas al vacío, específicamente en términos de estabilidad, eficiencia y escalabilidad. El enfoque seguido incluye la optimización de interfaces, la mejora de la eficiencia de la celda, y la optimización de las conexiones necesarias para generar mini-modulos eficientes y estables.

Se ha prestado especial atención a la interfase ITO/HTL, identificada como un cuello de botella crítico para lograr estabilidad en dispositivos con arquitectura *p-i-n*. Empleando materiales alternativos basados en SAMs, se han logrado una mejora significativa en la estabilidad general del dispositivo. Además, modificando la composición de la perovskita también se ha reducido con éxito la densidad de defectos cristalinos, aumentando así la eficiencia final del dispositivo. Este trabajo también ha demostrado pérdidas mínimas a la hora de escalar el área activa de los dispositivos, destacando el potencial de técnicas de deposición al vacío para la fabricación de celdas de alto rendimiento.

Capítulo 3: Ingeniería de contactos *-p* estables para celdas solares de perovskita completamente depositadas al vacío

En este capítulo, hemos introducido varias SAMs de estructura simple, no conjugada, como capas intermedias para la interfase ITO/HTL. Estos materiales proporcionan una alta función de trabajo en el ITO, ideales para utilizar como contactos de tipo *-p* en combinación con semiconductores intrínsecos sublimables (TaTm). El principal objetivo del estudio es precisamente evitar el uso de dopantes químicos, factor limitante en la estabilidad de las celdas solares preparadas enteramente por evaporación. Para ello se incorpora en el proceso de lavado y preparación del electrodo un último paso de recubrimiento por inmersión en etanol no dañino, cuyo resultado es la minimización de su barrera energética respecto al TaTm, resultando en una mejora de la eficiencia y estabilidad. Es de destacar que la integración de estos electrodos modificados preserva la estabilidad del FF a lo largo del tiempo. Esta modificación de interfaz, sencilla pero efectiva, ha permitido fabricar celdas solares de MAPbI3 completamente evaporadas con una PCE superior al 19%, manteniendo el 90% de la eficiencia inicial tras más de 1,000 horas de estrés térmico.

Capítulo 4: Celdas solares de alto rendimiento fabricadas mediante co-evaporación de perovskita de doble catión A

En este capítulo, utilizando técnicas de caracterización como EDX, NMR y SEM, hemos profundizado sobre el efecto que el ratio de cationes A produce en tipología de granos de cristal, optimizando el proceso de deposición de la capa absorbente. Los resultados fotovoltaicos indican que una composición rica en MA puede reducir los defectos estructurales en comparación con otras de mayor contenido en FA. Además, haciendo uso del software SIMsalabim, se ha confirmado que esta estrategia genera menor densidad de trampas de carga (generadas por defectos cristalinos generalmente), y mitiga aún más las pérdidas por recombinación. Esta es la razón del mayor rendimiento fotovoltaico, generando superior J_{sc}, llegando a alcanzar una mejora notable en la eficiencia, PCE 21.83%, el valor más alto reportado hasta la fecha para una PSC co-evaporada, realizada en su totalidad utilizando técnica de sublimación al vacío.

Capítulo 5: Co-evaporación para minimódulos escalables de perovskita: un enfoque íntegramente sublimado

En este capítulo, hemos estudiado el potencial de escalabilidad de dispositivos de perovskita completamente evaporados, a la vez que mitigamos pérdidas de eficiencia. Para ello, se ha optimizado el grabado láser de celdas solares y MMs procesados completamente al vacío. Así, se ha fabricado un MM con un área de apertura de 4 cm^2, un GFF del 99% y una PCE del 17.45%. La estrategia ha comenzado con la búsqueda de HTL estables pero compatibles con evaporación térmica, tales como SAMs, que han resultado idóneos para aplicaciones de gran área. Además, se ha sustituido MAPbI3 por una perovskita mixta de MA-FA, con el objetivo de obtener un absorbente más estable y de menor bandgap. Posteriormente, se ha integrado una capa selectiva de electrones ETL compacta y repelente a la humedad, que a su vez actúa como encapsulante. La combinación de estas estrategias ha permitido fabricar MMs de eficiencia similar pero mucho más estables, que conservan el 98% de su eficiencia inicial tras más de 500 horas de almacenamiento en la oscuridad. Con idéntica estrategia, se fabricaron minimódulos semitransparentes (STMMs) reemplazando el electrodo opaco de cobre con ITO depositado por pulverización catódica suave (Soft sputtering en inglés), logrando una eficiencia del 15.69% con un GFF del 99%.

Esta tesis marca un avance significativo en las PSCs depositadas al vacío, abordando desafíos clave en estabilidad, eficiencia y escalabilidad. Se ha optimizado la interfaz ITO-HTL para mejorar la estabilidad, se ha ajustado la composición iónica de la perovskita para alcanzar altas eficiencias, y se han desarrollado minimódulos de alto rendimiento, demostrando su viabilidad a mayor escala. No obstante, para liberar el verdadero potencial que esta tecnología puede aportar en nuestra sociedad, será esencial avanzar en la encapsulación de módulos, integración de dispositivos y evaluación de su ciclo de vida, requisitos que permitan garantizar un impacto sostenible en la sociedad y medio ambiente.

Chapter 8: Resum en valencià

8.1 Tecnologia Fotovoltaica

L'escalfament global és un dels desafiaments més urgents que afronta el món actual, provocat principalment per l'ús descontrolat de combustibles fòssils per a satisfer la gran demanda energètica. La temperatura mitjana de la superfície terrestre ja ha augmentat aproximadament 1,2 °C per damunt dels nivells preindustrials, causant esdeveniments climàtics extrems, contaminació de l'aire i un augment continu de les emissions de gasos d'efecte hivernacle. Entre les fonts d'energia renovable, l'energia solar ha destacat com una opció líder gràcies al seu subministrament abundant, àmplia disponibilitat i baix impacte ambiental. La transició cap a l'energia solar es considera una estratègia clau per a mitigar l'escalfament global i reduir la contaminació ambiental causada pel sector energètic.

El mercat fotovoltaic està actualment dominat per la tecnologia de silici cristal·lí, que representa aproximadament el 95% del mercat. Encara que les eficiències més altes aconseguides amb cèl·lules solars de silici d'unió simple han superat el 26-27% i continuen millorant, l'alta complexitat i els costos associats a la seua fabricació subratllen la necessitat d'investigar i desenvolupar tecnologies alternatives de cèl·lules solars.

8.2 La Cèl·lula Solar

La quantitat d'energia rebuda a la Terra pot quantificar-se mitjançant el concepte de massa d'aire (AM). L'espectre solar AM 1.5 representa una condició mitjana realista per a moltes ubicacions a la Terra. Aquest estàndard és àmpliament utilitzat per a provar i qualificar el rendiment dels panells solars, ja que resulta en una irradiància mitjana d'aproximadament 1.000 W/m^2 a la superfície terrestre.

Els raigs del sol, en arribar a la Terra, poden ser aprofitats per a generar electricitat a través de l'efecte fotovoltaic, que és el mecanisme fonamental que permet la conversió de la llum solar en energia elèctrica en les cèl·lules solars. Aquest fenomen ocorre quan els fotons són absorbits per semiconductors, excitant electrons a estats d'energia més alta. Si l'energia dels fotons incident supera la diferència energètica entre la banda de València (BV) i la banda de conducció (BC), es generaran parells electró-forat. Els electrons són elevats a la banda de conducció, deixant "forats" a la banda de València. Aquest procés només pot ocórrer si l'energia del fotó iguala o supera la diferència d'energia, coneguda com la banda prohibida (bandgap), que pot ser de naturalesa directa o indirecta.

El coeficient d'absorció determina quina proporció de llum pot absorbir un material a una longitud d'ona específica, essent crucial per als materials fotovoltaics. Un coeficient alt permet absorbir més llum en capes fines, optimitzant la generació de parells electró-forat i reduint costos. Quan un fotó amb energia igual o superior al bandgap del material

és absorbit, un electró de la BV s'excita a la BC, generant un parell electró-forat, que pot dissociar-se i produir corrent elèctric. Tanmateix, els electrons i forats generats també poden recombinar-se entre si, limitant així la producció de corrent elèctric. Aquesta recombinació pot ser radiativa (emissió de fotons) o no radiativa, també coneguda com a recombinació Shockley-Read-Hall (SRH). Aquesta última es deu a defectes energètics en el bandgap, com impureses o dislocacions cristal·lines, que actuen com a trampes per als electrons i forats. Les pèrdues per recombinació també poden ocórrer en les interfícies, induïdes per defectes o una mala alineació energètica. Per evitar això, les capes d'absorció (intrínseques, i) es col·loquen entre materials de tipus p i n, formant una unió p-i-n. En aquesta estructura, la capa intrínseca proporciona una àrea per a l'absorció de fotons i generació de portadors, mentre que el camp elèctric incorporat facilita el transport de portadors cap a costats oposats.

Per a facilitar la separació de càrregues i minimitzar les pèrdues per recombinació, els dispositius solen incorporar capes de transport d'electrons (ETL) i de forats (HTL). Normalment, una capa de transport consisteix en un material selectivament permeable a un tipus de portador de càrrega, mentre bloqueja l'altre. Els materials selectius triats per a aquestes capes han de presentar mobilitats altes d'electrons i forats, que garantisquen una col·lecció de càrrega eficient, i minimitzar les pèrdues. A més, aquestes capes de transport han de tenir superfícies llises i lliures de defectes per a un transport de càrrega uniforme i un contacte òptim amb la capa absorbent. En l'etapa final, els elèctrodes formen contactes òhmics amb resistència mínima per a extraure la càrrega de la cèl·lula solar. Normalment, s'utilitzen elèctrodes basats en òxids conductors transparents (TCO), com l'òxid d'indi i estany (ITO), per a l'elèctrode frontal, permetent que la llum entre al dispositiu mentre es manté la conductivitat. Un elèctrode metàl·lic reflectant actua com a l'elèctrode contrari. L'estructura del dispositiu pot variar entre les configuracions p-i-n i n-i-p, segons l'ordre de les capes i la direcció d'extracció de càrrega.

Les cèl·lules solars enfronten limitacions inherents que impedeixen la conversió completa de la llum solar en energia elèctrica. Aquestes limitacions inclouen pèrdues degudes a energies insuficients dels fotons i processos de recombinació. El límit de Shockley-Queisser, sovint referit com a límit d'eficiència radiativa, defineix l'eficiència màxima teòrica d'una cèl·lula solar d'unió simple segons el bandgap del material. Addicionalment, hi ha limitacions extrínseques causades per factors com decisions de disseny, defectes de fabricació i condicions ambientals externes. Aquestes limitacions extrínseques poden categoritzar-se com a pèrdues per recombinació no radiativa, pèrdues per resistència en sèrie, pèrdues per resistència lateral, pèrdues per absorció parasitària i pèrdues per ombreig. A diferència de les limitacions intrínseques, aquests factors extrínsecs poden minimitzar-se o evitar-se mitjançant un disseny i una optimització curosa del dispositiu. Minimitzar aquests mecanismes de pèrdua és un dels passos clau per a millorar l'eficiència de les cèl·lules solars.

8.3 Perovskita d'Halur Metàl·lic

El terme "perovskita" es refereix a una àmplia varietat de materials sintètics i naturals que comparteixen una estructura cristal·lina comuna amb la fórmula ABX_3, on A és típicament un catió monovalent, B és un catió metàl·lic (sovint divalent) i X és un anió, usualment un halur. L'estructura tridimensional (3D) de la perovskita està principalment unida per enllaços iònics i consisteix en octaedres $[BX_6]^{4-}$ que comparteixen vèrtexs, amb els cations A ocupant els llocs intersticials o cavitats formades per la xarxa octaèdrica. En aplicacions fotovoltaiques, els cations al lloc A solen ser petites molècules orgàniques com metilamoni ($MA = CH_3NH_3$), formamidini ($FA = CH(NH_2)_2$) o ions petits com Cs^+. El lloc B típicament està ocupat per un catió metàl·lic com Pb^{2+} o Sn^{2+}, mentre que X és un halur o una mescla d'ells.

Els absorbidors de perovskita són materials prometedors per a aplicacions fotovoltaiques i altres dispositius optoelectrònics per les següents raons:

- **Bandgap Ajustable**: Els materials de perovskita ofereixen un bandgap ajustable que varia entre aproximadament 1,2 eV i 2,3 eV, aconseguit mitjançant modificacions en la composició química, cosa que els fa adaptables a diverses aplicacions fotovoltaiques. Això és particularment important, ja que d'acord amb el límit de Shockley-Queisser, la màxima eficiència assolible en una cèl·lula solar ocorre amb un bandgap d'aproximadament 1,48 eV.
- **Baixa energia d'enllaç d'excitons**: Amb energies d'enllaç d'excitons baixes, típicament entre 2-25 meV, les perovskites permeten una separació eficient d'excitons (parell electró-forat), crucial per a optimitzar el rendiment de les cèl·lules solars.
- **Alt coeficient d'absorció**: Amb coeficients d'absorció òptics que sovint superen els 10^5 cm^2, les perovskites poden absorbir llum de manera eficient fins i tot en capes fines, permetent tecnologies fotovoltaiques de pel·lícula fina.
- **Alta longitud de difusió**: Les perovskites demostren longituds de difusió de portadors llargues, generalment entre 1-10 micròmetres, cosa que ajuda a reduir les pèrdues per recombinació i millora l'eficiència global de les cèl·lules solars.
- **Alta tolerància als defectes**: Conegudes per la seua alta tolerància als defectes, les perovskites mantenen un rendiment robust malgrat la presència de defectes que normalment comprometrien l'eficiència del dispositiu en altres materials.

La estabilitat de les perovskites continua sent una de les barreres més crítiques per a la seua comercialització. Actualment, s'està abordant des de diverses perspectives, com ara ajustar la composició química, desenvolupar millors tècniques d'encapsulació i capes de transport de càrrega, i dissenyar estructures innovadores de dispositius. D'altra banda, encara que els dispositius d'àrea xicoteta han assolit eficiències altes, replicar aquests resultats en mòduls més grans és difícil, ja que hi ha desafiaments com garantir una deposició uniforme de les pel·lícules, gestionar defectes cristal·lins,

optimitzar les interfícies i abordar el problema de la resistència elèctrica lateral en l'elèctrode transparent. Les investigacions actuals, entre elles aquesta Tesi, se centren en mètodes de fabricació escalables, amb un èmfasi particular en tècniques de deposició en fase de vapor.

8.4 Fabricació

El desenvolupament de les cèl·lules solars de perovskita (PSCs) es pot aconseguir mitjançant mètodes de processament en dissolució, o per deposició tèrmica en buit, entre altres. Les tècniques de processament en dissolució permeten un ajust flexible de les propietats de la capa de perovskita, cosa que les fa adequades per a investigacions a xicoteta escala. No obstant això, aquests mètodes enfronten desafiaments significatius en traslladar la fabricació a gran escala, incloent-hi la necessitat de gestionar dissolvents, residus de materials, i dificultats per a aconseguir una deposició uniforme en grans àrees superficials.

8.5 Deposició Tèrmica en Buit

La deposició tèrmica en buit és una forma de deposició física de vapor que implica la sublimació dels precursors mitjançant temperatura controlada sota condicions d'alt buit (aproximadament 1×10^{-6} Pa). L'ús d'alt buit redueix significativament la temperatura de sublimació, minimitzant reaccions de descomposició d'aquests precursors. Encara que la deposició en buit ofereix avantatges per a la deposició de perovskita, la majoria dels dispositius fabricats completament per evaporació tèrmica utilitzen com a capes de transport de càrrega materials orgànics de molècules petites, o òxids metàl·lics en combinació amb altres materials. Aquests materials contenen dopants orgànics que condueixen a la migració iònica i a reaccions químiques en la interfície, convertint-la en un dels punts més probables d'inici de la degradació.

En l'arquitectura de dispositiu *p*-i-*n*, àmpliament adoptada, la capa de transport de forats (HTL) es deposita abans que la capa de perovskita. No obstant això, la disponibilitat de semiconductors HTL compatibles amb la deposició tèrmica en buit és limitada, i la seua rugositat superficial pot influir en la formació de la capa activa evaporada tèrmicament, destacant una vegada més la importància de la selecció de l'HTL. Entre les diverses opcions disponibles en la literatura, les monocapes autoensamblades (SAMs) de materials transportadors de càrrega han destacat recentment com una alternativa viable i econòmica, que proporciona major estabilitat tèrmica al dispositiu, especialment SAMs derivades de carbazol.

Les SAMs són assemblatges moleculars altament organitzats que es formen mitjançant adsorció espontània de molècules orgàniques funcionalitzades sobre una superfície sòlida, habitualment des d'una fase líquida. Les molècules que formen les SAMs consten típicament de tres components clau: un grup d'ancoratge (cap), un espaiador (cua) i un grup terminal o funcional, que li aporta les propietats desitjades. El grup d'ancoratge és la part reactiva que s'uneix al substrat, i la seua naturalesa química determina la força i el tipus d'interacció en la interfície. Entre les opcions existents, els àcids fosfònics destaquen per proporcionar un assemblatge més robust a través de

connexions mono, bi i tridentades. A això s'afegeix l'efecte del grup espaiador, que determina l'orientació i la densitat d'empaquetament molecular. Aquesta organització impacta directament en les propietats físiques i químiques de les SAMs, com la conductivitat electrònica, les característiques òptiques i la capacitat per a facilitar o inhibir el transport de càrrega. Finalment, el grup terminal defineix les propietats afegides específiques de la nova superfície.

8.6 L'objectiu de la tesi

Aquesta tesi té com a objectiu apropar la tecnologia de cèl·lules solars de perovskita depositades al buit un pas més cap a la comercialització, millorant tres aspectes crítics: eficiència, estabilitat i escalabilitat. L'objectiu principal de la tesi inclou l'optimització d'interfícies clau, en especial la interfície de la capa HTL, un dels punts més dèbils en termes d'estabilitat, així com la formació de connexions efectives que incrementen el rendiment sense comprometre l'eficiència. Això s'ha dut a terme mitjançant millores en les interfícies entre el TCO, la capa d'extracció de càrrega i la perovskita, afegint metodologies que permeten augmentar l'àrea activa:

Estabilitat: Per a millorar l'estabilitat del dispositiu, és necessari eliminar la capa intermèdia fortament oxidant composta per F6-TCNNQ (o dopants moleculars similars).

Eficiència: Per a millorar l'eficiència de conversió, és necessari superar la bretxa entre el rendiment obtingut experimentalment i el límit teòric radiatiu. L'objectiu és aconseguir-ho ajustant la composició de la perovskita i minimitzant pèrdues per recombinació, modificant la proporció de MA a FA per a estabilitzar la perovskita de baix bandgap $FAMAPbI_3$.

Escalabilitat: L'objectiu és augmentar l'àrea de la cèl·lula solar utilitzant òxids conductors transparents de baixa conductivitat com a elèctrode frontal. Això implica que les cèl·lules han de col·locar-se en sèrie, i és important explorar com es pot aconseguir això de manera eficient.

Encara que cada capítol aborda un desafiament diferent dins de l'àmbit de les PSC, en conjunt contribueixen a millorar les interfícies i formar connexions fiables, amb l'objectiu final d'apropar aquesta tecnologia de perovskita a la comercialització. En abordar els problemes d'estabilitat, eficiència i escalabilitat, aquesta tesi busca fer una contribució significativa al camp de la generació d'energia solar.

8.7 Capítol 3:

Aquest capítol investiga l'aplicació de SAMs no conjugades com a noves capes intermèdies per a cèl·lules solars de perovskita fabricades mitjançant tècniques de deposició al buit, amb un enfocament en millorar l'eficiència i l'estabilitat tèrmica. L'estudi se centra en la interfície ITO/HTM, en particular TaTm (N4,N4,N4,N4-tetra([1,1-bifenil]-4-il)-[1,1:4,1-terfenil]-4,4-diamina), i aborda desafiaments relacionats amb la necessitat d'incloure capes d'activació intermèdies d'alta funció de treball, com MoO_3 o

1,3,4,5,7,8-hexafluorotetracianonaftoquinodimetà (F6-TCNNQ), necessàries per a proporcionar un bon contacte òhmic, però altament inestables sota estrès tèrmic.

S'han investigat cinc SAMs comercialment disponibles, cadascuna amb diferents estructures moleculars, que permeten modular el moment dipolar superficial en la interfície de l'ITO, facilitant així una millor extracció de càrrega i alineació d'energia. S'han utilitzat tècniques analítiques com AFM i XPS per a estudiar la morfologia, la química superficial i les configuracions d'enllaç en les interfícies modificades amb SAM.

Les mesures d'AFM mostren superfícies uniformes i llises, amb valors de rugositat RMS consistentment inferiors a 5 nm, confirmant l'absència de formació d'illes significatives. Al seu torn, les anàlisis via XPS han revelat que les SAMs derivades d'arils (per exemple, SAM 2 i SAM 3) tendeixen a formar multicapes, cosa que afecta el gruix òptim de la capa de TaTm. En canvi, les SAMs alifàtiques (per exemple, SAM 5) formen monocapes amb enllaços químics forts a la superfície de l'ITO. Aquestes característiques d'enllaç solen correlacionar-se amb una millor extracció de càrrega i menors pèrdues per recombinació.

Les superfícies d'ITO modificades amb SAMs s'han analitzat en termes de canvis en la hidrofobicitat de la superfície i propietats electròniques, revelant un augment gradual en l'angle de contacte i la funció de treball (ϕ), proporcional al contingut de fluor en la seua estructura molecular.

Per a comprendre l'impacte de les SAMs en el rendiment del dispositiu, s'han fabricat PSCs amb l'arquitectura ITO-SAM/TaTm/$MAPbI_3$/C_{60}/BCP/Ag. El gruix de la capa de TaTm es va optimitzar per a cada molècula SAM, confirmant una dependència d'aquest amb la seua estructura molecular. Per exemple, les SAMs derivades d'arils (SAM 2 i SAM 3) requereixen capes més primes de TaTm (~5 nm) per a un rendiment òptim, mentre que la SAM alifàtica 5, que forma monocapes robustes, proporciona millors resultats amb capes de TaTm lleugerament més gruixudes (~7 nm). Aquestes variacions destaquen la importància de dissenyar interfícies adaptades a les propietats específiques de cada SAM.

Aquestes diferències també es reflecteixen en el rendiment fotovoltaic, ja que SAM 5 mostra major eficiència i estabilitat, atribuïda al seu enllaç robust i empaquetament molecular uniforme, assolint una eficiència de conversió de potència (PCE) del 19,65%, comparable amb les PSCs totalment depositades al buit de l'última generació. Aquest rendiment s'atribueix al seu enllaç robust amb la superfície de l'ITO i la seua capacitat per a induir un dipol superficial favorable.

A més d'assolir una alta eficiència, els dispositius basats en SAM mostren una notable durabilitat tèrmica. Sota proves contínues a 85 °C durant 1.000 hores en atmosfera controlada de nitrogen, SAM 5 reté més del 90% de la seua eficiència inicial, en contrast amb els dispositius amb capes intermèdies tradicionals com MoO_3 i F6-TCNNQ, que es degraden després de 500 hores de prova. A més, les proves d'estabilitat també indiquen descensos mínims en FF i Voc, cosa que demostra una estabilitat robusta de la interfície durant períodes prolongats.

8.8 Capítol 4

Aquest capítol presenta una investigació sobre la deposició al buit de pel·lícules fines de perovskita, centrant-se en mètodes de co-sublimació per a la fabricació de perovskites de iodur de plom basades en FA i MA. El treball detalla els procediments experimentals, tècniques de caracterització i resultats de rendiment de dispositius per a dues composicions de perovskita, FAMAPI i MAFAPI, destacant la influència de la proporció MA/FA en el rendiment fotovoltaic i l'estabilitat.

Les capes actives s'han fabricat mitjançant co-evaporació de tres precursors: PbI_2, MAI i FAI. L'estudi requereix una especial atenció al monitoratge de les velocitats d'evaporació per als components orgànics, ja que només poden mesurar-se de manera fiable en presència de PbI_2. Les velocitats de deposició utilitzades per a MAFAPI han sigut 0,50 Å/s per a PbI_2, 0,04 Å/s per a FAI i 0,17 Å/s per a MAI, mentre que per a les pel·lícules FAMAPI han sigut 0,50 Å/s, 0,16 Å/s i 0,05 Å/s, respectivament. Aquestes composicions s'han confirmat mitjançant anàlisis EDX i ^{1}H-NMR.

La caracterització estructural ha revelat diferències entre ambdues composicions. Els difractogrames de XRD indiquen que les pel·lícules MAFAPI presenten una orientació preferencial [111], mentre que les pel·lícules FAMAPI no mostren una orientació clara. Al mateix temps, les imatges de SEM mostren que les pel·lícules MAFAPI exhibeixen grandàries de gra més grans, una característica atípica en perovskites depositades al buit. El bandgap de les pel·lícules, calculat mitjançant gràfics de Tauc, també és lleugerament major per a MAFAPI (1,55 eV) que per a FAMAPI (1,52 eV), la qual cosa pot correlacionar-se amb la menor grandària iònica del MA en comparació amb el FA.

Per a avaluar el rendiment d'aquestes pel·lícules, s'han fabricat cèl·lules solars completament evaporades amb l'estructura vidre/ITO/F6-TCNNQ/TaTm/perovskita (FAMAPI o MAFAPI)/C60/BCP/(plata)Ag. Els dispositius MAFAPI han demostrat una eficiència PCE màxima del 21,8%, significativament superior al 19,45% registrat per als dispositius FAMAPI. Aquesta millora s'atribueix principalment a un major Jsc, cosa que s'ha recolzat amb mesures d'EQE, assolint un valor màxim del 92,84 % a 720 nm per a dispositius basats en MAFAPI. Cal destacar que aquestes cèl·lules mostren una histèresi insignificant i un rendiment estable sota seguiment de MPP.

Les proves d'estabilitat durant l'emmagatzematge en foscor també han proporcionat resultats molt positius, on els dispositius MAFAPI mantenen el 90% de la seua eficiència inicial després de 1.000 hores de test en atmosfera controlada de nitrogen. La degradació existent es deu principalment a una reducció en FF i Voc, mentre que el Jsc es manté estable. Això suggereix que la major estabilitat de les pel·lícules MAFAPI podria estar vinculada a la major concentració de MA, ja que redueix la prevalença de defectes planars intergranulars, com fallades d'apilament i dislocacions. Per a comprendre millor les diferències de rendiment entre els dispositius FAMAPI i MAFAPI, s'han analitzat les corbes J-V utilitzant simulacions de drift-diffusion amb l'ajuda del programari SIMsalabim. Els resultats indiquen que les pel·lícules MAFAPI exhibeixen menors densitats de trampes per defectes en comparació amb les pel·lícules FAMAPI. Això és

consistent amb la hipòtesi que un major contingut de MA redueix els defectes estructurals, factor clau per a obtenir un superior Jsc i major eficiència.

Aquest estudi demostra el potencial dels mètodes de co-sublimació per a controlar la composició de MA i FA en pel·lícules de perovskita depositades al buit. La composició optimitzada de MAFAPI condueix a majors eficiències i millor estabilitat, assolint un 21,8%. Aquest descobriment subratlla la importància d'un ajust precís en la composició, destacant la viabilitat d'aconseguir cèl·lules de perovskita eficients i completament depositades al buit.

8.9 Capítol 5

Aquest capítol presenta un estudi sobre el desenvolupament i l'escalabilitat cap a mini-mòduls (MMs) de perovskita completament depositats al buit, amb un enfocament en l'optimització de materials, tècniques de fabricació i avaluació del rendiment. Els MMs s'han dissenyat utilitzant un mètode rendible per a connectar cèl·lules en sèrie mitjançant ablació làser. L'estudi experimental s'ha dut a terme en tres configuracions de dispositiu amb àrees actives creixents.

El procés ha constat de tres etapes diferenciades: en primer lloc, s'han fabricat cèl·lules d'àrea xicoteta (0,05 cm^2) a la Universitat de València (UVEG), utilitzades com a control per a avaluar el rendiment base (denominades *in situ*). Aquestes cèl·lules han assolit una eficiència PCE màxima del 20,29%. En segon lloc, s'han fabricat MMs de quatre cèl·lules connectades en sèrie (1 cm^2), combinant passos de processament entre dos centres d'investigació, UVEG i el Centre Interuniversitari de Microelectrònica situat a Bèlgica (IMEC). En tercer lloc, s'han processat cèl·lules de referència (0,125 cm^2) fabricades parcialment entre UVEG i IMEC (de manera idèntica als MMs), la qual cosa ha permés estudiar la degradació del rendiment durant el transport (anomenades *ex situ*). Després d'aquest anàlisi, les cèl·lules *ex situ* han mostrat una pèrdua significativa d'eficiència (~12%) a causa de la degradació de les interfícies durant el transport.

Per a abordar aquest problema, s'han investigat alternatives més robustes per a utilitzar com a transportadors de càrrega, com ara l'ús de SAMs depositades al buit i SnO_2 depositat per ALD. Basant-nos en l'optimització del capítol 3, s'ha investigat la viabilitat de tres tipus de HTLs: SAM 5, TaTm i un SAM derivat del carbazol àmpliament utilitzat en literatura (MeO-2PACz). Aquests materials han sigut seleccionats pel seu alt potencial per a millorar l'estabilitat interfacial, la uniformitat i la durabilitat general del dispositiu. Els resultats han corroborat que les SAMs depositades al buit proporcionen una cobertura uniforme i milloren la reproductibilitat en comparació amb les capes processades en dissolució. Com a dada rellevant, les cèl·lules d'àrea xicoteta **in situ** fabricades amb HTLs basades en SAM mostren una millor estabilitat tèrmica, mantenint la seua eficiència sota proves d'estrès a 85 °C.

Les anàlisis estructurals i morfològiques també han revelat que les SAMs depositades al buit milloren la qualitat de les pel·lícules de perovskita, promovent un creixement de

gra més gran i reduint la densitat de defectes. A més, els dispositius basats en SAM mostren pèrdues *ex situ* mínimes (~10%) i mantenen una alta eficiència després de 500 hores d'emmagatzematge en la foscor.

Una vegada comprovada l'estabilitat, l'optimització dels paràmetres d'ablació làser ha sigut crítica per a aconseguir alts valors de FF geomètric (GFF) i minimitzar l'àrea inactiva existent en els MMs. De fet, mitjançant ablació precisa s'aconsegueixen interconnexions eficients sense danyar les capes crítiques del dispositiu, preservant la seua integritat durant el procés d'escalabilitat. D'aquesta manera, s'ha aconseguit un GFF del 99%, amb pèrdues mínimes de rendiment.

Per a millorar encara més l'estabilitat del dispositiu, s'han fabricat MMs basats en FAMAPI. Mitjançant anàlisis ^{1}H-NMR s'ha verificat el control precís de les proporcions de MA i FA en les composicions de perovskita, assegurant la reproductibilitat i la formació de pel·lícules d'alta qualitat, en concordança amb les mesures òptiques del bandgap. També s'ha optat per incorporar SnO_2 depositat per ALD com a ETL i encapsulant, cosa que ha millorat encara més l'estabilitat del dispositiu, reduint la degradació *ex situ* durant el transport. En concret, s'ha demostrat una transició des de cèl·lules d'àrea xicoteta a MMs amb pèrdues mínimes d'eficiència: la cèl·lula *ex situ* ha assolit un PCE del 18,37%, mentre que el MM corresponent ha aconseguit una eficiència d'obertura del 17,45%, reflectint una pèrdua de tan sols ~3,3% durant l'escalabilitat.

A més, els MMs han mostrat un rendiment estable amb una degradació insignificant, retenint el 98% de la seua eficiència inicial després de 500 hores d'emmagatzematge en atmosfera inerta de nitrogen. Alhora, s'han fabricat mini-mòduls semitransparents (STMMs), substituint l'elèctrode opac de coure per ITO depositat per polvorització catòdica, aconseguint una eficiència del 15,69% amb un GFF del 99%. Malgrat la major resistència lateral de l'ITO, la minimització de les regions inactives mitjançant gravat làser òptim ha permés pèrdues d'escalabilitat mínimes, pròximes al ~1,6%.

8.10 Conclusió

En resum, aquesta tesi, titulada **"Interfícies i Connexions en Cèl·lules Solars de Perovskita Basades en Buit,"** s'ha centrat en abordar els desafiaments crítics en les PSCs depositades al buit, específicament en termes d'estabilitat, eficiència i escalabilitat. L'enfocament seguit inclou l'optimització d'interfícies, la millora de l'eficiència de la cèl·lula i l'optimització de les connexions necessàries per a generar mini-mòduls eficients i estables.

S'ha prestat especial atenció a la interfície ITO/HTL, identificada com un coll de botella crític per a aconseguir estabilitat en dispositius amb arquitectura p-i-n. Emprant materials alternatius basats en SAMs, s'ha aconseguit una millora significativa en l'estabilitat general del dispositiu. A més, modificant la composició de la perovskita, també s'ha reduït amb èxit la densitat de defectes cristal·lins, augmentant així l'eficiència

final del dispositiu. Aquest treball també ha demostrat pèrdues mínimes a l'hora d'escalar l'àrea activa dels dispositius, destacant el potencial de les tècniques de deposició al buit per a la fabricació de cèl·lules d'alt rendiment.

Capítol 3: Enginyeria de contactes -p estables per a cèl·lules solars de perovskita completament depositades al buit

En aquest capítol, hem introduït diverses SAMs d'estructura simple, no conjugada, com a capes intermèdies per a la interfície ITO/HTL. Aquests materials proporcionen una alta funció de treball en l'ITO, ideals per a utilitzar com a contactes de tipus -p en combinació amb semiconductors intrínsecs sublimables (TaTm). L'objectiu principal de l'estudi és precisament evitar l'ús de dopants químics, un factor limitant en l'estabilitat de les cèl·lules solars preparades completament per evaporació. Per a això, s'incorpora en el procés de rentada i preparació de l'elèctrode un últim pas de recobriment per immersió en etanol no nociu, amb el resultat de minimitzar la barrera energètica respecte al TaTm, cosa que resulta en una millora de l'eficiència i l'estabilitat. Cal destacar que la integració d'aquests elèctrodes modificats preserva l'estabilitat del FF al llarg del temps. Aquesta modificació d'interfície, senzilla però efectiva, ha permés fabricar cèl·lules solars de $MAPbI_3$ completament evaporades amb una PCE superior al 19%, mantenint el 90% de l'eficiència inicial després de més de 1.000 hores d'estrès tèrmic.

Capítol 4: Cèl·lules solars d'alt rendiment fabricades mitjançant co-evaporació de perovskita de doble catió A

En aquest capítol, utilitzant tècniques de caracterització com EDX, NMR i SEM, hem aprofundit sobre l'efecte que el ràtio de cations A produeix en la tipologia de grans de cristall, optimitzant el procés de deposició de la capa absorbent. Els resultats fotovoltaics indiquen que una composició rica en MA pot reduir els defectes estructurals en comparació amb altres amb major contingut en FA. A més, fent ús del programari SIMsalabim, s'ha confirmat que aquesta estratègia genera menor densitat de trampes de càrrega (generalment causades per defectes cristal·lins), i mitiga encara més les pèrdues per recombinació. Aquesta és la raó del major rendiment fotovoltaic, generant un superior Jsc, arribant a aconseguir una millora notable en l'eficiència, PCE 21,83%, el valor més alt reportat fins ara per a una PSC co-evaporada, realitzada en la seua totalitat utilitzant tècniques de sublimació al buit.

Capítol 5: Co-evaporació per a mini-mòduls escalables de perovskita: un enfocament íntegrament sublimat

En aquest capítol, hem estudiat el potencial d'escalabilitat de dispositius de perovskita completament evaporats, al mateix temps que mitigàvem les pèrdues d'eficiència. Per a això, s'ha optimitzat el gravat làser de cèl·lules solars i MMs processats completament al buit. Així, s'ha fabricat un MM amb una àrea d'obertura de 4 cm^2, un GFF del 99% i una PCE del 17,45%. L'estratègia ha començat amb la recerca de HTLs estables però compatibles amb evaporació tèrmica, com ara SAMs, que han resultat ideals per a aplicacions de gran àrea. A més, s'ha substituït $MAPbI_3$ per una perovskita mixta de MA-

FA, amb l'objectiu d'obtenir un absorbent més estable i de menor bandgap. Posteriorment, s'ha integrat una capa selectiva d'electrons (ETL) compacta i repel·lent a la humitat, que al mateix temps actua com a encapsulant. La combinació d'aquestes estratègies ha permés fabricar MMs d'eficiència similar però molt més estables, que conserven el 98% de la seua eficiència inicial després de més de 500 hores d'emmagatzematge en la foscor. Amb una estratègia idèntica, s'han fabricat mini-mòduls semitransparents (STMMs), substituint l'elèctrode opac de coure per ITO depositat per polvorització catòdica suau, aconseguint una eficiència del 15,69% amb un GFF del 99%.

Aquesta tesi marca un avanç significatiu en les PSCs depositades al buit, abordant desafiaments clau en estabilitat, eficiència i escalabilitat. S'ha optimitzat la interfície ITO-HTL per a millorar l'estabilitat, s'ha ajustat la composició iònica de la perovskita per a aconseguir altes eficiències, i s'han desenvolupat mini-mòduls d'alt rendiment, demostrant la seua viabilitat a major escala. No obstant això, per a alliberar el veritable potencial que aquesta tecnologia pot aportar a la nostra societat, serà essencial avançar en l'encapsulació de mòduls, integració de dispositius i avaluació del seu cicle de vida, requisits que permeten garantir un impacte sostenible en la societat i el medi ambient.

Appendix A: List of Abbreviations

- **AFM** - Atomic Force Microscopy
- **ALD**- Atomic Layer Deposition
- **AM** - Air Mass
- **ASTM** - American Society for Testing and Materials
- **BCP** - Bathocuproine
- **CB** - Conduction Band
- **CIGS** - Copper Indium Gallium Selenide
- **CTM**- Cell to module
- **CPS** - Concentrated Solar Power
- **c-Si** - Crystalline Silicon
- **DSSCs** - Dye-Sensitized Solar Cells
- **EDX** - Energy Dispersive X-ray Spectroscopy
- **EQE** - External Quantum Efficiency
- **ETL** - Electron Transport Layer
- **FA** - Formamidinium ($CH(NH_2)_2$, CH_3NH_3)
- **FF** - Fill Factor
- **FTO** - Fluorine-Doped Tin Oxide
- **GaAs** - Gallium Arsenide
- **Gehp** - Generated Electron Hole Pairs
- **GFF** - Geometrical Fill Factor
- **HOMO** - Highest Occupied Molecular Orbital
- **HTL** - Hole Transport Layer
- **HTMs** - Hole Transport Materials
- **IEA** - International Energy Agency
- **IoT** - Internet of Things
- **IPCE** - Incident Photon to Current Efficiency
- **ISOS** - Summit on Organic Photovoltaic
- **ist** – interface traps
- **ITO** - Indium Tin Oxide
- **Jmpp** - Maximum Power Point Current
- **KE** - Kinetic Energy of the Electron
- **KP** - Kelvin Probe Technique

- **LUMO** - Lowest Unoccupied Molecular Orbital
- **MA** - Methylammonium (CH_3NH_3)
- **MAPI** - Methylammonium Lead tri-Iodide
- **MMs** - Minimodules
- **MPP** - Maximum Power Point
- **NMR** - Nuclear Magnetic Resonance Spectroscopy
- $\mathbf{n_t}$ – Bulk traps
- **OPVs** - Organic Photovoltaics
- **PCE** - Power Conversion Efficiency
- **PSCs** - Perovskite Solar Cells
- **PV** - Photovoltaics
- **QCM** - Quartz Crystal Microbalances
- **RMS** - Root Mean Square
- **SAMs** - Self-Assembled Monolayers/Molecules
- **SC** – Solar Cells
- **SEM** - Scanning Electron Microscopy
- **SRH** - Shockley-Read-Hall Recombination
- **STSC -** Semitransparent Solar Cells
- **TCO** - Transparent Conductive Oxide
- **UV-Vis** - Ultraviolet-Visible Spectroscopy
- **VD** - Vacuum Deposition
- **VD-PSCs** - Vapor-Deposited Perovskite Solar Cells
- **VB** - Valence Band
- **XPS** - X-ray Photoelectron Spectroscopy

Appendix B: List of Figures

Figure 1-1: Historical and predicted generated energy from photovoltaic technologies from1999-2030.[4] 13

Figure 1-2: Market share distribution of thin-film PV in the commercial sector (2020-2023). Adapted from reference [5] 14

Figure 1-3: a) Schematic of sun radiation towards the earth. **b)** The spectral irradiance from the sun as a black body, just outside the atmosphere (AM0) and (AM1.5G) terrestrial solar spectrum. 15

Figure 1-4: The schematic of the **a)** indirect bandgap material and **b)** direct bandgap material. 17

Figure 1-5: Different types of recombination mechanism of electron-hole pair. adapted from reference [20] 18

Figure 1-6: The potential profile of a p-i-n junction, **a)** in equilibrium state and **b)** sandwiched with extrinsic doped semiconductors and the introduction of the built-in electric field. 20

Figure 1-7: The extraction and injection mechanism in p-i-n (**left** panel) and n-i-p (**right** panel) single junction solar cell. 21

Figure 1-8: a) The maximum theoretical conversion efficiency of the solar cell base on the radiative limit as a function of its bandgap adapted from reference [28]. **b)** Different single junction photovoltaic materials efficiency based on the radiative limit adapted from reference [30] 22

Figure 1-9: The conversion loss mechanisms of a PV cell illustrated on a p–n junction diagram adapted from reference [36] 23

Figure 1-10: Perovskite unit cell for 3D structure illustration. 25

Figure 1-11: The possible A and B site cations for the perovskite based on tolerance and octahedral factor. Adapted from reference [40] 26

Figure 1-12: a) Cubic phase of $CsPbBr_3$ achieved in high temperature. **b)**Tetragonal phase in middle temperature. **c)** Orthorhombic phase of the inorganic perovskite in room temperature. 27

Figure 1-13: Illustration of bandgap change in form of is the photoluminescence for different perovskite compositions adapted from reference [45] 28

Figure 1-14: a) Schematic of size increment in MA, FA and Guanidinium cation. **b)** Compositional mapping of cation degradation gained with thermogravimetry analysis (TGA) for the cations at 200C based on their thermal degradation rate adapted from reference [48] **c)** Perovskite crystal stability factor for hybrid lead halide composition of $MA_{1-x}FA_xPbI_3$, considering $0.3 < x < 0.8$ shows the greatest structural stability in cubic phase adapted from reference [49] 29

Figure 1-15: Best solar cell efficiencies chart throughout years of research with focus on emerging photovoltaics adapted from NREL website. 30

Figure 1-16: Best solar cell efficiencies chart throughout years of research with focus on emerging photovoltaics adapted from NREL website. 31

Figure 1-17: The comparison of perovskite and silicon solar cells golden triangle of solar cells, cost, efficiency, and stability. The cost has been considered for the silicon wafer, cell processing, and module assembly however the perovskite is an estimation because it still has not entered the market. 32

Figure 1-18: Various solution-based fabrication methods of the perovskite solar cell adapted from reference[65] 34

Figure 1-19: a) Flash evaporation or single source thermal vacuum deposition. **b)** Co-evaporation of a double source perovskite. **c)** Sequential vacuum deposition of the perovskite. 35

Figure 1-20: Evaporated perovskite active layer deposited on the textured silicon as an indication of conformal coating of co-evaporation. 36

Figure 1-21: The schematic of self-assembled monolayers different parts. 37

Figure 2-1: A picture of the cleanroom environment, the gloveboxes and different thermal vacuum chambers. 42

Figure 2-2: Inside one of the vacuum chambers used for vacuum sublimation in the current thesis. 42

Figure 2-3: The molecular structure of self-assembled monolayers and common charge transport layers used in this thesis. 43

Figure 2-4: Left panel) Picture of the vacuum chamber. **Right panel)**The schematic of the evaporator sources used for the fabrication of double A-cation perovskite and their position. 44

Figure 2-5: Left) A p-i-n baseline device stack. **Right)**The improved structure used in this thesis. 45

Figure 2-6: Fully evaporated MM fabricated by the template patterning. 46

Figure 2-7: Schematic illustration of a P1,P2,P3 laser ablation pattern. 47

Figure 2-8: a) a mechanical P2 scribe, and **b)** a laser-scribed line adapted from reference.[86] 48

Figure 2-9: An example of an XRD spectra of MAPbI perovskite with excessive PbI_2 peak. 50

Figure 2-10: Scheme of the XPS rays and also the spectrum adapted from reference [91] 52

Figure 2-11: Schematic of the UV-Vis absorption measurement setup for perovskite film. 54

Figure 2-12: a) The photoluminescent spectra(purple) and the absorbance spectra(magenta) of MAPI film on glass. **b)** The optical bandgap of a MAPI film calculated by Equation 2—6 using the absorbance spectra on the panel a. 55

Figure 2-13: A Simplified equivalent circuit of a solar cell under illumination conditions. 56

Figure 2-14:: The current-voltage behavior of a solar cell under dark and illumination conditions. 57

Figure 2-15: The external quantum efficiency as the function of the wavelength and bandgap energy. _____59

Figure 3-1-a shows the chemical structures of the SAM molecules and TaTm, along with the device architecture used in this study. We selected commercially available SAMs with phosphonic acid as the anchoring group to ensure a strong, reproducible interaction with the ITO surface, as this group can form multiple stable bonds.[156] The investigated SAM molecules feature increasing levels of fluorine-terminated groups, contributing to variations in dipole moment, film coverage and packing. After modifying the ITO electrodes with SAMs deposition, they were transferred directly to the vacuum deposition system without any additional processing for the fabrication of fully evaporated stack as explained in chapter 2 in detail._____69

Figure 3-2 illustrates the changes in wettability of the ITO surface, measured by water contact angle. The contact angle (θ) of bare-ITO (UV-ozone treated) increases significantly after surface treatment, from ~ 0º to 43º for SAM 1, due to the presence of the hydrocarbon tail group. The introduction of fluorine enhances this effect, with θ reaching 50.7º for SAM 2 (1 fluorine) and 71.2º for SAM 3 (3 fluorine moieties). The most dramatic increase occurs for the aliphatic SAMs – 90º for SAM 4 and 97º for SAM 5 – indicating strong hydrophobicity at these new interfaces. This increased hydrophobicity is noteworthy because polar hydrophilic oxides like ITO are often chemically incompatible with non-polar organic thin films.[157] Therefore the enhanced surface hydrophobicity improves direct electrical contact with TaTm, reducing the risk of delamination of the upper organic. Additionally **Figure 3-2** presents the 3D scan images and root mean square (RMS) roughness data for the same contacts, measured by AFM. The RMS roughness of the bare-ITO surface remains relatively unchanged after different monolayers deposition (3.6 nm to 4.7 nm), indicating a uniform and flat surface without significant island formation. However, there is a complete transformation in the energy landscape of the interfaces. _____69

Figure 3-3: a) High resolution P 2p, O 1 s, and In 3d XPS spectra of SAMs 1- 5 deposited on ITO (1×1)cm^2. The intensity of the In 3d signals for SAMs 1-3 have been multiplied by a factor of 10^3. **b)** Schematic sketch of the binding configurations of phosphonic acids to oxide surfaces. The label shows each type of oxygen chemical environment in a different color, with the theoretical intensity ratio of the O 1s components in brackets. _____72

Figure 3-4: XPS spectra of **a)**P 2p,**b)** O 1s and obtained for SAMs 1-5 in powder state. **c)**The F 1s spectra for the powder and thin films for F containing SAMs. _____73

Figure 3-5: a) XRD patterns, **b)** UV-Vis optical absorption and PL spectra, of co-sublimed perovskite films. **c)** J–V and **d)** EQE curves obtained for the reference vacuum deposited p-i-n PSCs, under 100 mW/cm^2 illumination. **e)** Statistical analysis of photovoltaic parameters obtained for cells containing SAM-modified ITO interfaces. _75

Figure 3-6: Statistical data for PCE, Voc, Jsc and FF obtained from more than 100 cells (at least 23 cells per condition) prepared with the different interlayers investigated in this

study. The top bar shows the maximum value, the bottom bar shows the minimum value, and the rectangle shows the region containing 25–75% of the data, obtained for each condition. _____77

Figure 3-7: Thickness optimization for TaTm using **a.** SAM 2 and **b.** SAM 3 as interlayer. The data include typical J–V curves obtained for each condition, including the forward and reverse scans. It also contains statistical data for PCE, V_{oc}, J_{sc} and FF obtained from a minimum of 50 cells (at least 16 cells per condition). The top bar shows the maximum value, the bottom bar shows the minimum value, and the rectangle shows the region containing 25–75% of the data, obtained for each condition. _____78

Figure 3-8: Thickness optimization for TaTm using SAM 5 as interlayer. The data include typical J–V curves obtained for each condition, including the forward and reverse scans. It also contains statistical data for PCE, V_{oc}, J_{sc} and FF obtained from more than 70 cells (at least 13 cells per condition). The top bar shows the maximum value, the bottom bar shows the minimum value, and the rectangle shows the region containing 25–75% of the data, obtained for each condition. _____79

Figure 3-9: a) J-V and **b)** EQE curves of the champion cells using SAM 2, 3, and 5. **c)** Device stability under continuous thermal stress at 85 ºC, measured in N_2 atmosphere. _____80

Figure 3-10: J-V scans obtained under forward and reverse bias of (-0.2 to 1.2V), for the champion cells containing SAM 2, SAM 3 and SAM 5 as interlayers. _____81

Figure 3-11: a) Thermal stability test of $MAPbI_3$ PSCs at 85 °C containing reference interlayers, MoO_3 and F6-TCNNQ. The dashed line indicates the value for 90 % drop of initial efficiency. **b)** Photovoltaic parameters of the champion cells for 1000h under heating temperature of 85˚C in N_2 atmosphere. _____82

Figure 4-1: The ^{1}H-NMR spectra of **a)** MAFAPI and **b)**FAMAPI perovskite film dissolved in d-DMSO with the attribution of each proton. _____89

Figure 4-2: the ^{1}H-NMR spectra of the commercial FAI powder indicating the protons in accordance with Figure 4-1 symbolization. _____90

Figure 4-3: a) XRD pattern of the FAMAPI and MAFAPI perovskite films and the reference of single A-cation counterparts. **b)** Schematic of the device structure. **c)** SEM image of the cross section of a fully evaporated solar cell using MAFAPI as the absorber layer. The different layers in the cross section are identified with colors and are correlated to the device layout scheme depicted in panel b. _____91

Figure 4-4: The band gap of FAMAPI and MAFAPI perovskite measured by direct bandgap Tauc plot. _____92

Figure 4-5: Characterization of the MAFAPI solar cell while illuminated at 1 sun intensity. **a)** The J-V curve under illumination on forward (solid line) reverse (dotted line) and power output of the device (right axis). **b)** The external quantum efficiency (left axis) and integrated short circuit current density (right axis). **c)** The mpp tracking of the cell and applied voltage at Vmpp obtained from a panel. **d)** The band gap of FAMAPI, Eg= 1.513 calculated by EQE derivative (solid line) and Eg= 1.520 Tauc-plot (dotted line)

calculations compared to the band gap of the MAFAPI Eg=1.555 calculated by EQE derivative and Eg= 1.550 by Tauc-plot calculations. _____94

Figure 4-6: shelf-life of the fully evaporated MAFAPI PSC **a)**The PCE **b)** The V_{oc} **c)** The J_{sc}. **d)** The FF evolution over 1000 hours storage in the glovebox in the dark. _____95

Figure 4-7: **a)** Experimental and fitted JV curves for MAFAPI and FAMAPI devices. **b)** The bulk trap density required to enable a fit with an RMS below 2 %. _____97

Figure 4-8: The ^{1}H-NMR Spectra of the FAMAPI with the estimated ratios of the cations._____98

Figure 4-9: The ^{1}H-NMR Spectra of the MAFAPI with the estimated ratios of the cations._____98

Figure 5-1: a) Different solar cell device layouts used in this chapter with their respective active areas of each cell. **b)** The schematic of a MM device stack fabricated by laser scribing with a zoomed-in SEM image of the area distance between P1 to P3. **c)** J-V sweep and photovoltaic parameters of cell of ex situ of 0.125 cm^2 and MM with an inset of mpp tracking of the cell and module. _____ 105

Figure 5-2: The XPS spectra of SAM 5 from top to bottom from vacuum deposited, solution deposited or powder from left to right of F 1s, O 1s, P 2p, and In 3d. _____ 106

Figure 5-3: The distribution of grain sizes for **a)** cross section and **b)** top view SEM of co-evaporated perovskite on evaporated SAM 5/ TaTm and C-SAM._____ 107

Figure 5-4: a) The device configuration for SAM 5/TaTm. **b)** The device configuration for C-SAM. **c** to **f)** The distribution of PV parameters for evaporated and solution-processed SAMs in 3x3 cm^2 with 16-pixel devices, each with an active area of 0.05 cm^2. _____ 108

Figure 5-5: a) EQE and integrated current density. **b)** The current-voltage graph of the champion solution processed and evaporated SAM 5/TaTm and C-SAM. _____ 109

Figure 5-6: Comparison of the shelf life stability of PV parameters of solution processed (-Sol) and vacuum deposited(-Eva) SAM 5/TaTm and C-SAM interlayers. **a)** PCE with a zoomed in inset at 1000h. **b)** The Voc with a zoomed in inset. **c)** The Jsc. **d)** the FF with a zoomed in inset at 1000h. _____ 110

Figure 5-7: The thermal stability of fully evaporated stacks with alternative HTLs for 500h at 85°C._____ 111

Figure 5-8: a) The J-V curve for the ex situ cells with different evaporated HTL employed. **b)** The J-V graph of the ex situ MMs fabricated with different evaporated HTLs. The inset shows the MPP tracking of the MMs with their corresponding V_{mpp}. _____ 112

Figure 5-9: The efficiency and its decline in different stacks due to in-situ and ex-situ fabrication and the upscaling loss contributed to cell to module fabrication._____ 113

Figure 5-10: a) The UV-Vis and PL of MAPI and FAMAPI perovskite. **b)** The XRD pattern of MAPI and FAMAPI showing the shift in peaks that confirms the incorporation of FA in the structure. _____ 114

Figure 5-11: a) The optimized device structure incorporating ALD SnO_2. **b)** An actual picture of opaque MM. _____ 114

Figure 5-12: a) The ex situ cell and module J-V graph and the mpp tracking of cell and MM. **b)** The comparison of call and its corresponding module in zero hour and after 500h of storage in the dark. _____ 115

Figure 5-13: The current voltage behavior of cell and STMM of 7 series cells in a semitransparent structure with the picture of an actual cell.**Error! Bookmark not defined.**

Figure 6-1:The thermal efficiency improvement employing SAM5 in comparison to F6-TCNNQ dopant._____ 121

Figure 6-2: The fully sublimed stack and the champion J-V curve of MAFAPI solar cell achieved with it. _____ 122

Figure 6-3: The efficiency of fabricated in situ cells, ex situ cells and ex situ MMs aperture area PCE for different device stack. The first three have been employed to lower the ex situ loss (red arrow) and the last 2 for upscaling loss blue arrow._____ 123

Appendix C: List of Equations

Equation 1—1 15
Equation 1—2 26
Equation 1—3 26
Equation 2—1 45
Equation 2—2 50
Equation 2—3 51
Equation 2—4 53
Equation 2—5 54
Equation 2—6 54
Equation 2—7 56
Equation 2—8 56
Equation 2—9 57
Equation 2—10 57
Equation 2—11 57
Equation 2—12 59
Equation 2—13 60
Equation 4—1 96
Equation 5—1 112

Bibliography:

1. NASA/GISS. NASA's Goddard Institute for Space Studies (GISS).

2. Saxena, P. & Sonwani, S. Criteria Air Pollutants: Chemistry, Sources and Sinks. in *Criteria Air Pollutants and their Impact on Environmental Health* (eds. Saxena, P. & Sonwani, S.) 7–48 (Springer Singapore, Singapore, 2019). doi:10.1007/978-981-13-9992-3_2.

3. IEA (2023). Solar PV capacity additions in the Stated Policies Scenario. *https://www.iea.org/data-and-statistics/charts/solar-pv-capacity-additions-in-the-stated-policies-scenario-2015-2030, Licence: CC BY 4.0* (2023).

4. *GLOBAL PHOTOVOLTAIC POWER POTENTIAL BY COUNTRY*. https://solargis.com (2020).

5. Hannah Ritchie, Max Roser & Pablo Rosado. Renewable Energy" Published online at OurWorldinData.org. (2020).

6. *Photovoltaics Equipment International Technology Roadmap for Photovoltaics (ITRPV) 2023 Results*. https://www.vdma.org/international-technology-roadmap-photovoltaic (2024).

7. Yu, C., Xu, S., Yao, J. & Han, S. Recent Advances in and New Perspectives on Crystalline Silicon Solar Cells with Carrier-Selective Passivation Contacts. *Crystals (Basel)* **8**, (2018).

8. MA, G. *et al*. Solar cell efficiency tables (Version 61). *Prog Photovolt* **31**, 3–16 (2023).

9. Green, M. A. *et al*. Solar cell efficiency tables (Version 64). *Progress in Photovoltaics: Research and Applications* **32**, 425–441 (2024).

10. Gueymard, C. A. A reevaluation of the solar constant based on a 42-year total solar irradiance time series and a reconciliation of spaceborne observations. *Solar Energy* **168**, 2–9 (2018).

11. Perez, M. & Perez, R. Update 2022 – A fundamental look at supply side energy reserves for the planet. *Solar Energy Advances* **2**, 100014 (2022).

12. Gueymard, C. A., Myers, D. & Emery, K. Proposed reference irradiance spectra for solar energy systems testing. *Solar Energy* **73**, 443–467 (2002).

13. Standard Table for Reference Solar Spectral Distributions: Direct and Diffuse on 20° Tilted and Vertical Surfaces. *ASTM G197-14(2021)* **14.04**, 36 (2021).

14. Bird, R. E. & Riordan, C. Simple Solar Spectral Model for Direct and Diffuse Irradiance on Horizontal and Tilted Planes at the Earth's Surface for Cloudless Atmospheres. *Journal of Climate and Applied Meteorology* **25**, 87–97 (1986).

15. Nelson, J. *The Physics of Solar Cells*. (PUBLISHED BY IMPERIAL COLLEGE PRESS AND DISTRIBUTED BY WORLD SCIENTIFIC PUBLISHING CO., 2003). doi:doi:10.1142/p276.

16. Asif, A. A., Singh, R. & Alapatt, G. F. Technical and economic assessment of perovskite solar cells for large scale manufacturing. *Journal of Renewable and Sustainable Energy* **7**, 043120 (2015).

17. Gray, J. L. The Physics of the Solar Cell. in *Handbook of Photovoltaic Science and Engineering* 61–112 (2003). doi:https://doi.org/10.1002/0470014008.ch3.

18. Steinhauser, B., Niewelt, T., Richter, A., Eberle, R. & Schubert, M. C. Extraordinarily High Minority Charge Carrier Lifetime Observed in Crystalline Silicon. *Solar RRL* **5**, 2100605 (2021).

19. Guo, J. *et al.* Ultralong Carrier Lifetime Exceeding 20 μs in Lead Halide Perovskite Film Enable Efficient Solar Cells. *Advanced Materials* **35**, 2212126 (2023).

20. Xia, J., Sohail, M. & Nazeeruddin, M. K. Efficient and Stable Perovskite Solar Cells by Tailoring of Interfaces. *Advanced Materials* **35**, 2211324 (2023).

21. Guo, Z. *et al.* Understanding Defects in Perovskite Solar Cells through Computation: Current Knowledge and Future Challenge. *Advanced Science* **11**, 2305799 (2024).

22. Brandt, R. E. *et al.* Searching for "Defect-Tolerant" Photovoltaic Materials: Combined Theoretical and Experimental Screening. *Chemistry of Materials* **29**, 4667–4674 (2017).

23. Aspnes, D. E., Studna, A. A. & Kinsbron, E. Dielectric properties of heavily doped crystalline and amorphous silicon from 1.5 to 6.0 eV. *Phys Rev B* **29**, 768–779 (1984).

24. Su, R. *et al.* Dielectric screening in perovskite photovoltaics. *Nat Commun* **12**, 2479 (2021).

25. Moore, W. J. & Holm, R. T. Infrared dielectric constant of gallium arsenide. *J Appl Phys* **80**, 6939–6942 (1996).

26. Simbula, A. *et al.* Exciton dissociation in 2D layered metal-halide perovskites. *Nat Commun* **14**, 4125 (2023).

27. Hirst, L. C. & Ekins-Daukes, N. J. Fundamental losses in solar cells. *Progress in Photovoltaics: Research and Applications* **19**, 286–293 (2011).

28. Rühle, S. Tabulated values of the Shockley–Queisser limit for single junction solar cells. *Solar Energy* **130**, 139–147 (2016).

29. Polman, A., Knight, M., Garnett, E. C., Ehrler, B. & Sinke, W. C. Photovoltaic materials: Present efficiencies and future challenges. *Science (1979)* **352**, aad4424 (2016).

30. Ehrler, B. *et al.* Photovoltaics Reaching for the Shockley–Queisser Limit. *ACS Energy Lett* **5**, 3029–3033 (2020).

31. Wolff, C. M., Caprioglio, P., Stolterfoht, M. & Neher, D. Nonradiative Recombination in Perovskite Solar Cells: The Role of Interfaces. *Advanced Materials* **31**, 1902762 (2019).

32. Shen, L., Li, Z. & Ma, T. Analysis of the power loss and quantification of the energy distribution in PV module. *Appl Energy* **260**, 114333 (2020).

33. Wang, A. & Xuan, Y. A detailed study on loss processes in solar cells. *Energy* **144**, 490–500 (2018).

34. Oni, A. M., Mohsin, A. S. M., Rahman, Md. M. & Hossain Bhuian, M. B. A comprehensive evaluation of solar cell technologies, associated loss mechanisms, and efficiency enhancement strategies for photovoltaic cells. *Energy Reports* **11**, 3345–3366 (2024).

35. Abdullah, M. F. *et al*. Research and development efforts on texturization to reduce the optical losses at front surface of silicon solar cell. *Renewable and Sustainable Energy Reviews* **66**, 380–398 (2016).

36. Dupré, O., Vaillon, R. & Green, M. A. A full thermal model for photovoltaic devices. *Solar Energy* **140**, 73–82 (2016).

37. Chakhmouradian, A. R. & Woodward, P. M. Celebrating 175 years of perovskite research: a tribute to Roger H. Mitchell. *Phys Chem Miner* **41**, 387–391 (2014).

38. Li, C. *et al*. Formability of ABX 3 (X = F, Cl, Br, I) halide perovskites. *Acta Crystallographica Section B* **64**, 702–707 (2008).

39. Goldschmidt, V. M. Die Gesetze der Krystallochemie. *Naturwissenschaften* **14**, 477–485 (1926).

40. Chen, X., Cheng, S., Xiao, L. & Sun, H. Identifying, understanding and controlling defects and traps in halide perovskites for optoelectronic devices: a review. *J Phys D Appl Phys* **53**, 373001 (2020).

41. Xu, L., Yuan, S., Zeng, H. & Song, J. A comprehensive review of doping in perovskite nanocrystals/quantum dots: evolution of structure, electronics, optics, and light-emitting diodes. *Mater Today Nano* **6**, 100036 (2019).

42. Hoffman, A. E. J. *et al*. Understanding the phase transition mechanism in the lead halide perovskite CsPbBr3 via theoretical and experimental GIWAXS and Raman spectroscopy. *APL Mater* **11**, 041124 (2023).

43. He, Y. *et al*. High spectral resolution of gamma-rays at room temperature by perovskite CsPbBr3 single crystals. *Nat Commun* **9**, 1609 (2018).

44. Tao, S. *et al*. Absolute energy level positions in tin- and lead-based halide perovskites. *Nat Commun* **10**, 2560 (2019).

45. Gholipour, S. & Saliba, M. Chapter 1 - Bandgap tuning and compositional exchange for lead halide perovskite materials. in *Characterization Techniques for Perovskite Solar Cell Materials* (eds. Pazoki, M., Hagfeldt, A. & Edvinsson, T.) 1–22 (Elsevier, 2020). doi:https://doi.org/10.1016/B978-0-12-814727-6.00001-3.

46. Lee, J.-W., Tan, S., Seok, S. Il, Yang, Y. & Park, N.-G. Rethinking the A cation in halide perovskites. *Science (1979)* **375**, eabj1186 (2024).

47. Moeini, A. *et al*. Semitransparent near-infrared Sn–Pb hybrid perovskite photodetectors. *J Mater Chem C Mater* **10**, 13878–13885 (2022).

48. Minussi, F. B., Silva, R. M., Carvalho, J. F. & Araújo, E. B. Thermal degradation in methylammonium–formamidinium–guanidinium lead iodide perovskites. *J Mater Chem C Mater* **12**, 5138–5149 (2024).

49. Charles, B., Dillon, J., Weber, O. J., Islam, M. S. & Weller, M. T. Understanding the stability of mixed A-cation lead iodide perovskites. *J Mater Chem A Mater* **5**, 22495–22499 (2017).

50. Green, M. A., Ho-Baillie, A. & Snaith, H. J. The emergence of perovskite solar cells. *Nat Photonics* **8**, 506–514 (2014).

51. Miyata, A. *et al*. Direct measurement of the exciton binding energy and effective masses for charge carriers in organic–inorganic tri-halide perovskites. *Nat Phys* **11**, 582–587 (2015).

52. Tanaka, K. *et al*. Comparative study on the excitons in lead-halide-based perovskite-type crystals CH3NH3PbBr3 CH3NH3PbI3. *Solid State Commun* **127**, 619–623 (2003).

53. Stranks, S. D. *et al*. Electron-Hole Diffusion Lengths Exceeding 1 Micrometer in an Organometal Trihalide Perovskite Absorber. *Science (1979)* **342**, 341–344 (2013).

54. Dong, Q. *et al*. Electron-hole diffusion lengths > 175 μm in solution-grown CH3NH3PbI3 single crystals. *Science (1979)* **347**, 967–970 (2015).

55. Yin, W.-J., Shi, T. & Yan, Y. Unusual defect physics in CH3NH3PbI3 perovskite solar cell absorber. *Appl Phys Lett* **104**, 063903 (2014).

56. Kojima, A., Teshima, K., Shirai, Y. & Miyasaka, T. Organometal Halide Perovskites as Visible-Light Sensitizers for Photovoltaic Cells. *J Am Chem Soc* **131**, 6050–6051 (2009).

57. Liu, C. *et al*. Bimolecularly passivated interface enables efficient and stable inverted perovskite solar cells. *Science (1979)* **382**, 810–815 (2023).

58. Matteocci, F. *et al*. Fabrication and Morphological Characterization of High-Efficiency Blade-Coated Perovskite Solar Modules. *ACS Appl Mater Interfaces* **11**, 25195–25204 (2019).

59. Čulík, P. *et al*. Design and Cost Analysis of 100 MW Perovskite Solar Panel Manufacturing Process in Different Locations. *ACS Energy Lett* **7**, 3039–3044 (2022).

60. Meng, L., You, J. & Yang, Y. Addressing the stability issue of perovskite solar cells for commercial applications. *Nat Commun* **9**, 5265 (2018).

61. Tongwei Co. What is the cost of silicon solar cell？. (2023).

62. Ke, W. & Kanatzidis, M. G. Prospects for low-toxicity lead-free perovskite solar cells. *Nat Commun* **10**, 965 (2019).

63. Du, P. *et al*. Thermal Evaporation for Halide Perovskite Optoelectronics: Fundamentals, Progress, and Outlook. *Adv Opt Mater* **10**, 2101770 (2022).

64. Lee, J.-H., Kim, B. S., Park, J., Lee, J.-W. & Kim, K. Opportunities and Challenges for Perovskite Solar Cells Based on Vacuum Thermal Evaporation. *Adv Mater Technol* **8**, 2200928 (2023).

65. Bhati, N., Nazeeruddin, M. K. & Maréchal, F. Critical analysis of decision variables for high-throughput experimentation (HTE) with perovskite solar cells. *Solar Energy* **262**, 111810 (2023).

66. Mitzi, D. B., Prikas, M. T. & Chondroudis, K. Thin Film Deposition of Organic−Inorganic Hybrid Materials Using a Single Source Thermal Ablation Technique. *Chemistry of Materials* **11**, 542–544 (1999).

67. Era, M., Hattori, T., Taira, T. & Tsutsui, T. Self-Organized Growth of PbI-Based Layered Perovskite Quantum Well by Dual-Source Vapor Deposition. *Chemistry of Materials* **9**, 8–10 (1997).

68. Leyden, M. R. *et al*. High performance perovskite solar cells by hybrid chemical vapor deposition. *J Mater Chem A Mater* **2**, 18742–18745 (2014).

69. Liu, D., Gangishetty, M. K. & Kelly, T. L. Effect of CH3NH3PbI3 thickness on device efficiency in planar heterojunction perovskite solar cells. *J Mater Chem A Mater* **2**, 19873–19881 (2014).

70. Liu, M., Johnston, M. B. & Snaith, H. J. Efficient planar heterojunction perovskite solar cells by vapour deposition. *Nature* **501**, 395–398 (2013).

71. Huang, K.-W. *et al*. Fast fabrication of μm-thick perovskite films by using a one-step doctor-blade coating method for direct X-ray detectors. *J Mater Chem C Mater* **12**, 1533–1542 (2024).

72. Momblona, C. *et al*. Efficient vacuum deposited p-i-n and n-i-p perovskite solar cells employing doped charge transport layers. *Energy Environ Sci* **9**, 3456–3463 (2016).

73. Pérez-del-Rey, D., Boix, P. P., Sessolo, M., Hadipour, A. & Bolink, H. J. Interfacial Modification for High-Efficiency Vapor-Phase-Deposited Perovskite Solar Cells Based on a Metal Oxide Buffer Layer. *J Phys Chem Lett* **9**, 1041–1046 (2018).

74. Pérez-del-Rey, D. *et al*. Molecular Passivation of MoO3: Band Alignment and Protection of Charge Transport Layers in Vacuum-Deposited Perovskite Solar Cells. *Chemistry of Materials* **31**, 6945–6949 (2019).

75. Al-Ashouri, A. *et al*. Conformal monolayer contacts with lossless interfaces for perovskite single junction and monolithic tandem solar cells. *Energy Environ Sci* **12**, 3356–3369 (2019).

76. Xue, D.-J. *et al*. Regulating strain in perovskite thin films through charge-transport layers. *Nat Commun* **11**, 1514 (2020).

77. Boyd, C. C., Cheacharoen, R., Leijtens, T. & McGehee, M. D. Understanding Degradation Mechanisms and Improving Stability of Perovskite Photovoltaics. *Chem Rev* **119**, 3418–3451 (2019).

78. Zhang, D., Li, D., Hu, Y., Mei, A. & Han, H. Degradation pathways in perovskite solar cells and how to meet international standards. *Commun Mater* **3**, 58 (2022).

79. Kim, B.-S., Gil-Escrig, L., Sessolo, M. & Bolink, H. J. Deposition Kinetics and Compositional Control of Vacuum-Processed CH3NH3PbI3 Perovskite. *J Phys Chem Lett* **11**, 6852–6859 (2020).

80. Walter, D., Peng, J., Weber, K., Catchpole, K. R. & White, T. P. Performance limitations imposed by the TCO heterojunction in high efficiency perovskite solar cells. *Energy Environ Sci* **15**, 5202–5216 (2022).

81. Galagan, Y., Coenen, E. W. C., Verhees, W. J. H. & Andriessen, R. Towards the scaling up of perovskite solar cells and modules. *J Mater Chem A Mater* **4**, 5700–5705 (2016).

82. Merckx, T. *et al*. Stable Device Architecture With Industrially Scalable Processes for Realizing Efficient 784 cm2 Monolithic Perovskite Solar Modules. *IEEE J Photovolt* **13**, 419–421 (2023).

83. Li, Z. *et al*. Ammonia for post-healing of formamidinium-based Perovskite films. *Nat Commun* **13**, 4417 (2022).

84. Castro, D., Duarte, V. C. M. & Andrade, L. Perovskite Solar Modules: Design Optimization. *ACS Omega* **7**, 40844–40852 (2022).

85. Li, J. *et al*. Highly Efficient Thermally Co-evaporated Perovskite Solar Cells and Mini-modules. *Joule* **4**, 1035–1053 (2020).

86. Jamaatisomarin, F., Chen, R., Hosseini-Zavareh, S. & Lei, S. Laser Scribing of Photovoltaic Solar Thin Films: A Review. *Journal of Manufacturing and Materials Processing* **7**, (2023).

87. Seo, S., Jeong, S., Park, H., Shin, H. & Park, N.-G. Atomic layer deposition for efficient and stable perovskite solar cells. *Chemical Communications* **55**, 2403–2416 (2019).

88. Raval, N. *et al*. Chapter 10 - Importance of Physicochemical Characterization of Nanoparticles in Pharmaceutical Product Development. in *Basic Fundamentals of Drug Delivery* (ed. Tekade, R. K.) 369–400 (Academic Press, 2019). doi:https://doi.org/10.1016/B978-0-12-817909-3.00010-8.

89. Baer, D. R. & Thevuthasan, S. Chapter 16 - Characterization of Thin Films and Coatings. in *Handbook of Deposition Technologies for Films and Coatings (Third Edition)* (ed. Martin, P. M.) 749–864 (William Andrew Publishing, Boston, 2010). doi:https://doi.org/10.1016/B978-0-8155-2031-3.00016-8.

90. Stevie, F. A. & Donley, C. L. Introduction to x-ray photoelectron spectroscopy. *Journal of Vacuum Science & Technology A* **38**, 063204 (2020).

91. ChemViews. X-Ray Photoelectron Spectroscopy (XPS). *ChemViews* (2017) doi:10.1002/chemv.201700006.

92. Abdi-Jalebi, M., Ibrahim Dar, M., Sadhanala, A., Johansson, E. M. J. & Pazoki, M. Chapter 3 - Optical absorption and photoluminescence spectroscopy. in *Characterization Techniques for Perovskite Solar Cell Materials* (eds. Pazoki, M., Hagfeldt, A. & Edvinsson, T.) 49–79 (Elsevier, 2020). doi:https://doi.org/10.1016/B978-0-12-814727-6.00003-7.

93. Tauc, J., Grigorovici, R. & Vancu, A. Optical Properties and Electronic Structure of Amorphous Germanium. *physica status solidi (b)* **15**, 627–637 (1966).

94. Davis, E. A. & Mott, N. F. Conduction in non-crystalline systems V. Conductivity, optical absorption and photoconductivity in amorphous semiconductors. *The Philosophical Magazine: A Journal of Theoretical Experimental and Applied Physics* **22**, 903–922 (1970).

95. Makuła, P., Pacia, M. & Macyk, W. How To Correctly Determine the Band Gap Energy of Modified Semiconductor Photocatalysts Based on UV–Vis Spectra. *J Phys Chem Lett* **9**, 6814–6817 (2018).

96. Yin, H., Zadshir, M. & Pao, F. 2 - Fundamentals of BIPVT design and integration. in *Building Integrated Photovoltaic Thermal Systems* (eds. Yin, H., Zadshir, M. & Pao, F.) 45–129 (Academic Press, 2022). doi:https://doi.org/10.1016/B978-0-12-821064-2.00003-1.

97. Shockley, W. The theory of p-n junctions in semiconductors and p-n junction transistors. *The Bell System Technical Journal* **28**, 435–489 (1949).

98. Dongaonkar, S. *et al*. Universality of non-Ohmic shunt leakage in thin-film solar cells. *J Appl Phys* **108**, 124509 (2010).

99. Fong, K. C., McIntosh, K. R. & Blakers, A. W. Accurate series resistance measurement of solar cells. *Progress in Photovoltaics: Research and Applications* **21**, 490–499 (2013).

100. Mundhaas, N. *et al*. Series Resistance Measurements of Perovskite Solar Cells Using J–V Measurements. *Solar RRL* **3**, 1800378 (2019).

101. Saliba, M. & Etgar, L. Current Density Mismatch in Perovskite Solar Cells. *ACS Energy Lett* **5**, 2886–2888 (2020).

102. Saliba, M., Unger, E., Etgar, L., Luo, J. & Jacobsson, T. J. A systematic discrepancy between the short circuit current and the integrated quantum efficiency in perovskite solar cells. *Nat Commun* **14**, 5445 (2023).

103. Chen, B., Yang, M., Priya, S. & Zhu, K. Origin of J–V Hysteresis in Perovskite Solar Cells. *J Phys Chem Lett* **7**, 905–917 (2016).

104. Wali, Q. *et al*. Fundamentals of Hysteresis in Perovskite Solar Cells: From Structure-Property Relationship to Neoteric Breakthroughs. *The Chemical Record* **22**, e202100150 (2022).

105. Holzhey, P. & Saliba, M. A full overview of international standards assessing the long-term stability of perovskite solar cells. *J Mater Chem A Mater* **6**, 21794–21808 (2018).

106. Khenkin, M. V *et al*. Consensus statement for stability assessment and reporting for perovskite photovoltaics based on ISOS procedures. *Nat Energy* **5**, 35–49 (2020).

107. Fan, Z. *et al*. Layer-by-Layer Degradation of Methylammonium Lead Tri-iodide Perovskite Microplates. *Joule* **1**, 548–562 (2017).

108. Kranthiraja, K. *et al*. Stability and degradation in triple cation and methyl ammonium lead iodide perovskite solar cells mediated via Au and Ag electrodes. *Sci Rep* **12**, 18574 (2022).

109. Green, M. A. *et al*. Solar cell efficiency tables (version 54). *Progress in Photovoltaics: Research and Applications* **27**, 565–575 (2019).

110. Stranks, S. D. & Snaith, H. J. Metal-halide perovskites for photovoltaic and light-emitting devices. *Nat Nanotechnol* **10**, 391–402 (2015).

111. D'Innocenzo, V. *et al*. Excitons versus free charges in organo-lead tri-halide perovskites. *Nat Commun* **5**, 3586 (2014).

112. Rehman, W. *et al*. Photovoltaic mixed-cation lead mixed-halide perovskites: links between crystallinity, photo-stability and electronic properties. *Energy Environ Sci* **10**, 361–369 (2017).

113. McMeekin, D. P. *et al*. A mixed-cation lead mixed-halide perovskite absorber for tandem solar cells. *Science (1979)* **351**, 151–155 (2016).

114. Liu, C. *et al*. Bimolecularly passivated interface enables efficient and stable inverted perovskite solar cells. *Science (1979)* **382**, 810–815 (2023).

115. Park, N.-G. & Zhu, K. Scalable fabrication and coating methods for perovskite solar cells and solar modules. *Nat Rev Mater* **5**, 333–350 (2020).

116. Hu, H. *et al*. Room-Temperature Meniscus Coating of >20% Perovskite Solar Cells: A Film Formation Mechanism Investigation. *Adv Funct Mater* **29**, 1900092 (2019).

117. Deng, Y. *et al*. Surfactant-controlled ink drying enables high-speed deposition of perovskite films for efficient photovoltaic modules. *Nat Energy* **3**, 560–566 (2018).

118. Park, M. *et al*. Highly Reproducible Large-Area Perovskite Solar Cell Fabrication via Continuous Megasonic Spray Coating of CH3NH3PbI3. *Small* **15**, 1804005 (2019).

119. Karunakaran, S. K. *et al*. Recent progress in inkjet-printed solar cells. *J Mater Chem A Mater* **7**, 13873–13902 (2019).

120. Kim, Y. Y. *et al.* Roll-to-roll gravure-printed flexible perovskite solar cells using eco-friendly antisolvent bathing with wide processing window. *Nat Commun* **11**, 5146 (2020).

121. Huang, F., Li, M., Siffalovic, P., Cao, G. & Tian, J. From scalable solution fabrication of perovskite films towards commercialization of solar cells. *Energy Environ Sci* **12**, 518–549 (2019).

122. Vidal, R. *et al.* Assessing health and environmental impacts of solvents for producing perovskite solar cells. *Nat Sustain* **4**, 277–285 (2021).

123. Li, J. *et al.* Highly Efficient Thermally Co-evaporated Perovskite Solar Cells and Mini-modules. *Joule* **4**, 1035–1053 (2020).

124. Vaynzof, Y. The Future of Perovskite Photovoltaics—Thermal Evaporation or Solution Processing? *Adv Energy Mater* **10**, 2003073 (2020).

125. Ávila, J., Momblona, C., Boix, P. P., Sessolo, M. & Bolink, H. J. Vapor-Deposited Perovskites: The Route to High-Performance Solar Cell Production? *Joule* **1**, 431–442 (2017).

126. Kottokkaran, R., Gaonkar, H. A., Abbas, H. A., Noack, M. & Dalal, V. Performance and stability of co-evaporated vapor deposited perovskite solar cells. *Journal of Materials Science: Materials in Electronics* **30**, 5487–5494 (2019).

127. Pham, H. D. *et al.* Organic interfacial materials for perovskite-based optoelectronic devices. *Energy Environ Sci* **12**, 1177–1209 (2019).

128. Avila, J. *et al.* Influence of doped charge transport layers on efficient perovskite solar cells. *Sustain Energy Fuels* **2**, 2429–2434 (2018).

129. Li, H. *et al.* Sequential vacuum-evaporated perovskite solar cells with more than 24% efficiency. *Sci Adv* **8**, eabo7422 (2024).

130. Pérez-del-Rey, D., Boix, P. P., Sessolo, M., Hadipour, A. & Bolink, H. J. Interfacial Modification for High-Efficiency Vapor-Phase-Deposited Perovskite Solar Cells Based on a Metal Oxide Buffer Layer. *J Phys Chem Lett* **9**, 1041–1046 (2018).

131. Lohmann, K. B. *et al.* Solvent-Free Method for Defect Reduction and Improved Performance of p-i-n Vapor-Deposited Perovskite Solar Cells. *ACS Energy Lett* **7**, 1903–1911 (2022).

132. Zuo, C. & Ding, L. Solution-Processed Cu2O and CuO as Hole Transport Materials for Efficient Perovskite Solar Cells. *Small* **11**, 5528–5532 (2015).

133. Bai, S. *et al.* Planar perovskite solar cells with long-term stability using ionic liquid additives. *Nature* **571**, 245–250 (2019).

134. Tseng, Z.-L. *et al.* Efficient inverted-type perovskite solar cells using UV-ozone treated MoOx and WOx as hole transporting layers. *Solar Energy* **139**, 484–488 (2016).

135. Boyd, C. C. *et al*. Overcoming Redox Reactions at Perovskite-Nickel Oxide Interfaces to Boost Voltages in Perovskite Solar Cells. *Joule* **4**, 1759–1775 (2020).

136. Olthof, S. & Meerholz, K. Substrate-dependent electronic structure and film formation of MAPbI3 perovskites. *Sci Rep* **7**, 40267 (2017).

137. Abzieher, T. *et al*. Electron-Beam-Evaporated Nickel Oxide Hole Transport Layers for Perovskite-Based Photovoltaics. *Adv Energy Mater* **9**, 1802995 (2019).

138. Schloemer, T. H., Christians, J. A., Luther, J. M. & Sellinger, A. Doping strategies for small molecule organic hole-transport materials: impacts on perovskite solar cell performance and stability. *Chem Sci* **10**, 1904–1935 (2019).

139. Polander, L. E. *et al*. Hole-transport material variation in fully vacuum deposited perovskite solar cells. *APL Mater* **2**, 081503 (2014).

140. Susic, I. *et al*. Intrinsic Organic Semiconductors as Hole Transport Layers in p–i–n Perovskite Solar Cells. *Solar RRL* **6**, 2100882 (2022).

141. Abzieher, T. *et al*. From Groundwork to Efficient Solar Cells: On the Importance of the Substrate Material in Co-Evaporated Perovskite Solar Cells. *Adv Funct Mater* **31**, 2104482 (2021).

142. Gil-Escrig, L. *et al*. Efficient and Thermally Stable Wide Bandgap Perovskite Solar Cells by Dual-Source Vacuum Deposition. *Adv Funct Mater* **33**, 2214357 (2023).

143. Babaei, A. *et al*. Efficient Vacuum Deposited P-I-N Perovskite Solar Cells by Front Contact Optimization. *Front Chem* **7**, (2020).

144. Shin, S. S., Lee, S. J. & Seok, S. Il. Metal Oxide Charge Transport Layers for Efficient and Stable Perovskite Solar Cells. *Adv Funct Mater* **29**, 1900455 (2019).

145. Schloemer, T. H. *et al*. The Molybdenum Oxide Interface Limits the High-Temperature Operational Stability of Unencapsulated Perovskite Solar Cells. *ACS Energy Lett* **5**, 2349–2360 (2020).

146. Choi, Y. *et al*. Toward All-Vacuum-Processable Perovskite Solar Cells with High Efficiency, Stability, and Scalability Enabled by Fluorinated Spiro-OMeTAD through Thermal Evaporation. *Solar RRL* **5**, 2100415 (2021).

147. Arivazhagan, V. *et al*. All-vacuum deposited and thermally stable perovskite solar cells with F4-TCNQ/CuPc hole transport layer. *Nanotechnology* **31**, 065401 (2020).

148. Lin, D. *et al*. Stable and scalable 3D-2D planar heterojunction perovskite solar cells via vapor deposition. *Nano Energy* **59**, 619–625 (2019).

149. Chiang, Y.-H. *et al*. Vacuum-Deposited Wide-Bandgap Perovskite for All-Perovskite Tandem Solar Cells. *ACS Energy Lett* **8**, 2728–2737 (2023).

150. Aktas, E. *et al*. Understanding the perovskite/self-assembled selective contact interface for ultra-stable and highly efficient p–i–n perovskite solar cells. *Energy Environ Sci* **14**, 3976–3985 (2021).

151. Farag, A. *et al*. Evaporated Self-Assembled Monolayer Hole Transport Layers: Lossless Interfaces in p-i-n Perovskite Solar Cells. *Adv Energy Mater* **13**, 2203982 (2023).

152. Jiang, W. *et al*. π-Expanded Carbazoles as Hole-Selective Self-Assembled Monolayers for High-Performance Perovskite Solar Cells. *Angewandte Chemie International Edition* **61**, e202213560 (2022).

153. Magomedov, A. *et al*. Self-Assembled Hole Transporting Monolayer for Highly Efficient Perovskite Solar Cells. *Adv Energy Mater* **8**, 1801892 (2018).

154. Gu, Z. *et al*. Interfacial engineering of self-assembled monolayer modified semi-roll-to-roll planar heterojunction perovskite solar cells on flexible substrates. *J Mater Chem A Mater* **3**, 24254–24260 (2015).

155. Liu, L. *et al*. Fully Printable Mesoscopic Perovskite Solar Cells with Organic Silane Self-Assembled Monolayer. *J Am Chem Soc* **137**, 1790–1793 (2015).

156. Hotchkiss, P. J. *et al*. The Modification of Indium Tin Oxide with Phosphonic Acids: Mechanism of Binding, Tuning of Surface Properties, and Potential for Use in Organic Electronic Applications. *Acc Chem Res* **45**, 337–346 (2012).

157. Isikgor, F. H. *et al*. Molecular engineering of contact interfaces for high-performance perovskite solar cells. *Nat Rev Mater* **8**, 89–108 (2023).

158. Dänekamp, B. *et al*. Influence of hole transport material ionization energy on the performance of perovskite solar cells. *J Mater Chem C Mater* **7**, 523–527 (2019).

159. Kröger, M. *et al*. Role of the deep-lying electronic states of MoO3 in the enhancement of hole-injection in organic thin films. *Appl Phys Lett* **95**, 123301 (2009).

160. Schulz, P. *et al*. High-Work-Function Molybdenum Oxide Hole Extraction Contacts in Hybrid Organic–Inorganic Perovskite Solar Cells. *ACS Appl Mater Interfaces* **8**, 31491–31499 (2016).

161. Paniagua, S. A. *et al*. Phosphonic Acid Modification of Indium−Tin Oxide Electrodes: Combined XPS/UPS/Contact Angle Studies. *The Journal of Physical Chemistry C* **112**, 7809–7817 (2008).

162. Lange, I. *et al*. Zinc oxide modified with benzylphosphonic acids as transparent electrodes in regular and inverted organic solar cell structures. *Appl Phys Lett* **106**, 113302 (2015).

163. Textor, M. *et al*. Structural Chemistry of Self-Assembled Monolayers of Octadecylphosphoric Acid on Tantalum Oxide Surfaces. *Langmuir* **16**, 3257–3271 (2000).

164. Diyuk, V. E. *et al*. Surface chemistry of fluoroalkylated nanoporous activated carbons: XPS and 19F NMR study. *Appl Nanosci* **12**, 637–650 (2022).

165. Roldán-Carmona, C. *et al*. High efficiency methylammonium lead triiodide perovskite solar cells: the relevance of non-stoichiometric precursors. *Energy Environ Sci* **8**, 3550–3556 (2015).

166. Malinkiewicz, O. *et al*. Perovskite solar cells employing organic charge-transport layers. *Nat Photonics* **8**, 128–132 (2014).

167. Ng, A. *et al*. Efficiency enhancement by defect engineering in perovskite photovoltaic cells prepared using evaporated PbI2/CH3NH3I multilayers. *J Mater Chem A Mater* **3**, 9223–9231 (2015).

168. Chen, Y., Chen, T. & Dai, L. Layer-by-Layer Growth of CH3NH3PbI3−Cl for Highly Efficient Planar Heterojunction Perovskite Solar Cells. *Advanced Materials* **27**, 1053–1059 (2015).

169. Kam, M. *et al*. Efficient Mixed-Cation Mixed-Halide Perovskite Solar Cells by All-Vacuum Sequential Deposition Using Metal Oxide Electron Transport Layer. *Solar RRL* **3**, 1900050 (2019).

170. Roß, M. *et al*. Co-Evaporated Formamidinium Lead Iodide Based Perovskites with 1000 h Constant Stability for Fully Textured Monolithic Perovskite/Silicon Tandem Solar Cells. *Adv Energy Mater* **11**, 2101460 (2021).

171. Gil-Escrig, L. *et al*. Efficient Vacuum-Deposited Perovskite Solar Cells with Stable Cubic FA1–xMAxPbI3. *ACS Energy Lett* **5**, 3053–3061 (2020).

172. Paliwal, A., Zanoni, K. P. S., Roldán-Carmona, C., Hernández-Fenollosa, M. A. & Bolink, H. J. Fully vacuum-deposited perovskite solar cells in substrate configuration. *Matter* **6**, 3499–3508 (2023).

173. Li, W. *et al*. The critical role of composition-dependent intragrain planar defects in the performance of MA1–xFAxPbI3 perovskite solar cells. *Nat Energy* **6**, 624–632 (2021).

174. Kim, B.-S., Gil-Escrig, L., Sessolo, M. & Bolink, H. J. Deposition Kinetics and Compositional Control of Vacuum-Processed CH3NH3PbI3 Perovskite. *J Phys Chem Lett* **11**, 6852–6859 (2020).

175. Bi, D. *et al*. Efficient luminescent solar cells based on tailored mixed-cation perovskites. *Sci Adv* **2**, e1501170 (2024).

176. Ueoka, N. & Oku, T. Stability Characterization of PbI2-Added CH3NH3PbI3–xClx Photovoltaic Devices. *ACS Appl Mater Interfaces* **10**, 44443–44451 (2018).

177. Gordillo, G., Torres, O. G., Abella, M. C., Peña, J. C. & Virguez, O. Improving the stability of MAPbI3 films by using a new synthesis route. *Journal of Materials Research and Technology* **9**, 13759–13769 (2020).

178. Pareja-Rivera, C., Solís-Cambero, A. L., Sánchez-Torres, M., Lima, E. & Solis-Ibarra, D. On the True Composition of Mixed-Cation Perovskite Films. *ACS Energy Lett* **3**, 2366–2367 (2018).

179. Valenzano, V. *et al*. Methylammonium-formamidinium reactivity in aged organometal halide perovskite inks. *Cell Rep Phys Sci* **2**, (2021).

180. Bravetti, G. *et al*. Solution Aging Promotes the Formation of Hexagonal Polytypes in Mixed-Cation/-Halide Perovskites. *Chemistry of Materials* **36**, 3150–3163 (2024).

181. Van Gompel, W. T. M. *et al*. Degradation of the Formamidinium Cation and the Quantification of the Formamidinium–Methylammonium Ratio in Lead Iodide Hybrid Perovskites by Nuclear Magnetic Resonance Spectroscopy. *The Journal of Physical Chemistry C* **122**, 4117–4124 (2018).

182. Gil-Escrig, L. *et al*. Efficient Vacuum-Deposited Perovskite Solar Cells with Stable Cubic FA1–xMAxPbI3. *ACS Energy Lett* **5**, 3053–3061 (2020).

183. Paliwal, A., Zanoni, K. P. S., Roldán-Carmona, C., Hernández-Fenollosa, M. A. & Bolink, H. J. Fully vacuum-deposited perovskite solar cells in substrate configuration. *Matter* **6**, 3499–3508 (2023).

184. Rodkey, N. *et al*. Efficient Micrometer Thick Bifacial Perovskite Solar Cells. *Adv Energy Mater* **14**, 2400058 (2024).

185. Koopmans, M., Corre, V. & Koster, L. SIMsalabim: An open-source drift-diffusion simulator for semiconductor devices. *J Open Source Softw* **7**, 3727 (2022).

186. Sherkar, T. S. *et al*. Recombination in Perovskite Solar Cells: Significance of Grain Boundaries, Interface Traps, and Defect Ions. *ACS Energy Lett* **2**, 1214–1222 (2017).

187. Rodkey, N. *et al*. Close-Space Sublimation as a Scalable Method for Perovskite Solar Cells. *ACS Energy Lett* **9**, 927–933 (2024).

188. Park, N.-G. & Zhu, K. Scalable fabrication and coating methods for perovskite solar cells and solar modules. *Nat Rev Mater* **5**, 333–350 (2020).

189. Wang, F., Bai, S., Tress, W., Hagfeldt, A. & Gao, F. Defects engineering for high-performance perovskite solar cells. *npj Flexible Electronics* **2**, 22 (2018).

190. Li, H. *et al*. Applications of vacuum vapor deposition for perovskite solar cells: A progress review. *iEnergy* **1**, 434–452 (2022).

191. Ye, T. *et al*. Large area, high efficiency and stable perovskite solar cells enabled by fine control of intermediate phase. *Solar Energy Materials and Solar Cells* **201**, 110113 (2019).

192. Li, J. *et al*. Design of Perovskite Thermally Co-Evaporated Highly Efficient Mini-Modules with High Geometrical Fill Factors. *Solar RRL* **4**, 2000473 (2020).

193. Burkitt, D. *et al*. Roll-to-roll slot-die coated P–I–N perovskite solar cells using acetonitrile based single step perovskite solvent system. *Sustain Energy Fuels* **4**, 3340–3351 (2020).

194. Li, J. *et al*. Design of Perovskite Thermally Co-Evaporated Highly Efficient Mini-Modules with High Geometrical Fill Factors. *Solar RRL* **4**, 2000473 (2020).

195. Chiang, Y.-H. *et al*. Efficient all-perovskite tandem solar cells by dual-interface optimisation of vacuum-deposited wide-bandgap perovskite. (2022).

196. Ritzer, D. B. *et al*. Upscaling of perovskite solar modules: The synergy of fully evaporated layer fabrication and all-laser-scribed interconnections. *Progress in Photovoltaics: Research and Applications* **30**, 360–373 (2022).

197. Tan, L. *et al*. Combined Vacuum Evaporation and Solution Process for High-Efficiency Large-Area Perovskite Solar Cells with Exceptional Reproducibility. *Advanced Materials* **35**, 2205027 (2023).

198. Di Giacomo, F., Castriotta, L. A., Matteocci, F. & Di Carlo, A. Beyond 99.5% Geometrical Fill Factor in Perovskite Solar Minimodules with Advanced Laser Structuring. *Adv Energy Mater* **14**, 2400115 (2024).

199. Rakocevic, L. *et al*. Perovskite modules with 99% geometrical fill factor using point contact interconnections design. *Progress in Photovoltaics: Research and Applications* **28**, 1120–1127 (2020).

200. Flick, A. C., Rolston, N. & Dauskardt, R. H. Indirect Liftoff Mechanism for High-Throughput, Single-Source Laser Scribing for Perovskite Solar Modules. *Adv Energy Mater* **14**, 2303175 (2024).

201. Moon, S.-J. *et al*. Laser-Scribing Patterning for the Production of Organometallic Halide Perovskite Solar Modules. *IEEE J Photovolt* **5**, 1087–1092 (2015).

202. Wang, Z. *et al*. One-step P2 scribing of organometal halide perovskite solar cells by picosecond laser of visible wavelength. *Appl Surf Sci* **505**, 144408 (2020).

203. Roß, M. *et al*. Co-Evaporated p-i-n Perovskite Solar Cells beyond 20% Efficiency: Impact of Substrate Temperature and Hole-Transport Layer. *ACS Appl Mater Interfaces* **12**, 39261–39272 (2020).

204. Gu, Z. *et al*. Interfacial engineering of self-assembled monolayer modified semi-roll-to-roll planar heterojunction perovskite solar cells on flexible substrates. *J Mater Chem A Mater* **3**, 24254–24260 (2015).

205. Liu, L. *et al*. Fully Printable Mesoscopic Perovskite Solar Cells with Organic Silane Self-Assembled Monolayer. *J Am Chem Soc* **137**, 1790–1793 (2015).

206. Xiao, K. *et al*. Scalable processing for realizing 21.7%-efficient all-perovskite tandem solar modules. *Science (1979)* **376**, 762–767 (2022).

207. Futscher, M. H. *et al*. Quantification of ion migration in CH3NH3PbI3 perovskite solar cells by transient capacitance measurements. *Mater Horiz* **6**, 1497–1503 (2019).

208. Zhang, T. *et al*. Profiling the organic cation-dependent degradation of organolead halide perovskite solar cells. *J Mater Chem A Mater* **5**, 1103–1111 (2017).

209. Tan, W., Bowring, A. R., Meng, A. C., McGehee, M. D. & McIntyre, P. C. Thermal Stability of Mixed Cation Metal Halide Perovskites in Air. *ACS Appl Mater Interfaces* **10**, 5485–5491 (2018).

210. Turren-Cruz, S.-H., Hagfeldt, A. & Saliba, M. Methylammonium-free, high-performance, and stable perovskite solar cells on a planar architecture. *Science (1979)* **362**, 449–453 (2018).

Acknowledgment:

First and foremost, I would like to thank **Henk** for being the most understanding boss that ever existed. I am so lucky that you chose me as an outsider to join your group. It is very rare to meet someone who is devoting himself to research, meanwhile changing life and shaping the careers of so many people with his social and scientific intelligence. You are the best boss I have ever had. I have told you this so many times, however I have no words for your understanding and consideration during the ups and downs of my life and the change you have made in my life. You would always remain an important figure in my life wherever I would be. Thank you for making my difficult life easier during these years. It has been so good that it makes saying goodbye almost impossible.

Cristina, thank you! Being your first PhD student is something I will always remember. I came a very long way from the very first messy graphs to almost perfect ones, some “cutre” ones in the middle of the way. We definitely made a journey together with many ups and downs, you as a supervisor and me as a PhD student. I hope after this you will continue with more ups, and you grow as much as you deserve!

Michele, thank you for your forever guidance and tips on science career decisions, wine and eventual cigarettes. You are not the man of many words, but your few selected words are always helpful. I was very happy to be there to see your achievements(specially a permanent position) which have been well-deserved and long overdue.

Lidón, your dedication to work is exemplary for me. I have asked you hundred thousand of questions, and you answered all of them patiently, thank you so much! Where do you find the stamina to work so much and so perfect?! You are a true hero, and the labs would not survive without you. It was very nice going to Pilates with you. Thank you for being an example of success these years in the lab for me.

Kassio, thank you for your dark sarcasm. You know that my love language is teasing another, and you get it very right. I guess people who suffer enough develop that. You are the only person who gets that. Thank you for being the louder complainer in the lab so I am not the only one! Thank you for teaching me many many things, starting from evaporator 2 to NMR and always answering my mostly dumb questions. I can seriously admit that without you this would never have been possible. Thank you for listening to my complaints, breakdowns and eventual emotional crying. Thank you for waiting 1 hour in Singapore airport when I got detained! Always remember we have to go back again eventually so be prepared for at least one hour of waiting! I believe you deserve more than you have, and you always underestimate yourself. Know your worth and believe in yourself. I believe in you, a lot! I believe in your kind spirit, beautiful soul(not Saul, I believe in him as well though) and intelligent mind. Nunca pare de ser um idiota! Você está fazendo um

favor ao mundo dizendo coisas que os outros não dizem. Sempre permaneça corajoso, meu amigo.

Paz, Paz, Paz the first day that I saw you I never thought I would want you to stay my friend forever. Your kindness and beautiful heart have helped me a lot during hard times and gave me warm feeling that there is someone that I can always go to and she would always help me with my hundred thousand problems from complaint forms from airlines to my emotional problems and she is a true friend who really cares. This is very rare, and I cherish it truly. We travelled and went to many conferences together; we giggled a lot over who knows what but my highlight is your wedding. I was truly honored when I got an invitation. You have no idea what it means for an immigrant to go to a wedding in the destination country and feel like a family. My first Spanish wedding with napkins stirring in the air and limitless reggaeton playlist! It still feels like a dream! Thank you for highlighting my doctorate with support and laughter. I learned a lot from you in many ways. Thank you for translating Persian texts and writing speeches with me even if you don't understand them. Continue being amazing or just simply Paz! també deixar de guanyar tots els preus del món!

Lucia, honey, I am so happy you decided to start a PhD in Covid time, how else would I find a friend like you? You do so many activities that you are never in the same place for a long time to be found! You are a hard worker, and you have always tried to be helpful to me even by explaining dark current to me hundred times! Thank you for being the energy by my side even on the sad days. Thank you for painting me a souvenir that I am going to cherish forever. Thank you for having my back in protests even if it is not your fight. And thank you for being so self-sufficient to repair the souvenir that I brought you. Te quiero mucho!

Isabella, you had a designated place in the office before you even arrived. I was so happy to have you there being all calm but remembering every single details about every conversations you ever had. It is amazing! You are becoming the new me by writing. It is the most difficult time ever but eventually it will pass. I am here for you, and I know that you can do this. I think you are the sweetest person in our group.

Isidora, you are the first "international friend" that Henk introduced to me and said I can ask all my immigration questions from her. We called the office, and you were not back from the Holiday´s trip yet. It was Jan so you were celebrating Christmas! Of course, I didn't know on that time how close we are going to become through all these years suffering from the same "It is such a disaster" problems. Thank you for always being there for me and providing support and listening to my never ending tragedies and problems. Thank you for making the office bearable with you "á la mode" fashion styles. I will truly miss your daily compliments. I am very

proud of how independent you become. We made a journey together and I am sure you will continue to grow and become super successful in the future. Волим те, мој модни моделу.

Bas, Thank you for your high spirit. Having you in the group made me very happy. Maybe it was the alcoholic you made us though! We worked many hours together and it was always nice to have you there after a long day. Thank you for helping me with broken Dutch in Belgium in finding a house! I am sure you would be successful wherever you are, and I am happy to know that there is a slight possibility you would settle in one place after so much time! Verlies nooit je vriendelijke geest en zorg goed voor mijn goede vriend.

Chris, it has been a true privilege to work with someone who knows so many things and having discussions that opens so many doors showing me how much I do not know! Your calmness has always been helpful even in stressful situations. I am sure you will continue in science for science path and truly enjoy it. I remember you told me the very first night we went out to try to be more like Kassio and let go! Haha! It was very nice! I don't know where I and you are going to end up, but I hope next time you would come to visit! Versuche, deine Dissertation schließlich zu verteidigen. Glaub mir, ich weiß, dass es schwer ist, aber irgendwann müssen wir es alle tun, auch wenn wir nicht genug Anleitung haben!

Abhyuday, you have always been my company during the night working hours, and we have spent many Christmas nights being the last people to leave and had many conversations regarding work. Taking care of evaporator 2. Your dance moves in the cleanroom and your energy have definitely been helpful with long hours. Continue rocking science in Germany and being a husband! Also, I am writing your full name because you never gave me a nickname!

آذین، از روز اول اومدنم به والنسیا کمک هات شروع شد، شاید دوستیمون ۲ ساله که نزدیک شده ولی ساپورت های عاطفیت از همون اول شروع شده، ممنونم که تو زندگیم اومدی و به درددل های بدون پایانم گوش کردی و همیشه بهم باور داشتی. بدون تو خیلی سخت میشد. مرسی که با اینکه کارهایی کردم که اذیتت کرد دوستیمون برات انقدر مهم بود که حلش کنیم.پیدا کردن همچین دوستی تو غربت مثل بردن بلیط بخت آزمایی میمونه. از کوین Kevin هم ممنونم برای ساپورتاش و خیلی خوشحالم که شما دوتا رو دارم،(اول خواستم براش اسپانیایی بنویسم ولی اگه تو براش ترجمه کنی به نظر نرمال تره) امیدوارم موفق بشی (و بشم) که من رو نزدیک نگه داری!

María, the PhD starts and finishes with you. This is the real truth. Without you no work will be done. Sorry for making so many mistakes with everything that you asked! I came here when you gave birth, and I am living with knowing your beautiful daughter. I enjoyed our deep conversations in the office on the 3rd floor, but I enjoy more the ones done over Merinda in Benimaclet with our profesora "Balma". You have helped me with many things over these years from university to my house. I

appreciate you in my life and hope to be around to continue our lunch/merienda meetings. Thank you for all the help and thank you for caring about my country.

Dani Tordera, Thank you for making tin-lead a paper even if it was completely hopeless and thank you for being understanding with my breakdowns. Thank you for inviting me to your beach house and giving us delicious paella.

Dani Peréz, you were the one who taught me how to use the molecular which is now called evaporator 2. It became all remote access after you, sorry! Everyone have always told me Dani has the record in the group, and I have always looked up to you in that case, you are not anymore though! Thank you for teaching me the lab. I have learned from the best!

Fede, it has always been very nice to have someone who knows what it feels to be a non-European immigrant. Thank you for caring about what is happening in my country and backing me up. I remember once that I had a not acceptable presentation you cheered me up by saying it was fine. I knew it was not but hearing it from you helped me get myself together. I hope both our countries someday will be a place that we want to go back to live in them!

Javi, it is amazing how moments can change life. I was there when your life changed. I take credit for selling MOED group so well that you were tempted to be a part of it. Of course, I regret it right away, haha, but it was already done! It has been nice getting to know you and I truly believe you are a good human being with a good heart and that will help you find the best place in the world. Here I give SAMs to you, take good care of them!

Inma, you have a lot of energy and a good heart. I am sure you will be successful wherever you go. Having your energy has always been heartwarming even if it is too much because it is very real. I am proud of you for your mindset! Thank you for caring about women in my country and supporting me on this. We, women in science will continue to fight our way in the world, yes, we can!

Gracias, **Jorge,** por estar siempre ahí y por responder a los miles de problemas que causé. Sin ti, de verdad, nada de esto habría sido posible y ninguno de nosotros llegado a ser doctor. Realmente creo que eres un genio, y MOED tiene muchísima suerte de tenerte. Piensas que arreglar cosas rotas no es importante, pero créeme, todos estamos rotos de alguna manera. Todos necesitamos a alguien que arregle. Este es un trabajo muy importante.

Joost, chicken curry sandwiches for breakfast, yes that is the first thing I remember when I think about you. You have been in the group before but I was not the whole time here so I am glad you came back and became a permanent member so we would have a chance to go to Strasbourg together. Thank you for making it more fun. I found out how fun you are there. Except when I ask you to turn on my PC

and you make stickers out of my silly profile pic. Toon wat respect voor de privacy van mensen, man!

Сергій (Serhii I hope it is correct if it's not I am sure you would remind me), thank you for always knowing more about my country than me. It is very refreshing to know someone that knows so many things and it is very logical, and fact orientated. I enjoyed our conversations a lot. I hope both our countries will be free and prosperous in the near future. But finish your PhD first! The photo detectors need you.

Michelino, you are a disciplined and clean worker. You took care of evaporator 1 and made it better and automated. That is amazing. I know you will be a successful scientist in the future. The bikes come and go, the thieves are always there. Just live your life. I will always remember you saying that me being robbed made you feel better about your bike being stolen! If someone robs me again, I will let you know ASAP!

Lennart, I am happy to have met you. Thank you for being understanding with my peculiar nature. I really appreciate someone who can take criticism even if they don't like it and only talk about this when they are drunk! I believe that you are a valuable addition to the group, and I am proud of your fighter spirit. I think that is because we share the same trait. I hope that the secret project that I cannot write here which starts with "V.." would bring you and the group so many success and papers published.

I would also like to thank other group members **Paco, Nathan, Lorenzo, Manu, Sang, Laura, Anna, Jorge Avila, Yous, Beom-soo, Sang, Sofia, Ana, Alejandra, Maxi, Vlado, Yun, Carsen**.

Genk´s Gang:

Tom, thank you for having me as a part of your group. I have learned a lot and felt very important to give a talk for the thin film PV in Energyville. Please do it again. I promise to make it shorter next time. I hope you recover ASAP.

Arantxa, gracias por apoyarme desde el primer día y por ser siempre comprensivo y atento conmigo. ¡Gracias por todo el chocolate que me diste! Gracias por llevarme en tu coche a Lovaina para recoger mi tarjeta, pero, más importante aún, gracias por confiarme tu querido láser y enseñarme con paciencia sobre los minimódulos, que conformaron un capítulo de esta tesis. Sin ti, esta tesis perdería un capítulo.

Tamara, thank you for teaching me everything in the lab. I came to you so many times with questions and you always responded welcomingly and with laughter.

Yinghuan, thank you for showing interest in my research and always helping. Your guidance has been very valuable. First in science and later in an immigrant life. We had many car conversations and lunch conversations regarding our lives, adult decisions and how it changes you. Your insight has always been super helpful. 你是我的答辩委员会成员，所以我在这里不能多说！

Cristian, Gracias por encargarte de mí desorden en el laboratorio y por enseñarme tantas cosas. También gracias por escuchar pacientemente mis preguntas tontas y responderlas. Ha sido un placer trabajar contigo en el laboratorio. Además, gracias por acompañarme en bicicleta de regreso a la ciudad cuando no tenía luz por la noche. Espero que puedas defender tu tesis pronto también. Y publica ese 20% de FAPI lo antes posible.

Brecht, thank you for making my suffering easier with your dad delivering me a microwave! You keep reminding me but believe me I need no reminder!

I would also like to thank other colleagues in Imec, **Anurag, Sujit, Sownder, Stijn, Dennis, Silvia** and **Selin** for the friendship and smiley faces.

مامان،فروزنده مدارا، ممنونم برای تموم چیزهایی که ازشون گذشتی تا من بتونم آینده بهتری داشته باشم، متشکرم برای ساپورت کردن من توی این سالها با تموم بالا و پایینایی که داشتیم. مرسی برای مستقل تربیت کردنم تا من بتونم مهاجرت کنم و روی پای خودم وایسم. ممنونم ازت که با وجود تموم دردی که برات داشت، قبول کردی دختری که بزرگ کردی ازت دور باشه و نبینیش به قیمت موفقیتش. بدون تو نمیشد !

بابا،حمیدرضا معینی، ممنونم برای باوری که همیشه بهم داشتی و اجازه دادی که ریسک کنم و دل به دریا بزنم، مرسی برای تمام فشارایی تحمل کردی و حرفهایی که با سختی شنیدی تا بچه هات موفق بشن، بدون تو و باوری که بهم داشتی من هیچ وقت نمیتونستم کار سخت مهاجرت و تحصیل توی یک کشور خارجی رو انجام بدم. ممنونم که حامیم بودی !

میخوام این کتاب رو به خاطره **بابزرگ** تقدیم کنم، جاش برام خیلی خالیه ولی مطمئنم که خیلی خوشحال میشد از دکتر شدن نوه بزرگش.

ممنونم از همه اعضای خانواده ام، **مادربزرگهام، خاله هام، عمه هام، کازینام، عمو** و **دایی** هام و همه بستگان دور و نزدیک !

خشایار، این راه رو باهم رفتیم، روزهای سختی رو گذروندیم، هیچ کس اندازه تو این بالا پایین ها رو از نزدیک ندید و با پوست و جونش حس نکرد، با هم صیغل خوردیم و با موجهاش بالا پایین رفتیم. داشتنت توی این سالها بی تردید نقش خیلی مهمی داشت، ممنونم از کمک هات، درکت و آرامشت. میدونم که آینده هر دومون هرچی که توش باشه خیلی روشنه. همینجور ادامه بده موفقیت خیلی نزدیکه!

غزاله، خوشحالم که انقدری صبر کردیم تا بالاخره تو قصه ات رو باهامون در میون بذاری، خیلی طول کشید ولی ارزشش رو داشت. تو برای من الگو پشتکار و محبت بی نهایت بدون هیچ چشم داشتی هستی. ممنونم که خواهری رو برام تموم کردی مخصوصا توی روزهای سخت آخر.

شبنم، ممنونم برای تمام حرف های روانشناسی و تحلیل هایی که با هم کردیم. خیلی توی روحیات من تأثیر داشت وبهم اعتماد بنفس داد. خوشحالم که والنسیا موندی و تونستم بیشتر نزدیک داشته باشمت، حتی اگر روی میوت باشی !

Fernando, thank you for being the most welcoming host ever and all those rides. Thank you for always trying to get us all together with our crazy schedule.

مریم، ممنون که راه مهاجرت و خوندن دکترا رو هموار کردی و نشون دادی که سخته ولی ما میتونیم. مرسی که اون دوستی بودی که توی سخت ترین روزهام میتونم بهش رجوع کنم حتی اگر ۲ ساله که ازش خبر ندارم. مرسی که همیشه آدم منطقی زندگی من میمونی و خیلی واضح بهم میگی اینجا اشتباه کردی و دلیلش رو هم توضیح میدی! تو تنها کسی که میتونه این کارو بکنه. **بهنام،** ببین مجبورم از تو هم تشکر کنم ولی تو به خودت نگیر :))) مرسی که اومدین والنسیا تا منو ببینین، خیلی برام ارزش داشت، بازم بیاین لطفا !

بهار جون مرسی برای تمام وقت و انرژی که برای طراحی کاور گذاشتید، تونستید که همون چیزی که میخواستم رو به تصویر بکشید، ببخشید که انقدر اذیتتون کردم!

حسام، ممنون برای تمام این سالها و خاطراتی که باهم ساختیم. مرسی برای تمام کمک های دیجیتالی. برات آینده خوب و روشنی آرزو دارم هرکجا که مقصدت باشه.

حمید، حامد، ثارالله، مینا، مینا، شیرین، سارا ،نغمه، امید خیلی ازتون ممنونم که دلم رو گرم کردید و برام نقطه عطف روزهای کاریم و سیزده بدرم بودید. شناختن شما و داشتنتون باعث افتخار منه. خیلی خوشحالم که همه چی جور شد تا شماهارو بشناسم. دلدور دلدور